Dithiocarbamate Complexes as Single Source Precursors to Metal Sulfide Nanoparticles for Applications in Catalysis

This thesis is submitted in partial fulfilment of the requirements for the degree of Doctor of Philosophy (Chemistry)

Anna Rose Roffey

Supervised by Dr Graeme Hogarth

University College London

Christopher Ingold Building

20 Gordon Street

WC1H 0AJ

I, Anna Roffey, confirm that the work presented in this thesis is my own. Where information has been derived from other sources, I confirm that this has been indicated in the thesis.

_____

Abstract

Herein we report the solvothermal decomposition of a range of metal dithiocarbamate complexes for the synthesis of metal sulfide nanoparticles. Metal sulfides exist in a variety of structural phases, some of which are known to be catalytically active towards various processes. The aim of this work was to synthesise a variety of different metal sulfide phases for future catalysis testing, particularly the iron sulfide greigite (Fe_3S_4, a thiospinel containing Fe^{2+} and Fe^{3+}) which is to be tested for CO_2 reduction.

A range of metal dithiocarbamate complexes were synthesised and Chapter 2 focusses on the synthesis of iron dithiocarbamates. Both iron(II) and iron(III) complexes were synthesised, the latter being a facile, open bench reaction producing a range of [$Fe(S_2CNRR')_3$] complexes. Iron(II) bis(dithiocarbamates) are extremely air sensitive therefore carbonyl protected [$Fe(S_2CNRR')_2(CO)_2$] complexes were prepared for ease of use as precursors. The stability of the complexes was tested by TGA to ensure they were suitable precursors for metal sulfide synthesis, *i.e.* that the carbonyl ligands were sufficiently labile to leave the complexes before decomposition, which proved to be successful.

In the following Chapter these iron dithiocarbamate complexes were solvothermally decomposed, but interestingly a combination of iron(II) and iron(III) precursors did not produce greigite as expected, but pyrrhotite (Fe_7S_8, containing only Fe^{2+}). Systematic studies into the effect of decomposition temperature, precursor concentration and precursor type, on the phase and morphology of the resulting iron sulfide nanoparticles were performed on the iron(III) dithiocarbamate precursor. The phase was found to be highly dependent on both concentration and temperature. The use of a redox active additive, thiuram disulfide, on the decomposition was also investigated and found to have a significant effect, promoting the formation of the metastable greigite phase.

Chapter 4 examines the nickel bis(dithiocarbamate) decomposition system to see if its behaviour was consistent with trends observed in the iron case. In general, similar trends were observed in the phase and morphology of the nickel sulfides when the decomposition parameters were varied, metastable phases were observed at lower temperature and higher concentration. The effect of thiuram disulfide on the system was greater, however, than in the iron case, whereby an additional nickel sulfide phase (NiS_2) was observed at high concentration in the presence of this additive.

Chapter 5 deals with a broader range of metal dithiocarbamate systems, to attempt to elucidate whether or not the trends seen for nickel and iron are universal for metal dithiocarbamate precursors. The Co, Cu, Zn and In dithiocarbamate systems were examined with and without thiuram disulfide, and some effect were seen on the phase of metal sulfide nanoparticle formed, but only at high concentration in the presence of the additive. Mixed-metal studies were performed to investigate the suitability of metal dithiocarbamates as precursors to ternary metal sulfides, and success was observed for iron-nickel, cobalt-nickel and iron-copper sulfides, though the iron-zinc and iron-indium systems only produced binary sulfides.

The final Chapter looks into the metal dithiocarbamate decomposition mechanism in detail, using $[Ni(S_2CN^iBu_2)_2]$ as a model system. NMR, *in situ* UV-vis, MS and powder XRD are all employed to probe the mechanism, in conjunction with XAS and computer modelling which was performed by others. The mechanism was found to rely heavily on an intermediate formed from amide exchange between the dithiocarbamate backbone and solvent amine, indicating the solvent plays an extremely significant role in the solvothermal synthesis of metal sulfides from dithiocarbamate precursors.

Acknowledgements

The last three and a half years have been, at times, enormously enjoyable, and as a whole, extremely formative. I would like to thank my supervisor, Dr Graeme Hogarth, for his guidance and for the very high standards he set, which pushed me to be better than I was. I would also like to thank the EPSRC for my studentship and Professor Nora de Leeuw for an extra 6 months funding.

I would particularly like to thank Dr Nathan Hollingsworth, for the guidance, support, unbounded enthusiasm and supervision he has provided me with at UCL, best PostDoc ever - Nathan you are a star! Thanks too to Abil Aliev, Steve firth and Gill Maxwell for their expert technical support.

To the people who encouraged me to go for this PhD and convinced me I could do it (Amaya Camara-Campos, Tim Simmance, Vibhuti Patel, Francesca Burgoyne and Byron Mitchell) – you are all in trouble. Seriously though, thank you all so much – without you I would not be here now.

I would like to thank my mum and sister for their unwavering support and for the freezer meals, invaluable. Special thanks too to Leanne Bloor, Isobel Rapoport, Neil Deacon, Steph Jones and Rob Downes for all their support and for putting up with the crazy.

Lastly, I would like to thank all the people who made this PhD so much fun: Penny Carmichael, Alison Cross, Pragna Kiri, Clair Chew, Ralph Leech, Nuru Noor, Pete Marchand, Husna Islam, Joe Bear, Joe Manzi, Nick Chadwick and the rest of 310.

Contents

Abstract iii

Acknowledgements v

Contents vi

Abbreviations x

List of Nomenclature xii

1 Introduction 1

1.1 Metal Sulfides 1

1.1.1 Applications in Catalysis 1

1.1.2 Structure 2

1.2 Nanoparticle Properties 4

1.3 Nanoparticle Synthesis 6

1.3.1 Theory 6

1.3.2 General Synthetic Methods 9

1.3.3 Solvothermal Synthesis 10

1.4 Precursors 13

1.4.1 Dithiocarbamate Ligands 14

1.5 Summary/Aims/Thesis Structure 15

1.6 References 15

2 Iron Dithiocarbamate Precursors 19

2.1 Introduction 19

2.1.1 Iron(III) tris(dithiocarbamate) Complexes 19

2.1.2 Iron(II) bis(dithiocarbamate) Complexes 21

2.1.3 Iron(II) bis(dithiocarbamate) Dicarbonyl Complexes 22

2.1.4 Precursor Choice 24

2.2 Results and Discussion 24

2.2.1 Iron(III) tris(dithiocarbamate) Complexes 24

2.2.2 Iron(II) bis(dithiocarbamate) Dicarbonyl Complexes 28
2.3 Conclusions 38
2.4 Experimental 39
2.5 References 46

3 Iron Sulfide Nanoparticles 48
3.1 Introduction 48
3.1.1 Decomposition of Non-Dithiocarbamate Single-Source Precursors 49
3.1.2 Decomposition of Dithiocarbamate Single-Source Precursors 52
3.2 Results and Discussion 53
3.3 Decomposition of Iron(II) Dithiocarbamate Precursors 54
3.3.1 Synthesis and Characterisation 55
3.3.2 Summary 57
3.4 Decomposition of Iron(III) Dithiocarbamate Precursors 57
3.4.1 Varying R-group 57
3.4.2 Varying Temperature 59
3.4.3 Varying Concentration 61
3.5 Decomposition of Iron(III) Dithiocarbamate Precursors with Thiuram Disulfide Additive 63
3.5.1 Varying Temperature 65
3.5.2 Varying Concentration 66
3.6 Conclusions 68
3.7 Experimental 68
3.8 References 70

4 Nickel Sulfide Nanoparticles 72
4.1 Introduction 72
4.1.1 Nickel Sulfide Nanoparticle Synthesis 72
4.1.2 Nickel Dithiocarbamate Complexes 75

4.2 Results and Discussion 76
4.3 Nickel Dithiocarbamate Complexes 76
4.3.1 Synthesis 76
4.3.2 Stability 78
4.4 Decomposition of Nickel(II) Dithiocarbamate Precursors 78
4.4.1 Varying R-group 79
4.4.2 Varying Temperature 81
4.4.3 Varying Concentration 83
4.5 Decompositions of Nickel(II) Dithiocarbamate Precursors with Thiuram Disulfide Additive 85
4.5.1 Varying Temperature 85
4.5.2 Varying Concentration 88
4.6 Conclusions 89
4.7 Experimental 90
4.8 References 94

5 Other Metal and Mixed-Metal Sulfides 96
5.1 Introduction 96
5.1.1 Cobalt Sulfides 97
5.1.2 Copper Sulfides 97
5.1.3 Zinc Sulfides 98
5.1.4 Indium Sulfide 99
5.1.5 Iron-Nickel Sulfides 99
5.1.6 Iron-Indium Sulfides 100
5.1.7 Iron-Zinc Sulfides 100
5.1.8 Iron-Copper Sulfides 101
5.1.9 Nickel-Cobalt Sulfides 101
5.2 Results and Discussion 102
5.2.1 Metal Dithiocarbamate Precursors 102

5.2.2 Binary Metal Sulfide Synthesis 103
5.2.3 Ternary Metal Sulfide Synthesis 109
5.3 Conclusions 122
5.4 Experimental 123
5.5 References 127

6 Decomposition Pathway Studies 130
6.1 Introduction 130
6.2 Results and Discussion 139
6.2.1 Nickel bis(dithiocarbamate) Precursor and Stability 139
6.2.2 Solvothermal Decomposition of $[Ni(S_2CN^iBu_2)_2]$ (21) 140
6.2.3 Nature of $[Ni(S_2CN^iBu_2)_2]$ (21) in *n*-hexylamine 141
6.2.4 Heating $[Ni(S_2CN^iBu_2)_2]$ (21) in *n*-hexylamine 143
6.2.5 Modelled Amide-Exchange 144
6.2.6 Solvothermal Decomposition of $[Ni(S_2CN\{H\}Hex)_2]$ (29) 145
6.2.7 Continued Monitoring of Solvothermal Decomposition of 21 in *n*-hexylamine 147
6.2.8 Monitoring the Solvothermal Decomposition of 21 in Oleylamine 148
6.2.9 Preliminary Iron and Zinc Dithiocarbamate Studies 151
6.3 Conclusions 152
6.4 Experimental 153
6.5 References 157

7 Conclusions and Future Work 159
7.1 Conclusions 159
7.2 Future Work 161

8 Appendix – Crystallographic Data 163

Abbreviations

Å	Ångström
acac	Acetylacetone
Anal.	Analysis
Bz	Benzyl
Calc.	Calculated
CI	Chemical ionisation
CVD	Chemical vapour deposition
d	Doublet
δ	Chemical shift / ppm
DCM	Dichloromethane
DDA	Dodecylamine
DDT	Dodecanethiol
DFT	Density function theory
DSC	Differential scanning calorimetry
EA	Elemental analysis
EDX	Energy-dispersive X-ray spectroscopy
EG	Ethylene glycol
EI-MS	Electron ionisation mass spectrometry
EN	Ethylenediamine
Et	Ethyl
g	Gram
GC-MS	Gas chromatography mass spectrometry
gHMBC	Gradient heteronuclear multiple-bond correlation
HDA	Hexadecylamine
hr	Hour
HPLC	High-performance liquid chromatography
^{i}Bu	Isobutyl
^{i}Pr	Isopropyl
IR	Infra-red
J	Coupling constant
m	Multiplet (NMR spectra)
Me	Methyl

4-MePip	4-Methylpiperidyl
2,6-Me_2Pip	2,6-Dimethylpiperidyl
mmol	Millimole
MOCVD	Metal organic chemical vapour deposition
MS	Mass spectroscopy
^{n}Bu	*n*-Butyl
NMR	Nuclear magnetic resonance
OA	Oleylamine
OD	Octadecene
OLA	Oleic acid
PEMFC	Proton-exchange membrane fuel cell
Pip	Piperidyl
ppm	Parts per million
q	Quartet (NMR spectra)
quin	Quintet (NMR spectra)
SEM	Scanning electron microscopy
t	Triplet (NMR spectra)
TEM	Transmission electron microscopy
TGA	Thermal gravimetric analysis
TLC	Thin layer chromoatography
TOP	Tri-*n*-octylphosphine
TOPO	Tri-*n*-octylphosphine oxide
TOPS	Tri-*n*-octylphosphine sulfide
UV-vis	Ultraviolet - visible
XAS	X-ray absorption spectroscopy
XRD	X-ray diffraction

List of Complex Nomenclature

1	$[Fe(S_2CNMe_2)_3]$
2	$[Fe(S_2CNEt_2)_3]$
3	$[Fe(S_2CN^iBu_2)_3]$
4	$[Fe(S_2CNMeBu)_3]$
5	$[Fe(S_2C(4\text{-}MePip))_3]$
6	$(S_2CN^iBu_2)_2$
7	$[Me_2NH_2][S_2CNMe_2]$
8	$[^iBu_2NH_2][S_2CN^iBu_2]$
9	$[4\text{-}MePipH_2][S_2C(4\text{-}MePip)]$
10	$[2,6\text{-}Me_2PipH_2][S_2C(2,6\text{-}Me_2Pip)]$
11	$[NMe_4][S_2CNEt_2]$
12	$[NMe_4][S_2CNMeBu]$
13	$[Fe(S_2CNMe_2)_2(CO)_2]$
14	$[Fe(S_2CNEt_2)_2(CO)_2]$
15	$[Fe(S_2CN^iBu_2)_2(CO)_2]$
16	$[Fe(S_2CNMeBu_2)_2(CO)_2]$
17	$[Fe(S_2C(4\text{-}MePip))_2(CO)_2]$
18	$[Fe(S_2C(2,6\text{-}Me_2Pip))_2(CO)_2]$
19	$[Ni(S_2CNMe_2)_2]$
20	$[Ni(S_2CNEt_2)_2]$
21	$[Ni(S_2CN^iBu_2)_2]$
22	$[Ni(S_2CNMeBu)_2]$
23	$[Ni(S_2C(4\text{-}MePip))_2]$
24	$[Co(S_2CN^iBu_2)_3]$
25	$[Cu(S_2CN^iBu_2)_2]$
26	$[Zn(S_2CN^iBu_2)_2]$
27	$[In(S_2CN^iBu_2)_3]$
28	$[Ni(S_2CN^iBu_2)(S_2CNH^nHex)]$
29	$[Ni(S_2CNH^nHex)_2]$
30	$[Ni(S_2CN^iBu_2)(S_2CNHC_{18}H_{35})]$

1 Introduction

1.1 Metal Sulfides

Metal sulfides are both abundant and cheap, in part due to the natural occurrence of many types in the earth's crust. Their chemistry is a rich field due to the wide range of known metal sulfide phases and their diverse properties. Bulk metal sulfide materials are used industrially for a variety of applications such as pigments, luminescent materials for cathode ray tubes, lubricants and in the production of sulphuric acid.[1–3] Nanoparticulate metal sulfides find further uses through their enhanced, size-dependant properties (see Section 1.2), including in fuel cells, solar cells, light emitting diodes, sensors, thermoelectric devices, lithium ion batteries, supercapacitors and memory devices, together with a range of catalytic applications which will be developed below.[4–11]

1.1.1 Applications in Catalysis

There are several well-established catalytic uses for metal sulfide materials, one being the hydrodesulfurization of fuels.[12–15] Here metal sulfides are employed to reduce sulfur dioxide emissions from the automotive industry, combustion fuels and oil-burning power plants. Typically the fuel is passed through a fixed-bed reactor at elevated temperature and pressure, where sulfur impurities such as benzothiophenes are reduced with hydrogen rich gas to produce hydrogen sulfide (H_2S) with the aid of a metal sulfide catalyst. Typical catalysts for this process include molybdenum sulfide and/or nickel and cobalt sulfides.[12–15] Nickel sulfides are also used as hydrogenation catalysts for the selective hydrogenation of chloronitrobenzene, the product of which, chloroaniline, is a useful chemical intermediate.[16]

As mentioned in Section 1.1, metal sulfides find applications in fuel cells, specifically proton exchange membrane fuel cells (PEMFCs) which are a potential alternative to fossil fuels.[17] PEMFCs use the chemical energy generated from the electrochemical reaction between hydrogen and oxygen and transform it into electrical energy. In PEMFCs the cathode and anode are separated by a membrane which allows only protons to pass. Hydrogen dissociates at the anode to form protons which pass through to the cathode side, reacting with oxygen which is reduced using a catalyst. Thus far, platinum based catalysts are used for the oxygen reduction reaction (ORR), but metal sulfides such as

CoS_2, NiS_2 and FeS_2 have been shown to have potential as effective, cheaper alternatives.[18, 19]

Conversely, metal sulfides have also shown potential as catalysts for the hydrogen evolution reaction (HER), where hydrogen is produced from water splitting for subsequent use in PEMFCs.[20, 21] Without the use of a catalyst, high overpotentials are required in order to electrochemically split water. Currently, platinum-based catalysts are used but platinum metal is expensive and scarce, so alternatives are being investigated. Molybdenum sulfide, in the form of crystalline MoS_2 and amorphous phases, has shown potential as cheaper, effective alternatives.[20, 21]

Iron and nickel sulfides have recently been suggested as potential CO_2 catalysts, through their suggested involvement in the origin of life.[22–27] Organisms able to reduce CO_2 to formate under mild conditions exist in nature, such as carbon monoxide dehydrogenase (CODH) and acetyl-coenzyme-A (CoA), and often possess an Fe_4S_4 cubane-like cluster at or very near to their active sites.[23, 28–30] This cluster is structurally similar to the repeating unit in the iron sulfide mineral greigite – which is found naturally occurring at hydrothermal vents in the ocean floor.[31, 32] The structural similarity between greigite and these enzymes have led to the iron-sulfur membrane theory, which proposes that iron sulfide membranes which were formed around 4 billion years ago on the Hadean ocean floor, were catalysts for the reduction of dissolved CO_2 in sea water to form the early molecules of life. [31, 33, 34] Nickel is also suggested as important for this catalysis,[34] often appearing alongside the Fe_4S_4 cluster in enzymes,[28] and as a common impurity in greigite.[32]

1.1.2 Structure

Metal sulfides exist in a variety of phases and naturally occurring examples, such as pyrite (FeS), chalcocite (Cu_2S) and millerite (β-NiS), are referred to as minerals. Properties of metal sulfides are structure dependant – pyrite (FeS_2) is a room temperature semiconductor, while pyrrhotite ($Fe_{1-x}S$) is not, making an understanding of the structure important when investigating the synthesis of different sulfides.[32] Of the numerous known metal sulfides, the work in this thesis focusses upon, but is not limited to, the chemistry of iron and nickel sulfide nanoparticles, so the structure of these species will be considered in some detail.

Material	Composition
Mackinawite	FeS
Pyrrhotite	$Fe_{1-x}S$ ($0 \leq x \leq 0.125$)
Smythite	Fe_9S_{11}
Greigite	Fe_3S_4
Pyrite	FeS_2
Marcasite	FeS_2

Table 1-1 - Selected iron sulfide mineral phases

Iron sulfides have been widely studied, as summarised in a comprehensive review by Rickard and Luther.[32] There are at least seven naturally occurring phases of iron sulfide, (a selection is shown in Table 1-1). Amongst the most interesting is greigite (Fe_3S_4), a potential CO_2 reduction catalyst (see Section 1.1.1). Greigite is a thiospinel, possessing iron in both the +2 and +3 oxidation states, along with S^{2-} ions (Figure 1-1). It has a cubic unit cell consisting of eight AB_2S_4 units, with Fe^{3+} cations situated in the tetrahedral A - sites, and both Fe^{2+} and Fe^{3+} ions in the octahedral B – sites.[32, 35] This makes it an inverse spinel structure (in a regular spinel the metal 2+ ions sit on the A - sites and the metal 3+ ions on the B - sites).

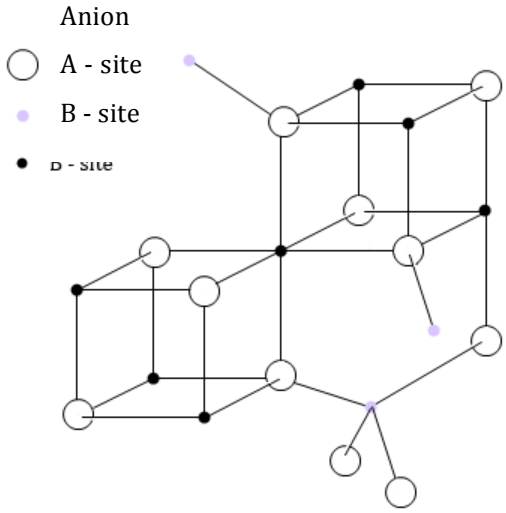

Figure 1-1 - The thiospinel structure showing tetrahedral A - cation sites and octahedral B - cation sites.

Another common iron sulfide is pyrrhotite, though this can actually be thought of as the name of a group of structurally related iron sulfide phases. The pyrrhotite group has the structure $Fe_{1-x}S$ ($0 \leq x \leq 0.125$), where troilite ($x = 0$) is the end member.[32] All pyrrhotites have a derivative of the NiAs structure (see Figure 1-2 for the NiAs structure). They are structurally complex, crystallising in hexagonal ($0 \leq x \leq 0.125$) or monoclinic systems ($0 <$

x < 0.125).[36] Briefly, the NiAs structure consists of hexagonal close packing of non-metal ions with metal ions in the octahedral holes. The non-metal ions have trigonal prismatic coordination (Figure 1-2).[37] Pyrrhotites can be found in several naturally occurring forms; 2C (troilite, FeS), 4C (most commonly occurring, Fe_7S_8) and 'NC', when N is an integer between 5 and 11. The composition varies due to the presence and ordering of vacancies within the NiAs structure.[38, 39]

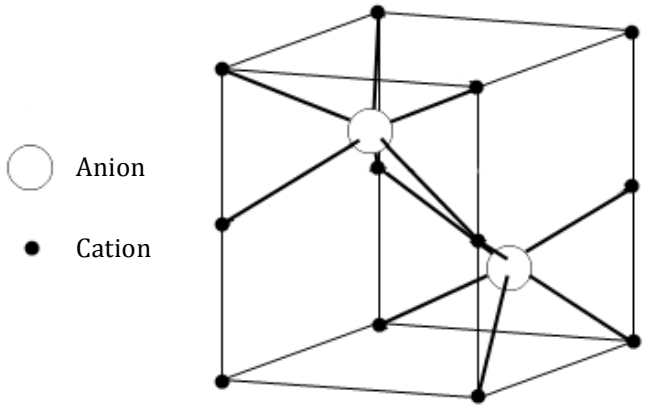

Figure 1-2 - NiAs structure showing trigonal prismatic coordination about the anions.

The binary nickel sulfide system is also complex, with even more known compositions than the iron sulfides. Naturally occurring minerals are; heazlewoodite (Ni_3S_2), polydymite (Ni_3S_4), millerite (β-NiS), vaesite (NiS_2) and godlevskite (Ni_9S_8), but many more have been synthesised including Ni_7S_6 and α-NiS.[40, 41] The NiS phase diagram was comprehensively investigated by Kullerund and Yund.[40] The α and β forms of NiS are polymorphs, α-NiS being the high temperature hexagonal form with NiAs structure (see Figure 1-2), and the β-NiS phase being the low temperature rhombohedral form.[4, 40, 42] Nickel sulfide has a thiospinel analogue, polydymite (Ni_3S_4), which, unlike greigite, takes the regular spinel structure.[43] There are various mixed iron and nickel sulfide phases possible, and interestingly the thiospinel violarite ($FeNi_2S_4$) takes on the inverse spinel structure.[44, 45, 35]

1.2 Nanoparticle Properties

The term 'nano' refers to the 10^{-9} m size regime and is typically considered to encompass material with at least one dimension measuring between 1 – 1000 nm.[46] It is the intermediate size range between bulk and molecular, and possesses properties distinct from those two species. Nanoparticles can be amorphous or crystalline, and in the latter case are sometimes referred to as nanocrystals. Dispersions of nanoparticles in liquid media are referred to as colloids and themselves possess distinct properties.

Size effects on gold nanoparticles were famously investigated by Michael Faraday as long ago as 1857.[47] The later emergence and potential of the field of nanoscience was foretold by Richard Feynman, in his 'There's Plenty of Room at the Bottom' talk at the American Chemical Society annual meeting in December 1959.[48] Developments in the field of nanoscience have necessarily accompanied developments in analytical techniques and equipment, exemplified in the 1925 Nobel Prize in Chemistry, awarded to Richard Zsigmondy for his work on metal colloids and the ultramicroscope.[49]

Nanoparticles possess unusual properties, differing from the bulk, which are partly due to their increased surface to volume ratio.[50] In addition, as particle diameter decreases, surface area per unit mass increases, such that nanoparticle materials have huge surface areas, in the range 100 – 1000 m^2/g.[46] Hence their activity towards any processes that occur at their surface (such as catalysis and sensing) is greatly increased compared to larger, bulk materials. Another consequence is a high surface energy, γ. The classical model to describe a nanoparticle depicts dangling bonds at the surface, where atoms are partially uncoordinated, which are reactive. The surface energy can be described using Equation 1-1, where n_{db} is the surface density of dangling bonds and ϕ is the energy of a dangling bond. The concentration of energy at the surface (the high γ in nanoparticles) can be reduced by surface functionalization to eliminate the dangling bonds.

$$\gamma = n_{db}\frac{\phi}{2}$$

Equation 1-1

Quantum size effects are another important outcome of the nanometre regime. One of the earliest observations of these effects was made by Faraday, who reported the red colour of colloidal gold solutions.[47] This feature is a direct consequence of surface plasmon resonance (SPR), which leads to the absorption profile of a nanoparticle being governed by its size.[51] When the wavelength of an electromagnetic wave directed at a nanoparticle is much greater than the particle diameter, electrons in its conduction band interact with the light such that a collective oscillation across the entire particle results.[52] A very strong SPR absorption is observed when the oscillation of the particles is equivalent to the oscillation of the electric field of the light wave, hence as the diameter of the particle varies, the wavelength of the light wave absorbed for SPR changes.[52]

Another quantum size property in nanoparticles is the quantum confinement effect. This is observed in semiconducting nanoparticles (quantum dots) and relates the band gap of the

material to the size of the nanoparticles. In a bulk semiconductor material the conduction and valance bands are separated by a band gap which is small enough to be overcome by exciting the system (for example heating). When an electron is promoted to the conduction band a hole is left in the valence band, and the pair are known as an exciton (a quasiparticle). An exciton is analogous to a hydrogen atom, comprising one electron and one positive charge at the nucleus. Due to shielding of the hole by other electrons and the small effective masses involved, the binding energy in the exciton is lower than in hydrogen and so the exciton is larger in size (roughly 1 – 10 nm compared to approximately 0.1 nm for hydrogen).[37] When a nanoparticle is smaller in diameter than the size of this electron hole separation, quantum confinement occurs, and the size of the band gap relates to the size of the nanoparticle, such that it increases with decreasing size, and so can be selectively controlled.[50]

1.3 Nanoparticle Synthesis

1.3.1 Theory

There are two general approaches to nanoparticulate materials: the top-down (physical destruction of larger material) and the bottom-up (build up from molecular precursors, often colloidal) approaches. Colloidal solutions are only stable if the van der Waals interactions between particles are overcome either electrostatically (charge the surface leading to Coulombic repulsion between particles) or sterically (attach sterically bulky ligands to the surface, typically macromolecules).

As so many properties depend on the size of the nanoparticles polydispersity is disfavoured, monodisperity being preferred. Monodispersity has been described as when 90 % of a population lies within ± 5 % of the mean particles size.[50] Nucleation and growth are thought to govern nanoparticle morphology and size, though the development of models to describe nanoparticle formation is ongoing.[53]

In order for a nanoparticle to form, the Gibbs free energy (ΔG) of the system must be negative, and a supersaturated concentration of the precursor in solution must be reached. Monomer units assemble into a lattice (a favourable process), but they must first break interactions with surrounding solvent molecules (an energy cost). Nucleation will occur if the favourable formation of the lattice is able to overcome the unfavourable removal of coordinated solvent molecules and the formation of dangling bonds on the surface of the new particle (see Section 1.1). For spherical particles, this can be expressed

as Equation 1-2, where r is the particle radius, ΔG_v is the change in energy per unit volume of removing solvent molecules and assembling the monomer into a lattice (positive when the monomer is supersaturated), and γ is the surface energy per unit area.[46]

$$\Delta G = -\frac{4}{3}\pi r^3 \Delta G_v + 4\pi r^2 \gamma$$

Equation 1-2

There are several processes at work during nucleation – precursor monomer approaches the interfacial layer about the particles and can add to the surface, while monomer in the particle can also re-dissolve back into the solution. Whether particle formation is favourable is partly governed by the radius of the particle, such that if it is below the critical radius (r^*), the γ term of Equation 1-2 dominates and ΔG is positive (so particle formation is disfavoured and the particle re-dissolves). If $r \geq r^*$ then the negative term of Equation 1-2 is dominant, ΔG is negative and the particle grows.

The LaMer Model for Particle Formation

Though many models now exist for the formation of nanoparticles, most are based on the model proposed by LaMer in 1950, to explain the formation of colloidal sulfur.[53–55] The model is divided into three phases: in phase one the monomer is generated (in this case S_2 was produced from the reaction of sodium thiosulfate with hydrochloric acid) and its concentration increases (Figure 1-3). This continues until the concentration reaches the critical supersaturation level, at which point nucleation of the particles occurs in a rapid burst (phase two). The concentration of monomer decreases rapidly as it is consumed by nucleation and quickly falls below the critical nucleation level and no new nucleation events occur. There is still monomer in the solution, however, and in phase three the particles continue to grow by diffusion of the remaining precursor monomer onto the surface of the particles.

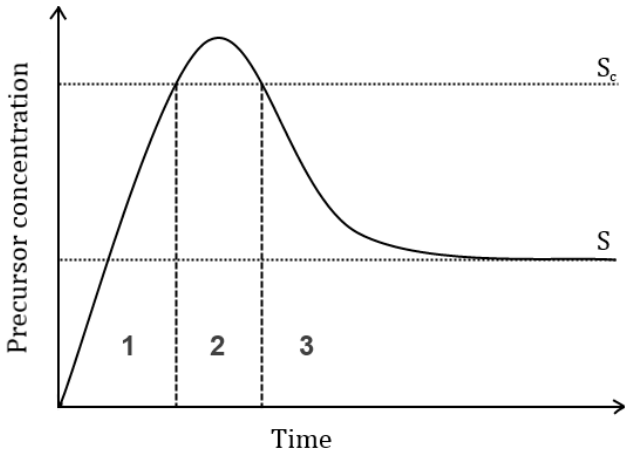

Figure 1-3 - The LaMer plot showing the three stages of particle formation, where S = supersaturation concentration and S_c = the critical supersaturation concentration for nucleation.[55]

Though this model has been found to not be applicable to most transition metal nanoparticle systems,[53] the general principle of a short burst of nucleation events followed by particle growth is important for monodispersity of particles. This process is known as 'burst nucleation' and leads to similar growth times for nuclei, conferring greater control over particle size.[53]

Ostwald Ripening

Subsequent to particle growth, particle ripening occurs. This can either focus or defocus the particle size distribution as there is an exchange of monomer from particle to particle in solution.[54] During Ostwald ripening it is thermodynamically more favourable for small particles to lose monomer and for large particles to gain, growing at the former's expense. This process is driven by the favourable reduction of the percentage of surface particles with dangling bonds, therefore increasing the monomer coordination and reducing particle surface energy.

Ostwald ripening leads to the larger particles growing faster than their slightly smaller neighbours as well as much smaller particles decreasing further in diameter, overall defocussing the particle size. Eventually this leads to the total dissolution of the smaller particles, thereby reducing the totally number of particles in the system. The process can be inhibited by the use of capping agents, lowering the reaction temperature or by adding more monomer.[54]

1.3.2 General Synthetic Methods

There have been numerous reported methods for the synthesis of nanoparticles, which generally follow two routes; precipitation from solution, often at room temperature and often involving the reduction of a metal salt and the decomposition of molecular precursors at elevated temperature in either the solid, liquid (solution) or vapour phase.[56]

Precipitation Methods

The size of the particles produced *via* the precipitation method depends on many variables including precursor type and concentration, reaction temperature, pH of the solution and diffusion and sorption properties of the precursors.[57] Controlling these parameters in order to obtain monodispersity can be challenging and some groups have gone to such lengths as post-preparation size-separation (such as size exclusion chromatography).[56, 58] The resulting nanoparticles may be stabilised to avoid aggregation by Coulombic repulsion, or the addition of a stabilising molecule (capping agent). In some cases one of the reactants (often the reducing agent) can also act as a stabiliser.[57]

The precipitation method was employed by Faraday in his early experiments on gold colloids.[47] Aqueous solutions of auric chloride were reduced with phosphorus to yield gold nanoparticles.[47] The synthesis was improved upon by Turkevitch *et al.*, who reduced chloroauric acid with boiling trisodium citrate in a relatively cheap and reliable method.[59] This yielded gold nanoparticles stabilised by the Coulombic repulsion of a charged bilayer created by citrate ions sitting on the positive metal surface.[59] This method has additionally been adapted to synthesise nanoparticles of other metals.[60, 61]

Another method towards gold nanoparticles was developed by Brust *et al.* and involves reduction of chloroauric acid by sodium borohydride in a multi-layered solvent system.[62] The particles are stabilised by the addition of dodecanethiol, which covalently binds to form strong sulfur-gold bonds on the surface of the particles as they grow.[62] A precipitation method for the synthesis of cadmium sulfide nanoparticles was proposed by Brust *et al.,* and involves the reaction of dilute solutions of cadmium sulphate and ammonium sulfide in the presence of a styrene/maleic anhydride copolymer, which coordinates to the particle surface, capping its growth and preventing flocculation.[63]

Thermal Decomposition Methods

As mentioned above, thermal decomposition of molecular precursors can be performed in the solid, liquid and gas phase, though solution phase decomposition is probably the most widely used and the focus of the work in this thesis. The solid state synthesis of nanoparticles has been described in numerous papers, often as a solventless route to nanoparticulate matter. Thermolysis can be carried out in a Teflon-lined steel autoclave,[64] or much simpler apparatus where heat is applied to a vessel containing solid precursor(s).[65, 42, 66] One potential advantage of this technique is that it does not involve toxic solvents. A disadvantage is that particle size can be difficult to control without solvent effects and capping agents present. Some groups have overcome this by incorporating a stabilising agent into the molecular precursor complex, for example Kang *et al.* synthesised iron oxide and silver nanoparticles from the metal oleate complex in air.[65]

Gas or vapour phase syntheses such as chemical vapour deposition (CVD) have been successfully employed in the synthesis of nanoparticle materials, particularly thin films. Several reviews have been published,[67, 68] and only the main points will be summarised here. In general, molecular precursor(s) are first vaporised (this can be under atmospheric or reduced pressure) and then brought into contact (possibly using an inert carrier gas) with a heated substrate, whereupon they decompose to form a thin film or particles of product.[56, 67] In the case of nanoparticle growth, in the absence of a capping agent, large particle size distributions can occur.[56] Historically, it should be noted, the gas phase decomposition of $Ni(CO)_4$ was successfully employed to process nickel oxide ore forming pure nickel metal, and was also used for nickel plating in some cases.[69] The success of this process lay in the reversibility of the carbon monoxide complexation of nickel, exploiting the carbonyl ligand's lability.[37]

1.3.3 Solvothermal Synthesis

Solution-based thermal synthesis of nanoparticles typically involves the dissolution of molecular precursors in a high boiling point solvent, which are then decomposed at high temperature (between 200 and 300 °C). In order to control particle size and protect the formed nanoparticles from oxidation, a capping agent is also required. The solvent can have dual functionality, acting as a capping agent in addition to a heat sink, if it has coordinating groups such as amines or thiols, or a stabiliser be added separately.

Depending on the composition of the desired nanoparticle, decomposition of a molecule containing all the required elements (a single-source precursor) or a mixture of several different molecular precursors can be performed. The work contained in this thesis is focussed on the solvothermal synthesis of metal sulfide nanoparticles, so there will be a larger discussion of this topic. There are two main types of solvothermal decomposition differing by the temperature at which the precursors are introduced into the solvent, namely the 'hot-injection' and 'heat-up' methods.

The 'hot-injection' method was pioneered by Bawedni *et al.* for the synthesis of cadmium chalcogenide quantum dots.[70] Binary precursors were employed, dimethylcadmium with a chalcogenide compound such as bis(trimethylsilyl)selenium, which were dissolved in tri-*n*-octylphosphine (TOP) and injected into a reaction flask containing tri-*n*-octylphosphine oxide (TOPO) at 300 °C under argon. Upon addition of room temperature (RT) precursor solution, decomposition and surpersaturation of precursor monomer occurred rapidly, producing burst nucleation. External heating was removed prior to injection and the addition was accompanied by a net temperature drop. This caused supersaturation to cease more quickly than it otherwise would have based solely on the drop in monomer concentration upon nucleation. Heating was then reapplied to the system to allow for particle growth (but not high enough for nucleation), all of which led to well-defined, 'temporally discrete', nucleation and growth phases, and nanoparticles with a low polydispersity (< 5 %) .[50, 70, 71] Kwon and Hyeon's review on the mechanism of solvothermal decomposition describes the 'hot-injection' method as conforming to LaMer's model, minus the first phase of monomer accumulation.[54] This method of nanoparticle synthesis has been widely used for the synthesis of nanoparticles of various compositions.[72, 19, 73–78]

The 'heat-up' method shares more similarities with the precipitation method modelled by LaMer than 'hot-injection', having all the reagents together at the start of the reaction so proceeding through monomer accumulation, to nucleation and then to particle growth in order to form nanoparticles.[54] The precursors are dissolved in a high boiling point solvent at room temperature, often in an oxygen-free atmosphere, and heated to the desired temperature. The reactions are typically held at this temperature for *ca.* one hour, to allow for complete decomposition of the precursors. There are many examples of this method in the literature, particularly in the synthesis of metal oxide nanoparticles.[79, 10, 80] Hyeon *et al.* reported the synthesis of Fe_2O_3 nanoparticles from the decomposition of iron

pentacarbonyl in oleic acid, with an average size of approximately 4 nm and a very narrow size distribution.[80]

The 'hot-injection' method has advantages over the 'heat-up' method, particularly the temporal separation of the nucleation and growth phases of particle formation, leading to small particles of low polydispersity. Narrow particle size distribution can be achieved in the 'heat-up' method too, as exemplified above. In addition, the 'heat-up' method is considered a more reproducible method, not having to inject any species into the reaction vessel (injection rate and precursor concentration can affect the decomposition), or adjust the temperature of the reaction at any point as with the 'hot-injection' method. The 'heat-up' method was employed in this work due to its simple effectiveness and reproducibility. Additionally the 'hot-injection' method is very rapid making *in situ* monitoring difficult. The 'heat-up' method is a slower, more gradual process allowing the progression to be easily observed and monitored. It was hoped that *in situ* monitoring could allow decompositions to be understood and controlled and thus allow the ability to selectively synthesise different materials.

Hydrothermal synthesis of nanoparticles has been reported as a greener alternative to the use of toxic and expensive high boiling organic solvents. In order to achieve precursor decomposition high temperatures and pressures are achieved using a sealed vessel, such as an autoclave.[81, 56] Continuous hydrothermal flow synthesis (CHFS) is another water-based technique for the synthesis of nanoparticles, which involves the reaction of precursors in supercritical water.[82] An advantage of this technique is that large quantities of material can be synthesised quickly, though because of this speed of formation the particles tend not to be very crystalline or well-faceted.[82] Though water is often termed a green solvent, in many cases a capping agent (which may not be benign) is added in order to prevent oxidation of the resulting nanoparticles obtained *via* hydrothermal synthesis.

As mentioned previously, nanoparticles can be synthesised solvothermally from the decomposition of one or more precursors. The decomposition of single source precursors has advantages over the binary (and greater) systems in that the close proximity and fixed geometry of the elements in the single source precursor molecule may inform the structure of the material produced, giving greater control and tunability to these reactions. In order to synthesise metal sulfide nanoparticles there are a number of metal-thiolate complexes which could be potential candidates and these are discussed below.

1.4 Precursors

The requirements of a metal sulfide single source precursor are: it should contain both the metal and sulfur (preferably bound to one another); it should be stable enough for easy handling (and won't become oxidised prior to decomposition); it should decompose relatively easily to yield a pure metal sulfide product; and any by-products should be unreactive and preferably volatile (so as to not contaminate the material formed). The obvious choice is a metal-dithiolate complex and there are various thiolate ligands able to stabilise metal centres in existence (see Figure 1-4 for a selection). Some of these ligands also contain other heteroatoms such as oxygen and phosphorus (like xanthates and diphosphates) which could lead to impurities in the material produced. It is particularly important to avoid oxidation which is a common problem in the synthesis of metal sulfides.

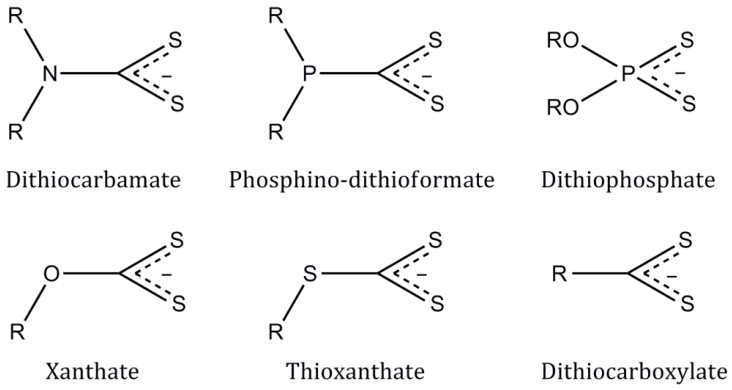

Figure 1-4 - A selection of dithiolate ligands

Dithiocarbamate complexes are widely used as single-source precursors for metal sulfide nanoparticles. One reason for this is the ability of dithiocarbamates to stabilise a wide range of oxidation states which related ligands, such as xanthates, cannot. The electronegativity of the oxygen atom in the latter is too high to form the analogue of the 'thioureide' resonance form (see Figure 1-5), so it is less able to stabilise higher oxidation states.[83] Dithiocarbamates can possess a wide range of different of R-groups, which may be helpful in tuning the molecular precursors to synthesise different structured nanoparticles. Another reason is that the C-S bonds are relatively easy to break compared to, say, P-S bonds, which is necessary so that there are decomposition pathways to leave only iron and sulfur behind when synthesising nanoparticles.[83]

1.4.1 Dithiocarbamate Ligands

Dithiocarbamates are a well-studied class of ligand which find applications in a wide variety of areas including vulcanization accelerators,[84] pesticides,[85] fungicides,[86] and high pressure lubricating agents.[87] They are particularly useful for their ability to form complexes with all the transition metals, stabilising both high and low oxidation states.[83] This special ability arises from the two resonance forms of a dithiocarbamate (Figure 1-5).[83] In the 'dithiocarbamate' resonance form there is a single bond between the nitrogen atom and the sulfur bearing carbon atom, and delocalisation of the -1 charge between the carbon and two sulfur atoms. In the second form, the 'thioureide', the lone pair on the nitrogen atom is delocalised, resulting in double bond character between it and the CS_2 carbon, while the two sulfur atoms both possess negative charges. The nitrogen is sp^2 hybridised in this resonance form. The latter form is described as a hard ligand (better to stabilise hard metal centres at higher oxidation states) while the former is a softer one (better to stabilise soft metals at lower oxidation states).

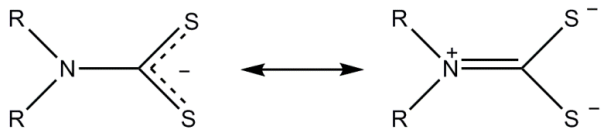

Dithiocarbamate Thioureide

Figure 1-5 - Resonance forms of the dithiocarbamate ligand

Another consequence of the above resonance behaviour is that dithiocarbamates can be both *strong*- and *weak-field* ligands depending on the substituents. If the 'dithiocarbamate' form dominates then it is considered a *strong-field* ligand and if the 'thioureide' form dominates it is considered *weak-field*.[83] This has consequences when the ligand is bound to a transition metal ion such as iron(III), where the high- and low-spin electronic configurations are different (see below).

Dithiocarbamates are generally synthesised in one of two ways. The most common is the reaction of carbon disulphide with a secondary amine in the presence of base, generally sodium or potassium hydroxide. Reactions can be performed in water, methanol or ethanol, at room temperature and produce a high yield of aqueous soluble product. The second method produces dithiocarbamates which are soluble in organic solvents and involves the reaction of carbon disulphide with two equivalents of secondary amine in the absence of any base. This produces the ammonium salt of the compound $[R_2NH_2][S_2CNR_2]$,

one equivalent of amine acts as a base and the second as a nucleophile.[83] Metal dithiocarbamate complexes can be synthesised by simply reacting dithiocarbamate and metal salts together in an appropriate solvent.[83] Metal dithiocarbamates have been successfully used as single-source precursors for metal sulfide nanoparticles by several groups.[88–91, 76] Pioneering work was performed by O'Brien in the synthesis of semiconducting cadmium sulfide and zinc sulfide nanoparticles, from the solvothermal decomposition of metal dithiocarbamate precursors.[89]

1.5 Summary/Aims/Thesis Structure

Herein we report the synthesis of several iron(II) and iron(III) dithiocarbamate complexes, investigate their chemistry and perform studies into their effectiveness as precursors for the synthesis of iron sulfide nanoparticles. Similar work is done with nickel dithiocarbamate complexes, with a detailed study into the morphology and phase of the nickel sulfide nanoparticles obtained from their decomposition. Other metal sulfides are then investigated, including cobalt, copper, zinc and indium, and an investigation into their ability to form mixed-metal sulfide nanoparticles with iron and nickel is described. The final Chapter is devoted to a detailed study of the solvothermal decomposition of nickel dithiocarbamate precursors, in order to understand it with a view to controlling the synthesis of further desirable metal sulfide materials.

1.6 References

1 K. A. Franz, W. G. Kehr, A. Siggel, J. Wieczoreck, and W. Adam, in *Ullmann's Encyclopedia of Industrial Chemistry*, Wiley-VCH, 2002.

2 G. Auer, P. Woditsch, A. Westerhaus, J. Kischkewitz, W.-D. Griebler, and M. Liedekerke, in *Ullmann's Encyclopedia of Industrial Chemistry*, Wiley-VCH, 2009.

3 W. O. Winer, *Wear*, 1967, 10, 422.

4 K. Ramasamy, M. A. Malik, N. Revaprasadu, and P. O'Brien, *Chem. Mater.*, 2013, 25, 3551.

5 T. Zhu, Z. Wang, S. Ding, J. S. Chen, and X. W. Lou, *RSC Adv.*, 2011, 1, 397.

6 C. Wadia, A. P. Alivisatos, and D. M. Kammen, *Environ. Sci. Technol.*, 2009, 43, 2072.

7 C.-H. Lai, M.-Y. Lu, and L.-J. Chen, *J. Mater. Chem.*, 2012, 22, 19.

8 M.-R. Gao, Y.-F. Xu, J. Jiang, and S.-H. Yu, *Chem. Soc. Rev.*, 2013, 42, 2986.

9 K. Aso, H. Kitaura, A. Hayashi, and M. Tatsumisago, *J. Mater. Chem.*, 2011, 21, 2987.

10 S. Sun and H. Zeng, *J. Am. Chem. Soc.*, 2002, 124, 8204.

11 H. K. Mulmudi, S. K. Batabyal, M. Rao, R. R. Prabhakar, N. Mathews, Y. M. Lam, and S. G. Mhaisalkar, *Phys. Chem. Chem. Phys.*, 2011, 13, 19307.

12 T. Tang, L. Zhang, W. Fu, J. Xu, J. Jiang, G. Fang, and F. Xiao, *J. Am. Chem. Soc.*, 2013, 135, 11437.

13 P. A. Nikul'shin, A. V. Mozhaev, D. I. Ishutenko, P. P. Minaev, A. I. Lyashenko, and A. A. Pimerzin, *Kinet. Catal.*, 2012, 53, 620.

14 I. Bezverkhyy, P. Afanasiev, and M. Danot, *J. Phys. Chem. B*, 2004, 108, 7709.

15 R. C. Hoodless, R. B. Moyes, and P. B. Wells, *Catal. Today*, 2006, 114, 377.

16 F. Cao, R. Liu, L. Zhou, S. Song, Y. Lei, W. Shi, F. Zhao, and H. Zhang, *J. Mater. Chem.*, 2010, 20, 1078.

17 R. Devanathan, *Energy Environ. Sci.*, 2008, 1, 101.

18 C. Zhao, D. Li, and Y. Feng, *J. Mater. Chem. A*, 2013, 1, 5741.

19 M.-R. Gao, J. Jiang, and S.-H. Yu, *Small*, 2012, 8, 13.

20 M. A. Lukowski, A. S. Daniel, F. Meng, A. Forticaux, L. Li, and S. Jin, *J. Am. Chem. Soc.*, 2013, 135, 10274.

21 X. Ge, L. Chen, L. Zhang, Y. Wen, A. Hirata, and M. Chen, *Adv. Mater.*, 2014, asap.

22 M. G. Vladimirov, Y. F. Ryzhkov, V. A. Alekseev, V. A. Bogdanovskaya, V. A. Otroshchenko, and M. S. Kritsky, *Orig. Life Evol. Biosph.*, 2004, 34, 347.

23 B. D. Yuhas, C. Prasittichai, J. T. Hupp, and M. G. Kanatzidis, *J. Am. Chem. Soc.*, 2011, 133, 15854.

24 M. J. Russell, *Science*, 2003, 302, 580.

25 M. Yücel, A. Gartman, C. S. Chan, and G. W. Luther, *Nat. Geosci.*, 2011, 4, 367.

26 S. Pérez-Rodríguez, G. García, L. Calvillo, V. Celorrio, E. Pastor, and M. J. Lázaro, *Int. J. Electrochem.*, 2011, 1.

27 J. B. Varley, H. A. Hansen, N. L. Ammitzboll, L. C. Grabow, A. A. Peterson, J. Rossmeisl, and J. K. Norskov, *ACS Catal.*, 2013, 3, 2640.

28 M. J. Russell and W. Martin, *Trends Biochem. Sci.*, 2004, 29, 358.

29 Y. Lu, Z. Jiang, S. Xu, and H. Wu, *Catal. Today*, 2006, 115, 263.

30 T. Reda, C. M. Plugge, N. J. Abram, and J. Hirst, *Proc. Natl. Acad. Sci. U. S. A.*, 2008, 105, 10654.

31 M. J. Russell and A. J. Hall, *J. Geol. Soc. London.*, 1997, 154, 377.

32 D. Rickard and G. W. Luther, *Chem. Rev.*, 2007, 107, 514.

33 G. Wachtershauser, *Microbiol. Rev.*, 1988, 52, 452.

34 C. Huber and G. Wachtershauser, *Science*, 1997, 276, 245.

35 S. Haider, R. Grau-Crespo, A. J. Devey, and N. H. de Leeuw, *Geochim. Cosmochim. Acta*, 2012, 88, 275.

36 H. Wang and I. Salveson, *Phase Transitions*, 2005, 78, 547.

37 P. Atkins, T. Overton, J. Rourke, M. Weller, and F. Armstrong, *Shriver & Atkins Inorganic Chemistry*, Oxford University Press, 4th edn., 2006.

38 M. Tokonami, K. Nishiguchi, and N. Morimoto, *Am. Mineral.*, 1972, 57, 1066.

39 N. Morimoto, H. Nakazawa, K. Nishiguchi, and M. Tokonami, *Science*, 1970, 168, 964.

40 G. Kullerud and R. A. Yund, *J. Petrol.*, 1962, 3, 126.

41 M. E. Fleet, *Can. Mineral.*, 1988, 26, 283.

42 A. Ghezelbash, M. B. Sigman, and B. A. Korgel, *Nano Lett.*, 2004, 4, 537.

43 S. Vedanand, B. J. Reddy, and Y. P. Reddy, *Radiat. Eff. Defects Solids*, 1994, 128, 257.

44 Terence E. Warner, *Synthesis, Properties and Mineralogy of Important Inorganic Materials*, Wiley-VCH, 2011.

45 D. J. Vaughan and J. R. Craig, *Am. Mineral.*, 1947, 70, 1036.

46 G. A. Ozin, A. C. Arsenault, and L. Cademartiri, *Nanochemistry: A Chemical Approach to Nanomaterials*, RSC Publishing, 2nd edn., 2009.

47 M. Faraday, *Philos. Trans. R. Soc. London*, 1857, 147, 145.

48 R. P. Feynman, *J. Microelectromechanical Syst.*, 1992, 1, 60.

49 R. Zsigmondy, *Coloids and the Ultramicroscope: a Manual of Coilloid Chemistry and Ultramicroscopy*, J. Wiley, 1st edn., 1914.

50 L. Cademartiri and G. A. Ozin, *Concepts of Nanochemistry*, Wiley-VCH, 1st edn., 2009.

51 G. Mie, *Ann. Phys.*, 1908, 330, 377.

52 K. L. Kelly, E. Coronado, L. L. Zhao, and G. C. Schatz, *J. Phys. Chem. B*, 2003, 107, 668.

53 E. E. Finney and R. G. Finke, *J. Colloid Interface Sci.*, 2008, 317, 351.

54 S. G. Kwon and T. Hyeon, *Small*, 2011, 7, 2685.

55 Victor K. LaMer and R. H. Dinegar, *J. Am. Chem. Soc.*, 1950, 72, 4847.

56 P. O'Brien and N. Pickett, in *The Chemistry of Nanomaterials: Synthesis, Properties and Applications, Volume 1*, eds. C. N. R. Rao, A. Müller, and A. K. Cheetham, Wiley-VCH, 1st edn., 2004, pp. 12–30.

57 G. B. Sergeev, *Nanochemistry*, Elsevier B.V., 1st edn., 2006.

58 C. H. Fischer, H. Weller, L. Katsikas, and A. Henglein, *Langmuir*, 1989, 5, 429.

59 J. Turkevich, P. C. Stevenson, and J. Hillier, *Discuss. Faraday Soc.*, 1951, 55.

60 W. G. Courtney, *J. Phys. Chem.*, 1956, 60, 1461.

61 C. Lee and D. Meisel, *J. Phys. Chem.*, 1982, 86, 3391.

62 M. Brust, M. Walker, D. Bethell, D. J. Schiffrin, and R. Whyman, *J. Chem. Soc., Chem. Commun.*, 1994, 801.

63 R. Rossetti, J. L. Ellison, J. M. Gibson, and L. E. Brus, *J. Chem. Phys.*, 1984, 80, 4464.

64 X. Wang, W. Zhou, Z. Chang, Z. Zhou, and S. Wu, *Chinese J. Chem.*, 2013, 31, 983.

65 H. G. Cha, D. K. Lee, Y. H. Kim, C. W. Kim, C. S. Lee, and Y. S. Kang, *Inorg. Chem.*, 2008, 47, 121.

66 A. S. Rosenberg, G. I. Dzhardimalieva, and A. D. Pomogailo, *Polym. Adv. Technol.*, 1998, 9, 527.

67 M. Afzaal, M. A. Malik, and P. O'Brien, *J. Mater. Chem.*, 2010, 20, 4031.

68 N.-M. Hwang and D.-K. Lee, *J. Phys. D. Appl. Phys.*, 2010, 43, 483001.

69 L. Mond, C. Langer, and F. Quincke, *J. Chem. Soc. Trans.*, 1890, 57, 749.

70 C. B. Murray, D. J. Noms, and M. G. Bawendi, *J. Am. Chem. Soc.*, 1993, 115, 8706.

71 C. de Mello Donegá, P. Liljeroth, and D. Vanmaekelbergh, *Small*, 2005, 1, 1152.

72 L. Zhu, B. J. Richardson, and Q. Yu, *Nanoscale*, 2014, 6, 1029.

73 J. H. L. Beal, S. Prabakar, N. Gaston, G. B. Teh, P. G. Etchegoin, G. Williams, and R. D. Tilley, *Chem. Mater.*, 2011, 23, 2514.

74 P. V Vanitha and P. O'Brien, *J. Am. Chem. Soc.*, 2008, 130, 17256.

75 D. Fan, M. Afzaal, M. A. Mallik, C. Q. Nguyen, P. O'Brien, and P. J. Thomas, *Coord. Chem. Rev.*, 2007, 251, 1878.

76 O. C. Monteiro, H. I. S. Nogueira, and T. Trindade, *Chem. Mater.*, 2001, 13, 2103.

77 A. L. Abdelhady, M. A. Malik, P. O'Brien, and F. Tuna, *J. Phys. Chem. C*, 2012, 116, 2253.

78 N. Revaprasadu, M. A. Malik, and P. O'Brien, *South African J. Chem.*, 2004, 57, 40.

79 J. Park, K. An, Y. Hwang, J.-G. Park, H.-J. Noh, J.-Y. Kim, J.-H. Park, N.-M. Hwang, and T. Hyeon, *Nat. Mater.*, 2004, 3, 891.

80 T. Hyeon, S. S. Lee, J. Park, Y. Chung, and H. B. Na, *J. Am. Chem. Soc.*, 2001, 123, 12798.

81 M. Rajamathi and R. Seshadri, *Curr. Opin. Solid State Mater. Sci.*, 2002, 6, 337.

82 P. W. Dunne, C. L. Starkey, M. Gimeno-Fabra, and E. H. Lester, *Nanoscale*, 2014, 6, 2406.

83 G. Hogarth, *Prog. Inorg. Chem.*, 2005, 53, 71.

84 J. D. J. Van Dyke, M. Gnatowski, A. Koutsandreas, and A. Burczyk, *J. Appl. Polym. Sci.*, 2002, 90, 871.

85 A. K. Malik and W. Faubel, *Pestic. Sci.*, 1999, 55, 965.

86 K. W. Weissmahr and D. L. Sedlak, *Environ. Toxicol. Chem.*, 2000, 19, 820.

87 J. Baladincz, I. Fekete, J. Petro, S. Szoboszlay, and J. Toth, *Pet. Coal*, 1998, 40, 73.

88 G. H. Singhal, R. I. Botto, L. D. Brown, and K. S. Colle, *J. Solid State Chem.*, 1994, 109, 166.

89 B. Ludolph, M. A. Malik, P. O'Brien, and N. Revaprasadu, *Chem. Commun.*, 1998, 1849.

90 P. O'Brien, D. J. Otway, and J. R. Walsh, *Thin Solid Films*, 1998, 315, 57.

91 N. Revaprasadu, M. A. Malik, J. Carstens, and P. O. Brien, *J. Mater. Chem.*, 1999, 9, 2885.

2 Iron Dithiocarbamate Precursors

2.1 Introduction

As previously detailed in Chapter 1, iron sulfide minerals are numerous and varied.[1] For the phases of interest to this project iron is in the +2 oxidation state, with the exception of the thiospinel greigite, which contains both iron(II) and (III). In order to synthesise these materials in nanoparticulate form *via* solvothermal methods, iron(II) and iron(III) precursors are required. As discussed in Chapter 1, dithiocarbamate complexes are excellent precursors for metal sulfide nanoparticles due to the ligand's high versatility. It is possible to synthesise dithiocarbamate complexes with all of the transition metals and in a variety of different oxidations states.[2] The relative weakness of the C-S bond (as compared to dithiophosphates which possess a P-S bond) also enables the formation of metal sulfide materials without other organic impurities from the precursor complex.[2]

This chapter is divided into two parts: the first being devoted to the synthesis and stability of the iron(III) dithiocarbamate complexes, and the second to the iron(II) dithiocarbamate complexes. This introduction will summarise the chemistry of both these species.

2.1.1 Iron(III) tris(dithiocarbamate) Complexes

Iron(III) tris(dithiocarbamate) complexes were first reported in 1907 in the pioneering paper by Delépine[3] and have since been extensively studied, in part for their unusual magnetic spin-crossover properties.[4–10] The main synthesis route, as described by Delépine and later refined by White *et al.*,[11] involves reacting the sodium salt of the dithiocarbamate with an iron(III) salt (Equation 2-1).

$$3NaS_2CNR_2 + FeCl_3 \longrightarrow [Fe(S_2CNR_2)_3] + 3NaCl$$

Equation 2-1

This method has been used to synthesise iron(III) tris(dithiocarbamate) complexes with a range of different substituents including unsymmetrical secondary amines such as $[Fe(S_2CNMePh)_3]$, and cyclic amines such as $[Fe(S_2CN(piperidyl))_3]$.[11–13] A slight variation on this method involves slow addition of carbon disulfide to a solution of iron hydroxide, $Fe(OH)_3$, and the appropriate secondary amine in absolute ethanol.[11] An electrochemical synthesis has also been reported which produces the iron(III) tris(dithiocarbamate) from the oxidation of a sacrificial anode of iron in a solution of the appropriate thiuram

disulfide.[14] This paper describes quantitative formation of the dimethyl and diethyl tris-derivatives. The results indicate the initial formation of the bis-complex with a further oxidative addition occurring in solution. This latter method is much less common in the literature.

Many different spectroscopic methods have been applied to the investigation of paramagnetic, pseudo octahedral iron(III) dithiocarbamates including infrared spectroscopy (IR), far-IR, nuclear magnetic spectroscopy (NMR), Mössbauer, magnetic moment studies and X-ray crystallography.[13, 15, 16] In many cases the subject of interest was the unusual magnetic behaviour of these complexes, being first reported in 1931.[17]

Iron(III) tris(dithiocarbamates) are d^5 metal-organic complexes and therefore can exist in two ground state spin configurations depending on several factors (ligand type, temperature, pressure, *etc.*). The complexes will be low spin when the ligand field strength (Δoctahedral) is greater than the mean electron pairing energy, and high spin when it is smaller. Both spin states have unpaired electrons leading to paramagnetism, though the high spin state has more unpaired electrons and therefore exhibits a larger magnetic moment (Figure 2-1).

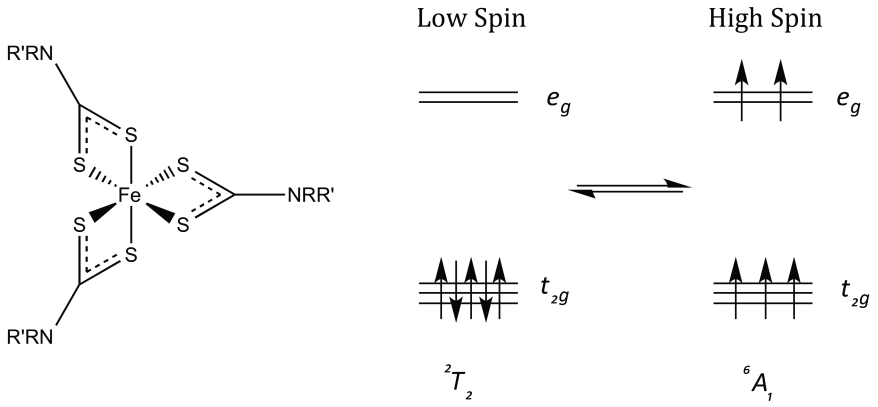

Figure 2-1 - The low- ($^2T_2$) and high- ($^6A_1$) spin state configurations of [Fe(S_2CNR_2)$_3$].

Regarding the reactivity of iron(III) tris(dithiocarbamate) complexes it should be noted that several mixed dithiocarbamate complexes, [Fe(S_2CNR_2)$_2$($S_2CNR'_2$)], have been synthesised, by the reaction of [Fe(S_2CNR_2)$_2$Cl] with one equivalent of dithiocarbamate salt, or upon mixing [Fe(S_2CNR_2)$_3$] and [Fe($S_2CNR'_2$)$_3$].[18, 19, 10] These complexes are difficult to characterise since ligand scrambling at the substitutionally labile iron(III) centre rapidly leads to mixtures of products. In addition, when in solution with non-halogenated solvents no photochemical activity has been observed for iron(III) tris(dithiocarbamate)

complexes, but when even small amount of chlorinated solvents are present they are seen to be extremely photosensitive, producing $[FeCl(S_2CNR_2)_2]$.[20] The reaction is believed to occur *via* an electron-transfer from an excited iron complex to the chlorocarbon with subsequent steps.[21] Indeed, $[Fe(S_2CNR_2)_2X]$ (X = halide), are another important class of iron(III) dithiocarbamate complexes whose chemistry is well reported and complex.[22–28, 20] First reported by White *et al*. in 1966,[29] synthesised *via* the addition of concentrated acids (HX) to benzene solutions of $[Fe(S_2CNR_2)_3]$. Crystal structures $[Fe(S_2CNR_2)_2X]$ show they are square-based pyramidal, with the halide atom in the apical position.[26]

2.1.2 Iron(II) bis(dithiocarbamate) Complexes

Iron(II) bis(dithiocarbamate) complexes were first prepared in 1950[30] as chocolate brown solids from the aqueous reaction of sodium dithiocarbamate salts with ferrous sulphate, $FeSO_4.7H_2O$, an inert atmosphere.[31, 32] They are very air sensitive, being readily oxidised to $[Fe(S_2CNR_2)_3]$.[2] In 1975 Ileperuma and Feltham published the crystal structure of $[Fe(S_2CNEt_2)_2]$,[33] which is dimeric in the solid state with a distorted trigonal-bipyramidal geometry about each iron (Figure 2-2). Thus each metal atom is bound to four sulfur atoms from two dithiocarbamate ligands, one sulfur atom attached to the dithiocarbamate ligand on the adjacent iron complex acts in a μ^2 manner.

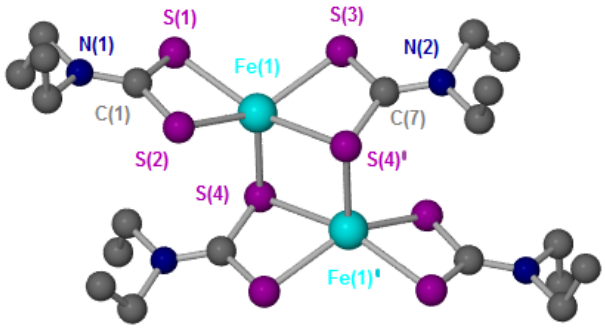

Figure 2-2 - Crystal structure of $[Fe(S_2CNEt_2)_2]$ dimer (hydrogen atoms omitted for clarity).[33]

The Fe-S bond lengths are all similar at approximately 2.4 Å, with the exception of the bridging sulfur bond, which is slightly longer at 2.613(2) Å. The Fe-S bond lengths in $[Fe(S_2CNEt_2)_2]$ are relatively long compared to those in $[Fe(S_2CNEt_2)_3]$ (approximately 2.29 Å, see below), and all the S-Fe-S bond angles are relatively far from the ideal 120° at 142.8(1), 107.3(1) and 109.5(1)°. This is the only reported crystal structure of an iron(II) bis(dithiocarbamate) complex and may not be representative of the whole class of complexes – with larger R-groups, dimerization in the solid state may be disfavoured.

Due to the extreme air sensitivity of iron(II) bis(dithiocarbamate) complexes, for ease of use a protected form of the complexes was required, such that the complexes would be stable enough to handle at room temperature, but the ligands would be labile enough to be expelled from the molecules at a temperature lower than decomposition (and not take part in the reaction in any way). There are several reports of iron(II) mixed ligand dithiocarbamate complexes of the type $[Fe(S_2CNR_2)_2L]$,[2, 34–38] (where L can be a neutral bidentate or monodentate ligand). If the ligand is monodentate, disubstitution can occur, as with isonitriles.[35] The iron(II) bis(dithiocarbamate) diisocyanide complex $[Fe(S_2CNR_2)_2(CNR)_2]$ is formed from the reaction of $[Fe(S_2CNR_2)_3]$ with isonitrile.[35]

The blue 1,10-phenanthroline (phen) and 2,2-bipyridine (bipy) adducts are synthesised by adding the respective ligands to THF solutions of iron(II) bis(dithiocarbamate),[34] or in a one pot reaction of ferrous chloride with three molar equivalents of ligand followed by slow addition of two equivalents of sodium diethyldithiocarbamate.[38] In addition, photoreduction of $[Fe(S_2CNEt_2)_3]$ with NaS_2CNEt_2 in the presence of 1,2-bis(diphenylphosphino)ethane (dppe) affords $[Fe(S_2CNEt_2)_2(dppe)]$ and tetraethylthiuram disulfide.[37] Iron(II) bis(dithiocarbamate) dicarbonyl complexes are another important class of coordinatively saturated iron(II) dithiocarbamates, and have been synthesised *via* a number of methods (see below).

2.1.3 Iron(II) bis(dithiocarbamate) Dicarbonyl Complexes

Cotton and McCleverty first reported $[Fe(S_2CNMe_2)_2(CO)_2]$ in 1964 formed upon reacting *cis*-$[Fe(CO)_4Br_2]$ with two equivalents of NaS_2CNMe_2 in ice-cooled acetone.[39] A similar synthesis was later reported by Dean who reacted *cis*-$[Fe(CO)_4I_2]$, with two equivalents of $[Me_2NH_2][S_2CNMe_2]$ in acetone.[40] Several other synthesis methods have followed. In 1971 Bernal *et al*. synthesised $[Fe(S_2CNC_5H_{10})_2(CO)_2]$ by reacting $Fe(CO)_5$ with tetrapiperidylthiuram disulfide at 78 °C,[41] while Duffy *et al*. used a similar method reacting $Fe_3(CO)_{12}$ with three equivalents of thiuram disulfide (Equation 2-2).[42]

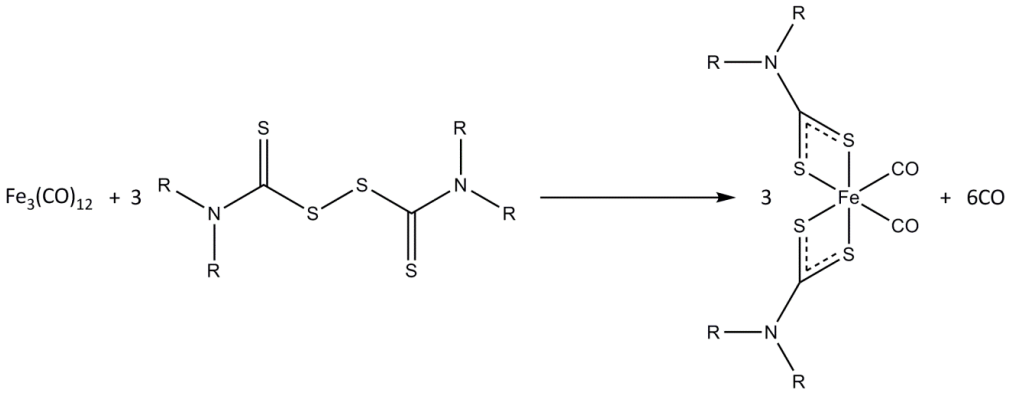

Equation 2-2

In 1972 Feltham reported the synthesis of dimethyl and diethyl derivatives *via* the addition of ferrous sulphate to the appropriate sodium dithiocarbamate salt in acetone, with carbon monoxide bubbled through the solution.[43] This produced the desired complexes in high yields (79 and 93 % respectively) and Houchin later reported a very similar synthesis using the iron perchlorate in dimethylformamide.[44]

Iron(II) bis(dithiocarbamate) dicarbonyl complexes have been studied by a number of techniques including NMR, IR and Mössbauer spectroscopy. Duffy et al. used all three techniques to investigate the inductive effect of the organo-substituents on the complexes,[42] finding that the greater the pK_a of the protonated form of the parent secondary amine functional group of the dithiocarbamate ligand (*i.e*. the more basic the nitrogen centre), the more electron density is donated to the CS_2 end of the ligand and so onto the iron centre. This is made possible by the fact that dithiocarbamate ligands have a thioureide resonance form (Figure 1-5).

Mössbauer spectroscopy shows that there is no build-up of electron density on the iron as ^{57}Fe Mössbauer parameters are the same regardless of R-groups. Duffy suggests electron density flows through the metal centre and onto the carbonyl ligands. This is revealed in the C-O stretching frequencies which are lower when the pK_a of the amine is higher.[42] Further evidence for this behaviour is reported in a later paper by Duffy and Appleton, in which they perform a detailed IR, ^{13}C- and ^{15}N-NMR spectroscopy study on iron(II) bis(dithiocarbamate) dicarbonyl complexes.[45] They report typical solution IR peaks for the carbonyl ligands at approximately 2025 and 1970 cm^{-1} in $CHCl_3$.

Recently, iron(II) bis(dithiocarbamate) dicarbonyl complexes have been tested for their potential as CO releasing molecules (CO-RMs).[46] Though CO is a highly toxic gas, it has

been shown to be an important signalling molecule in many biological systems,[47] as well as a bactericidal agent and a treatment for inflammation,[48] and as such safe ways to deliver CO to cells has gained recent attention. The results of the study on $[Fe(S_2CNR_2)_2(CO)_2]$ (R = Me, Et, $CH_2{=}CH_2$, $\{CH_2CH_2\}_2O$) indicate that the complexes have some potential as CO-RMs, but were surpassed in activity by complexes of the type $[Fe(CO)_3X(S_2CNR_2)]$.[46]

2.1.4 Precursor Choice

Based on the iron(II) and iron(III) dithiocarbamate chemistry detailed above the precursors chosen for this work were $[Fe(S_2CNR_2)_2(CO)_2]$ and $[Fe(S_2CNR_2)_3]$ respectively. $[Fe(S_2CNR_2)_3]$ was chosen because it has a facile, open bench synthesis and possess sulfur as the only heteroatom bonded to the iron centre. The alternative halide complexes, $[Fe(S_2CNR_2)_2X]$ (X = Cl, Br, I), have a strong iron-halide bond that could potentially lead to halide contamination in decomposition products.

$[Fe(S_2CNR_2)_2]$ was not selected as the iron(II) precursor for this study due to its extreme air sensitivity and so potential difficulty in handling. $[Fe(S_2CNR_2)_2(phen)]$ is a more stable, protected form of the complex and has been used by several groups to synthesise iron sulfide nanoparticles,[49, 50] however inclusion of the bulky phenanthroline group leads to a large mass wastage upon decomposition. A better alternative is the carbonyl protected complex $[Fe(S_2CNR_2)_2(CO)_2]$, which has small lightweight CO protecting groups and for which there is already a precedent for reversible CO binding (studied as CORMs).[46]

2.2 Results and Discussion

2.2.1 Iron(III) tris(dithiocarbamate) Complexes

2.2.1.1 Synthesis

Complexes were synthesised according to well-established literature methods[11] *via* the addition of three equivalents of sodium dithiocarbamate ligand (NaS_2CNRR') to an aqueous solution of ferrous iron chloride ($FeCl_3$) (Equation 2-3). In the case of the isobutyl, methylbutyl and 4-methylpiperideine derivatives, it was necessary to synthesise the sodium dithiocarbamate ligand by the slow addition of carbon disulfide to an aqueous solution of sodium hydroxide and the appropriate secondary amine. All the iron(III) tris(dithiocarbamate) complexes were relatively straightforward to prepare, though it was somewhat difficult to completely remove the water from the methyl derivative.

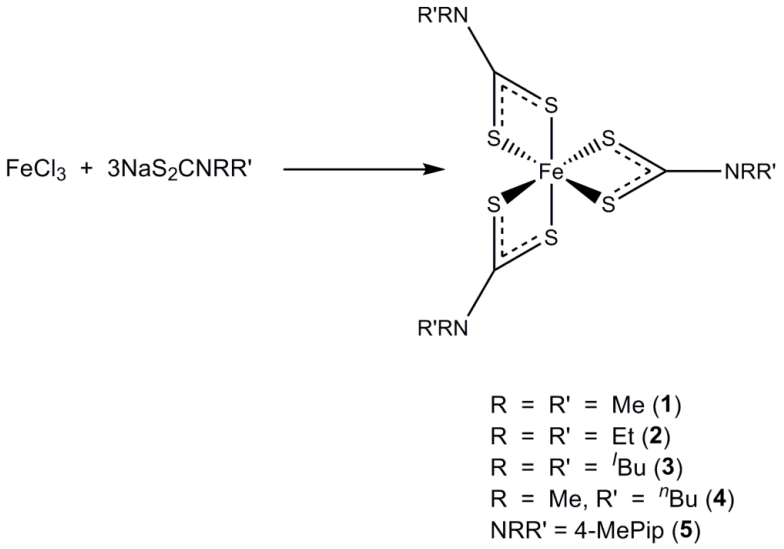

Equation 2-3

Iron(III) dithiocarbamates are paramagnetic d^5 spin crossover complexes and therefore could not be easily analysed by NMR spectroscopy. However it was possible to elucidate their structures using IR, mass spectrometry (MS), elemental analysis (EA) and, where crystals were obtained, single crystal X-ray diffraction. Crystals of the iron(III) tris(diethyldithiocarbamate) complex (**2**) were obtained when attempting to crystallise the iron(II) bis(diethyldithiocarbamate) dicarbonyl complex (see below) from a toluene/hexane layer – a testament to the instability of the iron(II) complexes (Figure 2-3).

There are a large number of X-ray crystal structure studies of iron(III) tris(dithiocarbamates),[6, 15, 51–53] and in general they report a distorted octahedral geometry. Leipoldt and Coppens report crystal structure of $[Fe(S_2CNEt_2)_3]$ at 297 and 79K and relate changes to the spin-crossover properties of the complex.[15] At room temperature the complex has a magnetic moment of 4.3 BM, indicating it is predominantly in the high spin state ($^6A_1$), while at the lower temperature it has a magnetic moment of 2.2 BM and is therefore chiefly in the low spin state ($^2T_2$). The space group changes on cooling from $P2_1/c$ to $C2/n$, the octahedral structure being less distorted at the lower temperature. The Fe-S bond lengths are 0.05 Å shorter at the lower temperature resulting from an increased bond order in the low spin state (electrons all occupy the non-bonding t_{2g} orbitals with none in the antibonding e_g orbitals – see Figure 2-1).

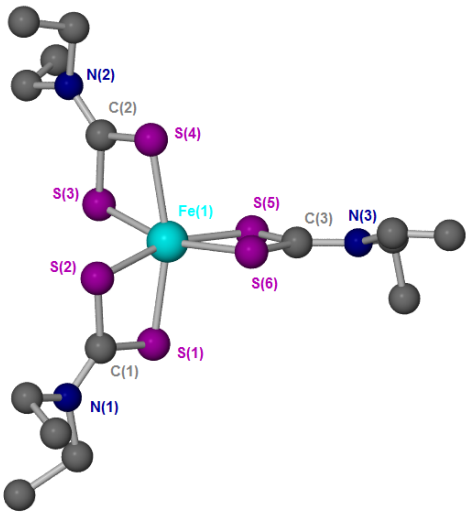

Figure 2-3 - Crystal structure of 2 (hydrogen atoms omitted for clarity).

The X-ray crystal structure of **2** obtained in this study has the space group $P2_1/c$ at 150 K. The Fe-S bond lengths are 0.015 Å shorter than in the crystal structure taken at 79 K.[15] One would expect the Fe-S distances to be at an intermediate value between the high and low temperature structures, though this could be within experimental error. Table 2-1 summarises the bond lengths and angles for **2**, revealing the axial S-Fe-S bond angle is far from 180° at 163.64(2)°. The origin of this distortion is the strain in the dithiocarbamate ligands where the intra-ligand S-Fe-S bite angle is less than 90° and so the inter-ligand S-Fe-S bite angle has to be greater than 90° to make up for this.

Atoms	Bond Angle (°)	Atoms	Bond length (Å)
S(1)–Fe(1)–S(4)	163.64(2)	Fe(1)–S(1)	2.2900(5)
S(1)–Fe(1)–S(2)	75.71(2)	Fe(1)–S(2)	2.2824(5)
S(1)–Fe(1)–S(6)	99.52(2)	Fe(1)–S(3)	2.2939(5)
S(1)–C(1)–S(2)	110.43(9)	C(1)–S(2)	1.708(2)
		C(1)–N(1)	1.314(2)

Table 2-1 - Selected bond lengths and angles for 2.

2.2.1.2 Stability

Thermogravimetric analysis (TGA) was performed on the iron(III) complexes to elucidate the temperature at which they begin to decompose. Though this data is not directly comparable to the solvothermal decomposition work (as it is carried out in the absence of a solvent/capping agent, which may play a role in the decomposition), it may act as a crude guide.

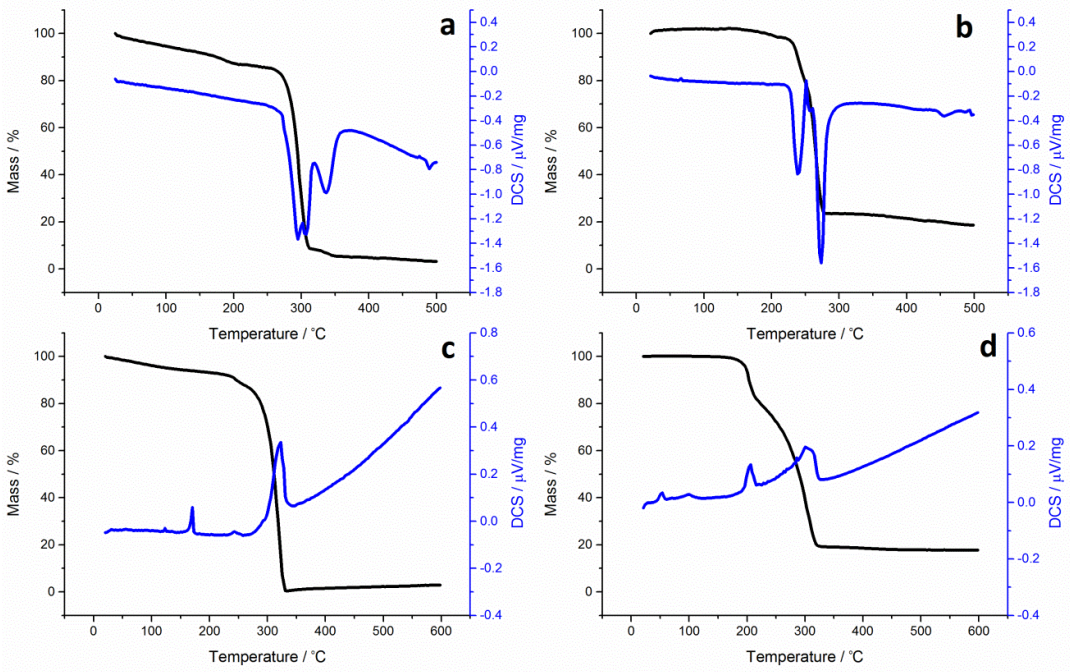

Figure 2-4 - TGA (black) and DSC (blue) graphs for a) 1, b) 2, c) 3 and d) 4

On initial inspection, the TGA graphs (Figure 2-4) for **1** and **3** appear to be similar, with an initial period of thermal stability until approximately 300 °C, whereupon there is a sharp mass loss. For **1** there is a gradual mass loss of 15 % from 0 – 259 °C when the main decomposition starts. This initial mass loss is likely to be due to residual solvent in the sample, and the total mass has been recalculated to take this into account. 89 % of the mass is lost between 259 – 312 °C, with a further 6 % lost shortly after this. Overall a residual mass of only 4 % remains, less than the mass of solely Fe remaining, indicating possible sublimation. The DSC graph for **1** is complex with several overlapping peaks (as with the iron(II) complexes), but enough can be seen to indicate several decomposition steps all very close together (seen as endothermic peaks in the DSC trace).

The TGA graph for **3** shows mass loss occurring sharply between 233 and 330 °C; 91 % of the mass is lost in at least two steps (a small mass loss can be seen in the TGA graph at 250 °C). The DSC graph also shows a complex endothermic hump for this loss, likely to be the result of a group of overlapping peaks (similar to that seen for the decomposition of some iron(II) complexes) indicating that this is a complex multistep process. Unlike for complex **1**, the DSC graph for **3** shows a small endotherm at 170 °C indicative of melting.

TGA graphs for **2** and **4** are superficially similar, both decomposing in several steps leaving a residual mass approximately equal to FeS. They are quite different, however, in their

apparent decomposition pathways. Complex **2** initially decomposes between 226 and 277 °C losing 73 % of its mass, approximately equal to the loss of $[(S_2CNEt_2)_2CNEt_2]$. As with **1**, overlapping peaks in the DSC graph are seen between these temperatures indicating a multistep decomposition. This is followed by the gradual loss of a further 5% up to 500 °C which approximately corresponds to the loss of one further sulfur atom.

This differs slightly from previous work by O'Brien et al, who observe a single mass loss of 79 % between 220 and 300 °C when they performed TGA on **2**, with no further losses up to 500 °C.[54] In an earlier paper on the thermal behaviour of dithiocarbamates by D'Ascenzo and Wendlendt, it was noted that although **2** appeared to lose most of its mass in one step, analysis of the DSC data revealed three endothermic peaks, which they attributed to fusion of the metal chelate, volatilisation and partial dissociation of the remaining precursor.[55]

The methylbutyl iron(III) derivative (**4**), decomposes between 174 and 321 °C. Not only is this a wider range of decomposition, but it is also a markedly lower starting temperature indicating instability due to the asymmetric methylbutyl ligand. Some 81 % of the mass is lost between 174 and 321 °C, which is approximately equivalent to the percentage mass of $[(S_2CNMeBu)_2(SCNMeBu)]$. There is a broad peak in the TGA graph indicating that the decomposition happens in at least two stages. The DSC graph shows several complex endothermic peaks in this temperature range, again indicating that several decomposition steps are overlapping here.

2.2.2 Iron(II) bis(dithiocarbamate) Dicarbonyl Complexes

2.2.2.1 Synthesis

The first method we attempted was based upon the work of Duffy *et al*.,[42] $Fe_3(CO)_{12}$ was reacted with three equivalents of thiuram disulfide ($(S_2CNR_2)_2$) in dry, degassed solvent and refluxed for 30 minutes in an inert atmosphere (Equation 2-2). This reaction was attempted using; tetra-methyl-, tetra-ethyl- and tetraisobutylthiuram disulfide (**6**), however, the reactions did not proceed cleanly and it proved difficult to separate out the product from the iron(III) by-product.

Initially experiments were conducted in THF at 65 °C and monitored by IR. This showed the presence of product carbonyl peaks after *ca*. 15 minutes. At this point, however, there was still a significant amount of $Fe_3(CO)_{12}$ present and a mixture of products detectable by

^{1}H-NMR spectroscopy. The resulting ^{1}H-NMR spectra gave very broad peaks, consistent with at least one of those products being paramagnetic, suggesting that some iron(III) was present in solution. This indicates that the iron(II) product may not be stable and was therefore oxidising under the reaction conditions.

The reaction was repeated in dichloromethane (DCM) at 45 °C to try to prevent iron(II) oxidation, but after several hours only trace amounts of product were detected by IR. The reaction was then attempted in toluene at 80 °C with promising results. Thus after 15 minutes it appeared to have gone to completion, however, paramagnetic species were still detected in the ^{1}H-NMR spectrum, and attempts to separate the product from these impurities by crystallisation failed, only leading to further oxidation of the product. A similar method to this has been shown to successfully synthesise both ruthenium and osmium bis(dithiocarbamate) dicarbonyl complexes, although these metals are in the same group as iron, they form more stable, less air sensitive complexes and so do no react further to form the M(III) tris(dithiocarbamate) species.[56–58]

An alternative synthesis based upon the work of Dean was then attempted.[40] This involved the reaction of $Fe(CO)_5$, with iodine in dry degassed diethylether (Et_2O) to synthesise the Fe(II) complex, *cis*-$[Fe(CO)_4I_2]$, *in situ*. This was then reacted further by the addition of two equivalents of dithiocarbamate salt. NaS_2CNRR' salts are usually employed to synthesise iron dithiocarbamate complexes, however, they are only soluble in aqueous solutions. Since this reaction was performed in an organic solvent, the ammonium stabilised dithiocarbamate salt $[RR'NH_2][S_2CNRR']$ was synthesised instead.

$$CS_2 + 2RR'NH \longrightarrow [H_2NRR'][S_2CNRR']$$

$$RR'NH + [Me_4N][OH] \longrightarrow [Me_4N][S_2CNRR'] + H_2O$$

Equation 2-4

This involved the reaction of carbon disulfide with two equivalents of the chosen secondary amine (Equation 2-4). ^{1}H-NMR spectroscopy confirmed the salt synthesised cleanly for NRR' = NMe_2 (**7**), $NiBu_2$ (**8**), 4-methylpiperidine (4-MePip, **9**) and 2,6-dimethylpiperidine (2,6-Me_2Pip, **10**), however, it was necessary to synthesise the tetramethylammonium salt for the NEt_2 (**11**) and NMeBu (**12**) derivatives, because NMR spectroscopy revealed there was not full conversion of carbon disulfide to dithiocarbamate.

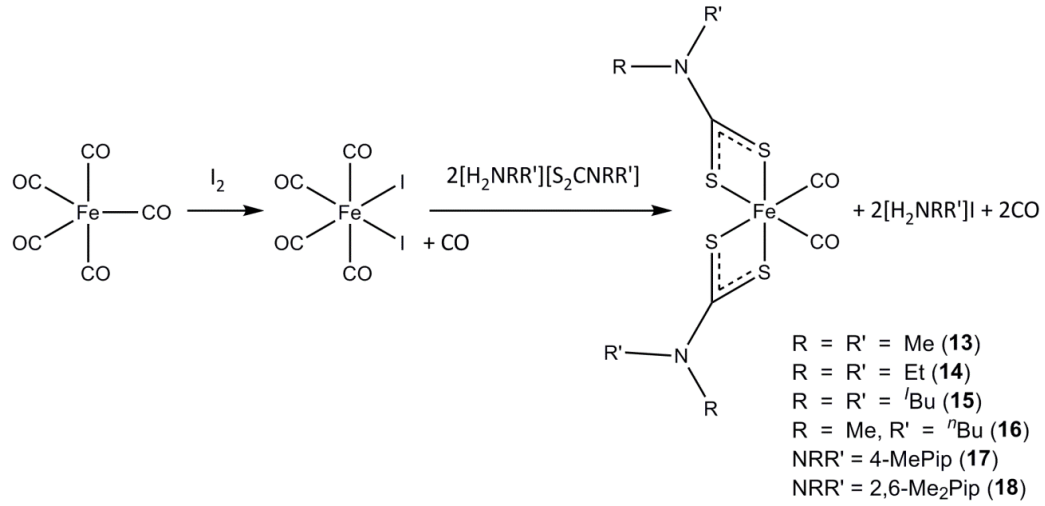

Equation 2-5

Using the method shown in Equation 2-5, iron(II) bis(dithiocarbamate) dicarbonyls **13** – **18** were synthesised. Reactions were performed in a mixture of dry, degassed Et_2O and DCM. DCM was required to dissolve the amine salts in all cases except for **15**, which is soluble in Et_2O. It was found that an excess of dithiocarbamate salt increased the rate of reaction dramatically, and the products were generally separable from the excess amine due to their increased solubility in non-polar organic solvents (such as toluene).

Complex **13** was most easily prepared, the product being readily separated from the dithiocarbamate iodide salt as the latter had very low solubility in organic solvents. The product was easily isolated by cannula filtration whereupon the solvent was removed *in vacuo* to leave a copper-coloured powder. In all other cases in order to obtain pure product, extraction with a less polar solvent was required. These products were then difficult to completely dry, leaving a viscous dark brown liquid after solvent removal *in vacuo*. However, when washed with pentane a dry copper coloured powder was obtained. Yields were relatively low (between 30 and 45 %) likely due to the multistep synthesis and separation issues.

Complexes **13** - **18** were characterised by ^{1}H- and $^{13}C\{^{1}H\}$-NMR, MS, EA, IR and, where crystals were obtained, by single crystal X-ray diffraction. It should be noted that the softest form of MS ionisation was employed to detect these complexes, fast atom bombardment (FAB), but only in the case of the dimethyl derivative (**13**) was the intact molecular ion observed. In all other cases the iron(II) bis(dithiocarbamate) complexes – minus the carbonyl ligands – were detected but not the molecular ion. Complex **13** appears to be slightly more stable to fragmentation by FAB than the other derivatives. IR

spectroscopic analysis confirmed the presence of two carbonyl ligands in *cis* conformation, all complexes exhibiting two peaks in their IR spectra in the 2200 – 1800 cm^{-1} region at approximately 2025 and 1965 cm^{-1} (very close to what was seen previously by Duffy).[45]

Since the one previous crystal structure of a complex of this type is the piperidine derivative,[41] the crystal structures of two such complexes have been obtained, namely the dimethyl (**13**) and diisobutyl (**15**) derivatives (Figure 2-5).

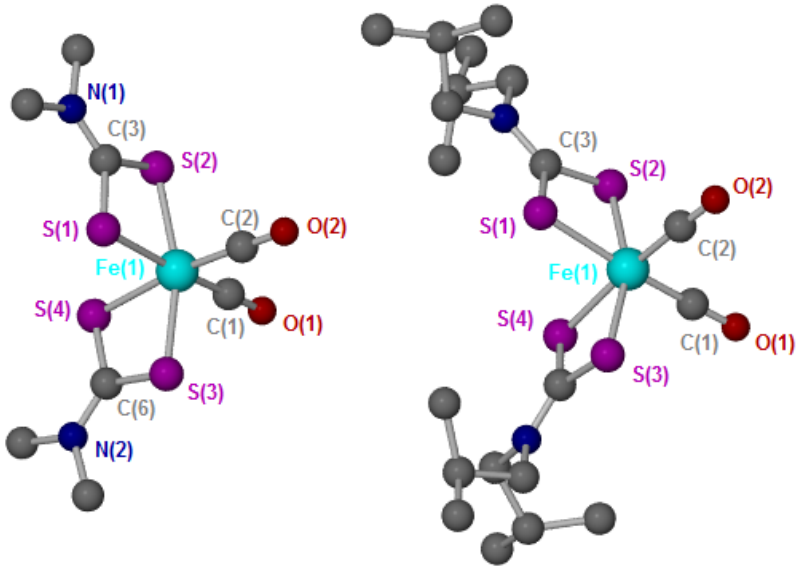

Figure 2-5 - Crystal structures of 13 (left) and 15 (right). Hydrogen atoms (and pentane molecule from 15) omitted for clarity.

The X-ray crystal structures of **13** and **15** both are in the space group $P2_1/c$ at 150 K. **13**, **15** and $[Fe(S_2C(Pip))_2(CO)_2]$ are all low spin d^6 complexes so octahedral geometry about iron is favoured, but all three are distorted from the ideal, the distortion arising from the small ligand bite angle, and visible from the axial S(2)-Fe(1)-S(3) bond (which is far from 180 ° for **13**, **15**, and $[Fe(S_2C(Pip))_2(CO)_2]$) and the remaining S-Fe-S and C-Fe-C bond angles (Table 2-2).

The Fe-S bond lengths are approximately the same as those in $[Fe(S_2C(Pip))_2(CO)_2]$. This is consistent with Duffy's work suggesting that differences in the amine group of the dithiocarbamate ligand leads to a difference in carbonyl stretching frequency, but not Fe-S bond distance.[42, 45] Analysis of the C-O and Fe-C bond distances, however, revealed no significant correlation to pK_a of the dithiocarbamate amine groups. In fact, all the bond lengths and angles in **13**, **15**, and $[Fe(S_2C(Pip))_2(CO)_2]$ are very similar and do not indicate any one structure possessing more strain than another.

Atoms	**13** bond angles (°)	**15** bond angles (°)	$[Fe(S_2C(Pip))_2(CO)_2]$ bond angles (°)	$[Fe(S_2CNEt_2)_2]$ bond angles (°)
S(1)–Fe(1)–S(2)	75.12(5)	74.72(3)	74.7(2)	74.3(1)
S(3)–Fe(1)–S(4)	75.15(5)	74.96(3)	74.6 (2)	71.4(1)
C(1)–Fe(1)–C(2)	92.9(2)	91.8(2)	92.3	-
S(2)–Fe(1)–S(3)	163.53(5)	160.04(4)	162.1(3)	159.1(1)
S(2)–Fe(1)–S(4)	93.88(5)	90.91(3)	91.5(2)	102.3(1)
S(1)–C(3)–S(2)	110.9(2)	110.3(2)	110(1)	115.7(3)

Atoms	**13** bond lengths (Å)	**15** bond lengths (Å)	$[Fe(S_2C(Pip))_2(CO)_2]$ bond lengths (Å)	$[Fe(S_2CNEt_2)_2]$ bond lengths (Å)
Fe(1)–S(1)	2.339(1)	2.336(1)	2.337(6)	2.453(2)
Fe(1)–S(2)	2.308(1)	2.300(1)	2.308(5)	2.402(2)
Fe(1)–C(1)	1.762(5)	1.754(4)	1.72(3)	-
Fe(1)–C(2)	1.781(5)	1.775(4)	1.83(2)	-
C(1)–O(1)	1.164(5)	1.152(4)	1.15(3)	-
C(3)–N(1)	1.311(5)	1.340(4)	1.27(2)	1.330(6)

Table 2-2 - Selected bond angles and lengths for 13, 15, $[Fe(S_2C(Pip))_2(CO)_2]$ and $[Fe(S_2CNEt_2)_2]$.

The Fe-S bonds in **13**, **15** and $[Fe(S_2C(Pip))_2(CO)_2]$ are closer in length to those in **2**, the iron(III) bis(dithiocarbamate) complex obtained in this study (Table 2-1), than those in $[Fe(S_2CNEt_2)_2]$. The crystal structure of the latter has a distorted trigonal bipyramidal geometry, while **2** is distorted octahedral, as with **13** and **15**. The trend in Fe-S bond lengths is presumably due to their similar geometries.

The X-ray crystal structure of **15** contains a pentane molecule (omitted from Figure 2-5 for clarity). As mentioned above, removing all the solvent from the iron(II) bis(dithiocarbamate) dicarbonyl complexes proved to be difficult - often oils were obtained that were then washed with pentane to obtain pure product. The isobutyl and methylbutyl derivatives were especially difficult to dry, their extended alkyl chains increasing solubility.

2.2.2.2 Stability

MS analysis indicates that the $[Fe(S_2CNRR')_2(CO)_2]$ complexes are not very stable to FAB ionisation, **13** being the least susceptible to fragmentation and most stable of the complexes. TGA was performed to investigate the stability of the carbonyl groups. At first

glance, graphs for **13** – **16** (Figure 2-6) look very similar, each showing a small mass loss at *ca.* 150 °C, followed by a much greater mass loss at *ca.* 250 °C. Both are sharp for all complexes, but occur at a temperature dependant on the R group of the dithiocarbamate ligand (Table 2-3). Complex **15** appears to exhibit an additional mass loss between 25 and 37 °C, but this can be accounted for by the presence of *n*-pentane (boiling point 36 °C) in the crystalline structure (as seen in the structure of **15**). This mass loss has been discounted and the new total mass adjusted appropriately.

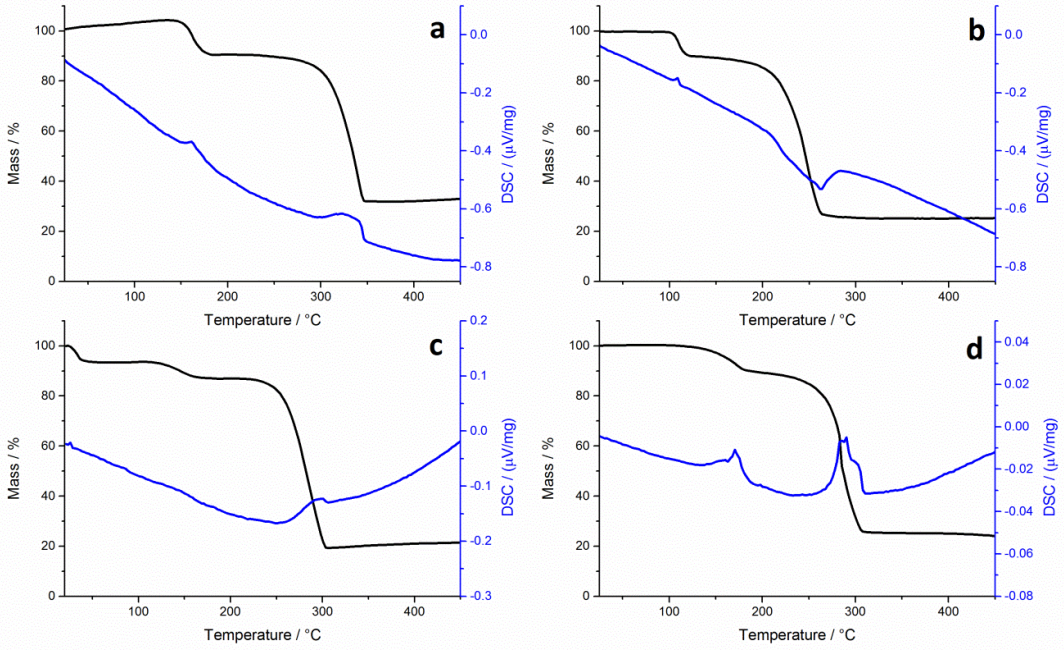

Figure 2-6 - TGA (black) and DSC (blue) graphs for a) 13, b) 14, c) 15 and d) 16.

In all four graphs the initial percentage mass loss occurring at approximately 150 °C can be attributed to the loss of two CO groups. This is then followed by a period of thermal stability for the generated $[Fe(S_2CNRR')_2]$ of between 32 and 83 °C, before this proceeds to decompose in a sharp curve on the TGA graph. This result is important as it indicates that all four complexes exhibit the level of stability required for solvothermal nanoparticle synthesis. They are stable at room temperature, so the iron(II) complexes can be delivered to the decomposition chamber, but the carbonyl ligands are also labile enough to dissociate from the complexes at a temperature lower than that at which the remaining $[Fe(S_2CNRR')_2]$ complexes decompose.

Consistent with the MS analysis, the most thermally stable dicarbonyl complex is the dimethyl derivative, **13**, which only begins to lose its carbonyl ligands at 144 °C. The $[Fe(S_2CNMe_2)_2]$ formed is also the most thermally stable of these fragments, going on to

decompose at 266 °C, some 44 °C higher than the next most stable fragment, [Fe(S_2-CN^iBu_2)$_2$]. The methyl complex is found to be the most insoluble of all the [Fe(S_2-CNRR')$_2$(CO)$_2$] complexes, indicating it packs well in the solid state and contains relatively strong intermolecular forces which could account for its high thermal stability.

Decomposition of [Fe(S_2CNMe_2)$_2$] begins at a similar temperature to the iron(III) methyl analogue studied (**1**, see Table 2-3) indicating similar stability, but **13** decomposed to a mass approximately equal to FeS_2, while virtually nothing is left of **1** after the vaporisation. The same trend is seen for the isobutyl derivatives **15** and **3**.

Complex	Start temp. of CO loss /°C	Start temp. of decomp. /°C	Complex	Start temp. of decomp. /°C
13	144	266	**1**	259
14	100	180	**2**	226
15	117	222	**3**	233
16	112	217	**4**	174
17	125	210		
18	118	166		

Table 2-3 - Temperatures of CO loss and [Fe(S_2CNRR')$_2$] decomposition for 13 - 18, with their iron(III) analogues (1-4 respectively).

Figure 2-6 shows the ethyl derivative (**14**) is less thermally stable than the isobutyl derivative (**15**). Complex **14** begins to lose its carbonyl ligands at 100 °C, 17 °C lower than **15**, but more significant is the temperature at which the resulting [Fe(S_2CNEt_2)$_2$] complex begins to decompose, 180 °C, some 42 °C lower than [Fe(S_2CN^iBu_2)$_2$]. Indeed this pattern is mirrored in the iron(III) data, where **2** decomposes at a temperature below **3.** It is expected that since the ethyl derivative has less bulky ligands than the large isobutyl derivative, it would have better packing in the solid state and so a higher thermal stability. One explanation could be that β-hydride elimination plays a role in the decomposition of **14** and **2**, but this process is disfavoured for **15** and **3** due to the isobutyl β-hydrogen being hindered by the CH_3 groups.

The TGA graphs for **14** and **16** are similar, both decomposing in several steps leaving a residual mass approximately equal to FeS, the same product to which their iron(III) analogues (**2** and **4** respectively) also decompose. However, **14**, has the lowest decomposition temperature of the four iron(II) complexes at 180 °C, while the methylbutyl derivative (**4**) has the lowest decomposition temperature of the iron(III)

dithiocarbamate species. The methylbutyl iron(II) derivative, **16**, decomposes at a similar temperature to **15**, 42 °C higher than **4**, indicating an increased thermal stability.

It should be noted that though the decompositions of the iron(II) bis(dithiocarbamate) complexes appear as a sharp drops in percentage mass on the TGA graph, the DCS graphs show that in all cases it is not as simple as the complexes falling apart in one step. The DSC graphs show complicated, overlapping peaks for all the complexes, some endothermic (as expected when a compound decomposes) and some overall exothermic. This indicates that though decomposition is rapid, it involves several steps. Complexes **13** and **15** decompose to leave a residual percentage mass approximately equal to FeS_2, and **14** and **16** decompose to leave FeS. The margin for error is quite large however, indicating that the residual matter is not pure in any case. If the residual FeS_2 left at the end of these experiments is crystalline, it could be one of the iron sulfide minerals pyrite or marcasite and the FeS could be mackinawite, pyrrhotite or troilite.

It can be concluded that under TGA conditions complexes **15**, **16**, and **2** decompose within a 9 °C temperature range, **1** and **13** decompose within a 7 °C temperature range and **4** and **14** decompose within a 6 °C temperature range of each other. If they behave in a similar way under solvothermal conditions, it is proposed that they could decompose simultaneously and therefore possibly produce greigite nanoparticles (nanoparticles that contain both Fe2+ and Fe3+ ions). These results also provide temperatures at which solvothermal decompositions may be carried out, however as stated previously the conditions in the solvothermal reaction chamber are different to solid state TGA.

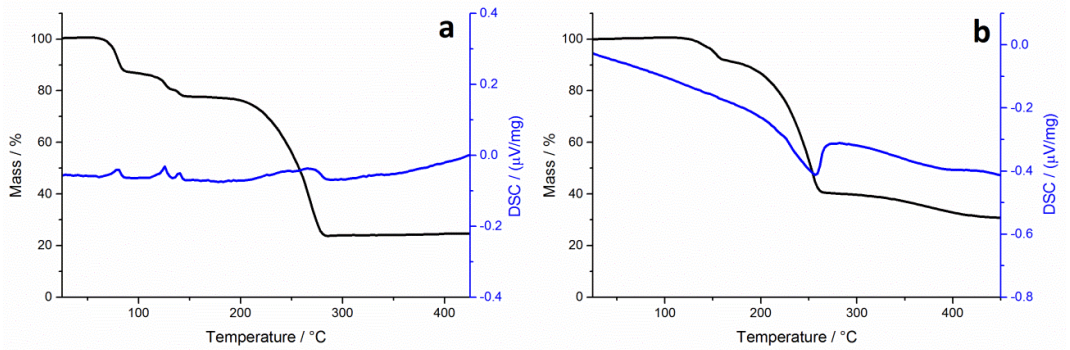

Figure 2-7 - TGA (black) and DSC (blue) graphs for a) 17 and b) 18.

TGA of **17** and **18** (Figure 2-7) show slightly more complicated decomposition processes compared to **13** – **16**. Complex **17** experiences a mass loss at 70 °C which is likely to be solvent evaporation and the total mass of complex was adjusted accordingly. For each an

initial mass loss approximately equal to two carbonyl ligands, is followed by decomposition of the rest of the complex. Carbonyl loss from **17** and **18** occurs at much the same temperature as with **15** and **16** (Table 2-3), but instead of a smooth drop in mass equivalent to two CO groups (as with the rest of the dicarbonyl complexes), **17** and **18** show a staggered loss, with individual mass losses approximately equivalent to one CO each.

The decomposition path may be more complex than for **13** – **16**, involving the rearrangement of fragments as has been seen in ruthenium(II) bis(dithiocarbamate) dicarbonyl complexes.[59, 60] Hogarth *et al.* showed the formation of the octanuclear $[Ru_8(\mu^5\text{-}S)_2(\mu^4\text{-}S)(\mu^3\text{-}S)(\mu\text{-}CNMe_2)_2(\mu\text{-}CO)(CO)_{15}]$ cluster when *cis*-$[Ru(S_2CNMe_2)_2(CO)_2]$ and $[Ru_3(CO)_{12}]$ were refluxed in xylene, which they believe is formed *via* the pentanuclear $[Ru_5(\mu^4\text{-}S)_2(\mu\text{-}CNMe_2)_2(CO)_{11}]$ intermediate.[60]

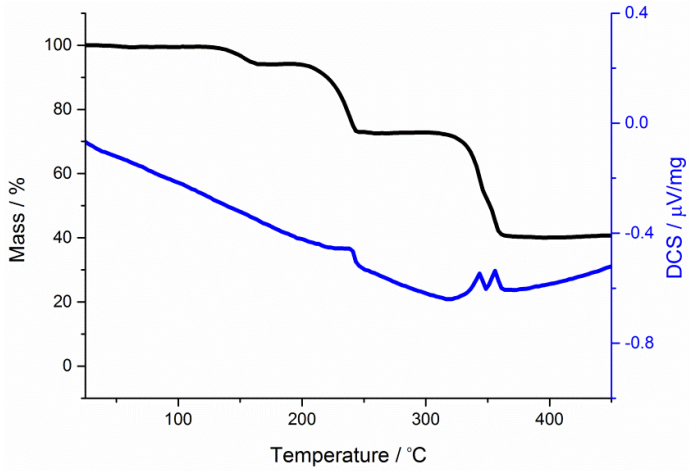

Figure 2-8 - TGA (black) and DSC (blue) graphs for $[Ru(S_2CNMe_2)_2(CO)_2]$.

The decomposition of $[Ru(S_2CNMe_2)_2(CO)_2]$ (previously prepared by Hogarth *et al.*) was investigated *via* TGA (Figure 2-8), the results of which were hoped to aid in the elucidation of the decomposition of **17** and **18**. The decomposition occurs in four stages (Equation 2-6). The first mass loss at 127 °C can be ascribed to one carbonyl group is observed, followed by a loss at 200 °C for an isothiocyanate group ($SCNMe_2$). The third and fourth stages occur in quick succession and are difficult to assign, though may be equivalent to the loss of NMe_2 and CO groups, while the final loss may be the SC fragment. The residual mass is equivalent to RuS_2, similar to many of the iron cases tested. Complexes **17** and **18** lose their carbonyl ligands in the first stage and there are no subsequent mass losses equivalent to an isothiocyanate group, indicating decomposition occurs *via* a different mechanism.

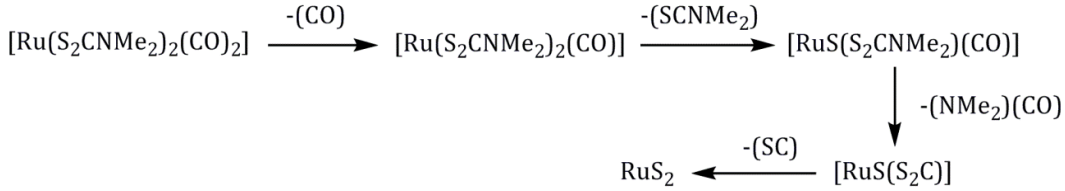

Equation 2-6

Following the loss of the carbonyl ligands from **17** and **18**, there is a large mass loss as the remaining iron(II) bis(dithiocarbamate) complexes decompose. For **17** this mass loss is equivalent to $S_2(C(4MePip))_2$, leaving a residue equivalent to FeS_2, however for **18** a mass equivalent to $(C(2,6Me_2Pip))_2$ is lost first (containing no sulfur), and subsequently one sulfur is lost gradually beginning at 330 °C leaving a mass equivalent to FeS_3.

In summary, these results show that under TGA conditions complexes **13** – **18** meet the requirements as molecular precursors for solvothermal nanoparticles synthesis. They are stable at room temperature, but the carbonyl ligands eliminate at temperatures lower than the decomposition temperatures of the resulting iron(II) bis(dithiocarbamate) complexes. Complex **14** has the lowest temperature for the removal of two carbonyl ligands and that with the smallest window of thermal stability is **18**. The iron(II) bis(dithiocarbamate) complexes decompose between 166 and 266 °C under TGA conditions, **13** being the most stable.

Duffy *et al* infer that the higher the pK_a of the secondary amine functional group of the dithiocarbamate ligand, the stronger the metal-carbonyl bonds and the higher the temperature at which the carbonyl ligands break away from the complex. The graph in shows these pK_a values versus the temperature found in this study at which CO is lost. There appears to be a general trend in the data that the higher the pK_a of the ligand amine, the lower the temperature at which the carbonyl ligands are lost. This contradicts the reported hypothesis in the literature, and indicates that the bonding may be more complicated than first thought and not easily explained by the resonance structures in Figure 1-5.

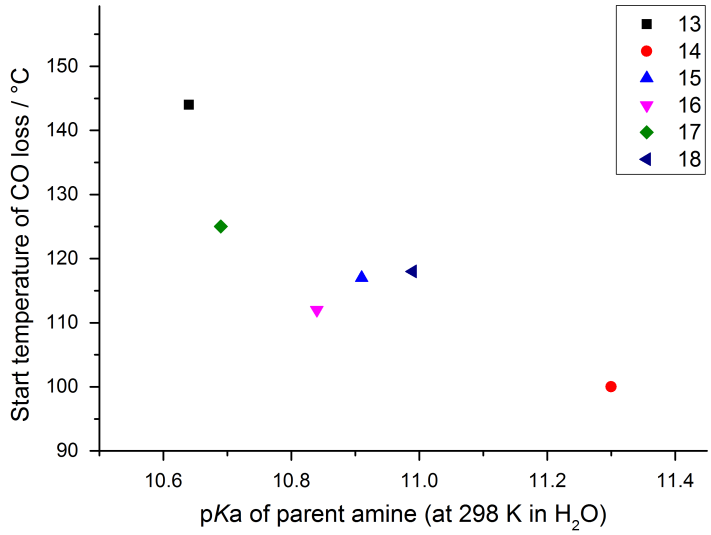

Figure 2-9 - Graph comparing the temperature at which carbonyls are lost against pK_a of ligand amine for complexes 13 – 18.

2.3 Conclusions

Chapter 2 focused on the synthesis of iron dithiocarbamate molecular precursors and assessed their suitability for subsequent decomposition to form iron sulfide nanoparticles.

The carbonyl protected forms of iron(II) bis(dithiocarbamate) complexes were synthesised as the iron(II) source since the unprotected complexes were known to be extremely air sensitive and thus difficult to handle. The iron(II) bis(dithiocarbamate) dicarbonyl complexes were found to be suitable replacements, being stable in the solid state at room temperature, but also decomposing to form the unprotected complex well before its subsequent decomposition thereby potentially avoiding any possible unwanted impurities in the resulting nanoparticles. Though the dicarbonyl complexes were found to be suitable it should be noted that they were non-trivial to synthesise. It was hoped that these complexes would prove to be effective precursors to a range of iron sulfide nanoparticles, containing iron in the +2 oxidation state.

The iron(III) tris(dithiocarbamate) complexes were in comparison facile to synthesise. Thus a range of iron(II) and iron(III) species have been produced, their relative stabilities assessed by TGA. TGA was performed in the solid state, and therefore could only be an indicator of the chemistry which might occur during actual solvothermal nanoparticle synthesis. Several combinations of iron(II) and iron(III) precursors were identified by TGA analysis, in particular the methyl derivatives **1** and **13** were found to decompose within a

7 °C temperature range. These complexes were also found to be the most stable of both species, especially important for the iron(II) complexes. For these reasons this combination of precursors appears to be the most suitable for the synthesis of greigite. Complex **13** was also had the most facile synthesis of the iron(II) complexes so was the most practical of these precursors to take forward for the synthesis of iron sulfide nanoparticles with iron solely in the +2 oxidation state.

2.4 Experimental

General Procedures

All manipulations were performed under a dry, oxygen-free dinitrogen atmosphere using standard Schlenk techniques or in a Mbraun Unilab glovebox. All solvents used were stored in alumina columns and dried with anhydrous engineering equipment, such that the water concentration was 5–10 ppm. All other reagents were procured commercially from Aldrich and used without further purification. Microanalytical data were obtained at University College London.

Physical Measurements

All ^{1}H and $^{13}C\{^{1}H\}$ NMR spectra were obtained on either a Bruker Avance III 400 or Avance 600 spectrometer, the latter being equipped with a cryoprobe. All spectra were recorded using $CDCl_3$ which was dried and degassed over molecular sieves prior to use; ^{1}H and $^{13}C\{^{1}H\}$ chemical shifts are reported relative to $SiMe_4$. Mass spectra were obtained using either Micromass 70-SE spectrometer using Electron Ionisation (EI) or a Thermo Finnigan MAT900xp spectrometer using Fast Atom Bombardment (FAB) ionisation. Elemental analysis was carried using Elemental Analyser (CE-440) (Exeter Analytical Inc). Thermogravimetric analysis (TGA) was performed using a Netzsch STA 449C TGA system. Data was recorded from 25 to 600 °C with a constant heating rate of 10 °C minute^{-1}.

$[Fe(S_2CNMe_2)_3]$ (1)

The complex was synthesised according to a literature report.[11] An example of the synthesis method is given below.

NaS_2CNMe_2 (4.30 g, 30 mmol) was dissolved into 60 mL water and added dropwise over 10 mins to a solution of $FeCl_3$ (1.62 g, 10 mmol) in water (50 mL), whereupon a black

precipitate formed. This mixture was vigorously stirred for 2 hrs, filtered, washed with water (3 x 30 mL) and evaporated to dryness. The resulting black powder was dissolved in 100 mL of dichloromethane (DCM) and stirred with magnesium sulphate for 30 mins, after which the mixture was filtered and the filtrate dried *in vacuo*. Yield 3.2882 g, 79 %. **Anal. Calc. for $C_9H_{18}N_3S_6Fe$:** C, 25.95; H, 4.36; N, 10.09. Found: C, 25.79; H, 4.37; N, 10.17. **MS:** *m/z* 416 [M^+], 296 [M^+ - $C_3H_6NS_2$]. **IR (ν_{max} cm^{-1}):** 1516 (s) [N=C], 972 (s), 1247 (s) [C=S], 1137 (s) [C_2N].

[Fe(S_2CNEt_2)$_3$] (2)

The complex was synthesised following the same method as with **1**, with the exception that NaS_2NCEt_2 (6.76 g, 30 mmol) was used as the reagent. Yield 4.2982 g, 86 %. **Anal. Calc. for $C_{15}H_{30}N_3S_6Fe$:** C, 35.99; H, 6.04; N, 8.39. Found: C, 35.88; H, 6.01; N, 8.40. **MS:** *m/z* 500 [M^+], 352 [M^+ - $C_5H_{10}NS_2$]. **IR (ν_{max} cm^{-1}):** 1485 (s) [N=C], 994 (s), 1270 (s) [C=S], 1133 (s) [C_2N].

[Fe($S_2CN^iBu_2$)$_3$] (3)

$^iBu_2NH$ (5.24 mL, 30 mmol) was added to NaOH (1.20 g, 30 mmol) in water (50 mL). To this mixture CS_2 (1.80 mL, 30 mmol) was added dropwise over 10 mins and the mixture stirred overnight. A solution of $FeCl_3$ (1.62 g, 10 mmol) in water (50 mL) was added dropwise over 5 mins, whereupon a black precipitate formed. This mixture was vigorously stirred for 2 hrs, filtered, washed with water (3 x 30 mL) and evaporated to dryness. The resulting black powder was dissolved in 100 mL of DCM and stirred with magnesium sulphate for 30 mins, after which the mixture was filtered and the filtrate dried *in vacuo*. Yield 5.5525 g, 83 %. **Anal. Calc. for $C_{27}H_{54}N_3S_6Fe$:** C, 48.48; H, 8.14; N, 6.23. Found: C, 48.52; H, 8.26; N, 6.23. **MS:** *m/z* 669 [M^+], 464 [M^+ - $C_9H_{18}NS_2$]. **IR (ν_{max} cm^{-1}):** 1482 (s) [N=C], 992 (s), 1244 (s) [C=S], 1145 (s) [C_2N].

[Fe($S_2CNMeBu$)$_3$] (4)

The complex was synthesised following the same method as with **3**, with the exception that MeBuNH (3.55 mL, 30 mmol) was used. Yield 0.3879 g, 43 %. **Anal. Calc. for $C_9H_{18}N_3S_6Fe$:** C, 39.83; H, 6.69; N, 7.74. Found: C, 39.54; H, 6.83; N, 7.61. **MS:** *m/z* 543 [M^+], 380 [M^+ – $C_6H_{12}NS_2$]. **IR (ν_{max} cm^{-1}):** 1496 (s) [N=C], 936 (s), 1246 (s) [C=S], 1144 (s) [C_2N].

[Fe(S_2C(4-MePip))$_3$] (5)

The complex was synthesised following the same method as with **3**, with the exception that 4-MePipH (3.55 mL, 30 mmol) was used. Yield 2.8939 g, 50 %. **Anal. Calc. for $C_{21}H_{36}N_3S_6Fe$:** C, 43.58; H, 6.27; N, 7.26. Found: C, 43.42; H, 6.21; N, 6.95. **MS:** *m/z* 577 [M^+]. **IR (ν_{max} cm^{-1}):** 1455 (s) [N=C], 948 (s), 1265 (s) [C=S], 1145 (s) [C_2N].

($S_2CN^iBu_2$)$_2$ (6)

^{i}Bu$_2$NH (2.62 mL, 15 mmol) was added to NaOH (0.60 g, 15 mmol) in water (50 mL). To this mixture CS_2 (0.90 mL, 15 mmol) was added dropwise over 10 mins and the mixture stirred overnight. An aqueous solution (20 mL) of $K_3[Fe(CN)_6]$ (4.94 g, 15 mmol) was added dropwise over 10 mins and stirred vigorously for two hrs. The solution was filtered using a Büchner funnel, washed with water (1 x 20 mL) and dried *in vacuo*. The resulting beige solid was crushed to a powder using a mortar and pestle, washed with water (3 x 30 mL) and dried *in vacuo* to produce a white powder. Yield 2.7897 g, 91 %. **^{1}H NMR δ/ppm ($CDCl_3$):** 0.93 (d, *J* = 6.3 Hz, 12H, C*H*$_3$), 1.04 (d, *J* = 6.3 Hz, 12H, C*H*$_3$), 2.49 (m, 4H, C*H*), 3.84 (m, 8H, C*H*$_2$). **^{13}C{^{1}H} NMR δ/ppm ($CDCl_3$):** 20.3 (*C*H$_3$), 20.5 (*C*H$_3$), 26.1 (*C*H), 28.7 (*C*H), 61.8 (*C*H$_2$), 65.5 (*C*H$_2$), 194.3 (*C*S$_2$). **Anal. Calc. for $C_{18}H_{36}N_2S_4$:** C, 52.89; H, 8.88; N, 6.85. Found: C, 52.73; H, 9.07; N, 6.90. **MS:** *m/z* 408 [M^+], 204 [M^+ - ($S_2CN^iBu_2$)], 172 [M^+ - (SCN^iBu_2)].

Attempted synthesis of Fe(S_2CNR_2)$_2$(CO)$_2$ (R = Me, Et, ^{i}Bu)

R = Me, Et

$Fe_3(CO)_{12}$ (1.00 g, 0.20 mmol) and (S_2CNR_2)$_2$ (0.14 g, 0.60 mmol) were refluxed in THF (20 mL) at 65 °C for one hr (toluene was used at 80 °C in the case of R = ^{i}Bu). During that time the solution changed from dark green to dark brown. The reaction was allowed to cool and the volatiles removed *in vacuo*. Product was detected by IR, but ^{1}H-NMR showed the presence of a paramagnetic species. **(Me) IR (ν_{max} cm^{-1}):** 2024, 1968. **^{1}H NMR δ/ppm ($CDCl_3$):** broad peaks at 0.29, 0.34, 1.36, 2.65, 2.88, 4.25. **(Et) IR (ν_{max} cm^{-1}):** 2023, 1965. **^{1}H NMR δ/ppm ($CDCl_3$):** broad peaks at 0.90, 1.12, 1.30, 3.70, 3.81, 4.06. **(^{i}Bu) IR (ν_{max} cm^{-1}):** 2022, 1965. **^{1}H NMR δ/ppm ($CDCl_3$):** broad peaks at 0.95, 1.07, 1.28, 1.87, 2.21, 2.52, 3.54, 3.87.

R = Et

The reaction was repeated as above in DCM (20 mL) at 45 °C and trace amounts of product were observed *via* IR spectroscopy after one hr. **IR (ν_{max} cm^{-1}):** 2088 (v. small), 2048 ($Fe_3(CO)_{12}$ reagent) , 2026 ($Fe_3(CO)_{12}$ reagent), 1969 (v. small).

The reaction was repeated again in toluene (20 mL) at 80 °C and after 15 minutes IR spectroscopy showed only product peaks, but ^{1}H-NMR showed the presence of a paramagnetic species. **IR (ν_{max} cm^{-1}):** 2025, 1968. **^{1}H NMR δ/ppm ($CDCl_3$):** 0.91, 1.36, 1.54, 4.08.

$[H_2NR_2][S_2CNR_2]$

$NR_2 = NMe_2$ (7)

Me_2NH (15 mmol, 7.50 mL of a 2M solution in THF) was dissolved in further THF (20 mL) CS_2 (0.45 mL, 7.5 mmol) was added slowly dropwise over five mins whereupon a white precipitate began to form. The mixture was stirred for two hrs, filtered using a Büchner funnel and washed with THF (3 x 10 mL). Yield 1.1200 g, 90 %. **^{1}H NMR δ/ppm ($CDCl_3$):** 2.78 (s, 6H, CH_3), 3.58 (s, 6H, CH_3), 8.42 (broad s, 2H, [$(CH_3)_2NH_2$]). **^{13}C{^{1}H} NMR δ/ppm ($CDCl_3$):** 35.4 (CH$_3$), 44.8 (CH$_3$), 210.2 (CS_2). **Anal. Calc. for $C_5H_{14}N_2S_2$:** C, 36.11; H, 8.49; N, 16.84. Found: C, 35.56; H, 8.38; N, 16.57. **MS(EI):** *m/z* 121 [$S_2CN(CH_3)_2 + H^+$].

NR_2 = N^{i}Bu$_2$ (8), 4-methylpiperidine (4-MePip, 9), 2,6-dimethylpiperidine (2,6-Me_2Pip, 10)

To a solution of R_2NH (15 mmol) in water (20 mL) CS_2 (0.45 mL, 7.5 mmol) was added slowly dropwise over five mins, whereupon a yellow precipitate began to form. The solution was stirred overnight and then filtered using a Büchner funnel and washed with water (3 x 10 mL) to yield a yellow crystalline powder.

(8) Yield 1.3400 g, 54 %. **^{1}H NMR δ/ppm ($CDCl_3$):** 0.93 (d, 12H, CH_2CHCH_3), 1.05 (d, 12H, CH_3), 2.13 (m, 2H, CH_2CHCH_3), 2.46 (m, 2H, CH_2CHCH_3), 2.78 (d, 4H, CH_2CHCH$_3$), 3.86 (d, 4H, CH_2CHCH$_3$), 9.37 (broad s, 2H, NH_2). **^{13}C{^{1}H} NMR δ/ppm ($CDCl_3$):** 19.9 (CH_3), 25.5 (CH), 26.5 (CH), 54.0 (CH_2), 61.5 (CH_2), 210.0 (CS_2). **Anal. Calc. for $C_{17}H_{38}N_2S_2$:** C, 61.02; H, 11.45; N, 8.37. Found: C, 61.33; H, 11.66; N, 8.39. **MS(EI):** *m/z* 205 [$S_2CN^iBu_2 + H^+$].

(9) Yield 0.9629 g, 52 %. **^{1}H NMR δ/ppm ($CDCl_3$): [S_2C(4-MePip)]** 0.95 (d, 3H, CH_3), 1.21 (m, 2H, C$H_{2(meta, ax)}$), 1.67 (m, 1H, C$H_{(ortho, ax)}$), 1.71 (m, 2H, C$H_{2(meta, eq)}$), 3.03 (m, 2H, C$H_{2(ortho, ax)}$), 5.70 (m, 2H, C$H_{2(ortho, eq)}$). **[4-MePipH]** 0.97 (d, 3H, CH_3), 1.53 (m, 1H, C$H_{(ortho, ax)}$), 1.57 (m, 2H, C$H_{2(meta, eq)}$), 1.77 (m, 2H, C$H_{2(meta, ax)}$), 2.82 (m, 2H, C$H_{2(ortho, ax)}$), 3.74 (m, 2H, C$H_{2(ortho, eq)}$), 7.06 (broad s, 2H, NH_2). **^{13}C{^{1}H} NMR δ/ppm ($CDCl_3$):** 21.7 (CH$_3$), 21.8 (CH$_3$), 29.5 (CH$_2$), 31.1 (CH), 31.4 (CH), 34.5 (CH$_2$), 44.9 (CH$_2$), 51.4 (CH$_2$), 208.8 (CS_2). **Anal. Calc. for $C_{13}H_{26}N_2S_2$:** C, 56.88; H, 9.55; N, 10.21. Found: C, 56.70; H, 9.65; N, 10.17. **MS(EI):** *m/z* 175 [S_2C(4-MePip) + H$^+$].

(10) Yield 1.6952 g, 75 %. **^{1}H NMR δ/ppm ($CDCl_3$):** 1.00 (m, 4H, C$H_{2((meta)}$), 1.06 (s, 6H, CH_3), 1.07 (s, 6H, CH_3), 1.35 (m, 2H, C$H_{2(para)}$), 1.58 (m, 4H, C$H_{2(meta)}$), 1.68 (s, 2H, NH_2), 1.75 (m, 2H, C$H_{2(para)}$), 2.65 (m, 2H, C$H_{(ortho)}$). **^{13}C{^{1}H} NMR δ/ppm ($CDCl_3$):** 23.1 (CH$_3$), 24.9 (CH$_{3(para)}$), 34.1 (CH$_{2(meta)}$), 52.6 (CH$_{(ortho)}$), 192.7 (CS_2). **Anal. Calc. for $C_{15}H_{30}N_2S_2$:** C, 59.55; H, 9.99; N, 9.26. Found: C, 59.34; H, 10.09; N, 9.35. **MS(EI):** *m/z* 189 [S_2C(2,6-Me_2Pip) + H$^+$].

[NMe_4][S_2CNR_2], RR' = Et_2 (11), MeBu (12)

To an ice-cooled solution of Me_4NOH (10 mmol, 3.65 g of a 25% wt solution in methanol) and RR'NH (10 mmol) in methanol (50 mL), CS_2 (10 mmol, 0.60 mL) was added dropwise over five mins. The solution was allowed to come to room temperature and stirred overnight. Methanol was removed *in vacuo* resulting in a pale yellow crystalline powder. **(11)** Yield 2.2075 g, 99 %. **^{1}H NMR δ/ppm ($CDCl_3$):** 1.23 (t, 6H, J = 7.0 Hz, CH_2CH_3), 4.14 (q, 4H, J = 7.0 Hz, CH_2CH_3). **^{13}C{^{1}H} NMR δ/ppm ($CDCl_3$):** 12.7 (CH_2CH_3), 47.5 (CH_2CH_3), 56.2 (N(CH_3)$_4$) 210.6 (CS_2). **Anal. Calc. for $C_9H_{22}N_2S_2$:** C, 48.60; H, 9.97; N, 12.06. Found: C, 48.41; H, 9.54; N, 11.73. **MS(EI):** *m/z* 148 [$S_2CN(CH_2CH_3)_2$].

(12) Yield 1.1578 g, 98 %. **^{1}H NMR δ/ppm ($CDCl_3$):** 0.91 (t, 3H, J = 7.4 Hz, $S_2CN(CH_3)(CH_2)_3CH_3$), 1.31 (m, 2H, CH_2), 1.65 (m, 2H, CH_2), 3.51 (s, 3H, $S_2CN(CH_3)(CH_2)_3CH_3$), 3.55 (s, 12H, N(CH_3)$_4$), 4.14 (m, 2H, CH_2). **^{13}C{^{1}H} NMR δ/ppm ($CDCl_3$):** 14.19 ($S_2CN(CH_3)(CH_2)_3CH_3$), 20.32 (CH_2), 29.44 (CH_2), 42.41 (CH_2), 59.00 ($S_2CN(CH_3)(CH_2)_3CH_3$), 56.17 (N(CH_3)$_4$) 211.77 (CS_2). **Anal. Calc. for $C_{10}H_{24}N_2S_2$:** C, 50.80; H, 10.23; N, 11.85. Found: C, 49.47; H, 10.13; N, 11.41. **MS(EI):** *m/z* 162 [$S_2CN(CH_3)(CH_2)_3CH_3$].

[Fe(S_2CNMe$_2$)$_2$(CO)$_2$] (13)

The complex was synthesised based on a literature report.[40] An example of the synthesis method is given below.

Fe(CO)$_4$I$_2$ was synthesised and used *in situ*. A solution of iodine (0.38 g, 1.5 mmol) in diethylether (10 mL) was added dropwise to a solution of $Fe(CO)_5$ (0.20 mL, 1.5 mmol) also in diethylether (10 mL). After stirring for 15 mins $Fe(CO)_4I_2$ was detected by IR. **IR (ν_{max} cm^{-1}):** 2137, 2090, 2072 (CO).

A solution of **7** (0.50 g, 3.0 mmol) in dichloromethane (20 mL) was added dropwise to the *in* situ formed $Fe(CO)_4I_2$ and the mixture stirred for 18 hrs. The product was separated from the dithiocarbamate iodide salt by cannula filtration and layered with heptane (10 mL) to obtain copper coloured crystals. Yield 0.2379 g, 45% **^{1}H NMR δ/ppm ($CDCl_3$):** 3.21 (s, 6H, CH_3), 3.28 (s, 6H, CH_3). **^{13}C{^{1}H} NMR δ/ppm ($CDCl_3$):** 38.3, 38.7 (*C*H$_3$), 206.9 (*C*S$_2$), 212.9 (*C*O). **Anal. Calc. for $C_8H_{12}N_2S_4O_2Fe$:** C, 27.27; H, 3.43; N, 7.95. Found: C, 27.92; H, 3.65; N, 7.44. **MS:** *m/z* 352 [M$^+$], 296 [M$^+$-2CO]. **IR (ν_{max} cm^{-1}):** 2023, 1967 (CO).

[Fe(S_2CNEt$_2$)$_2$(CO)$_2$] (14)

To an *in situ* formed solution of $Fe(CO)_4I_2$ a solution of excess **11** (1.07 g, 4.8 mmol) in dichloromethane (20 mL) was added dropwise and the mixture stirred for 18 hrs. The solid product was extracted in toluene (10 mL) and layered with heptane (10 mL) to obtain a copper-coloured oil. A dry powder was obtained by washing the product with pentane (5 mL). Further attempts to obtain crystals from the hexane washings in the freezer only produced further powder. Yield 0.2573 g, 42%. **^{1}H NMR δ/ppm ($CDCl_3$):** 1.27 (m, 12H, CH_2CH_3), 3.73 (m, 8H, CH_2CH_3). **^{13}C{^{1}H} NMR δ/ppm ($CDCl_3$):** 12.6, 12.6, 12.8 (CH_2CH_3), 43.4, 43.8, 43.8 (CH_2CH_3), 205.8 (CS_2), 213.1 (*C*O). **Anal. Calc. for $C_{12}H_{20}N_2S_4O_2Fe$:** C, 35.29; H, 4.94; N, 6.86. Found: C, 36.00; H, 5.08; N, 6.76. **MS:** *m/z* 393 [M$^+$-CH$_3$] 352 [M$^+$-2CO]. **IR (ν_{max} cm^{-1}):** 2022, 1966 (CO).

[Fe(S_2CN^{i}Bu$_2$)$_2$(CO)$_2$] (15)

To an *in situ* formed solution of $Fe(CO)_4I_2$ a solution of **8** (1.00 g, 3 mmol) in diethylether (10 mL) was added dropwise and the mixture stirred for 18 hrs. The solid product was extracted in hexane (10 mL) and put in the freezer to obtain copper-coloured crystals. Yield 0.3360 g, 43%. **^{1}H NMR δ/ppm ($CDCl_3$):** 0.93 (m, 24H, CH_3), 2.17 (m, *J* = 6.9 Hz, 2H,

C*H*), 2.23 (m, *J* = 6.9 Hz, 2H, C*H*), 3.52 (m, 8H, CH_2). **^{13}C{^{1}H} NMR δ/ppm ($CDCl_3$):** 20.2, 20.3, 20.3, 20.4 (*C*H_3), 27.1, 27.2 (*C*H), 58.9, 56.4 (*C*H_2), 208.1 (*C*S_2), 213.1 (*C*O). **MS:** *m/z* 464 [M$^+$-2CO]. **IR (ν_{max} cm^{-1}):** 2026, 1974 (CO).

[Fe(S_2CNMeBu$_2$)$_2$(CO)$_2$] (16)

To an *in situ* formed solution of $Fe(CO)_4I_2$ a solution of **12** (0.75 g, 3 mmol) in dichloromethane (20 mL) was added dropwise and the mixture stirred for 15 mins. The product was extracted in toluene (10 mL) and layered with heptane (10 mL) but no crystals could be obtained from the oily product. Extraction with pentane (5 mL) yielded a brown powder after two weeks in the freezer. Yield 0.2226 g, 34 %. **^{1}H NMR δ/ppm ($CDCl_3$):** 0.95 (m, 6H, $CH_2(CH_2)_2CH_3$), 1.50 (m, 8H, $CH_2(CH_2)_2CH_3$), 3.19 (m, 6H, NCH_3), 3.60 (m, 6H, $CH_2(CH_2)_2CH_3$). **^{13}C{^{1}H} NMR δ/ppm ($CDCl_3$):** 13.9, 13.9, 14.0 ($(CH_2)_3CH_3$), 19.9, 20.0, 20.1 (*C*H_2), 29.0, 29.1, 29.2 (*C*H_2), 36.2, 36.6, (*C*H_3), 50.9, 51.1, 51.4 (*C*H_2), 206.5 (*C*S_2), 213.0 (*C*O). **Anal. Calc. for $C_{18}H_{36}N_2S_4Ni$:** C, 38.53; H, 5.54; N, 6.42. Found: C, 38.84; H, 5.20; N, 6.03. **MS:** *m/z* 381 [M$^+$-2CO]. **IR (ν_{max} cm^{-1}):** 2036, 1967 (CO).

[Fe(S_2CNRR')$_2$(CO)$_2$], NRR' = 4-methylpiperidine (17), 2,6-dimethylpiperidine (18)

To an *in situ* formed solution of $Fe(CO)_4I_2$ a solution of [RR'NH_2][S_2CNRR'] (3 mmol) in dichloromethane (10 mL) was added dropwise and the mixture stirred for two hrs. The product was extracted in toluene (10 mL) and layered with heptane (10 mL) resulting in a brown oil. A dry red powder was obtained by washing the product with hexane (5 mL). **(17)** Yield 0.2210 g, 32 %. **^{1}H NMR δ/ppm ($CDCl_3$):** 0.99 (m, 6H, CH_3), 1.26 (m, 4H, C$H_{2(meta, ax)}$), 1.73 (m, 2H, C$H_{(para, ax)}$), 1.73 (m, 4H, C$H_{2(meta, eq)}$), 2.92 (m, 4H, C$H_{2(ortho, ax)}$), 4.67 (m, 4H, C$H_{2(ortho, eq)}$). **^{13}C{^{1}H} NMR δ/ppm ($CDCl_3$):** 21.4, 21.6 (*C*H_3), 30.8, 30.9 (*C*$H_{(para)}$), 33.2, 33.3, 33.4 (*C*$H_{2(meta)}$), 45.9, 46.0, 46.2, 46.5, 46.6, 46.7 (*C*$H_{2(ortho)}$), 204.8 (*C*S_2), 212.9 (*C*O). **Anal. Calc. for $C_{18}H_{36}N_2S_4Ni$:** C, 41.73; H, 5.25; N, 6.08. Found: C, 41.36; H, 5.37; N, 5.62. **MS:** *m/z* 404 [M$^+$-2CO]. **IR (ν_{max} cm^{-1}):** 2023, 1965 (CO).

(18) Yield 0.3078 g, 42 %. **^{1}H NMR δ/ppm ($CDCl_3$):** 1.32 (m, 12H, CH_3), 1.57 (m, 2H, C$H_{2(para)}$), 1.68 (m, 8H, C$H_{(meta)}$), 1.86 (m, 2H, C$H_{2(para)}$), 4.94 (m, 4H, C$H_{2(ortho)}$). **^{13}C{^{1}H} NMR δ/ppm ($CDCl_3$):** 14.0 (*C*$H_{2(para)}$), 19.4, 19.5, 19.6, 19.6, 19.6, 19.7, 19.8 (*C*H_3), 29.5, 29.5, 29.6, 29.7 (*C*$H_{2(meta)}$), 48.9, 48.9, 49.0, 49.0, 49.6, 49.6, 49.7 (*C*$H_{(ortho)}$), 206.2 (*C*S_2), 213.2 (*C*O). **Anal. Calc. for $C_{18}H_{36}N_2S_4Ni$:** C, 44.25; H, 5.78; N, 5.73. Found: C, 45.01; H, 5.95; N, 5.61. **MS:** *m/z* 432 [M$^+$-2CO]. **IR (ν_{max} cm^{-1}):** 2020, 1963 (CO).

2.5 References

1 D. Rickard and G. W. Luther, *Chem. Rev.*, 2007, 107, 514.
2 G. Hogarth, *Prog. Inorg. Chem.*, 2005, 53, 71.
3 M. Delépine, *C. R. Hebd. Seances Acad. Sci.*, 1907, 144, 1125.
4 K. B. Pandeya, R. Singh, C. Prakash, and J. S. Baijal, *Solid State Commun.*, 1987, 64, 801.
5 J. Albertsson and Å. Oskarsson, *Acta Crystallogr. Sect. B Struct. Crystallogr. Cryst. Chem.*, 1977, 33, 1871.
6 K. Stahl, *Inorg. Chim. Acta*, 1983, 75, 85.
7 B. Hutchinson, P. Neill, A. Finkelstein, and J. Takemoto, *Inorg. Chem.*, 1981, 20, 2000.
8 S. Singhal, A. Garg, and K. Chandra, *J. Alloys Compd.*, 2007, 443, 53.
9 K. Gregson and D. M. Doddrell, *Chem. Phys. Lett.*, 1975, 31, 125.
10 C. A. Tsipis, C. C. Hadjikostas, and G. E. Manoussakis, *Inorg. Chim. Acta*, 1977, 23, 163.
11 A. H. White, R. Roper, E. Kokot, H. Waterman, and R. L. Martin, *Aust. J. Chem.*, 1964, 17, 294.
12 R. M. Golding, W. C. Tennant, C. R. Kanekar, R. L. Martin, and A. H. White, *J. Chem. Phys.*, 1966, 45, 2688.
13 P. B. Merrithew and P. G. Rasmussen, *Inorg. Chem.*, 1972, 11, 325.
14 C. Geloso, R. Kumar, J. R. Lopez-Grado, and D. G. Tuck, *Can. J. Chem.*, 1987, 65, 928.
15 J. G. Leipoldt and P. Coppens, *Inorg. Chem.*, 1973, 12, 2269.
16 S. Singhal, C. L. Sharma, A. N. Garg, and K. Chandra, *Transit. Met. Chem.*, 2001, 2, 81.
17 L. Szegö and L. Cambi, *Berichte der Dtsch. Chem. Gesellschaft*, 1931, 64, 2591.
18 N. V. Duffy, W. G. Movius, and D. L. Uhrich, *Inorg. Chim. Acta*, 1982, 64, L91.
19 N. Duffy, *Inorg. Chim. Acta*, 1981, 47, 31.
20 G. L. Miessler, E. Zoebisch, and L. H. Pignolet, *Inorg. Chem.*, 1978, 17, 3636.
21 V. F. Plyusnin, V. P. Grivin, and S. V. Larionov, *Coord. Chem. Rev.*, 1997, 159, 121.
22 J. M. Stegge, S. M. Woessner, and P. E. Hoggard, *Inorg. Chim. Acta*, 1996, 250, 385.
23 G. A. Katsoulos, C. A. Tsipis, and F. D. Vakoulis, *Can. J. Chem.*, 1985, 63, 3249.
24 B. M. Ondo, J. P. Barbier, and R. P. Hugel, *Comptes Rendus l'Academie des Sci. Ser. II Mec. Phys. Chim. Sci. la Terre l'Univers*, 1985, 301, 225.
25 G. Crisponi, P. Deplano, and E. F. Trogu, *J. Chem. Soc., Dalton. Trans.*, 1986, 365.
26 V. Kettman, F. Pavelcik, and J. Majer, *Czech. Chem. Commun.*, 1981, 46, 2307.
27 D. L. Kepert, C. L. Raston, A. H. White, and D. Petridis, *J. Chem. Soc., Dalton. Trans.*, 1980, 1921.
28 D. Petridis, A. Kostikas, A. Simopoulos, and D. Niarchos, *Inorg. Chem.*, 1982, 21, 766.
29 B. F. Hoskins, R. L. Martin, and A. H. White, *Nature*, 1966, 211, 627.
30 K. Gleu and R. Schwab, *Angew. Chemie*, 1950, 62, 320.
31 J. P. J. Fackler and D. G. Holah, *Inorg. Nucl. Chem. Lett.*, 1966, 2, 251.
32 R. H. Holm, L. H. Pignolet, and R. A. Lewis, *J. Am. Chem. Soc.*, 1971, 93, 360.
33 O. A. Ileperuma and R. D. Feltham, *Inorg. Chem.*, 1975, 14, 3042.
34 B. L. Edgar, D. J. Duffy, M. C. Palazzotto, and L. H. Pignolet, *J. Am. Chem. Soc.*, 1972, 236, 1125.
35 A. K. M. Groves, N. Morrison, and J. A. McCleverty, *J. Organomet. Chem.*, 1975, 84, 5.
36 M. C. Palazzotto, D. J. Duffy, B. L. Edgar, L. Que, and L. H. Pignolet, *J. Am. Chem. Soc.*, 1973, 95, 4537.
37 H. Kunkely and A. Vogler, *Inorg. Chem. Commun.*, 2002, 5, 730.
38 D. G. Holah and C. N. Murphy, *Can. J. Chem.*, 1971, 49, 2726.

39 F. A. Cotton and J. A. McCleverty, *Inorg. Chem.*, 1964, 3, 1398.

40 W. K. Dean, *J. Organomet. Chem.*, 1977, 135, 195.

41 J. S. J. Ricci, C. Eggers, and I. Bernal, *Inorg. Chim. Acta*, 1971, 235, 97.

42 J. B. Zimmerman, T. W. Starinshak, D. L. Uhrich, and N. V. Duffy, *Inorg. Chem.*, 1977, 16, 3107.

43 H. Buettner and R. D. Feltham, *Inorg. Chem.*, 1972, 11, 971.

44 M. R. Houchin, *Inorg. Chim. Acta*, 1984, 83, 103.

45 N. V Duffy and T. G. Appleton, *Inorg. Chim. Acta*, 1988, 145, 273.

46 L. Hewison, S. H. Crook, B. E. Mann, A. J. H. M. Meijer, H. Adams, P. Sawle, and R. A. Motterlini, *Organometallics*, 2012, 31, 5823.

47 R. Foresti and R. Motterlini, *Curr. Drug Targets*, 2010, 11, 1595.

48 R. Foresti and R. Motterlini, *Nat. Rev. Drug Discov.*, 2010, 9, 728.

49 W. Han and M. Gao, *Cryst. Growth Des.*, 2008, 8, 1023.

50 Y. Zhang, Y. Du, H. Xu, and Q. Wang, *CrystEngComm*, 2010, 12, 3658.

51 A. Terzis, S. Filippakis, D. Mentzafos, V. Petrouleas, and A. Malliari, *Inorg. Chem.*, 1984, 23, 334.

52 J. Albertsson, Å. Oskarsson, and M. Nygren, *Acta Crystallogr. Sect. B Struct. Crystallogr. Cryst. Chem.*, 1979, 35, 1473.

53 B. F. Hoskins and B. P. Kelly, *Chem. Commun.*, 1968, 1517.

54 M. Akhtar, J. Akhter, M. A. Malik, P. O'Brien, F. Tuna, J. Raftery, and M. Helliwell, *J. Mater. Chem.*, 2011, 21, 9737.

55 G. D'Ascenzo and W. W. Wendlandt, *J. Inorg. Nucl. Chem.*, 1970, 32, 2431.

56 A. J. Deeming, C. Forth, and G. Hogarth, *Transit. Met. Chem.*, 2006, 31, 42.

57 A. Deeming and R. Vaish, *J. Organomet. Chem.*, 1993, 460, C8.

58 M. M. Karim, M. N. Abser, M. R. Hassan, N. Ghosh, H. G. Alt, I. Richards, and G. Hogarth, *Polyhedron*, 2012, 42, 84.

59 A. J. Deeming, C. S. Forth, and G. Hogarth, *J. Organomet. Chem.*, 2006, 691, 79.

60 A. J. Deeming, C. S. Forth, and G. Hogarth, *J. Organomet. Chem.*, 2007, 692, 4000.

3 Iron Sulfide Nanoparticles

3.1 Introduction

As detailed in Chapter 1, iron sulfide exists in many phases, including greigite (Fe_3S_4), pyrrhotite ($Fe_{1-x}S$, commonly Fe_7S_8 and Fe_8S_9), mackinawite (FeS), marcasite (FeS_2) and pyrite (FeS_2).[1] Iron sulfides have garnered considerable interest for their potential application as hydrogen evolution catalysts,[2] semiconductor materials for solar cells,[3, 4] photodiode materials,[5] photocatalysts and sensors,[6] information storage,[7, 8] and biomedicine.[9–11] Iron sulfide nanoparticles of various phases have been synthesised by numerous different techniques, which are summarised below.

Hydrothermal Synthesis

Hydrothermal synthesis has been widely employed to synthesise greigite,[12–14] pyrrhotite,[15] marcasite,[13] mackinawite[6] and pyrite.[16–18] It generally involves heating an aqueous solution of separate iron and sulfur sources in an autoclave for several hours at *ca.* 200 °C. Hydrothermal decomposition requires high temperatures and pressures and long reaction times, making it an energy intensive process. Water is often termed a green solvent, however in many cases a capping agent (which may not be benign) is added in order to prevent oxidation of the resulting iron sulfide nanoparticles.[6, 16–19] Other, less commonly used methods to synthesise iron sulfide nanoparticles include electrodeposition with anodic aluminium oxide producing pyrrhotite nanowire arrays,[7] and intracellular growth of greigite and pyrite nanoparticles in magnetotactic bacteria.[20] In addition a room temperature synthesis of nano-mackinawite is reported by Rickard *et al.* from the precipitation reaction between Mohr's salt (ammonium iron(II) sulphate) with sodium sulfide.[21]

Solvent-Free Synthesis

A variety of solvent free synthesis methods have been utilised. Pyrrhotite nanowires have been synthesised upon the thermal decomposition of an organic-inorganic composite species, described by the authors as $Fe_{1-x}S(EN)_{0.5}$ (EN = ethylenediamine), in argon at 200 °C.[22] While pyrrhotite nanoflowers have been synthesised in an autoclave under solvent free conditions from the single-source precursor, $[Fe(C_{16}H_{33}OCS_2)_3]$.[23] Chemical evaporation of ferric chloride and elemental sulfur in a tube furnace at 800 °C produced

dumbbell-like structures of pyrrhotite (Fe_8S_9) hexagons together with pyrrhotite (Fe_7S_8) nanowires.[24]

Solvothermal Synthesis

Solvothermal synthesis has several advantages over some of the other discussed methods. It is potentially simpler, occurs at lower temperature and pressure and has been widely used to synthesise iron sulfide nanoparticles.[25–31, 9, 32–37, 8, 2] There are many variables in a solvothermal decomposition, including solvent, precursor(s), decomposition temperature and duration. Considering solvent, it should be high boiling and able to coordinate to the resulting nanoparticles to prevent oxidation. Oleylamine (OA) is a commonly employed solvent/capping agent for solvothermal synthesis of iron sulfides.[27–33, 35–37, 8] Other solvents used include ethylene glycol (EG),[25, 9, 34] octylamine,[32, 2] dodecylamine (DDA),[32] trioctylphosphine oxide (TOPO),[38, 39] hexadecylamine (HDA),[27, 32, 8] octadecene (OD)[35–37, 8], dodecanethiol (DDT)[35] and oleic acid (OLA).[37, 40] Generally reactions are performed under nitrogen at approximately 200 °C.

Iron and sulfur precursors generally fall into two classes: binary and single-source. An advantage of the decomposition of binary precursors is that simple and relatively cheap compounds can be used. In many cases sulfur and a simple iron salt such as $FeCl_2$ are employed,[27–29, 31] although the more reactive Na_2S_3 and $(NH_4)_2S$ have also been used as sulfur sources.[26, 30] Li *et al.* report a pre-decomposition reaction between OA and $FeCl_2$ to give an Fe-OA complex, which then decomposed with sulfur at 220 °C to form nanocubes and nanodendrites, depending upon the $FeCl_2$ concentration.[29] Several other groups have suggested the preformation of such a complex, but generally present no evidence for such a species.[29, 39, 38]

Greigite and pyrite nanoparticles have been synthesised by the 'hot-injection' method, whereby a sulfur solution is injected into an already hot solution of iron precursor initiating nucleation.[27–29, 38, 39, 4] Autoclave methods have also been reported for the synthesis of greigite and pyrite nanoparticles from $FeSO_4{\cdot}7H_2O$ and Na_2S_3 in toluene.[26]

3.1.1 Decomposition of Non-Dithiocarbamate Single-Source Precursors

As discussed in Chapter 1, the solvothermal decomposition of single-source precursors has potential advantages over the binary systems such that the precise ratio of iron to sulfur in the molecular structure of the precursor can afford some level of control, and the

geometry of the sulfur atoms around the iron complex may inform the phase of iron sulfide produced, giving greater control and tuneability to these reactions. Solvothermal decomposition of single-source precursors can be carried out by hot-injection of single-source precursor into vessel containing heated solvent,[32, 33] or by heating the solvent-single-source precursor mixture from room temperature.[36, 37] The literature on solvothermal decomposition of single-source precursors will be divided into two types: iron dithiocarbamates and other iron sulfide single-source precursors.

Though it may not necessarily be considered a single-source precursor, Tilley and co-workers reported the synthesis of greigite nanocrystals from the hot-injection of [Fe(*N*-MeIm)$_6$][S$_8$] (*N*-MeIm = *N*-methylimidazole, Figure 3-1) into OA at 300 °C with immediate cooling.[33] Increasing the reaction time lead to a mixture of greigite and pyrrhotite phases, and after four hours submicrometer crystallites of pure pyrrhotite were formed, suggesting that pyrrhotite was the thermally more stable phase.[41] Maji *et al.* synthesised troilite ('hexagonal FeS') in EN, EG and NH_3 *via* a 15 min reflux at 120 °C followed by annealing at 450 °C for 30 min.[34] The morphology of the nanoparticles was shown to be affected by the solvent used, such that decomposition in EG and NH_3 produces nanoparticles, while EN produces nanorods.[34]

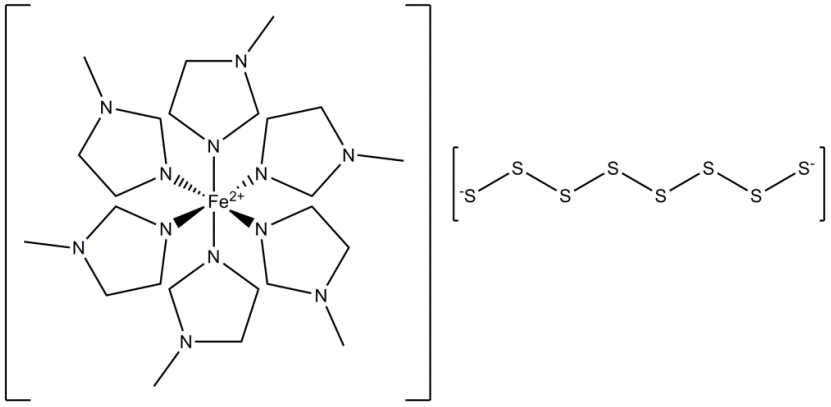

Figure 3-1 - Structure of [Fe(N-MeIm)$_6$]S$_8$

In 2008 O'Brien *et al.* reported the synthesis and solvothermal decomposition of the cubane-type single-source precursor [N^{n}Bu$_4$][Fe$_4$S$_4$(SPh)$_4$] (see Figure 3-2) in different coordinating solvents using the 'hot-injection' method at 180 – 230 °C. At 180 °C in octylamine, pyrrhotite nanoparticles were formed, while at 200 °C in DDA, 215 °C in HDA and 230 °C in OA greigite nanoparticles resulted, with the average particle diameter decreasing from ~4.5 to 2~2.5 nm as the temperature was increased. This is an accord with the findings of several other groups who have shown that by varying the temperature

of decomposition, different phases and sizes of iron sulfide nanoparticles can be formed.[31, 36, 8, 42]

That pyrrhotite is formed at low, and greigite at high, temperature is particularly interesting. The $[N^nBu_4]_2[Fe_4S_4(SPh)_4]$ cluster has an Fe_4S_4 core that is very similar to the repeating unit of greigite, so it is feasible that the molecular geometry of the precursor directs the nanoparticle growth at higher temperatures where decomposition is fast (though, conversely, under these conditions more energy is available for rearrangements). At 180 °C in octylamine kinetics could be more important, giving a slower decomposition and allowing the cluster to slowly rearrange, providing no molecular direction to the resultant particles so pyrrhotite is formed, which has a totally different repeating unit. This suggests that either a different mechanism of decomposition takes place at the lower temperature in octylamine, or that precursor structure does not direct material growth.

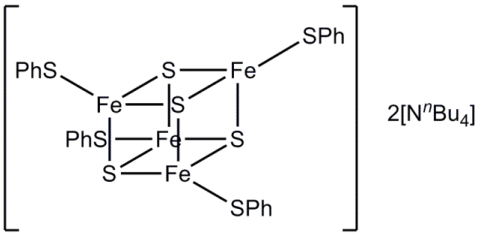

Figure 3-2 - Structure of $[N^nBu_4]_2[Fe_4S_4(SPh)_4]$

These decompositions were all performed over long periods (12-16 hrs), so it could also be that octylamine is unable to stabilise the greigite structure. In addition, at each different temperature the decomposition was performed in a different solvent. This could be important since it has later been shown that different phases of iron sulfide nanoparticles are formed under the same conditions using different coordinating solvents.[37, 8, 43] This solvent effect could explain why other groups have reported greigite as a metastable phase of iron sulfide, formed under milder conditions with pyrrhotite as the thermodynamically favoured phase, while O'Brien *et al.* seemingly see the opposite effect.[31, 33, 36, 8]

In a later paper, O'Brien *et al.* investigated the effect of single-source precursor concentration, decomposition temperature and solvent using the thiobiuret precursor $[Fe(SON(CN^iPr_2)_2)_3]$.[35] Similarly to the work of Maji,[34] O'Brien found that nanoparticle morphology could be tuned by changing the solvent. In pure OA at 200 °C, *ca.* spherical pyrrhotite nanoparticles were formed, whereas when OA/OD and OA/DDT were used,

nanowires resulted.[35] The authors noted that as single-source precursor concentration was increased, the average diameter of the resulting nanoparticles also grew (~5 nm at 5 mM single-source precursor compared to ~6 nm at 10 mM single-source precursor in OA at 200 °C), but at very high concentration (20 mM) only amorphous material was produced. The authors also noted a morphological effect upon varying the decomposition temperature. Thus, at low temperatures (200 °C) the nanoparticles were roughly spherical (believed to be the thermodynamically preferred shape), but rods and hexagonal nanosheets were formed at 240 and 280 °C, being attributed to a kinetically-controlled decomposition mechanism at higher temperature.[35] In a further contribution, O'Brien *et al.* detailed a similar study using xanthate [$Fe(S_2COR)_3$] (R = Me, Et, and ^{i}Bu) single-source precursors, being able to tune the iron sulfide phase and size by varying decomposition temperature and solvent.[43]

3.1.2 Decomposition of Dithiocarbamate Single-Source Precursors

In 2008, the first report of the decomposition of iron dithiocarbamates was detailed by Han and Gao, who investigated the effect of decomposition temperature and solvent on the iron(II) single-source precursor [$Fe(S_2CNEt_2)_2$(1,10-Phen)] and iron(III) single-source precursor [$Fe(S_2CNEt_2)_3$].[36] They found that when [$Fe(S_2CNEt_2)_2$(1,10-Phen)] was decomposed in OA for five mins, hexagonal nanosheets of monoclinic pyrrhotite were produced at intermediate temperatures (260 – 300 °C), while hexagonal troilite (FeS) was produced at high temperature (320 °C) and amorphous material at low (240 °C). In contrast, when [$Fe(S_2CNEt_2)_3$] was decomposed in OA it produced a mixture of pyrrhotite and greigite at all temperatures except 320 °C, where pure pyrrhotite nanosheets were formed. This reflects previous work with non-dithiocarbamate precursors, where greigite was shown to be a metastable phase of iron sulfide, and pyrrhotite is the more thermodynamically favoured phase formed at high temperatures and long reaction times.[31, 33] These authors also investigated solvent effects on the morphology of the nanoparticles, comparing decomposition of the single-source precursors at 280 °C in OA and OD, and a 1:5 mixture of the two. They found that in anything other than pure OA, irregularly shaped nanosheets were formed from [$Fe(S_2CNEt_2)_2$(1,10-Phen)]. The authors suggest that OA is required to form hexagonal nanosheets of pyrrhotite and the solvent stabilises growth in the <110> and <100> directions.[36] In the case of [$Fe(S_2CNEt_2)_3$], however, they find that the presence of OA only prevents agglomeration of the resulting greigite nanosheets.[36]

A similar study by Zhang *et al.* further investigated the effect of solvent system on the decomposition of $[Fe(S_2CNEt_2)_2(1,10\text{-Phen})]$ and $[Fe(S_2CNEt_2)_3]$.[37] Here also the effect of mixing OA and OD was noted, but with the addition of oleic acid (OLA) and similarly noted changes to the morphology of the resulting iron sulfide nanoparticles. Decomposition of $[Fe(S_2CNEt_2)_3]$ in OA/OD (1:1) produced greigite nanosheets similar to those synthesised by Gao, but in OA/OD/OLA (1:1:2) a narrower size distribution of nanosheets was obtained. Similarly the decomposition of $[Fe(S_2CNEt_2)_2(1,10\text{-Phen})]$ in OA/OD (1:1) produced pyrrhotite nanosheets akin to those synthesised by Gao, but in OA/OD/OLA (1:1:2) nanoribbons of ~15 nm by several microns of amorphous iron sulfide were produced. Zhang stated that no product was obtained from mixtures of OD/OLA in the absence of OA indicating that the latter solvent is important in the formation of crystalline material.[37]

While our work was in progress, O'Brien *et al.* reported effects of temperature (170 – 300 °C), solvent (OA, HDA and OD) and precursor type $[Fe(S_2CNRR')_3]$, with a range of symmetrical and unsymmetrical RR' groups.[8] Like other groups,[31, 36] they found that greigite was prevalent at lower temperatures and pyrrhotite at higher temperatures. When $[Fe(S_2CNEt^iPr)_3]$ was decomposed in OA/HDA a mixture of greigite and pyrrhotite was formed, but in OD a mixture of two types of pyrrhotite ('pyrrhotite (FeS)' and pyrrhotite (Fe_7S_8)), supporting other work on the effects of solvent on mineral phase.[8] Also, higher temperatures were required to produce crystalline nanoparticles for shorter chain length symmetrical and unsymmetrical single-source precursors. Interestingly they also observed that while pure greigite was accessible at lower temperatures for symmetrical single-source precursors, unsymmetrical single-source precursors produced a mixture of greigite and pyrrhotite at all temperatures, suggesting they may decompose *via* a different mechanism.[8]

3.2 Results and Discussion

In order to prepare a variety of iron sulfide nanoparticles, the solvothermal synthesis in OA was chosen, owing to a wide range of phases and morphologies being accessible. In addition, it has been suggested that OA is required for the formation of crystalline material.[37] A decomposition temperature of 230 °C was chosen as below this amorphous materials result, and at higher temperatures the thermodynamic phase, pyrrhotite, is favoured. The 'heat-up' method was chosen over hot-injection of single-source precursor because in some cases the single-source precursors employed in this study were sparingly

soluble in OA. The apparatus was set up as shown in Figure 3-3, with a three-necked round-bottomed flask attached to a condenser connected to a Schlenk line providing a flow of nitrogen. The flask sits in a heating mantle on a stirring plate, and a temperature probe is inserted through a rubber septum into the reaction mixture.

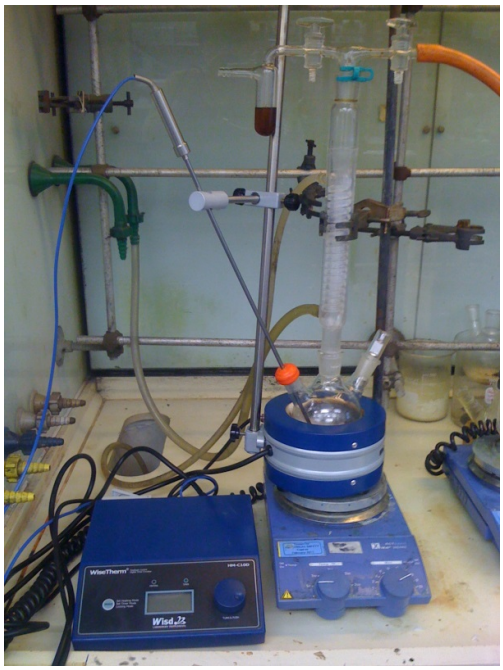

Figure 3-3 - Decomposition apparatus setup complete with thermostatically controlled heating mantle.

3.3 Decomposition of Iron(II) Dithiocarbamate Precursors

A plethora of iron sulfide phases consist of iron solely in the +2 oxidation state,[1] but only pyrrhotite and troilite have so far been reported from the decomposition of iron(II) bis(dithiocarbamate) single-source precursor $[Fe(S_2CNEt_2)_2(1,10\text{-Phen})]$.[36, 37] Here we explore the decomposition of a different iron(II) bis(dithiocarbamate) complex, namely $[Fe(S_2CNMe_2)_2(CO)_2]$ (**13**), and a combination of iron(II) and iron(III) dithiocarbamate single-source precursors. Greigite is an iron sulfide thiospinel possessing iron(II) and iron(III) ions. It has previously been synthesised solvothermally using iron(III) tris(dithiocarbamate) single-source precursors, indicating that part of the decomposition mechanism requires reduction of the precursor.[36, 37, 8]

3.3.1 Synthesis and Characterisation

The decomposition setup as described in Section 3.2 was utilised. Complex **13** was decomposed in OA at 230 °C for 1 hr. OA was degassed with a nitrogen purge (30 mins) before **13** was added, followed by further degassing (10 mins) to prevent oxidation of the precursor. Complex **13** was poorly soluble in OA at RT, but by 35 °C had fully dissolved to form a dark brown solution. The resulting nanoparticles were isolated after cooling the mixture by addition of excess methanol and separation by centrifugation. A similar decomposition was performed with a 1:1 mixture of **13** (2.5 mM) and $[Fe(S_2CNMe_2)_3]$ (**1**, 2.5 mM) resulting in a black powder.

Powder X-ray diffraction (XRD) analysis (Figure 3-4) revealed a match to pyrrhotite 4M Fe_7S_8 (ICDD card No. 029-0723) in both cases. The resulting pyrrhotite phase of for the decomposition of **13** is consistent with previous reported findings for the decomposition of iron(II) bis(dithiocarbamate) complex $[Fe(S_2CNEt_2)_2(1,10\text{-Phen})]$, however, Han *et al.* found that crystalline material could only be obtained above 240 °C.[36, 37] Low temperature access to crystalline pyrrhotite nanoparticles could result from using a different single-source precursor, or it could be a time effect. Han decomposed $[Fe(S_2CNEt_2)_2(1,10\text{-Phen})]$ for five mins at 240 °C and produced amorphous material, while **13** was decomposed for 1 hr at 230 °C. During this extra time the material has the opportunity to nucleate and grow into larger crystalline particles, as has been noted previously by Law *et al.*[28]

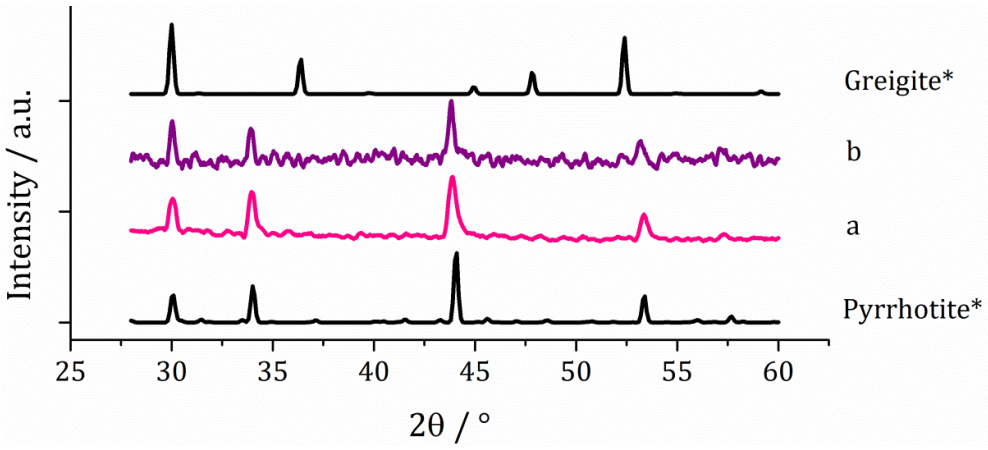

Figure 3-4 - XRD patterns for nanoparticles produced from (a) 13 and (b) 13 with 1, with reference patterns for bulk pyrrhotite 4M (ICDD card No. 29-0723) and greigite (ICDD card No. 16-0713).

Decomposition of **13** with **1** did not produce greigite, indicating full reduction of the iron(III) precursor during decomposition. This is interesting since even at lower temperatures (240 °C) Han obtained a mixture of greigite and pyrrhotite from

[$Fe(S_2CNEt_2)_3$].[36] O'Brien *et al.* also generated a mixture of greigite and pyrrhotite at 230 °C for a range of symmetrical and unsymmetrical iron(III) tris(dithiocarbamate) complexes.[8] This difference in product phase could result from the use of the iron(II) (dithiocarbamate) precursor **13**, or concentration may have an effect. O'Brien and Han both used higher precursor concentrations (46 and 39 mM respectively) as compared to this work (5 mM).

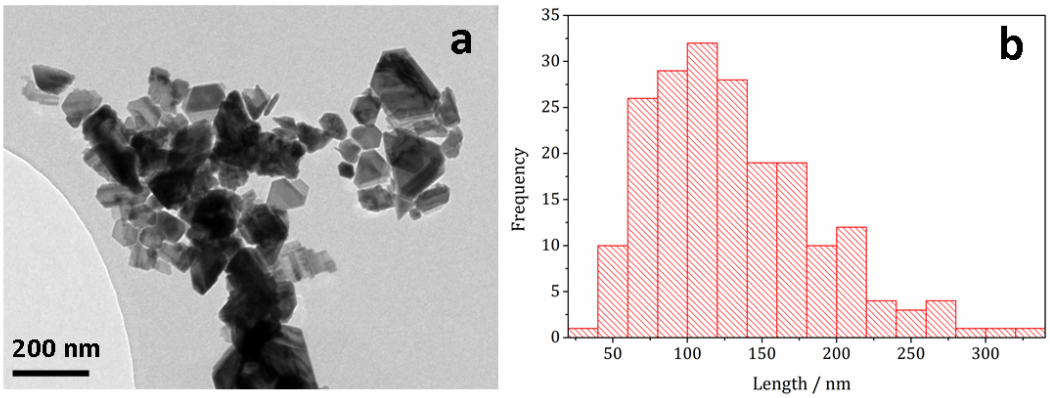

Figure 3-5 - (a) TEM image and (b) histogram of particle length for pyrrhotite particles obtained from decomposition of 13 with 1.

Transmission electron microscopy (TEM) of both samples show roughly hexagonal nanocrystals (see Figure 3-5), similar in appearance to the pyrrhotite material synthesised by Han, Zhang and O'Brien.[36, 37, 8] Han and Zhang report particle diameters in the range 500 nm – 1 μm from [$Fe(S_2CNEt_2)_2$(1,10-Phen)] at 280 °C for 5 minutes.[36, 37] They do not report an average particle size, but this range is higher than that found for the decomposition of **13** (30 – 500 nm). This may be attributed to concentration effects, Han and Zhang both using higher precursor concentrations so more precursor is available for particle growth.

The sample obtained from **13** with **1** had a particle diameter range of 20 – 320 nm, being lower than that obtained from **13** alone – which may be attributed to the presence of **1** in the precursor solution. Nanoparticles synthesised by Han, Zhang and O'Brien from iron(III) dithiocarbamate precursors exhibit lower size ranges (approximately 50 – 200 nm).[36, 37, 8] A possible explanation is the differences in precursor stability, but it was noted in Chapter 2 that the iron(III) tris(dithiocarbamate) and related iron(II) bis(dithiocarbamate) complexes (formed subsequent to CO loss) decompose at very similar temperatures under TGA conditions. Another possible explanation is that iron(III) dithiocarbamate complexes decompose *via* a different mechanism that promotes nucleation and slows growth of nanoparticles.

3.3.2 Summary

Decomposition of the iron(II) precursor **13** produced pure pyrrhotite (Fe_7S_8) nanoparticles, with similar morphology to those previously synthesised from iron(II) dithiocarbamate precursors in the literature. The addition of an iron(III) source (**1**), did not lead to the formation of greigite as predicted, but instead pure phase pyrrhotite. Other groups have been able to access greigite by decomposing iron(III) tris(dithiocarbamate) complexes, although in many cases with pyrrhotite impurities.[36, 37, 8]

3.4 Decomposition of Iron(III) Dithiocarbamate Precursors

Pyrrhotite has been suggested to be thermodynamically more stable than greigite under the conditions employed in this study,[31, 33, 36] it is also more readily formed upon decomposing certain single-source precursors.[8] The effect of varying the dithiocarbamate substituent in $[Fe(S_2CNR_2)_3]$, decomposition temperature and precursor concentration was investigated, in order to glean a deeper understanding of this system with the aim of synthesising a variety of different iron sulfide nanomaterials.

3.4.1 Varying R-group

Iron(III) tris(dithiocarbamate) complexes **1** – **4** (RR' = Me_2, Et_2, $^iBu_2$, MeBu) were decomposed as described in Section 3.2 at 230 °C for 1 hr (at a concentration of 5 mM in 20 mL OA). The complexes gave dark brown solutions in OA, but surprisingly at 75 °C these solutions turned pale yellow and clear, then at 80 °C quickly turned completely black. The clear solutions may contain some intermediate iron species which decompose at 80°C. After 1 hr the nanoparticles were isolated as black powders. XRD analysis revealed that pure pyrrhotite (Fe_7S_8, ICDD card No. 029-0723) was formed in most cases but for decomposition of **2**, where a small amount of greigite (ICDD card No. 016-0713) was also formed (see Figure 3-6). O'Brien *et al.* found that decomposition of a range of $[Fe(S_2CNRR')_3]$ precursors with other R-groups formed predominantly greigite, but showed peaks for pyrrhotite at higher temperatures (230 and 300 °C).[8] The lower concentration used in this work could be a factor as to why pyrrhotite was predominantly formed from **1** – **4**.

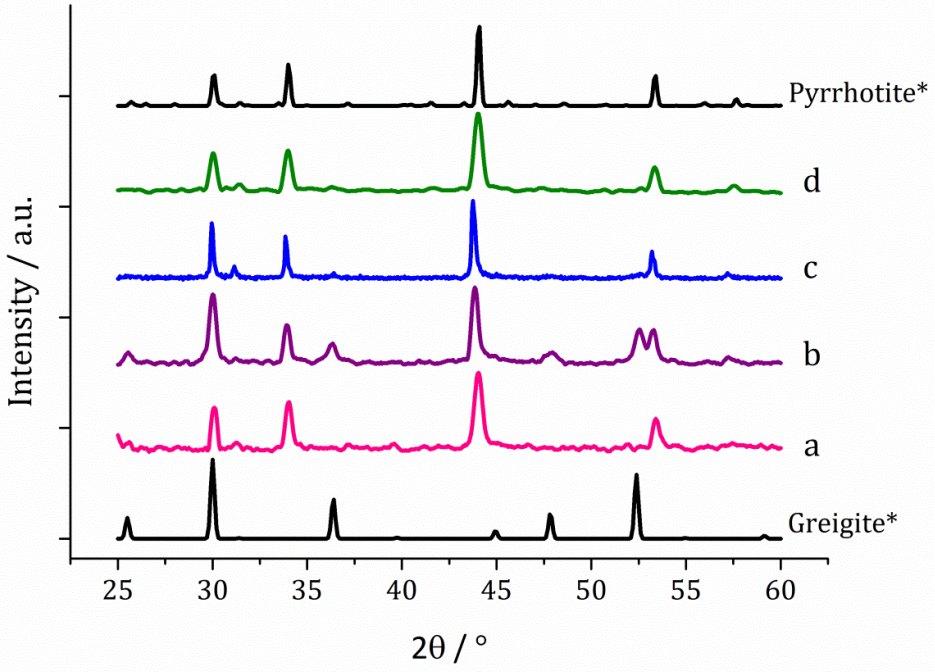

Figure 3-6 - XRD patterns for nanoparticles obtained from (a) 1, (b) 2, (c) 3 and (d) 4, with reference patterns for bulk greigite (ICDD card No. 16-0713) and pyrrhotite 4M (ICDD card No. 29-0723).

Formation of greigite from the decomposition of **2** (RR' = Et_2) is consistent with O'Brien's findings. The reason for this differing result for the diethyl derivative compared to the dimethyl, diisobutyl and methylbutyl, is unclear. In Chapter 2, TGA analysis revealed that the decomposition temperature of **2** is close to that of **3** (226 and 233 °C respectively) and that **2** and **4** both leave residues approximately equal to FeS, though TGA and DSC did not support the theory that there was a uniform decomposition route. Complex **2** may decompose *via* a different mechanism in solution with OA.

TEM analysis showed roughly hexagonal nanosheets, much like the pyrrhotite samples synthesised from **13** and **1** (an example TEM is shown in of nanoparticles synthesised from **3**). Average particle sizes appear to generally decrease as the precursor $[Fe(S_2CNRR')_3]$ RR'-group increases in steric bulk (the nanoparticles produced from **3** possess the smallest average length, 84 nm, and the largest R-group, $^{i}Bu_2$, see), though the standard deviations are large. An explanation is that precursors with shorter alkyl chains are more stable and so take longer to decompose, therefore forming larger nanoparticles (less nucleation sites so more growth). This is supported by the work of O'Brien *et al.* who noted that $[Fe(S_2CNRR')_3]$ precursors with shorter alkyl chains required higher temperatures to decompose.[8] HRTEM of the particles produced from **3** shows spacings of

2.67 Å, consistent with the [004] lattice plane of pyrrhotite-4M (2.64 Å, ICDD card No. 29-0723).

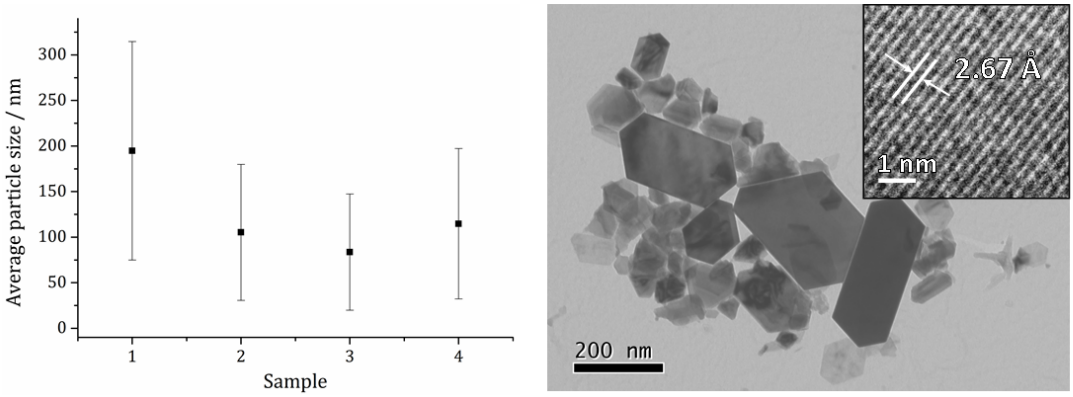

Figure 3-7 - Graph of average particle size, with one SD above and below, of samples prepared from single-source precursors 1 - 4 (left) and TEM image of the sample prepared from 3 with HRTEM insert (right).

The nanoparticles prepared from **3** exhibit the smallest average length and the lowest standard deviation (SD, 64 nm, shown above and below the average particle length in). These are desirable qualities in a catalyst – the smaller the nanoparticle, the larger the surface area and greater the activity. Although the diethyl derivative, **2** appears to be a better precursor for synthesising greigite, O'Brien *et al.* has shown that greigite is still accessible using other [$Fe(S_2CNRR')_3$] complexes,[8] and the di-*iso*-butyl derivative, **3,** produces nanoparticles with a more desirable morphology. The complex **3** was chosen to take forward for further studies into the decomposition system.

3.4.2 Varying Temperature

Complex **3** (5 mM) was decomposed in OA (20 mL) for 1 hr at 150, 180, 260 and 280 °C and compared to the already prepared sample at 230 °C. Black powders were isolated according to the method described in Section 3.3.1 and analysed *via* XRD (see Figure 3-8). Samples prepared below 230 °C were found to be mostly amorphous, with some very small broad peaks for greigite and pyrrhotite. This is in accordance with the findings of Han and O'Brien, who both produced amorphous material at low temperatures, and found greigite formed at intermediate temperatures while pyrrhotite was favoured as the temperature was increased.[36, 8] The samples produced at 150 and 180 °C were unstable in air and oxidised to orange/brown powder after two-three days, whereas all the other samples remained as black powders months after synthesis.

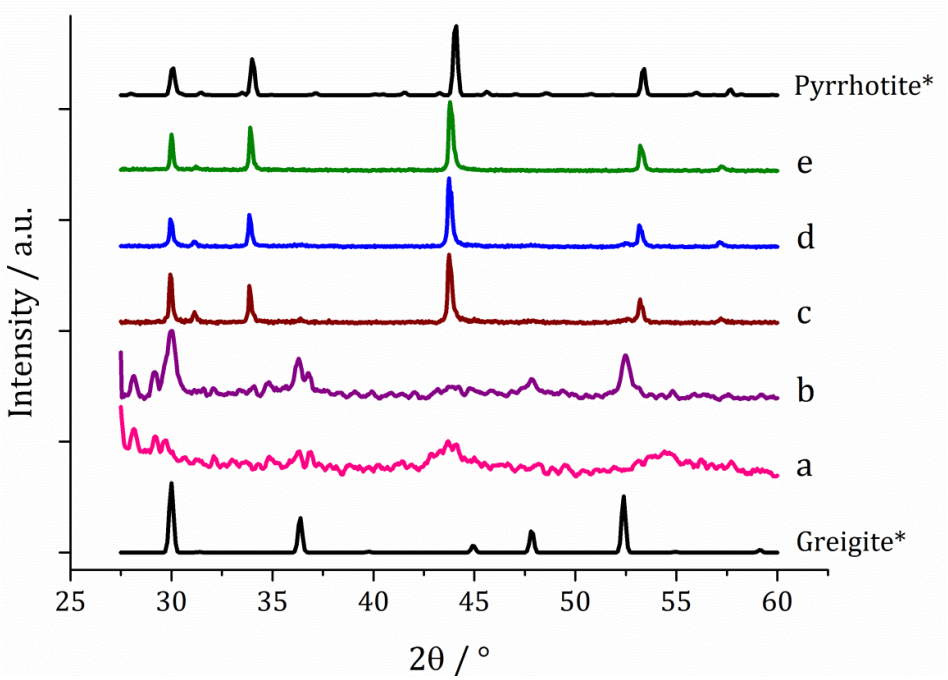

Figure 3-8 - XRD patterns for samples prepared from 3 at (a) 150 °C, (b) 180 °C, (c) 230 °C, (d) 260 °C and (e) 280 °C, with reference patterns for bulk greigite (ICDD card No. 16-0713) and pyrrhotite 4M (ICDD card No. 29-0723).

Analysing the particles by TEM the progression from amorphous material produced at low temperature, to a few crystallites forming as decomposition temperature is increased, to crystalline material at higher temperature (Figure 3-8), following the trend observed in the XRD. Nanoparticle shape does not appear to change as temperature is increased from 230 – 280 °C, consistent with previous findings.[36, 8] The average particle size decreases as temperature of decomposition is increased (see Figure 3-9 (f)), which could be an effect of decomposition rate. At higher temperature decomposition is likely to occur quickly, with many nucleation sites existing simultaneously, while at lower temperature decomposition is slower, so with less nucleation sites each particle is then able to grow larger.

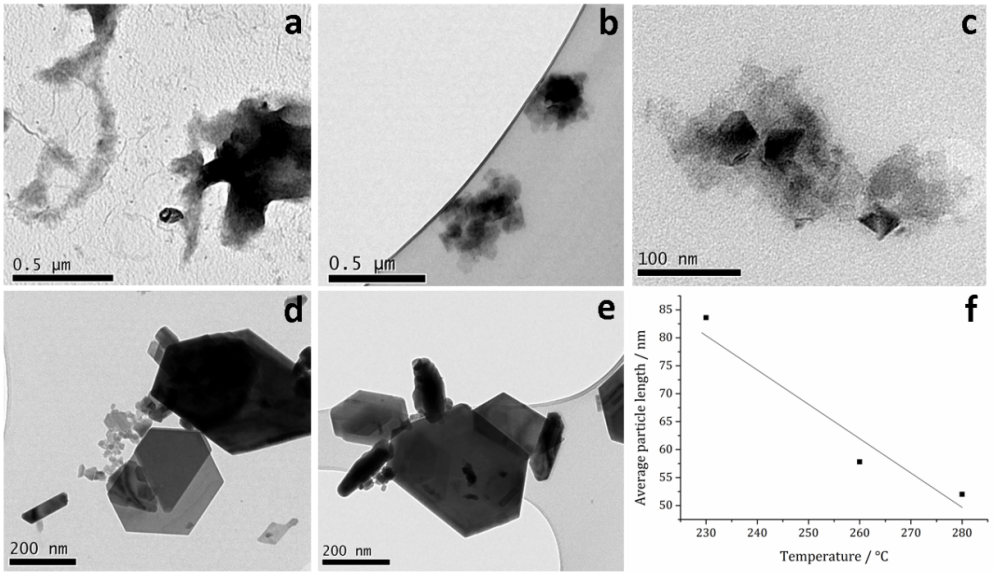

Figure 3-9 - TEM images of samples prepared from 3 at (a) 150, (b and c) 180, (d) 260 and (e) 280 °C. Graph of average particle length against temperature of decomposition (f).

It was noted that at lower temperature some greigite was formed so in order to try to access this, and other metastable phases of iron sulfide in crystalline form, 230 °C was chosen to take forward for concentration studies. In addition other researchers have found this temperature to be sufficient for synthesising greigite at higher concentrations.[36, 37, 8]

3.4.3 Varying Concentration

Complex **3** was decomposed in 20 mL OA for 1 hr at 230 °C at various different concentrations (10, 20, 40 and 50 mM). Black powders were obtained and compared to the sample previously prepared using 5 mM of **3**. XRD analysis shows a progression from pyrrhotite to greigite with increasing concentration (Figure 3-10). Formation of pure greigite when using 40 and 50 mM of **3** supports the work done by Han and O'Brien, who produced greigite from iron(III) tris(dithiocarbamate) precursors at approximately these concentrations.[36, 8] A HRTEM image of the sample prepared from **3** at a concentration of 40 mM is shown in , where *d*-spacings of 2.97 Å, consistent with the [311] lattice plane of greigite (2.98 Å, ICDD card No. 16-0713), can be seen.

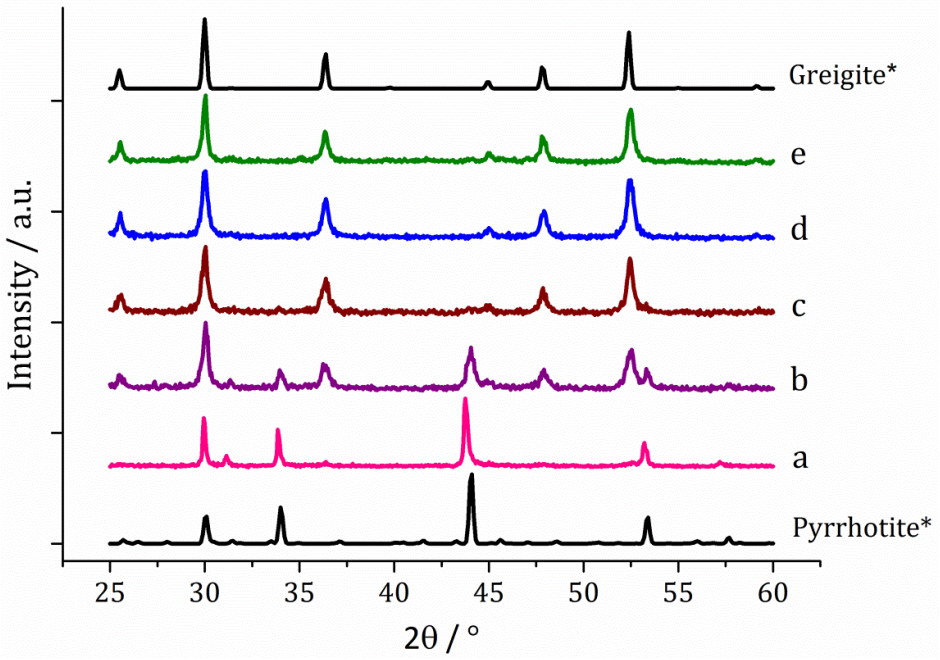

Figure 3-10 - XRD patterns for samples prepared from 3 at (a) 5, (b) 10, (c) 20, (d) 40 and (e) 50 mM concentration, with reference patterns for bulk pyrrhotite 4M (ICDD card No. 29-0723) and greigite (ICDD card No. 16-0713).

In another study by O'Brien, an iron(III) thiobiuret was decomposed at varying concentrations and the authors observed for 5 and 10 mM precursor concentration pyrrhotite was formed, but increasing to 20 mM produced amorphous material.[35] This suggests concentration may play a role in the crystallinity of the resultant material. The trend observed in the current study, suggests concentration may allow access to metastable phases such that at higher concentration the metastable phase greigite is formed.

In a further reaction, a 5 mM decomposition of **3** was repeated, but instead of holding at 230 °C for 1 hr (producing pure pyrrhotite), heating was halted upon reaching the desired temperature followed by rapid cooling in a cold water bath. XRD analysis of the material produced showed it to be pure greigite, suggesting that greigite is formed first in these decompositions and is converted to the thermodynamically favoured pyrrhotite phase over time (*i.e.* holding at high temperature for 1 hr). This is in agreement with the work of Tilley *et al*, who found the same results doing a similar study with $[Fe(N\text{-MeIm})_6]S_8$.[33] When the precursor was injected into hot OA and cooled immediately, greigite was formed, but increasing the reaction time led to the synthesis of pyrrhotite nanoparticles.

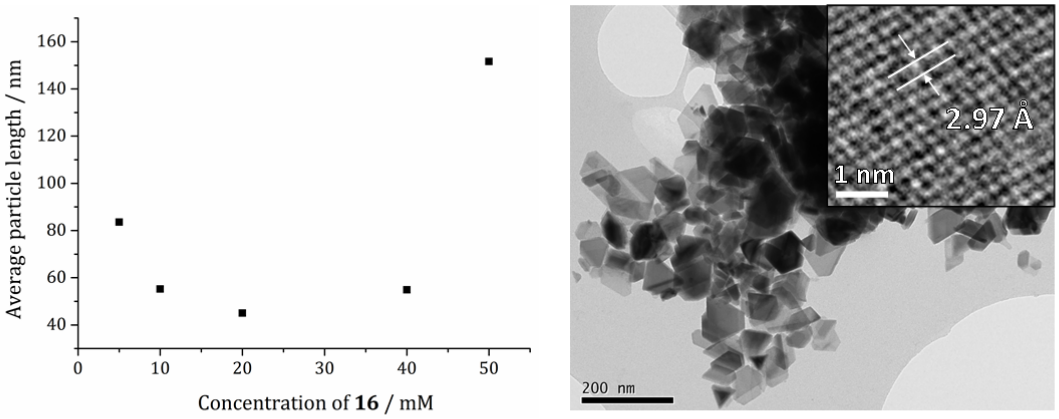

Figure 3-11 - Graph of average particle length of samples prepared from 3 (5 – 50 mM) (left) and TEM image of greigite prepared from 3 at 40 mM, with HRTEM insert (right).

The average particle size of the samples varies according to the concentration of the single-source precursor (see). It appears to be roughly similar between 5 and 40 mM, with a growth in particle size when the concentration is increased to 50 nm. The increase in nanoparticle size at high concentration may be attributed to the Ostwald ripening effect. The varying proportions of two different phases existing in these samples at higher concentrations may also play a role.

3.5 Decomposition of Iron(III) Dithiocarbamate Precursors with Thiuram Disulfide Additive

The only iron sulfide phases accessed in the previous studies have been greigite and pyrrhotite. In an attempt to synthesise more phases, tetra-*iso*-butylthiuram disulfide (**6**) was added to the decomposition mixture. Compound **6** is known to be an oxidising agent, oxidatively adding onto metal centres as two dithiocarbamate ligands (Equation 3-1), utilised in Chapter 2, Section 2.2.2.1.[44–50] It is also a potential source of sulfur, but the only reported instance of such a compound being used as such in connection with solvothermal synthesis of metal sulfides, was in a non-peer reviewed journal for the synthesis of cadmium sulfide.[51]

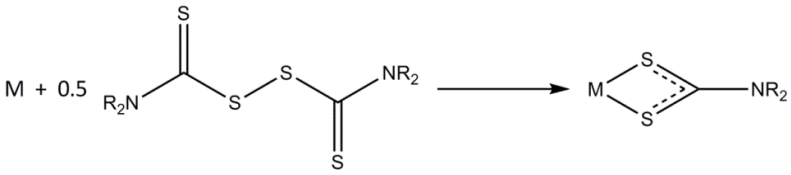

Equation 3-1

Pyrite and marcasite are sulfur rich iron sulfide phases compared to pyrrhotite and greigite, having FeS_2 structure, and in order to access these phases an additional sulfur source may be required, although it should be noted that the ratio of iron to sulfur in the $[Fe(S_2CNR_2)_3]$ single-source precursors is 1:4, so sulfur is already in excess. In addition thiuram disulfide readily forms from dithiocarbamate in the presence of an oxidant such as iodine, bromine, hydrogen peroxide, or $K_3[Fe(CN)_6]$ and has even been reported from the reaction between $[Fe(S_2CNR_2)_3]$ and iodine.[52–55]

Complex **3** (5 mM) was decomposed with one equivalent **6** in OA at 230 °C for 1 hr. The materials produced were then washed in methanol and isolated by centrifugation. The decanted supernatant appeared slightly yellow and gave off a sulphurous smell, indicating the presence of excess sulfur. The resulting black powder was analysed by XRD and found to be a mixture of pyrrhotite Fe_7S_8 and greigite (Figure 3-12 (a)).

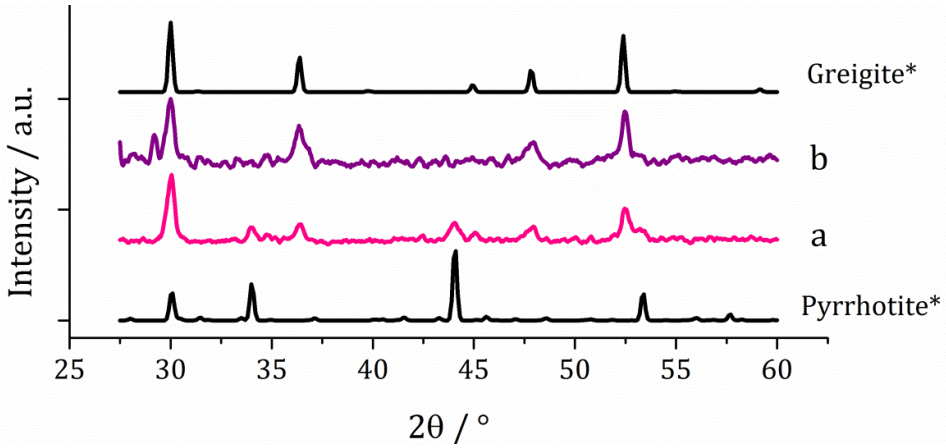

Figure 3-12 - XRD patterns for samples prepared from 3 (5 mM) with (a) one equivalent and (b) two equivalents of 6, with reference patterns for bulk pyrrhotite 4M (ICDD card No. 29-0723) and greigite (ICDD card No. 16-0713).

Addition of **6** promoted the stabilisation of the greigite phase, either by; providing an additional sulfur source, oxidising some of the Fe(2+) ions back to Fe(3+), preventing the reduction of some of the Fe(3+) ions, capping the greigite nanoparticles in such a way as to stabilise the phase and somehow preventing the further changes to pyrrhotite. In an attempt to remove the pyrrhotite and form pure greigite, the decomposition was repeated with two equivalents of **6,** analysis of the resulting particles showed pure greigite by XRD (Figure 3-12 (b)).

Systematic studies were performed varying the temperature of decomposition and concentration of **3** and **6** (in a 1:2 ratio) to investigate the effect of **6** on the system and to try to synthesise additional phases of iron sulfide.

3.5.1 Varying Temperature

Complex **3** (5 mM) and thiuram disulfide **6** (10 mM) were decomposed in OA for 1 hr at 150, 180, 260, 280 and 300 °C. The black powders produced were analysed by XRD and compared to the sample prepared at 230 °C (Figure 3-13). The low temperature samples consist of amorphous material (similar to the above temperature study without **6**). At intermediate temperatures greigite was produced, with greater purity at 260 °C (the sample prepared at 230 °C exhibits some low angle sulfur peaks, presumably from the decomposition of **6**). As the temperature is increased past 260 °C pyrrhotite becomes prevalent, consistent with pyrrhotite being the thermodynamic product. In comparison to the decompositions without **6**, pure crystalline material can be accessed due to the greater stability of greigite in the presence of **6**.

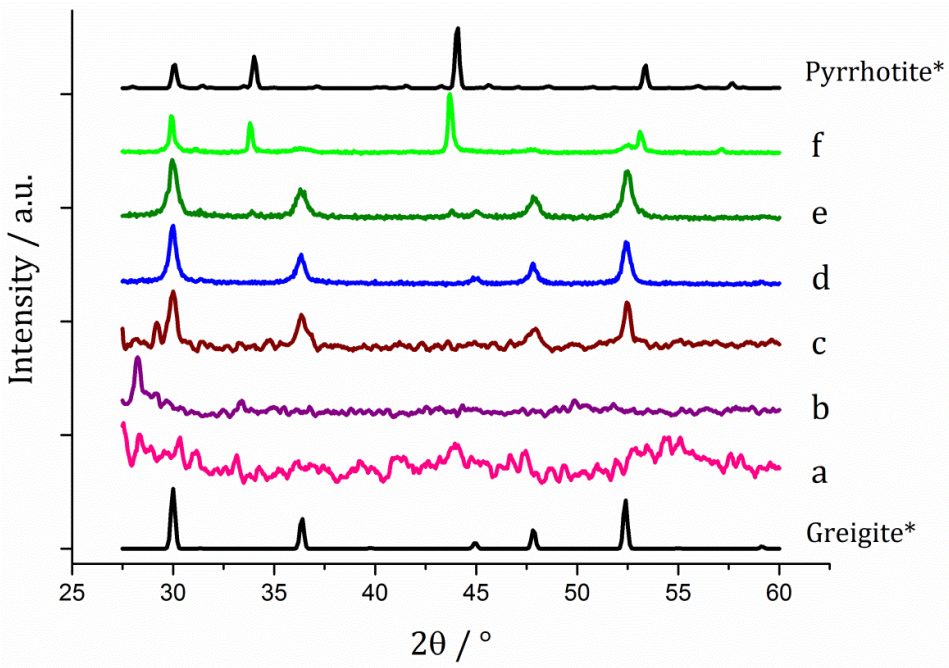

Figure 3-13 - XRD patterns for samples prepared from 3 (5 mM) and 6 (10 mM) at (a) 150, (b) 180, (c) 230, (d) 260, (e) 280 and (f) 300 °C, with reference patterns for bulk greigite (ICDD card No. 16-0713) and pyrrhotite 4M (ICDD card No. 29-0723).

Figure 3-14 shows a graph of the average particle size for samples prepared at 150 – 300 °C, from which it can be seen that the nanoparticles decrease slightly in size with increasing temperature, consistent with the trend seen in the samples prepared without **6**.

A TEM image of the material produced at 260 °C is also presented in Figure 3-14, showing the morphology of the particles is very similar to the greigite nanoparticles grown without thiuram disulfide **6** (see), although the average particle size of the former is slightly smaller (34nm compared to 55 nm respectively). HRTEM of the 260 °C sample shows spacings of 5.95 Å, consistent with the [111] lattice plane of greigite, and this temperature was chosen to take forward for concentration studies because this was the lowest temperature where pure crystalline material is produced. A low temperature is desirable in order to access metastable phases.

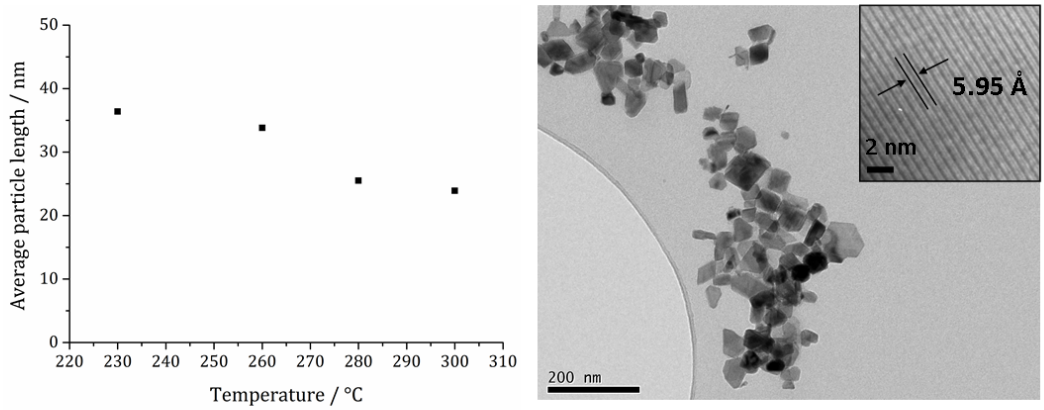

Figure 3-14 - Graph showing the average particle length against temperature of decomposition for precursors 3 (5 mM) and 6 (10 mM) (left). TEM image of sample prepared at 260 °C with HRTEM insert (right).

3.5.2 Varying Concentration

When **3** and **6** (in a 1:2 ratio) were decomposed at 260 °C with increasing concentration (10:20, 20:40, 40:80 and 50:100 mM) the black powders formed were found to be greigite in all cases (see XRD analysis in Figure 3-15), although at the higher concentrations there are anomalous low angle peaks believed to be due to excess sulfur from **6**. In order to confirm this, **6** was decomposed without **3** at a concentration of 80 mM and the XRD pattern of the resulting brown powder was a very good match to the anomalous peaks seen previously.

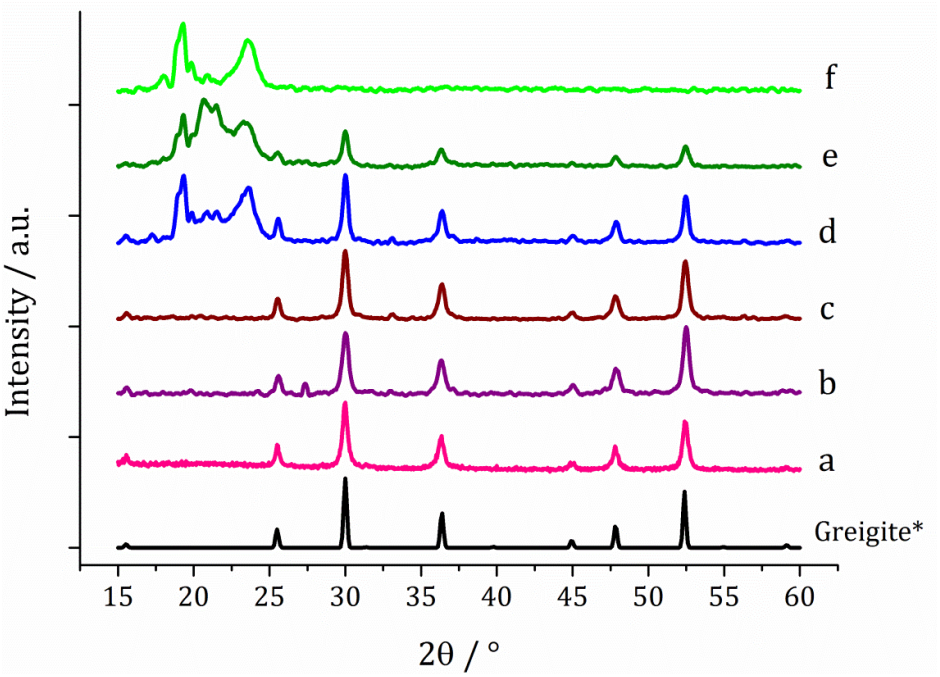

Figure 3-15 - XRD patterns for samples prepared from 3 and 6 at respective concentrations of (a) 5 and 10 mM, (b) 10 and 20 mM, (c) 20 and 40 mM, (d) 40 and 80 mM, and (e) 50 mM and 0.5 M, (f) 6 decomposed alone at 80 mM, with reference pattern for bulk greigite (ICDD card No. 16-0713).

Contrary to the concentration study performed in the absence of **6**, this study shows the average particle size varies very little with increasing concentration, suggesting that the TDS could indeed be acting as a capping/stabilising agent, stopping growth at approximately 40 nm. The implication of this result is that greigite can be consistently synthesised at reasonably high precursor concentrations, allowing doping of other metals into the greigite structure to be attempted.

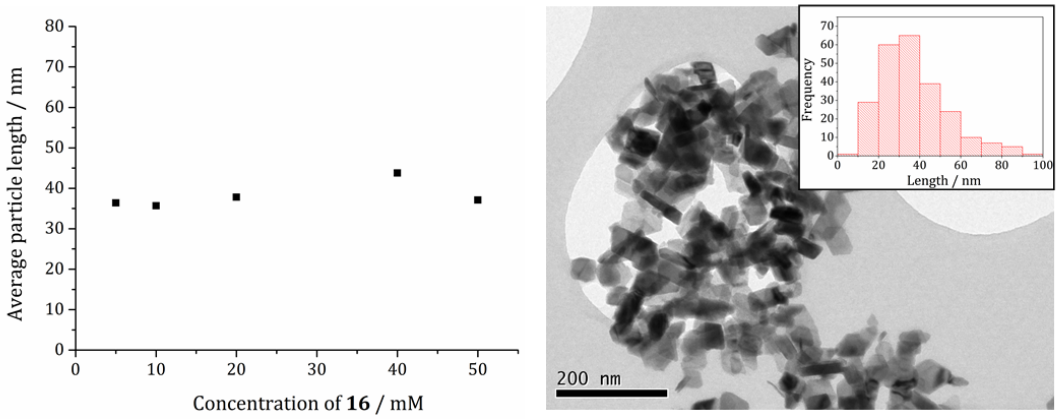

Figure 3-16 - Graph showing the average particle length of samples prepared from 3 and 6 at various concentrations (in a 1:2 ratio) (left). TEM image of greigite prepared from 16 (20 mM) and 1 (40 mM) with particle length histogram insert (right).

3.6 Conclusions

Solvothermal decomposition of iron(II) and iron(III) dithiocarbamate precursors has been investigated, systematically changing reaction variables in order to probe the changes to materials formed. It was found that iron(II) dithiocarbamate precursors were not required to produce iron sulfide nanoparticles containing Fe(2+) ions, because they are generated from the reduction of Fe(3+) species in solution. This process is relatively fast (decomposition of **3** halted immediately when the decomposition temperature had been reach produced pure greigite), but the greigite formed is a metastable phase and, if enough energy is supplied to the system, pyrrhotite will begin to form.

Greigite formation can be promoted by reducing the decomposition time, lowering the temperature and increasing the precursor concentration. All these factors decrease the amount of energy transferred to each precursor unit and so prevent the formation of the more thermodynamically favoured phase (pyrrhotite). In addition, precursor choice can have an effect. Thus **2** showed greater propensity towards the formation of greigite, which may be due to a different decomposition mechanism being at work, or to the formation of a by-product that stabilises the greigite phase.

Addition of a redox-active additive to the decomposition system had a significant effect on the product produced. When sufficient levels were used, addition of **6** changed the decomposition system conditions such that greigite survived at higher temperatures and lower concentrations of **3**. This could be the result of **6** forming a capping layer around the greigite nanoparticles. Thereby stabilising the iron sulfide phase, or it could be due to a change in the overall decomposition mechanism.

3.7 Experimental

XRD patterns were measured on a Bruker AXS D4 diffractometer using $CuK\alpha_1$ radiation. The diffraction patterns obtained were compared to database standards. For TEM characterisation a 4 μl droplet of nanoparticle suspension (chloroform) was placed on a holey carbon-coated copper TEM grid and allowed to evaporate in air under ambient laboratory conditions for several minutes. TEM images were obtained using a JEOL-1010 microscope at 100 kV equipped with a Gatan digital camera. HRTEM measurements were collected using a Jeol 2100 (high resolution) TEM with a LaB_6 source operating at an

acceleration voltage of 200 kv. Micrographs were taken on a Gatan Orius Charge-coupled device (CCD).

3.7.1 General method

The decomposition setup as described in Section 3.2 was utilised. In a typical synthesis **3** (5 mM) was added to OA (20 mL) in a three-neck RBF attached to a condenser and evacuated and refilled with nitrogen repeatedly for 15 minutes. The solution was heated to 230 °C and held there for 1 hr. The mixture was allowed to cool to RT slowly, whereupon methanol (80 mL) was added with stirring. The mixture was centrifuged and then the solution decanted leaving behind the resultant nanoparticles. This procedure was repeated 3 times and finally the material was allowed to dry in air.

3.7.2 Decomposition of Iron(II) Dithiocarbamate Precursors

Decompositions as in Section 3.7.1 but using: 1) **13**; 2) **13** (2.5 mM) and **1**(2.5 mM).

3.7.3 Decomposition of Iron(III) Dithiocarbamate Precursors

3.7.3.1 Varying R-group

Decompositions as above but using: 1) **1**; 2) **2**; 3) **3**; 4) **4**.

3.7.3.2 Varying Temperature

Decompositions as in Section 3.7.1 but at decomposition temperatures: 1) 150 °C; 2) 180 °C; 3) 260 °C; 4) 280 °C.

3.7.3.3 Varying Concentration

Decompositions as in Section 3.7.1 but using concentrations of **3** of: 1) 10 mM; 2) 20 mM; 3) 40 mM; 4) 50 mM. An additional decomposition was performed as above, but with immediate cooling when 230 °C had been reached using a cold water bath.

3.7.4 Decompositions of Iron(III) Dithiocarbamate Precursor with Thiuram Disulfide Ddditive

Decompositions as in Section 3.7.1 but using: 1) **3** (5 mM) and **6** (5 mM); 2) **3** (5 mM) and **6** (10 mM).

3.7.4.1 Varying Temperature

Decompositions as in Section 3.7.1 but decomposing **3** (5 mM) and **6** (10 mM) at 1) 150 °C; 2) 180 °C; 3) 260 °C; 4) 280 °C; 5) 300 °C.

3.7.4.2 Varying Concentration

Decompositions as in Section 3.7.1 but at 260 °C and using **3** and **6** at respective concentrations of: 1) 5 and 10 mM; 2) 10 and 20 mM; 3) 20 and 40 mM; 4) 40 and 80 mM; 5) 50 mM and 0.1 M. An additional decomposition was performed as above using **6** (80 mM) at 260 °C.

3.8 References

1 D. Rickard and G. W. Luther, *Chem. Rev.*, 2007, 107, 514.

2 C. Di Giovanni, W. Wang, S. Nowak, J. Grene, L. Mouton, M. Giraud, and C. Tard, *ACS Catal.*, 2014, 4, 681.

3 K. Ramasamy, M. A. Malik, N. Revaprasadu, and P. O'Brien, *Chem. Mater.*, 2013, 25, 3551.

4 H. A. Macpherson and C. R. Stoldt, *ACS Nano*, 2012, 6, 8940.

5 D.-Y. Wang, Y.-T. Jiang, C.-C. Lin, S.-S. Li, Y.-T. Wang, C.-C. Chen, and C.-W. Chen, *Adv. Mater.*, 2012, 24, 3415.

6 A. K. Dutta, S. K. Maji, D. N. Srivastava, A. Mondal, P. Biswas, P. Paul, and B. Adhikary, *ACS Appl. Mater. Interfaces*, 2012, 4, 1919.

7 G. H. Yue, P. X. Yan, L. S. Wang, W. Wang, Y. Z. Chen, and D. L. Peng, *Nanotechnology*, 2008, 19, 195706.

8 M. Akhtar, J. Akhter, M. A. Malik, P. O'Brien, F. Tuna, J. Raftery, and M. Helliwell, *J. Mater. Chem.*, 2011, 21, 9737.

9 M. Feng, Y. Lu, Y. Yang, M. Zhang, Y.-J. Xu, H.-L. Gao, L. Dong, W.-P. Xu, and S.-H. Yu, *Sci. Rep.*, 2013, 3, 2994.

10 Y.-S. Chang, S. Savitha, S. Sadhasivam, C.-K. Hsu, and F.-H. Lin, *J. Colloid Interface Sci.*, 2011, 363, 314.

11 Y.-W. Jun, J.-W. Seo, and J. Cheon, *Acc. Chem. Res.*, 2008, 41, 179.

12 F. Cao, W. Hu, L. Zhou, W. Shi, S. Song, Y. Lei, S. Wang, and H. Zhang, *Dalton. Trans.*, 2009, 9246.

13 Z. He, S.-H. Yu, X. Zhou, X. Li, and J. Qu, *Adv. Funct. Mater.*, 2006, 16, 1105.

14 X. Chen, X. Zhang, J. Wan, Z. Wang, and Y. Qian, *Chem. Phys. Lett.*, 2005, 403, 396.

15 Y. Xie, L. Zhu, X. Jiang, J. Lu, X. Zheng, W. He, and Y. Li, *Chem. Mater.*, 2001, 13, 3927.

16 D. Wang, Q. Wang, and T. Wang, *CrystEngComm*, 2010, 12, 3797.

17 Y. Bai, J. Yeom, M. Yang, S. Cha, K. Sun, and N. A. Kotov, *J. Phys. Chem. C*, 2013, 117, 2567.

18 C. Wadia, Y. Wu, S. Gul, S. K. Volkman, J. Guo, and A. P. Alivisatos, *Chem. Mater.*, 2009, 21, 2568.

19 P. W. Dunne, C. L. Starkey, M. Gimeno-Fabra, and E. H. Lester, *Nanoscale*, 2014, 6, 2406.

20 S. Mann, N. H. C. Sparks, R. B. Frankel, D. A. Bazylinksy, and H. W. Jannasch, *Nature*, 1990, 343, 258.

21 D. Rickard, A. Griffith, A. Oldroyd, I. Butler, E. Lopezcapel, D. Manning, and D. Apperley, *Chem. Geol.*, 2006, 235, 286.

22 M. Nath, A. Choudhury, A. Kundu, and C. N. R. Rao, *Adv. Mater.*, 2003, 15, 2098.

23 X. Wang, W. Zhou, Z. Chang, Z. Zhou, and S. Wu, *Chinese J. Chem.*, 2013, 31, 983.

24 X. L. Yu, Y. Wang, R. K. Zheng, J. F. Qu, H. L. W. Chan, and C. B. Cao, *Cryst. Growth Des.*, 2009, 9, 1293.

25 D.-W. Wang, Q.-H. Wang, and T.-M. Wang, *CrystEngComm*, 2010, 12, 755.

26 X. F. Qian, X. M. Zhang, C. Wang, Y. Xie, W. Z. Wang, and Y. T. Qian, *Mater. Sci. Eng. B*, 1999, 64, 170.

27 J. H. L. Beal, S. Prabakar, N. Gaston, G. B. Teh, P. G. Etchegoin, G. Williams, and R. D. Tilley, *Chem. Mater.*, 2011, 23, 2514.

28 J. Puthussery, S. Seefeld, N. Berry, M. Gibbs, and M. Law, *J. Am. Chem. Soc.*, 2011, 133, 716.

29 W. Li, M. Döblinger, A. Vaneski, A. L. Rogach, F. Jäckel, and J. Feldmann, *J. Mater. Chem.*, 2011, 21, 17946.

30 H. Zhang, B.-R. Hyun, F. W. Wise, and R. D. Robinson, *Nano Lett.*, 2012, 12, 5856.

31 J. H. L. Beal, P. G. Etchegoin, and R. D. Tilley, *J. Solid State Chem.*, 2012, 189, 57.

32 P. V Vanitha and P. O'Brien, *J. Am. Chem. Soc.*, 2008, 130, 17256.

33 J. H. L. Beal, P. G. Etchegoin, and R. D. Tilley, *J. Phys. Chem. C*, 2010, 114, 3817.

34 S. K. Maji, A. K. Dutta, P. Biswas, D. N. Srivastava, P. Paul, A. Mondal, and B. Adhikary, *Appl. Catal. A Gen.*, 2012, 419, 170.

35 A. L. Abdelhady, M. A. Malik, P. O'Brien, and F. Tuna, *J. Phys. Chem. C*, 2012, 116, 2253.

36 W. Han and M. Gao, *Cryst. Growth Des.*, 2008, 8, 1023.

37 Y. Zhang, Y. Du, H. Xu, and Q. Wang, *CrystEngComm*, 2010, 12, 3658.

38 L. Zhu, B. J. Richardson, and Q. Yu, *Nanoscale*, 2014, 6, 1029.

39 Y. Bi, Y. Yuan, C. L. Exstrom, S. A. Darveau, and J. Huang, *Nano Lett.*, 2011, 11, 4953.

40 B. Yuan, W. Luan, and S.-T. Tu, *Dalton. Trans.*, 2012, 41, 772.

41 Msayuki Uda, *Zeit. Anorg. Allg. Chem.*, 1967, 543, 105.

42 X. Chen, Z. Wang, X. Wang, J. Wan, J. Liu, and Y. Qian, *Inorg. Chem.*, 2005, 44, 951.

43 M. Akhtar, M. A. Malik, F. Tuna, and P. O'Brien, *J. Mater. Chem. A*, 2013, 1, 8766.

44 G. Hogarth, *Prog. Inorg. Chem.*, 2005, 53, 71.

45 L. I. Victoriano, *Coord. Chem. Rev.*, 2000, 196, 383.

46 L. I. Victoriano, *Polyhedron*, 2000, 19, 2269.

47 M. M. Karim, M. N. Abser, M. R. Hassan, N. Ghosh, H. G. Alt, I. Richards, and G. Hogarth, *Polyhedron*, 2012, 42, 84.

48 S. Åkerström and P. E. B. Lindahl, *Acta Chem. Scand.*, 1962, 16, 1206.

49 J. S. J. Ricci, C. Eggers, and I. Bernal, *Inorg. Chim. Acta*, 1971, 235, 97.

50 J. B. Zimmerman, T. W. Starinshak, D. L. Uhrich, and N. V. Duffy, *Inorg. Chem.*, 1977, 16, 3107.

51 X. D. Hu and H. Q. Zhang, *Mater. Sci. Forum*, 2011, 688, 301.

52 G. Crisponi, P. Deplano, and E. F. Trogu, *J. Chem. Soc., Dalton. Trans.*, 1986, 365.

53 P. Nichols and M. Grant, *Aust. J. Chem.*, 1989, 42, 1085.

54 V. F. Plyusnin, E. P. Kuznetzova, G. A. Bogdanchikov, V. P. Grivin, V. N. Kirichenko, and S. V. Larionov, *J. Photochem. Photobiol. A Chem.*, 1992, 68, 299.

55 D. J. Halls, *Microchim. Acta*, 1969, 57, 62.

4 Nickel Sulfide Nanoparticles

4.1 Introduction

4.1.1 Nickel Sulfide Nanoparticle Synthesis

Nickel sulfide has a complex phase diagram and can take many possible forms including α-NiS, β-NiS, NiS_2, Ni_3S_2, Ni_3S_4, Ni_7S_6, Ni_9S_8, *etc*., as previously detailed in Chapter 1.[1] They are desirable materials to produce due to the many applications they find in alternative energy. For example, the Ni_3S_2 phase has shown potential as a low cost counter electrode material in dye sensitised solar cells,[2] while the α-NiS phase has been applied as a cathode material in lithium-ion batteries.[3] Nickel sulfides have also been investigated as potential competitors to silicone in thin film photovoltaic cells,[4] as well as being used in the photocatalytic generation of hydrogen from water and other protic solvents.[5, 6]

There are many reports on the synthesis of nanoparticulate nickel sulfides and, as with the iron sulfides, these can be subdivided into hydrothermal[7–11] and solvothermal decomposition methods.[12–21] Hydrothermal synthesis of nickel sulfide involves the reaction of a nickel salt with a sulfur source, generally in an autoclave. An alternative method was employed by Tilley and Jefferson which involved sulfurization of nickel nanoparticles using H_2S/H_2 gas.[22] Varying reaction time, H_2S concentration and temperature lead to the selective synthesis of β-NiS, Ni_3S_2, Ni_9S_8, and Ni_7S_6.[22]

Hollow α-NiS submicro-spheres have been synthesised using poly(methyl methacrylate) gel system and γ-radiation,[23] while the same material was made using SiO_2 templates with hydrothermal decomposition of first a nickel precursor to make core-shell SiO_2/nickel silicate structures, followed by Na_2S to make the NiS/SiO_2 spheres.[11] Another template-based method was used by Barry *et al.* to synthesise α-NiS nanoparticles inside an anodic aluminium oxide (AAO) membrane, decomposing $[Ni(S_2COEt_2)_2TMEDA]$ (TMEDA = tetramethyl-ethylenediamine), in supercritical CO_2 at 450 °C, 4000 psi for 90 mins.[24]

Korgel *et al*. reported a solventless route to nickel sulfide nanoparticles using a nickel thiolate single-source precursor in octanoate.[25] Here β-NiS nanorods and triangular nanoprisms (with some Ni_3S_4 nanorod impurity) were synthesised by heating the reagents in air for 1.5 hrs at 170 °C. The morphology of the particles was found to be dependent

upon reaction temperature (higher temperatures lead to longer nanorods) and, to a lesser extent, reaction time. Shorter decomposition times (*ca.* 5 mins) produced an amorphous material and longer decomposition times led to the rounding of the prisms into quasi-spherical nanoparticles.[25]

Solvothermal decomposition has also been employed to successfully synthesise a wide range of nickel sulfide phases. Synthesis methods can be divided into those involving binary and single-source precursors, the former involving a nickel salt and a sulfur source and a high boiling solvent, often in an autoclave. Chen *et al.* synthesised β-NiS nanorods by decomposing $NiCl_2$ and $Na_2S_2O_3$ in EN in an autoclave at 200 °C for 20 hrs, and found that by lowering the temperature and reaction time they were able to access metastable NiS_2 dodecahedrons, though they were relatively large (>2 μm).[12] Interestingly, when thiourea was introduced as the sulfur source, β-NiS was produced with a small impurity of α-NiS which disappeared when the reaction time was increased (20 – 60 hrs). This indicates the β phase is thermodynamically more stable in this system, counter to their relationship in the nickel sulfide phase diagram.[12, 1]

The α- and β-NiS phases were selectively prepared by Meng *et al*. *via* the solvothermal reaction of $NiCl_2$ with sulfur in an autoclave, with either ethanol or pyridine respectively.[13] The authors claim that the reaction in ethanol proceeds quickly to produce the α phase, while in the latter case a pyridine adduct of the nickel precursor is formed initially, which then goes on to slowly form the β-NiS phase.[13] In another paper by Meng *et al*. α- and β-NiS phases were selectively synthesised by adjusting the molar ratio of the precursors $NiCl_2$ and thiourea, though this work was performed in water.[26] Wang *et al*. synthesised Ni_3S_2 nanotubes by decomposing $NiCl_2$ with dimethyl sulfoxide (DMSO) (loaded into an AAO template in a quartz tube oven at 150 °C for 10 hrs), annealing the Ni_3S_2 for 15 hrs at 700 °C resulted in the high temperature α-NiS phase.[27] Nanotubes of NiS_2 were accessed by adding additional sulfur to the precursor mix in the form of thiourea.[27]

Clearly precursor type and ratio as well as reaction time and temperature are factors in controlling the phase of nickel sulfide nanoparticle produced using binary precursors. In similar work to Chen, Yang *et al*. prepared NiS_2 dodecahedra by reacting $NiCl_2$ with sulfur in EN/EG in an autoclave at 200 °C for 6 hrs. Morphological dependence on solvent ratio is demonstrated, such that, when pure EN or a mixture of EN and EG is used, the product is pure NiS_2, but when pure EG is used a mixed phase product of NiS_2 and β-NiS is formed. [16]

Further solvent dependence was demonstrated by Aso *et al*. who obtained Ni_9S_8 nanorods from the decomposition of nickel acetylacetonate with DDT in OA and, β-NiS in octadecene.[28]

Solvothermal decomposition has been performed on a range of single-source precursors, including thiazole,[29] polysulfide,[17] thiobiuret,[19] imidodiphosphinate,[18] thiobenzoate,[20] and xanthate nickel complexes.[30] Additionally, various studies on the effects of decomposition temperature, time, precursor concentration and type and solvent on the nickel sulfide product have been investigated. Geng *et al*. decomposed [Ni(2-mercaptobenzothiazole)$_2$] ([Ni{Mer}$_2$]) in OA at 230 °C for 6 hrs producing ellipsoidal α-NiS nanoparticles.[29] Tilley *et al.* also synthesised α-NiS nanoparticles, by gradual heating of [Ni(*N*-MeIm)$_6$S$_8$] (*N*-MeIm = *N*-methylimidazole) to 300 °C in OA.[17] Rapid injection of [Ni(*N*-MeIm)$_6$S$_8$] into OA at 300 °C, however, resulted in nanoparticles of the metastable NiS_2 phase. A change in particle size was also noted, the NiS_2 measuring 6 ± 1 nm in diameter, while the α-NiS particles were 45 ± 15 nm. The authors attribute this to continual nucleation and size-defocusing in the synthesis of α-NiS.[17] The effect of decomposition time was also investigated by O'Brien *et al.*, who formed a mixture of nanorods and nanoparticles of Ni_3S_4 by hot injection of [Ni(SON(CN^{i}Pr$_2$)$_2$)$_2$] into OA at 200°C, and holding for 1 hr.[19] When the decomposition time was decreased, a decrease in nanorod length and nanoparticle diameter was observed, which the authors suggest can be attributed to a decrease in the Ostwald ripening effect.[19]

O'Brien also reported the effect of concentration on the nanoparticles, noting that at higher precursor concentrations impurities of Ni_8S_9 were formed as well as Ni_3S_4.[19] In addition, the morphology of the materials was affected such that at 5 mM single-source precursor concentration nanowires were formed, at 10 mM nanorods and at 20 mM a mixture of nanorods and nanoparticles were produced. Temperature had a similar effect on the nickel sulfide materials, such that at low temperature (200 °C) long nanowires were formed, increasing the temperature to 240 °C produced first shorter nanowires and then a mixture of nanorods and nanoparticles at 280 °C. The authors attribute this trend to a lower number of nucleation sites at low concentration or low temperature, favouring the growth of elongated nanocrystals.[19]

The effect of solvent was investigated in the same paper, and was seen to influence both the phase and morphology of the material produced, as with the binary solvothermal syntheses. In pure OA at 240 °C, Ni_3S_4 nanowires were produced, but when an OA/OD

(1:3) mixture was used α-NiS nanowires were formed and an OA/DDT (1:3) solution resulted in Ni_3S_4 triangular nanoparticles.[19] This latter trend may be attributed to the preferential binding of different capping agents to different crystal facets, leading to preferential growth in certain directions.

Tian *et al.* also observed the effect of solvent on nickel sulfide phase, decomposing $[(TMEDA)Ni(SC\{O\}C_6H_5)_2]$ in OLA at 180 °C for 1 hr to obtain α-NiS nanoparticles of polyhedral morphology.[20] When DDT was used as the solvent, polyhedral nanoparticles of β-NiS were produced, however, when an OA/DDT (1:3) mixture was used at 300 °C, well faceted nanocubes of β-NiS were formed.[20] Since both temperature and solvent were changed it is difficult to know what this difference can be attributed to. Altering decomposition time to 30 mins produced nanorods, and nanocubes were obtained at 3 and 6 hrs, with a wider size distribution after the longer reaction time (due to Ostwald ripening).[20] Tian has therefore shown that the α- and β-NiS phases can be selectively synthesised using decomposition solvent in a single-source precursor system.[20] This selectivity can be extended to precursor type, as shown by Babashkina *et al*.[18] Nickel imidodiphosphinate complexes $[Ni\{RC(S)NP(S)(O^iPr)_2\}_2]$, R = C_6H_5 and 2-MeC_6H_4NH, were decomposed in HDA/TOP (TOP = tri-*n*-octylphosphine) at 190 °C forming α- and β-NiS nanoparticles respectively.[18]

There are very few reports on the use of dithiocarbamate nickel complexes as single-source precursors for the synthesis of nickel sulfide nanoparticles,[31–33] and no solvothermal decomposition studies. In one case $[Ni(S_2CNEt_2)_2]$ was decomposed hydrothermally in an autoclave at 180 °C for 12 hrs resulting in Ni_3S_4 crystallites of approximately 2 μM diameter.[33] In another report the same precursor was decomposed in the absence of solvent in a reactor tube at 525 °C for 3 hrs in a flow of H_2/H_2S gas, producing Ni_3S_2 nanoparticles of approximately 350 nm diameter.[31] $[Ni(S_2CN\{H\}^nBu)_2]$ and $[Ni(S_2CN^nBu_2)_2]$ have been decomposed on a heated XRD stage with different nickel sulfide phases being prepared in the presence of N_2 and H_2/N_2 atmospheres, and at different temperatures.[32] O'Brien and co-workers use symmetric and asymmetric nickel dithiocarbamate complexes to synthesise $NiS_{1.03}$ and a mixture of $NiS_{1.03}$ and NiS.[34]

4.1.2 Nickel Dithiocarbamate Complexes

Nickel(II) bis(dithiocarbamate) complexes, $[Ni(S_2CNR_2)_2]$, have been widely studied and were first reported by Delépine in 1907.[35] Like the iron(III) dithiocarbamates,

$[Ni(S_2CNR_2)_2]$ can be easily synthesised on the bench from the addition of the appropriate dithiocarbamate salt to a nickel(II) salt (see Equation 4-1).[36–41] Many different $[Ni(S_2CNR_2)_2]$ complexes have been reported with varying R groups, from simple diethyl derivatives[37, 36, 42] to amino acid derivatives[40] to ferrocenyl bearing derivatives.[41] In the previous Chapter, iron sulfide nanoparticles were successfully synthesised solvothermally using iron dithiocarbamate single-source precursors and the current Chapter aims to investigate if nickel sulfide nanoparticles can be synthesised with similar success using this method.

4.2 Results and Discussion

Herein, the synthesis of a range of $[Ni(S_2CNR_2)_2]$ is described, and their thermal stability assessed. Following this, decomposition studies into the effect of precursor R-group, concentration and decomposition temperature on the resulting nickel sulfide nanoparticles are described.

4.3 Nickel Dithiocarbamate Complexes

4.3.1 Synthesis

Complexes were synthesised according to well established literature methods[37] *via* the addition of two equivalents of sodium dithiocarbamate ligand (NaS_2CNRR') to an aqueous solution of nickel chloride (Equation 4-1). As with the iron(III) dithiocarbamate complexes, in the case of the isobutyl, methylbutyl and 4-methylpiperideine derivatives, it was necessary to synthesise the sodium dithiocarbamate ligand by the slow addition of carbon disulfide to an aqueous solution of sodium hydroxide and the appropriate secondary amine. All the nickel(II) bis(dithiocarbamate) complexes were relatively straightforward to prepare, though the methyl derivative (**19**) was only sparingly soluble in chlorinated solvents.

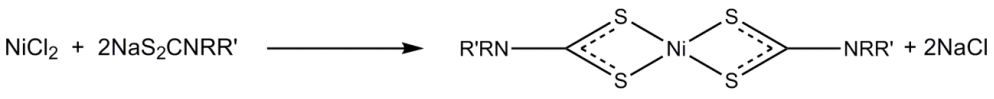

R = R' = Me (**19**)
R = R' = Et (**20**)
R = R' = ^{i}Bu (**21**)
R = Me, R' = ^{n}Bu (**22**)
NRR' = 4-MePip (**23**)

Equation 4-1

All complexes were analysed by NMR spectroscopy, IR, MS, EA and, where crystals were obtained, single crystal X-ray diffraction. A great number of crystallographic studies have been carried out on nickel(II) bis(dithiocarbamate) complexes, all report nickel in a square-planar coordination environment, with intra-ligand bite-angles at nickel ranging from 78 – 80 ° and Ni–S bond distances between 2.16 and 2.23 Å.[43–46, 39] Groups have reported both intramolecular S•••H hydrogen bonds and intermolecular Ni•••H and S•••H interactions.[39]

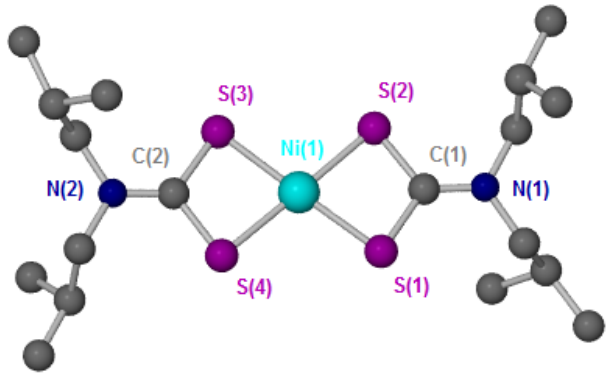

Figure 4-1 - Crystal structure of [Ni($S_2CN^iBu_2$)$_2$] (21, hydrogen atoms omitted for clarity).

In this study, crystals of **21** were obtained by slow evaporation from chloroform solution (Figure 4-1), and a crystal structure was obtained at 150 K. The axial S(1)–Ni(1)–S(3) bond angle is close to 180 ° at 178.88(1), showing some strain in the square planar geometry (Table 4-1). This is further exemplified by the S(2)–Ni(1)–S(3) and S(1)–Ni(1)–S(2) bond angles being approximately 10 ° away from the expected 90 ° (99.32{2} and 79.61{2} respectively). As with the iron dithiocarbamate complexes, this strain arises from the restrictive bite angle of the dithiocarbamate ligand, leading to an accute S–Ni–S intra-ligand bond angle. The average Ni–S bond length is 2.2024 Å which falls within the expected range of between 2.16 and 2.23 Å. The square planar geometry of these complexes allows for good packing in the solid state. This is particularly obvious for the methyl derivative (**19**), which packs so well it was found to be relatively insoluble in chlorinated solvents.

Atoms	Bond Angle (°)	Atoms	Bond length (Å)
S(1)–Ni(1)–S(3)	178.88(1)	Ni(1)–S(1)	2.2095(6)
S(1)–Ni(1)–S(2)	79.61(2)	Ni(1)–S(2)	2.1936(5)
S(2)–Ni(1)–S(3)	99.32(2)	C(1)–S(2)	1.729(1)
S(1)–C(1)–S(2)	109.47(8)	C(1)–N(1)	1.313(2)

Table 4-1 - Selected bond lengths and angles for 21.

4.3.2 Stability

The relative stability of the $[Ni(S_2CNRR')_2]$ complexes was investigated with the aid of TGA. The volatility of $[Ni(S_2CNRR')_2]$ complexes has been well-studied, initial studies indicating that the complexes sublime,[35] later work shows most melt and evaporate (with some decomposition) though a select few do appear to sublime, depending on R-group.[47–51] The TGA graphs for **20 – 22** are very similar, exhibiting thermal stability until approximately 300 °C, whereupon they lose *ca.* 95 % of their mass in one sharp step. The DSC graphs for **20 – 22** show melting peaks at 235, 177 and 118 °C respectively, consistent with literature values.[47–49]

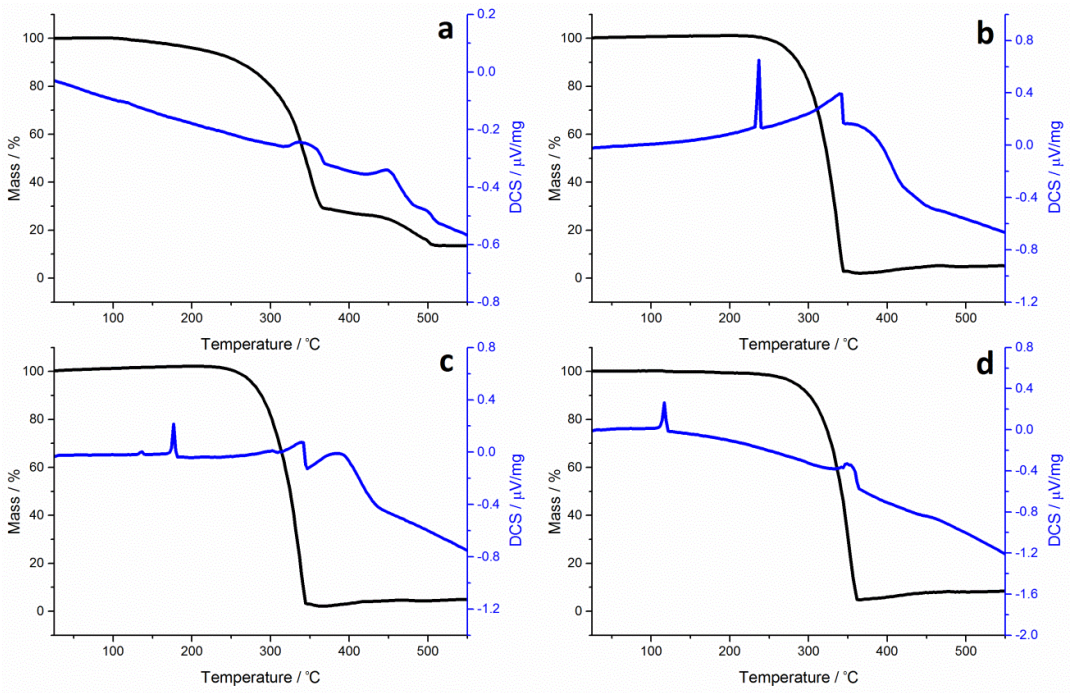

Figure 4-2 - TGA (black) and DSC (blue) graphs for complexes a) 19, b) 20, c) 21 and d) 22.

The dimethyl derivative, **19**, shows an unusual trace compared to **20** – **22**. Loss of a mass equivalent to $S(SCNMe_2)_2$ occurs gradually, beginning at 106 °C and continuing to 367 °C, suggesting this complex decomposes rather than evaporating or subliming. At this point the remaining mass is equal to NiS, but the sample continues to lose mass, leaving a percentage equal to less than that of elemental nickel, as with **20** - **22**. Consistent with the literature, the DSC trace shows no melting peak,[47] and some endothermic peaks associated with the mass losses. The dimethyl derivative is likely to pack well in the solid state and this is perhaps why a melting peak is not observed. These strong intermolecular forces may also be the reason it decomposes rather than sublimes.

From these results it can be concluded that the nickel complexes tested have differing stability in the solid state, with melting temperature ranging from 118 to 235 °C. The complexes first melting and then evaporating in one step to leave less than 5 % of their mass, with the exception of the dimethyl derivative which decomposes in two stages, the first a slow loss leaving NiS, followed by a further loss to leaving less than elemental nickel.

4.4 Decomposition of Nickel(II) Dithiocarbamate Precursors

There are very few reports on the use of nickel dithiocarbamate complexes as single source precursors for the synthesis of nickel sulfide nanoparticles, and no reports on their use in a solvothermal decomposition system. However, metal dithiocarbamate complexes have been shown as excellent precursors for metal sulfide nanoparticles. The following section will describe the solvothermal decomposition of $[Ni(S_2CNR_2)_2]$ complexes, and the effect of dithiocarbamate ligand R-group, decomposition temperature and precursor concentration on the resultant nickel sulfide nanoparticle phase and morphology.

4.4.1 Varying R-group

Nickel(II) dithiocarbamate complexes **19** – **22** were decomposed according to the setup described in Section 3.2 at 230 °C with a single-source precursor concentration of 5 mM in OA. It was noted that the complexes formed a green solution in OA at room temperature (except **19** which only dissolved at *ca.* 30 °C), and as the solution was heated started slowly becoming brown at 60 °C, appearing to become darker as the temperature was raised until 130 – 140 °C, where upon the clear brown solution became opaque black (with the exception of **19**, which started to become brown at 90 °C , and black at 140 – 150 °C). Upon cooling the particles were worked up by washing with methanol and centrifuging to give dry black powders.

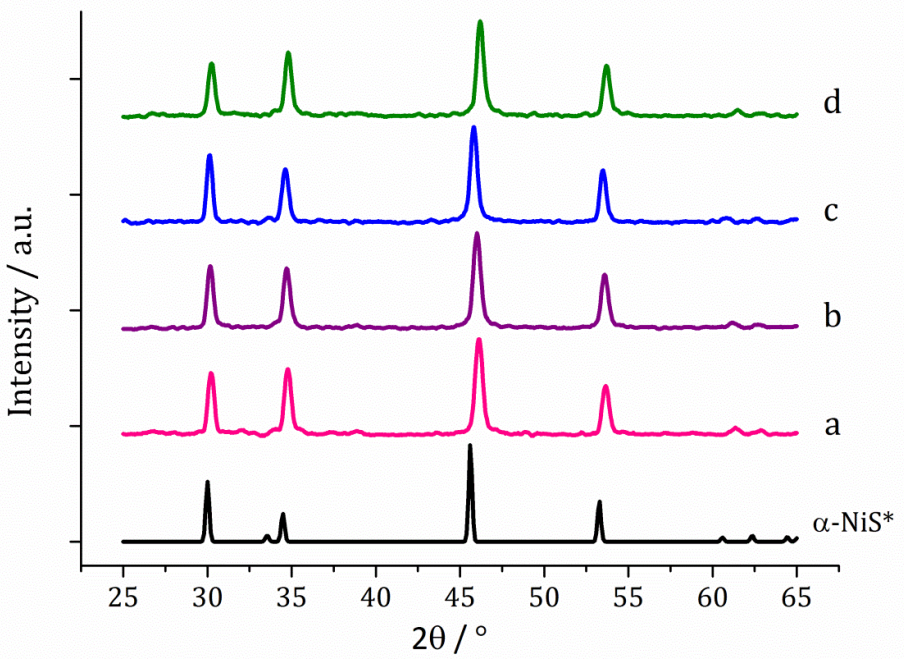

Figure 4-3 - XRD patterns for NPs obtained from (a) 19, (b) 20, (c) 21 and (d) 22, with reference pattern for bulk α-NiS (ICDD card No. 02-1273).

The crystalline phase of the decomposed black powders were characterised by powder XRD. XRD analysis revealed pure α-NiS (ICDD card No. 02-1273) was formed in all cases, suggesting that R-group does not affect the phase of nickel sulfide formed under these conditions. This differs from the findings of Babashkina *et al.* who decomposed [Ni{RC(S)NP(S)(O^{i}Pr)$_2$}$_2$] and found that changing R-group from phenyl to 2-MeC_6H_4NH produced α- and β-NiS respectively.[18] In addition, when iron(III) dithiocarbamates of different R-groups were studied in Chapter 3, the ethyl derivative (**2**) was found to give a mixture of phases.

The TGA analysis of **19** – **22** revealed similar thermal decomposition profiles, with the exception of the dimethyl derivative (**19**) which decomposed rather than evaporating as with **20** – **22**. That α-NiS is formed from the solvothermal reaction **19** – **22** suggests solvent interactions play an important role in the mechanism of decomposition. TEM analysis of the resulting nanoparticles reveals a roughly hexagonal morphology for **19** – **22** (particles synthesised from **21** are shown as an example in Figure 4-4), showing the morphology is largely unaffected by precursor R-group. HRTEM of particles produced from **21** shows *d*-spacings of 2.95 Å, consistent with the [100] plane of α-NiS (2.98 Å). Considering the size of the errors, the average particle diameter does not vary significantly with R-group (Figure 4-4).

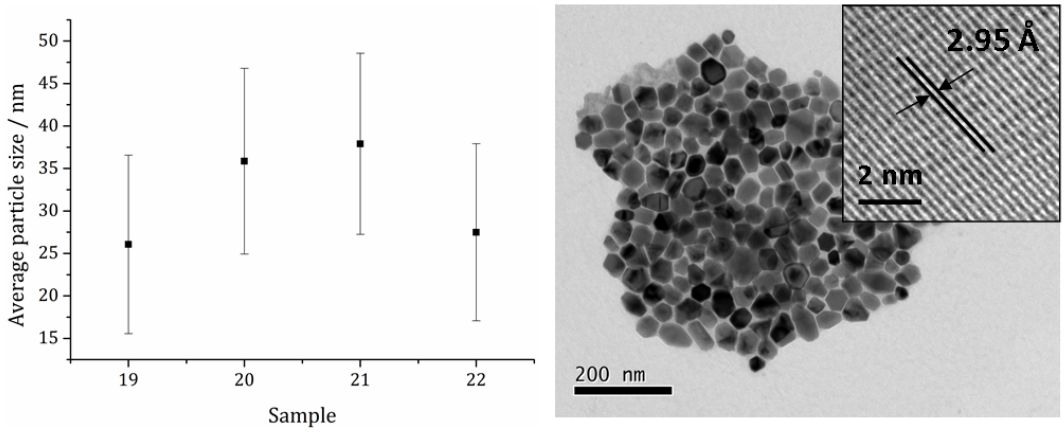

Figure 4-4 - Graph of average particle diameter, with one SD above and below, of samples prepared from 19 – 22 (left) and TEM image of the sample prepared from 21 with HRTEM insert (right).

Precursor **21** was chosen to take forward for further studies as it produced well-faceted nanoparticles, was easy to synthesise, purify and handle (highly soluble in OA, *etc.*).

4.4.2 Varying Temperature

Complex **21** was decomposed in OA according to the method described in Section 3.2 at a concentration of 5 mM at 150, 180, 230, 260 and 280 °C. Temperature dependent colour changes were observed as with previous decompositions (described in Section 4.4.1), with no noticeable difference at higher temperature. XRD analysis of the resultant nanoparticles reveals a relationship between decomposition temperature and the crystalline nickel sulfide phase (Figure 4-5). At low temperature (150 °C) α-NiS is formed, however at 260 °C, the majority of the crystalline material is β-NiS, with a small α-NiS impurity. At 280 °C α-NiS is removed and pure β-NiS produced.

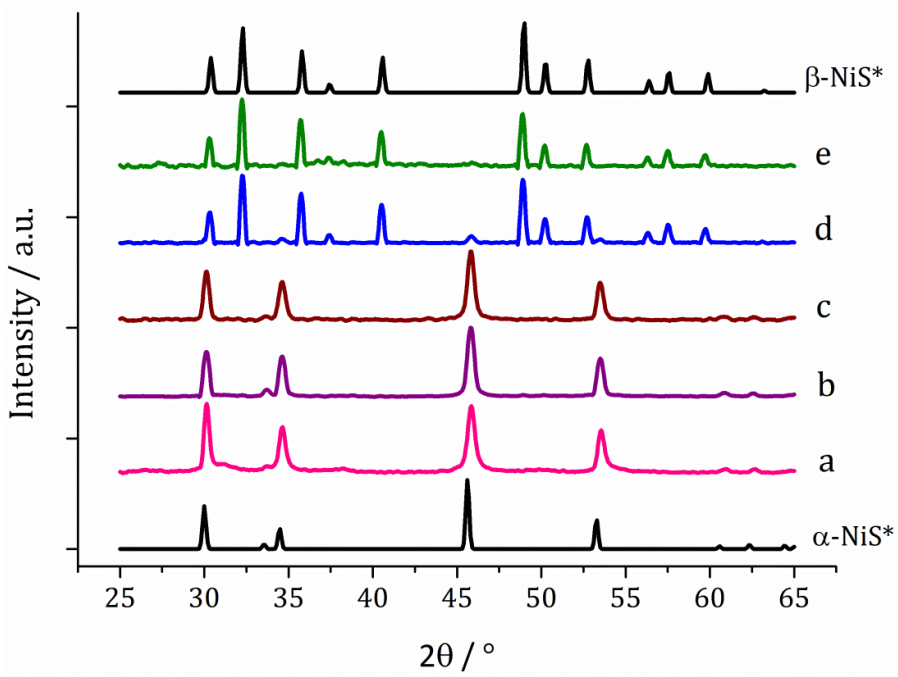

Figure 4-5 - XRD patterns for samples prepared from 21 at (a) 150 °C, (b) 180 °C, (c) 230 °C, (d) 260 °C and (e) 280 °C, with reference patterns for bulk α-NiS (ICDD card No. 02-1273) and β-NiS (ICDD card No. 86-2281).

This contradicts what is generally accepted of the α and β phases of NiS, being the high and low temperature phases respectively.[1] There is some precedent for this reversal of behaviour. Thus Chen *et al.* report the synthesis of β-NiS nanoparticles with some α-NiS impurity which was eliminated by increasing reaction time.[12] This would indicate that the β phase is actually the thermodynamically favoured phase in the solvothermal system.

The morphology of the particles also depended on the decomposition temperature (see Figure 4-4 and Figure 4-6). The β-NiS nanoparticles formed at 260 and 280 °C exhibit a larger average diameters than the α-NiS formed at lower temperatures (150 – 230 °C). In both samples of β-NiS the nanoparticles appear agglomerated with a large size distribution. The difference in morphology appears to correlate with the difference in NiS phase. HRTEM of particles produced at 280 °C shows spacings of 2.54 and 2.98 Å, consistent with the [-111] and [010] planes of β-NiS (2.51 and 2.95 Å respectively).

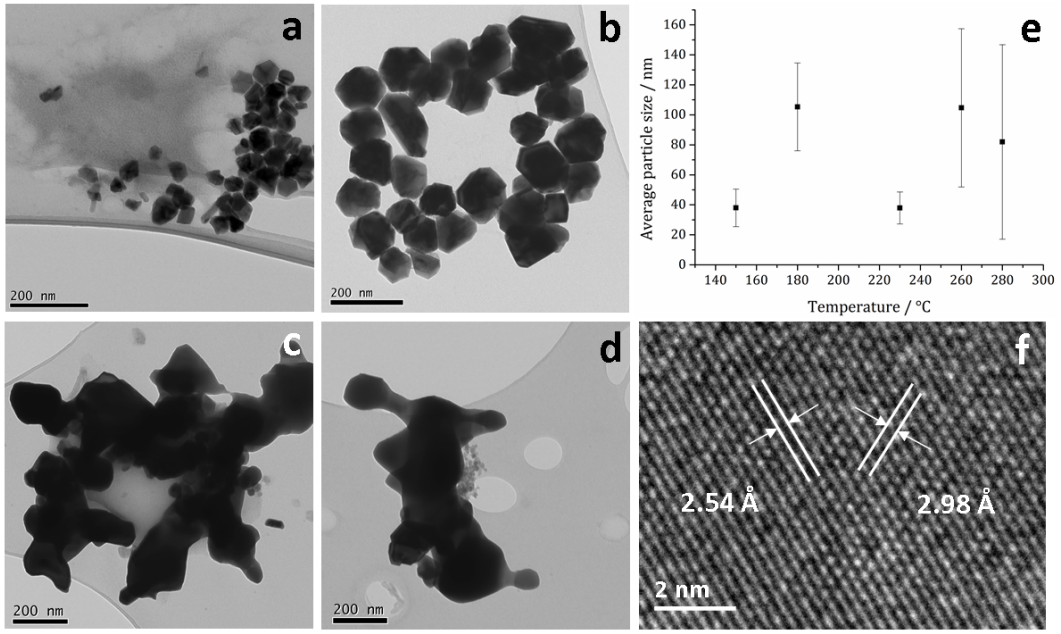

Figure 4-6 - TEM images of samples prepared from 21 at (a) 150, (b) 180, (c) 260 and (d) 280 °C. (e) Graph of average particle size against temperature of decomposition, with one SD above and below. (f) HRTEM image of β-NiS synthesised at 280 °C.

TEM images of the particles synthesised at 150 °C show an amorphous component to the sample, indicating there was insufficient energy for crystallisation to complete after one hr at this temperature. This was also observed for the iron(III) single-source precursor **16** at both 150 and 180 °C. When **21** was decomposed at 150 and 230 °C, α-NiS nanoparticles of average diameter 38 nm were formed, while at 180 °C much larger α-NiS nanoparticles were produced (105 nm). The reason for this is unclear. A temperature of 180 °C was chosen to take forward for a concentration study on the system, as it is the lowest at which pure crystalline material could be produced, and so might provide the best conditions to access metastable nickel sulfide phases.

4.4.3 Varying Concentration

Complex **21** was decomposed in OA according to the method described in Section 3.2, at 180 °C and varying concentrations of 10, 20, 40 and 50 mM. XRD analysis of the products (combined with the previous result for 5 mM) reveals varying precursor concentration has no effect on the phase of the resulting nickel sulfide nanoparticles, α-NiS being formed in all instances (Figure 4-7).

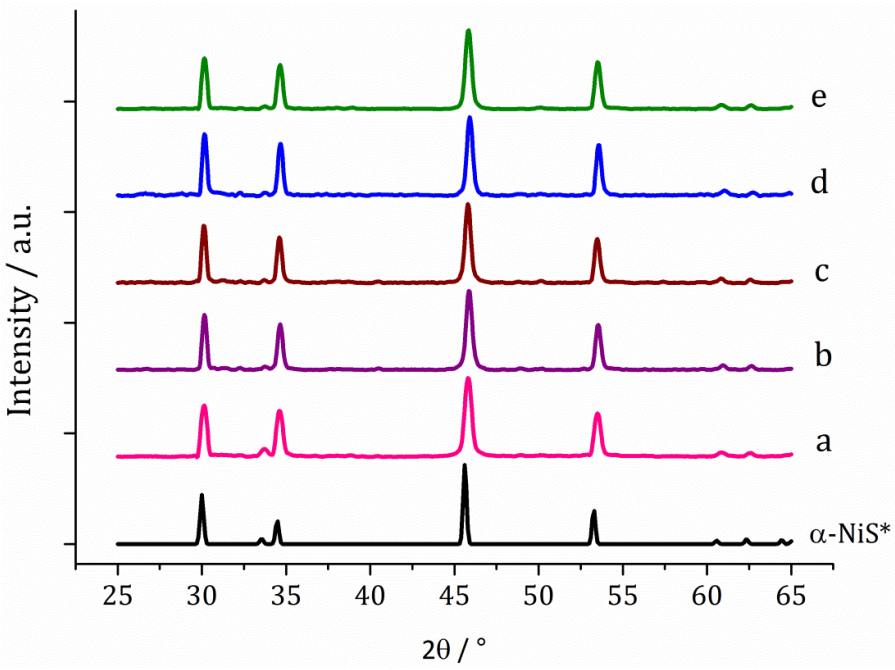

Figure 4-7 - XRD patterns for samples prepared from 21 at (a) 5, (b) 10, (c) 20, (d) 40 and (e) 50 mM concentration, with reference pattern for bulk α-NiS (ICDD card No. 02-1273).

TEM analysis of the resultant samples reveals no change to the morphology of the nanoparticles upon increasing precursor concentration, all being roughly hexagonal in shape in accordance with the sample produced at 5 mM (Figure 4-6 (b)). In addition, the average size of the nanoparticles was not greatly affected by varying precursor concentration (Figure 4-8).

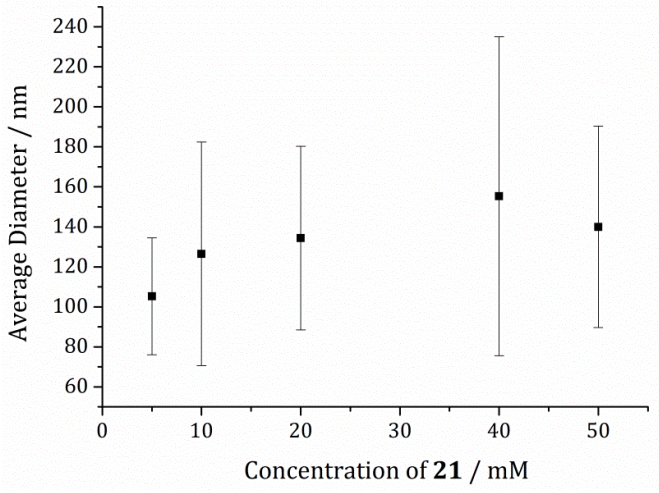

Figure 4-8 - Graph of average particle diameter against concentration of precursor (21).

In summary, nanoparticles of both α- and β-NiS are accessible *via* the solvothermal decomposition of nickel(II) dithiocarbamate complexes in OA by varying reaction

temperature. The results indicate that precursor R-group and concentration have little effect on the phase or morphology of the resulting nickel sulfide nanoparticles.

4.5 Decompositions of Nickel(II) Dithiocarbamate Precursors with Thiuram Disulfide Additive

As mentioned in Section 4.1.1, nickel sulfide has a complex phase diagram which encompasses numerous phases.[1] In order to access additional nickel sulfide structures, the thiuram disulfide additive **6** was added to the decomposition solution. In the previous Chapter, **6** was shown to facilitate the synthesis of a metastable phase of iron sulfide, and it was hoped that it would behave similarly in the nickel sulfide system. Studies into the effect of decomposition temperature and precursor concentration on this new system are herein described.

4.5.1 Varying Temperature

Complex **21** (5 mM) and **6** (10 mM) were decomposed in OA according to the method described in Section 3.2, at 150, 180, 230, 260 and 280 °C. The complexes formed a green solution in OA at room temperature, and subsequent colour changes were in accordance with those described previously for **21** decomposed in the absence of **6**. The black powders obtained were analysed by XRD and the results can be seen in Figure 4-9. Samples synthesised at 230 °C and above match the reference pattern for α-NiS, which is contrary to the results found without the thiuram disulfide additive **6**, where β-NiS was previously formed. This suggests that the addition of **6** stabilises the metastable α-NiS phase (as was seen in the previous Chapter with the iron sulfides pyrrhotite and greigite).

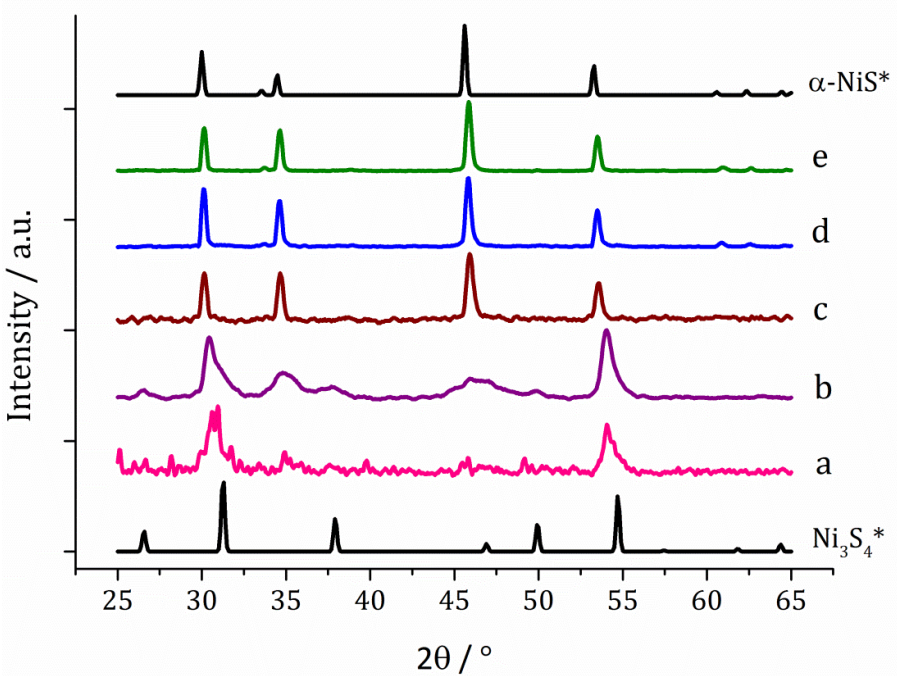

Figure 4-9 - XRD patterns for samples prepared from 21 with 6 at (a) 150 °C, (b) 180 °C, (c) 230 °C, (d) 260 °C and (e) 280 °C, with reference patterns for bulk Ni_3S_4 (ICDD card No. 43-1469) and α-NiS (ICDD card No. 02-1273).

XRD patterns for samples prepared at 150 and 180°C show mixtures of both α-NiS and Ni_3S_4, though the pattern for 150°C is of poor quality being indicative of low crystallinity and a higher amorphous content. At 180 °C there appears to be a mixture of a large component of α-NiS and a smaller component of Ni_3S_4. Ni_3S_4 is a metastable phase in this system and is accessible by the presence of **6**. Polydymite (Ni_3S_4) is a thiospinel of nickel sulfide, and the fact that it can be accessed at low temperature using the additive **6**, mirrors the work done in Chapter 2 with iron sulfides, in particular the thiospinel greigite (Fe_3S_4). TEM imaging of the sample produced at 150 °C supports the XRD analysis, showing some very small particulates and amorphous areas (Figure 4-10 (b)). This is consistent with the sample produced in the absence of thiuram disulfide (**6**) at 150 °C, which was also found to be partly amorphous.

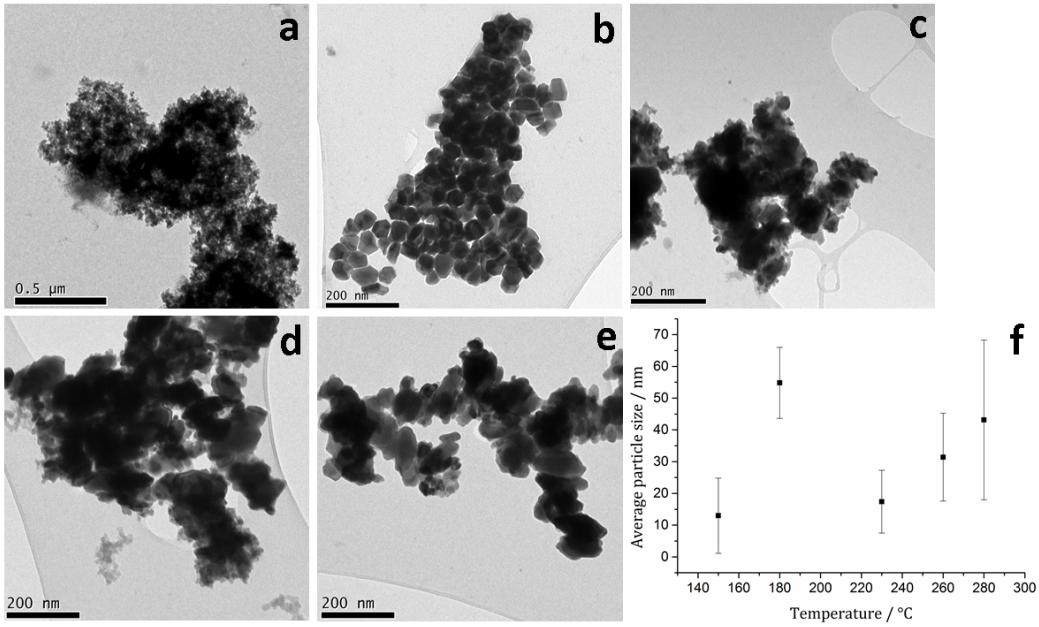

Figure 4-10 - TEM images of samples prepared from 21 with 6 at (a) 150, (b) 180, (c) 230, (d) 260 and (e) 280 °C. (f) Graph of average particle size against temperature of decomposition, with one SD above and below.

TEM analysis of the rest of the samples shows a progression from small, partly amorphous material, to large well-faceted particles (resembling the α-NiS samples previously prepared) when decomposition temperature is increased from 150 to 180 °C. This increase in size could be due to increased Ostwald ripening at the higher temperature of 180 °C. The average particle size drops on increasing decomposition temperature from 180 to 230 °C. This could be due to an increased rate of decomposition and so number of nucleation sites at the higher temperature.

Samples prepared at 230 °C and above increase in size as the decomposition temperature is increased. The sample prepared at 230 °C is made up of many small particles agglomerated together, while the sample at 280 °C may be the result of Ostwald ripening of these smaller particles. As with the samples prepared without **6**, the particles prepared at 180 °C are larger than those prepared at other temperatures. This temperature appears to be significant in the nickel sulfide decomposition system. In addition, this is the lowest temperature at which crystalline material is produced and so has potential for accessing other metastable nickel sulfide phases, 180 °C was therefore taken forward for a concentration study.

4.5.2 Varying Concentration

When **21** and **6** (in a 1:2 ratio) were decomposed at 180 °C with increasing concentration (10:20, 20:40, 40:80 and 50:100 mM) various phases of nickel sulfide were formed (see XRD analysis in Figure 4-11). At low precursor concentration a mixture of α-NiS and Ni_3S_4 were formed, with a growing proportion of Ni_3S_4 as the concentration of precursor is increased to 10 mM. The sample prepared using 20 mM of **21** (and 40 mM of **6**) matches well to the pattern for NiS_2 (ICDD card No. 89-3058). As the concentration is increased peaks for α-NiS appear and grow alongside the NiS_2 peaks. NiS_2 is a metastable phase of nickel sulfide, only accessible in this system by the use of the thiuram disulfide additive **6**, and at high precursor concentrations.

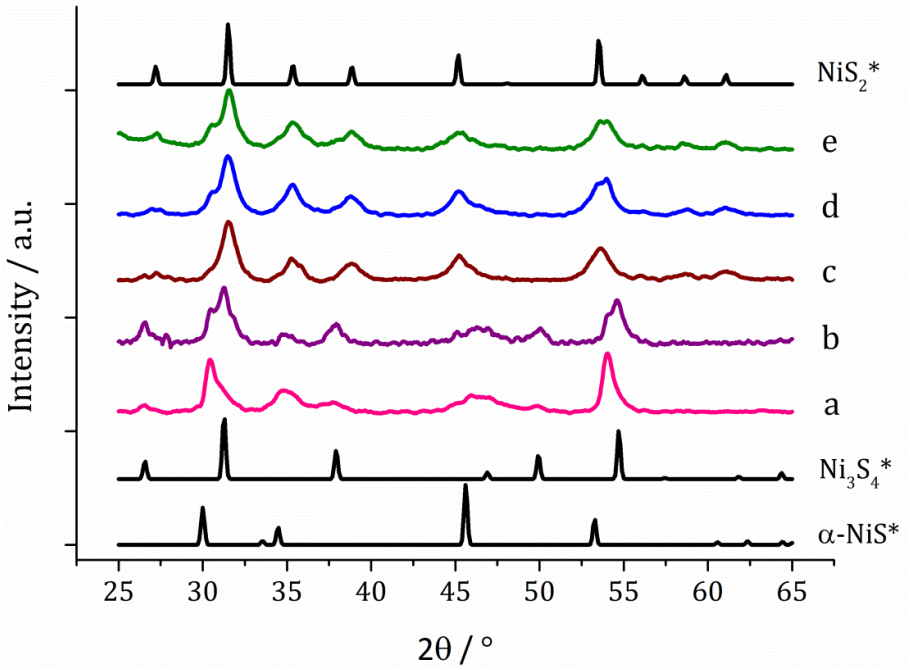

Figure 4-11 - XRD patterns for samples prepared from 21 with 6 at (a) 5, (b) 10, (c) 20, (d) 40 and (e) 50 mM concentration, with reference patterns for bulk α-NiS (ICDD card No. 02-1273), Ni_3S_4 (ICDD card No. 43-1469) and NiS_2 (ICDD card No. 89-3058).

The XRD pattern for all samples show broad peaks indicative of small crystallite size, and TEM images of the particles confirm this for the NiS_2 containing samples, which all have very small particles (Figure 4-12). The particles prepared from 5 and 10 mM solutions of **21** are larger (*ca.* 50 nm), though the broadening of their XRD peaks may be due to the samples being made of mixtures of phases. The sample prepared from 10 mM of **21** contains a higher proportion of Ni_3S_4 which was imaged *via* HRTEM, showing *d*-spacings of 5.50 Å, matching well to literature values for the [111] plane (5.48 Å, ICDD card 43-1469).

The morphology of this phase shows interlocking irregularly shaped sheets, quite unlike the morphology of the particles prepared at higher precursor concentration.

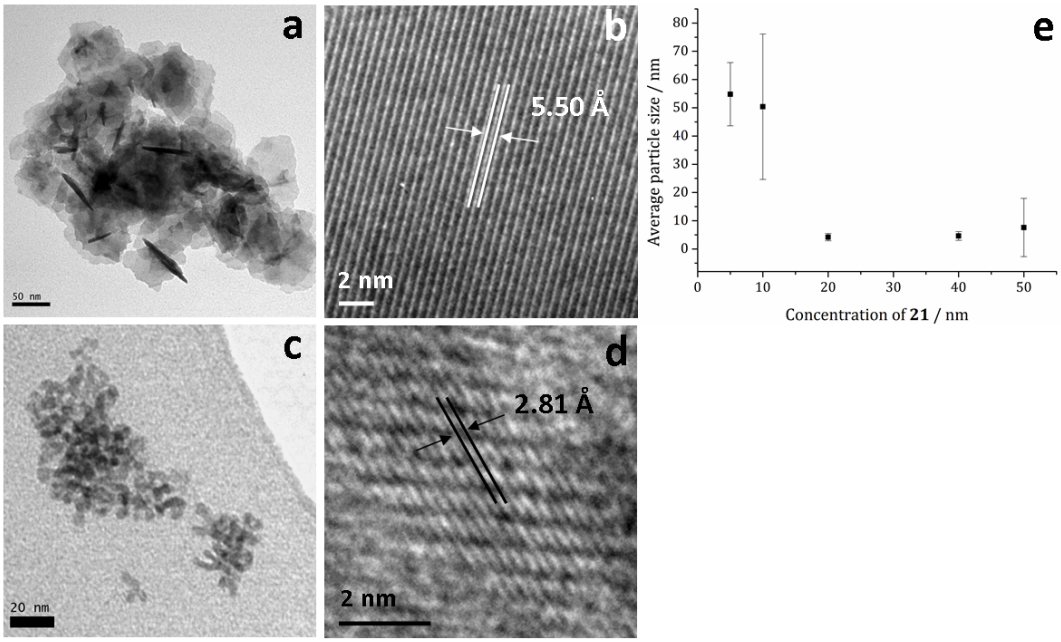

Figure 4-12 - TEM images of samples prepared from 21 with 6 at 180 °C at (a, b) 10 and (c, d) 20 mM. (e) Graph of average particle size against concentration of 16, with one SD above and below.

The particles formed from the decomposition of **21** at concentrations of 20 – 50 mM are very small (*ca.* 5 nm) and do not appear to aggregate in the same way (Figure 4-12). HRTEM analysis reveals a *d*-spacing of 2.81 Å, which matches the [200] plane of NiS_2 (2.81 Å, ICDD card No. 89-3058). The particles have a very narrow size dispersion; those formed from a solution of 20mM of **21** have a standard deviation of 1.3 Å, and at 40 mM of **21**, 1.5 Å. Particles formed from 50 mM of **21** have a larger average diameter and standard deviation (7.60 and 10.3 Å respectively), due to the presence of other large particles, likely to be the α-NiS impurity. The reason for the small size of the NiS_2 particles may be that the increase in precursor concentration provides many more nucleation sites.

4.6 Conclusions

By varying decomposition temperature, precursor concentration and the use of a reductive additive, nickel sulfide nanoparticles of various mineral phases have been produced (Table 4-2). These conditions can be tuned to obtain α-NiS, β-NiS, Ni_3S_4 and NiS_2. The decomposition study on precursor **21** (without additive) showed that in the solvothermal system α-NiS is formed at low temperature, while β-NiS at high – suggesting

the former is a kinetically favoured, metastable phase compared to the latter, being a more thermodynamically favoured phase of nickel sulfide. This is contrary to their relationship in the nickel sulfide phase diagram, where α-NiS is regarded as the high temperature phase compared to β-NiS. The reasons for this are unclear, though may be attributed to solvent interactions and is suggestive of the solvent having an important role in the decomposition mechanism.

The addition of two equivalents of thiuram disulfide (**6**) to the decomposition system allows access to the metastable phase Ni_3S_4. Similar to the iron sulfide case with greigite, **6** is able to promote the formation of or prolong the existence of Ni_3S_4. Both nickel(II) and nickel(III) ions are present in Ni_3S_4, meaning nickel(II) in the $[Ni(S_2CN^iBu_2)_2]$ precursor has been partially oxidised. **6** is a reducing agent, and so unlikely to be able to make this change the metal's oxidation state (it was suggested **6** could possibly be reducing some of the iron(III) in the formation of greigite), so it is more likely that the role of **6** is to stabilise metastable mineral phases, rather than affecting any redox process.

At high precursor concentration, with two equivalents of **6** present, NiS_2 was produced. Nickel is in the 2+ oxidation state in this phase with an S_2^{2-} dianion, further support for the hypothesis that the role of **6** in the decomposition mechanism is not to change the oxidation state of the metal, but to stabilise metastable phases of nickel sulfide in the system. The addition of **6** to the synthesis of other metal sulfides may have a similar stabilising effect, enabling the formation of metastable phases not easily prepared otherwise.

Variable	Nickel sulfide phase			
	α-NiS	β-NiS	Ni_3S_4	NiS_2
R-Group	**X** (for all R-Groups)	–	–	–
Temperature	**X** (150–230 °C)	**X** (260–280 °C)	–	–
Concentration	**X** (for 5–50 mM)	–	–	–
Temperature (with additive **6**)	**X** (150–280 °C)	–	**X** (150–180 °C)	–
Concentration (with additive **6**)	**X** (5–10, 40–50 mM)	–	**X** (5–10 mM)	**X** (20–50 mM)

Table 4-2 - Summary of nickel sulfide phases produced in decomposition studies.

4.7 Experimental

Chemicals

All reagents were procured commercially from Aldrich and used without further purification.

Physical Measurements

All ^{1}H and $^{13}C\{^{1}H\}$ NMR spectra were obtained on either a Bruker Avance III 400 or Avance 600 spectrometer, the latter being equipped with a cryoprobe. All spectra were recorded using $CDCl_3$ which was dried and degassed over molecular sieves prior to use; ^{1}H and $^{13}C\{^{1}H\}$ chemical shifts are reported relative to $SiMe_4$. The mass spectra were obtained using either Micromass 70-SE spectrometer using Electron Ionisation (EI) or a Thermo Finnigan MAT900xp spectrometer using Fast Atom Bombardment (FAB). Elemental analysis was carried using Elemental Analyser (CE-440) (Exeter Analytical Inc). Thermogravimetric analysis (TGA) was performed using a Netzsch STA 449C TGA system. Data was recorded from 25 to 600 °C with a constant heating rate of 10 °C minute^{-1}.

XRD patterns were measured on a Bruker AXS D4 diffractometer using $CuK\alpha_1$ radiation. The diffraction patterns obtained were compared to database standards. For TEM characterisation a 4 µl droplet of nanoparticle suspension (chloroform) was placed on a holey carbon-coated copper TEM grid and allowed to evaporate in air under ambient laboratory conditions for several minutes. TEM images were obtained using a JEOL-1010 microscope at 100 kV equipped with a Gatan digital camera. HRTEM measurements were collected using a Jeol 2100 TEM with a LaB_6 source operating at an acceleration voltage of 200 kv. Micrographs were taken on a Gatan Orius Charge-coupled device (CCD).

4.7.1 Nickel Dithiocarbamate Precursor Synthesis

$[Ni(S_2CNMe_2)_2]$ (19)

The complex was synthesised according to the literature.[37] An example of the synthesis method is given below.

NaS_2CNMe_2 (2.86 g, 20 mmol) was dissolved into 50 mL water and added dropwise over 10 mins to a solution of $NiCl_2{\cdot}6H_2O$ (2.38 g, 10 mmol) dissolved in 50 mL of water,

whereupon a green precipitate formed. This mixture was vigorously stirred for 2 hrs, filtered, washed with water (3 x 30 mL) and evaporated to dryness. The resulting green powder was dissolved in 100 mL of dichloromethane (DCM) and stirred with magnesium sulphate for 30 mins, after which the mixture was filtered and the filtrate dried *in vacuo*. Yield 2.2420 g, 75 %. **Anal. Calc. for $C_6H_{12}N_2S_4Ni$:** C, 24.09; H, 4.04; N, 9.37. Found: C, 24.42; H, 4.17; N, 8.81. **^{1}H NMR δ/ppm ($CDCl_3$):** 3.18 (s, 12H, CH_3). **^{13}C{^{1}H} NMR δ/ppm ($CDCl_3$):** 38.4 (*C*H_3), 207.7 (*C*S_2). **MS:** *m/z* 298 [M^+], 88 [$SCNMe_2$]. **IR (ν_{max} cm^{-1}):** 1516 (s) [N=C], 970 (s) [C=S].

[Ni(S_2CNEt_2)$_2$] (20)

The complex was synthesised following the same method as with **19**, with the exception that NaS_2NCEt_2 (4.51 g, 20 mmol) was used as the reagent. Yield 2.8656 g, 81 %. **Anal. Calc. for $C_{10}H_{20}N_2S_4Ni$:** C, 33.81; H, 5.67; N, 7.89. Found: C, 33.76; H, 5.66; N, 7.90. **^{1}H NMR δ/ppm ($CDCl_3$):** 1.22 (t, *J* = 7.2 Hz, 12H, CH_2CH_3), 3.59 (q, *J* = 7.2 Hz, 8H, CH_2CH_3). **^{13}C{^{1}H} NMR δ/ppm ($CDCl_3$):** 12.5 (CH_2CH_3), 43.9 (CH_2CH_3), 206.1 (*C*S_2). **MS:** *m/z* 354 [M^+], 116 [$SCNEt_2$]. **IR (ν_{max} cm^{-1}):** 1512 (s) [N=C], 991 (s) [C=S].

[Ni($S_2CN^iBu_2$)$_2$] (21)

^{i}Bu_2NH (3.49 mL, 20 mmol) was added to NaOH (0.80 g, 20 mmol) dissolved in 50 mL distilled H_2O. To this mixture CS_2 (1.20 mL, 20 mmol) was added dropwise over 10 minutes and the mixture stirred overnight. A solution of $NiCl_2{\cdot}6H_2O$ (2.38 g, 10 mmol) dissolved in 50 mL of water was added dropwise over 5 minutes, whereupon a green precipitate formed. This mixture was vigorously stirred for 2 hrs, filtered, washed with water (3 x 30 mL) and evaporated to dryness. The resulting green powder was dissolved in 100 mL of dichloromethane (DCM) and stirred with magnesium sulphate for 30 mins, after which the mixture was filtered and the filtrate dried *in vacuo*. Yield 3.9734 g, 85 %. **Anal. Calc. for $C_{18}H_{36}N_2S_4Ni$:** C, 46.25; H, 7.76; N, 5.99. Found: C, 46.23; H, 7.81; N, 6.03. **^{1}H NMR δ/ppm ($CDCl_3$):** 0.91 (d, *J* = 6.6 Hz, 24H, CH_3), 2.17 (m, *J* = 6.8 Hz, 4H, C*H*), 3.40 (d, *J* = 7.7 Hz, 8H, CH_2). **^{13}C{^{1}H} NMR δ/ppm ($CDCl_3$):** 20.1 (*C*H_3), 27.0 (*C*H), 56.3 (*C*H_2), 208.4 (*C*S_2). **MS:** *m/z* 467 [M^+], 171 [$S_2CN^iBu_2$]. **IR (ν_{max} cm^{-1}):** 1508 (s) [N=C], 981 (s) [C=S].

[Ni(S_2CNMeBu)$_2$] (22)

The complex was synthesised following the same method as with **21**, with the exception that MeBuNH (2.37 mL, 20 mmol) was used. Yield 1.6485 g, 43 %. **Anal. Calc. for $C_6H_{12}N_2S_4Ni$:** C, 37.60; H, 6.31; N, 7.31. Found: C, 37.51; H, 6.35; N, 7.30. **^{1}H NMR δ/ppm ($CDCl_3$):** 0.94 (t, *J* = 7.3 Hz, 6H, $CH_2(CH_2)_2CH_3$), 1.33 (m, 4H, $CH_2(CH_2)_2CH_3$), 1.61 (m, 4H, $CH_2(CH_2)_2CH_3$), 3.13 (2, 6H, NCH_3), 3.57 (m, 6H, $CH_2(CH_2)_2CH_3$). **^{13}C{^{1}H} NMR δ/ppm ($CDCl_3$):** 13.9 ($(CH_2)_3CH_3$), 19.9 (CH_2), 29.0 (CH_2), 36.5 (CH_3), 51.2 (CH_2), 207.0 (CS_2). **MS:** *m/z* 382 [M^+], 130 [S_2CNMeBu]. **IR (ν_{max} cm^{-1}):** 1512 (s) [N=C], 966 (s) [C=S].

[Ni(S_2C(4-MePip))$_2$] (23)

The complex was synthesised following the same method as with **21**, with the exception that 4-MePipH (2.37 mL, 20 mmol) was used. Yield 3.3399 g, 82 %. **Anal. Calc. for $C_{14}H_{24}N_2S_4Ni$:** C, 41.28; H, 5.94; N, 6.88. Found: C, 40.61; H, 5.94; N, 6.67. **^{1}H NMR δ/ppm ($CDCl_3$):** 0.97 (d, *J* = 6.3 Hz, 6H, CH_3), 1.21 (m, 4H, $CH_{2(meta, ax)}$), 1.73 (m, 2H, $CH_{(para, ax)}$), 1.73 (m, 4H, $CH_{2(meta, eq)}$), 2.92 (m, 4H, $CH_{2(ortho, ax)}$), 4.50 (m, 4H, $CH_{2(ortho, eq)}$). **^{13}C{^{1}H} NMR δ/ppm ($CDCl_3$):** 21.4 (CH_3), 31.0 ($CH_{(para)}$), 33.5 ($CH_{2(meta)}$), 47.0 ($CH_{2(ortho)}$), 204.9 (CS_2)**MS:** *m/z* 406 [M^+], 142 [S_2C(4-MePip)]. **IR (ν_{max} cm^{-1}):** 1500 (s) [N=C], 948 (s) [C=S].

4.7.2 Decomposition of Nickel(II) bis(dithiocarbamate) Precursors

The decomposition setup as described in Chapter 3, Section 3.2 was utilised. In a typical synthesis **21** (5 mM) was added to OA (20 mL) in a three-neck RBF attached to a condenser and evacuated and refilled with nitrogen repeatedly for 15 minutes. The solution was heated to 230 °C and held there for 1 hr. The mixture was allowed to cool to RT slowly, whereupon methanol (80 mL) was added with stirring. The mixture was centrifuged and then the solution decanted leaving behind the resultant nanoparticles. This procedure was repeated 3 times and finally the material was allowed to dry in air.

4.7.2.1 Varying R-group

Decompositions as above but using: 1) **19**; 2) **20;** 3) **21;** 4) **22**.

4.7.2.2 Varying Temperature

Decompositions as above but at decomposition temperatures: 1) 150 °C; 2) 180 °C; 3) 260 °C; 4) 280 °C.

4.7.2.3 Varying Concentration

Decompositions as above but using concentrations of **21** of: 1) 10 mM; 2) 20 mM; 3) 40 mM; 4) 50 mM.

4.7.3 Decomposition of Nickel(II) bis(dithiocarbamate) Precursor with Thiuram Disulfide Additive

4.7.3.1 Varying Temperature

Decompositions as above but decomposing **21** (5 mM) and **6** (10 mM) at 1) 150 °C; 2) 180 °C; 3) 230 °C; 4) 260 °C; 5) 280 °C

4.7.3.2 Varying Concentration

Decompositions as above but at 1800 °C and using **21** and **6** at respective concentrations of: 1) 5 and 10 mM; 2) 10 and 20 mM; 3) 20 and 40 mM; 4) 40 and 80 mM; 5) 50 mM and 0.1 M.

4.8 References

1 G. Kullerud and R. A. Yund, *J. Petrol.*, 1962, 3, 126.

2 H. K. Mulmudi, S. K. Batabyal, M. Rao, R. R. Prabhakar, N. Mathews, Y. M. Lam, and S. G. Mhaisalkar, *Phys. Chem. Chem. Phys.*, 2011, 13, 19307.

3 S. Han, K. Kim, H. Ahn, J. Ahn, and J. Lee, *J. Alloys Compd.*, 2003, 361, 247.

4 C. Wadia, A. P. Alivisatos, and D. M. Kammen, *Environ. Sci. Technol.*, 2009, 43, 2072.

5 W. Zhang, Y. Wang, Z. Wang, Z. Zhong, and R. Xu, *Chem. Commun.*, 2010, 46, 7631.

6 L. Zhang, B. Tian, F. Chen, and J. Zhang, *Int. J. Hydrogen Energy*, 2012, 37, 17060.

7 G. Shen, D. Chen, K. Tang, C. An, Q. Yang, and Y. Qian, *J. Solid State Chem.*, 2003, 173, 227.

8 B. Zhang, X. Ye, W. Dai, W. Hou, and Y. Xie, *Chem. Eur. J.*, 2006, 12, 2337.

9 H. Li, L. Chai, X. Wang, X. Wu, G. Xi, Y. Liu, and Y. Qian, *Cryst. Growth Des.*, 2007, 7, 1918.

10 Y. Wang, Q. Zhu, L. Tao, and X. Su, *J. Mater. Chem.*, 2011, 21, 9248.

11 T. Zhu, Z. Wang, S. Ding, J. S. Chen, and X. W. Lou, *RSC Adv.*, 2011, 1, 397.

12 S. Chen, K. Zeng, H. Li, and F. Li, *J. Solid State Chem.*, 2011, 184, 1989.

13 Z. Meng, Y. Peng, W. Yu, and Y. Qian, *Mater. Chem. Phys.*, 2002, 74, 230.

14 A. Ghezelbash and B. A. Korgel, *Langmuir*, 2005, 21, 9451.

15 W. Zhang, L. Xu, K. Tang, F. Li, and Y. Qian, *Eur. J. Inorg. Chem.*, 2005, 2005, 653.
16 S.-L. Yang, H.-B. Yao, M.-R. Gao, and S.-H. Yu, *CrystEngComm*, 2009, 11, 1383.
17 J. H. L. Beal, P. G. Etchegoin, and R. D. Tilley, *J. Phys. Chem. C*, 2010, 114, 3817.
18 M. G. Babashkina, D. A. Safin, and Y. Garcia, *Dalton. Trans.*, 2012, 41, 2234.
19 A. L. Abdelhady, M. A. Malik, P. O'Brien, and F. Tuna, *J. Phys. Chem. C*, 2012, 116, 2253.
20 L. Tian, L. Y. Yep, T. T. Ong, J. Yi, J. Ding, and J. J. Vittal, *Cryst. Growth Des.*, 2009, 9, 352.
21 K. Ramasamy, M. A. Malik, N. Revaprasadu, and P. O'Brien, *Chem. Mater.*, 2013, 25, 3551.
22 R. D. Tilley and D. A. Jefferson, *J. Phys. Chem. B*, 2002, 106, 10895.
23 Y. Hu, J. Chen, W. Chen, X. Lin, and X. Li, *Adv. Mater.*, 2003, 15, 726.
24 L. Barry, J. D. Holmes, D. J. Otway, M. P. Copley, O. Kazakova, and M. A. Morris, *J. Phys. Condens. Matter*, 2010, 22, 076001.
25 A. Ghezelbash, M. B. Sigman, and B. A. Korgel, *Nano Lett.*, 2004, 4, 537.
26 Z. Meng, Y. Peng, L. Xu, and Y. Qian, *Mater. Lett.*, 2002, 53, 165.
27 W. Wang, S.-Y. Wang, Y.-L. Gao, K.-Y. Wang, and M. Liu, *Mater. Sci. Eng. B*, 2006, 133, 167.
28 K. Aso, H. Kitaura, A. Hayashi, and M. Tatsumisago, *J. Mater. Chem.*, 2011, 21, 2987.
29 B. Geng, X. Liu, J. Ma, and Q. Du, *Mater. Sci. Eng. B*, 2007, 145, 17.
30 N. Pradhan, B. Katz, and S. Efrima, *J. Phys. Chem. B*, 2003, 107, 13843.
31 H. Cui, R. D. Pike, R. Kershaw, K. Dwight, and A. Wold, *J. Solid State Chem.*, 1992, 101, 115.
32 G. H. Singhal, R. I. Botto, L. D. Brown, and K. S. Colle, *J. Solid State Chem.*, 1994, 109, 166.
33 X. Chen, Z. Wang, X. Wang, J. Wan, J. Liu, and Y. Qian, *Chem. Lett.*, 2004, 33, 1294.
34 P. O'Brien, J. H. Park, and J. Waters, *Thin Solid Films*, 2003, 431, 502.
35 M. Delépine, *C. R. Hebd. Seances Acad. Sci.*, 1907, 144, 1125.
36 R. Dingle, *Inorg. Chem.*, 1971, 10, 1141.
37 F. A. Cotton and J. A. McCleverty, *Inorg. Chem.*, 1964, 3, 1398.
38 R. L. Carlin, J. S. Dubnoff, and W. T. Huntress, *Proceeding Chem. Soc.*, 1964, 228.
39 C. L. Raston and A. H. White, *Aust. J. Chem.*, 1976, 29, 523.
40 M. Castillo, J. J. Criado, B. Macias, and M. V. Vaquero, *Inorg. Chim. Acta*, 1986, 124, 127.
41 K. Oyaizu, K. Yamamoto, Y. Ishii, and E. Tsuchida, *Chem. Eur. J.*, 1999, 5, 3193.
42 L. Tosi and A. Garnier, *J. Chem. Soc., Dalton. Trans.*, 1978, 53.
43 G. Rajput, V. Singh, A. N. Gupta, M. K. Yadav, V. Kumar, S. K. Singh, A. Prasad, M. G. B. Drew, and N. Singh, *CrystEngComm*, 2013, 15, 4676.
44 V. Kettmann, J. Garaj, and Š. Kúdela, *Collect. Czech. Chem. Commun.*, 1978, 43, 1204.
45 J. Lokaj, F. Pavelčik, V. Kettmann, J. Masaryk, V. Vrábel, and J. Garaj, *Acta Crystallogr. Sect. B*, 1981, 37, 926.
46 J. Kamenfček, R. Pastorek, B. Cvek, and J. Taraba, *Z. Kristallogr. - New Cryst. Struct.*, 2003, 218, 205.
47 J. Krupčík, J. Garaj, Š. Holotík, D. Oktavec, and M. Košík, *J. Chromatogr. A*, 1975, 112, 189.
48 M. L. Riekkola and O. Mäkitie, *J. Therm. Anal. Calorim.*, 1982, 25, 89.
49 G. D'Ascenzo and W. W. Wendlandt, *J. Therm. Anal.*, 1969, 1, 423.
50 E. T. G. Cavalheiro, M. Ionashiro, G. Marino, S. T. Breviglieri, and G. O. Chierice, *Transit. Met. Chem.*, 2000, 25, 69.
51 A. K. Sharma, *Thermochim. Acta*, 1986, 104, 339.

5 Other Metal and Mixed-Metal Sulfides

5.1 Introduction

Following the success in synthesising iron and nickel sulfide nanoparticles *via* the solvothermal decomposition of metal dithiocarbamate complexes (Chapters 3 and 4), other transition and main-group metal sulfides were investigated. In particular cobalt sulfide, a well-known hydrodesulphurisation catalyst,[1, 2] is of interest. Copper sulfide, zinc sulfide and indium sulfide, all semiconducting materials with potential applications as cathode materials for lithium-ion batteries, nonlinear optical materials, photocatalyst for dye degradation, water splitting catalysts and photocatalytic materials for solarcells,[3–5] were also studied. It has been shown by others that mixed-metal sulfide materials exhibit altered semiconducting properties, making them excellent photo-absorbers for solar cells and photocatalysts for hydrogen production.[4, 6–8] In addition, doping transition metal ions into the iron sulfide material greigite (Fe_3S_4), particularly nickel, is thought to improve both its catalytic activity regarding reduction of CO_2, and solid state stability. Hence a study into ternary metal sulfides based on iron was also performed.[9–15]

Nanoparticulate materials of these metal sulfides (Co, Cu, Zn, In) have been synthesised previously using a number of different binary and single-source precursors and methods. For example, chemical vapour deposition (CVD),[8, 16–20] microwave-assisted synthesis,[21, 22] hydrothermal and solvothermal decomposition,[23–27] and autoclave decomposition, have all been employed.[28–30] For the purposes of brevity, the literature discussed here will be limited to information regarding metal sulfide synthesis *via* solvothermal decomposition of metal dithiocarbamate complexes (as performed in the work reported in this chapter), unless little or no literature exists on the synthesis of a material by decomposition of dithiocarbamate complexes.

In Chapters 3 and 4, iron and nickel metal sulfide nanoparticles were successfully synthesised in a variety of phases, sizes and morphologies *via* the solvothermal decomposition of metal dithiocarbamate complexes as precursors. Similar precursors were synthesised for this work, in order to investigate their applicability as precursors for other metal sulfide nanoparticles, and in particular ternary metal sulfide phases.

5.1.1 Cobalt Sulfides

Cobalt sulfide possesses many naturally and non-naturally occurring phases akin to the diversity of the nickel sulfide system, including Co_4S_3, Co_9S_8 (cobalt pentlandite, pentlandite structure), CoS, $Co_{1-x}S$, Co_3S_4 (linnaeite, with thiospinel structure), Co_2S_3 and CoS_2 (catteirite, with pyrite structure).[31, 20, 32] Very little literature exists on the formation of cobalt sulfide nanomaterials *via* the decomposition of cobalt dithiocarbamate complexes, though, O'Brien *et al.* reported the synthesis of thin films of several phases by metal-organic chemical vapour deposition (MOCVD); films comprised of a mixture of $Co_{1-x}S$ and CoS_2 were deposited from $[Co(S_2CNMe^nHex)_3]$ at 425 °C, while at the higher temperature of 450 °C pure Co_3S_4 was accessed.[20]

O'Brien has also reported the synthesis of cobalt sulfide nanomaterials from several other single-source precursors (SSPs), including $[Co(S_2P^iBu_2)_3]$ and several thio- and dithiobiurets .[33, 19, 34, 35] The precursor $[Co(S_2P^iBu_2)_3]$ was solvothermally decomposed *via* both the 'heat-up' and 'hot-injection' methods in several solvents including hexadecylamine (HDA), tri-*n*-octylphosphine (TOP) and tri-*n*-octylphosphine oxide (TOPO) at 300 °C, yielding Co_9S_8 nanoparticles.[33] Cobalt thio- and dithiobiuret complexes $[Co\{N(SCNR_2)_2\}_3]$ (R = Me, Et) and $[Co\{N(SOCN^iPr_2)_2\}_2]$ were also used as precursors for the solvothermal synthesis and aerosol assisted chemical vapour deposition (AACVD) of $Co_{1-x}S$ and Co_4S_3 nanoparticles and thin films, respectively.[35, 34, 19]

5.1.2 Copper Sulfides

Like cobalt, copper possesses many known sulfide phases, with at least 14 have been reported including; Cu_2S (chalcocite), Cu_9S_5 (or $Cu_{1.8}S$, digenite), Cu_7S_4 (or $Cu_{1.75}S$, anilite), CuS (covelite) and CuS_2 (villamaninite, pyrite structure).[36, 37] There have been various reports in the literature regarding the synthesis of copper sulfide nanomaterials prepared *via* hydrothermal and solvothermal decomposition of binary and single-source precursors,[38, 24, 39] using autoclaves,[4, 38] and even solventless synthesis.[40, 36] Copper dithiocarbamate complexes have been employed as SSPs for the synthesis of copper sulfide materials by several groups, including O'Brien *et al.* who deposited thin films of $Cu_{1.8}S$, CuS and $Cu_{1.96}S$ *via* MOCVD and AACVD from $[Cu(S_2CNMe^nHex)_2]$.[17] They then went on to use the same SSP to synthesise Cu_2S nanoparticles using the 'hot-injection' solvothermal method in TOP/TOPO at 200 °C.[41]

Other groups have employed copper dithiocarbamate SSPs to synthesise copper sulfide nanoparticles including Burda *et al.*, who formed $Cu_{1.8}S$ by decomposing $[Cu(S_2CNEt_2)_2]$ using the 'hot-injection' method with TOP/TOPO, at 250 °C.[42] In order to obtain pure $Cu_{1.8}S$, tri-*n*-octylphosphine sulfide (TOPS) was added to the decomposition solution, which may have acted as a sulfur source.[42] Another group to report the decomposition of a copper dithiocarbamate complex to synthesise copper sulfide nanomaterials was Qian *et al.* who in 2005, formed the $Cu^{(I)}$ complex $[Cu(S_2CNEt_2)]$ from the *in situ* addition of $CuCl_2$ and NaS_2CNEt_2 in dodecanethiol (DDT)/oleylamine (OA), before heating the solution at 160 °C for 12 hrs.[43] This produced nanowires of approximately 2.5 nm by 50 μm and of Cu_2S phase.[43] This morphology is not uncommon, nanorods and nanowires having previously been reported.[24, 40]

5.1.3 Zinc Sulfides

Sphalerite (zinc blende) and wurtzite, the low temperature cubic and high temperature hexagonal polymorphs of ZnS respectively, are the most common phases of zinc sulfide.[32, 44] There have been numerous reports on the synthesis of both phases by the solvothermal decomposition of zinc dithiocarbamate complexes.[45, 22, 46, 47, 27, 48] In a recent contribution by O'Brien *et al.*, $ZnS_{(S)}$ (sphalerite) nanoparticles of *ca.* 5 nm diameter (± 0.6 nm) were prepared *via* the 'hot-injection' method in TOP/TOPO and TOP/hexadecylamine (HDA). Complexes with heterocyclic dithiocarbamates derived from piperidine and ditetrahydro-quinoline were used as SSPs.[47] In another synthesis of $ZnS_{(S)}$ nanoparticles by the same authors, a series of *N*-alkyl dithiocarbamate zinc (II) complexes were decomposed, also using the 'hot-injection' technique, in TOP/HDA.[45] The $ZnS_{(S)}$ nanoparticles produced were, again, approximately 5 nm in diameter and close to monodisperse.[45]

Nanoparticles of the high temperature polymorph, $ZnS_{(W)}$ (wurtzite), have been accessed *via* the 'heat-up' method by several groups. In general this method appears to produce nanowires and nanorods,[46, 27, 48] though Shen *et al.* prepared $ZnS_{(W)}$ nanoparticles of approximately 5nm diameter by decomposing $[Zn(S_2CNEt_2)_2]$ in ethylene glycol (EG) in a microwave reactor for 5 minutes at 110 °C.[22] The same precursor has been used to synthesise nanowires (approximately 4 by 300 nm) by solvothermal decomposition in OA at 300 °C.[46] Nanowires of $ZnS_{(W)}$ with an even higher aspect ratio (2 nm by 10 μm) have been synthesised by Xu *et al.*, using $[Zn\{S_2CN^nBu_2\}_2]$ in dodecylamine at 280 °C.[48] By altering the solvent to a 1:1 mixture of OA and oleic acid (OLA), $ZnS_{(W)}$ nanoparticles with

an average diameter of 9.5 nm, were produced, showing how solvent interactions can play a role in the formation of high aspect ratio morphologies.[48]

5.1.4 Indium Sulfide

There are no naturally occurring phases of pure indium sulfide, but some phases have been synthesised including InS, α-, β- and γ-In_2S_3 and In_6S_7.[49, 50] There have been several reports on the synthesis of indium sulfide thin films from indium dithiocarbamate SSPs.[18, 5, 51, 52] O'Brien and co-workers used $[In(S_2CNR_2)_3]$ (R = ^{n}Bu, ^{n}Hex) to deposit β-In_2S_3 thin films *via* MOCVD. In similar work by Mazhur *et al.*, other dialkyl and heterocyclic indium(III) tri(dithiocarbamate) complexes were decomposed and deposited *via* AACVD as thin films of β-In_2S_3.[5] Other indium sulfide phases were accessed by O'Brien using a slightly different type of precursor, namely $[R_2In(S_2CNEt_2)]$ (R = Me, Et, neopentyl). Thin films of InS, β-In_2S_3 and In_6S_7 were deposited by MOCVD by varying reaction temperature (325 – 425 °C).[51]

There are few reports on the synthesis of nanoparticulate indium sulfide from indium dithiocarbamate SSPs. O'Brien and co-workers have synthesised films of β-In_2S_3 nanorods from $[Et_2In(S_2CNMe^nBu)]$ *via* AACVD,[52] and InS nanoparticles (of indeterminate phase) using the 'hot-injection' method.[53] When $[In(S_2CNEt_2)_3]$ was decomposed in TOP/TOPO at 250 °C for 30 mins, the material co-precipitated with TOPO, making XRD analysis of the indium sulfide phase challenging, and in addition the particles degraded under the TEM beam.[53] Other single source precursors (SSPs) have been studied for the synthesis of indium sulfide nanomaterials, including thiobiuret and thiolate indium complexes, generally yielding β-In_2S_3.[50, 54]

5.1.5 Iron-Nickel Sulfides

Ternary iron-nickel sulfide materials can take a number of phases, most commonly $(Fe,Ni)_9S_8$ (pentlandite, pentlandite structure) and $FeNi_2S_3$ (violarite, inverse thiospinel structure), though a pyrite type structure $(Fe,Ni)S_2$ (bravoite) has also been reported.[55–59] There are very few examples in the literature of the synthesis of nanoparticulate materials of these phases. In 2004 Bezverkhyy *et al.* synthesised pentlandite nanoparticles *via* a multistep process involving the pyrolysis in H_2S/N_2 of a precursor synthesised from $Fe(SO_4)\cdot 7H_2O$ and $Ni(SO_4)\cdot 7H_2O$.[2] In a report by Travnicek in 2011, a residue of $Fe_5Ni_4S_8$ was left when the complex $[Ni(S_2CNBz^iPr)_3][FeCl_4]$ was decomposed in an argon

atmosphere on a TGA stage up to 800 °C.[60] There are no reports of either violarite or bravoite being synthesised in the nanoparticle regime.

5.1.6 Iron-Indium Sulfides

The most common iron-indium mixed-metal sulfide phase is $FeIn_2S_4$ (indite), which, like $FeNi_2S_4$, possess the inverse thiospinel structure.[37, 61] There have been few reported syntheses of nanoparticulate $FeIn_2S_4$, and none using solvothermal methods. The first report on the synthesis of nanoparticulate indite was in 1999 by Tang *et al.*, who decomposed elemental indium and sulfur with $FeCl_3$ in benzene in an autoclave and produced nanoparticles of approximately 5 nm diameter.[61] Another autoclave synthesis was reported by Chen and co-workers in 2005, who decomposed $FeCl_3$, $InCl_3$ and thiourea in water to produce $FeIn_2S_4$ microspheres of approximately 5 μm in diameter.[62] Recently Wu *et al.* also synthesised $FeIn_2S_4$ microspheres of similar size and morphology using an indium dithiocarbamate precursor.[63] Precursors $FeCl_3$ and $[In(S_2CNC_8H_{17})_3]$ were pyrolyzed in a silicon tube oven in an argon atmosphere.[63]

5.1.7 Iron-Zinc Sulfides

There are several known phases of the ternary sulfide of iron and zinc: (Zn,Fe)S wurtzite ($\{ZnFe\}S_{(W)}$, an iron doped wurtzite), (Zn,Fe)S marmatite ($\{ZnFe\}S_{(S)}$, an iron rich sphalerite) and $ZnFe_2S_4$, a thiospinel.[37, 64, 65] As with the indium-iron sulfides, there are very few reports on the nanoparticulate synthesis of iron-zinc sulfide materials, and none involving a metal dithiocarbamate precursor. Feng and co-workers reported the synthesis of $(Zn,Fe)S_{(W)}$ thin films from $Fe(CO)_5$, Me_2Zn and H_2S by MOCVD at 350 °C.[66] The same material was synthesised in nanoparticulate form by Garje *et al.* by the solvothermal decomposition of $[Zn(Aftscz)_2]$ and $[Zn(AftsczH)_2Cl_2]$ (AftsczH = monoacetylferrocene thiosemicarbazole, see Figure 5-1) in ethylene glycol at 198 °C for 6 hrs.[67] Nanoparticles of $(Zn,Fe)S_{(S)}$ have also been synthesised, Chen *et al.* prepared $Zn_{0.9}Fe_{0.1}S$ by annealing iron-zinc sulfide nanoparticles produced from a microemulsion of $Fe(CO)_5$, $Zn(O_2CCH_3)_2$ and $CH_3(CH_2)_{11}OSO_3Na$ (sodium dodecyl sulphate) in water with thioacetamide.[68]

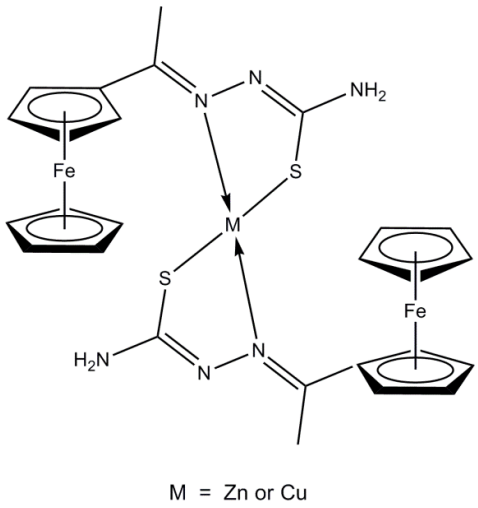

Figure 5-1 - Proposed structures for [Zn(Aftscz)2] and [Cu(Aftscz)2].[67, 69]

5.1.8 Iron-Copper Sulfides

Copper-iron sulfide has many known phases including Cu_5FeS_4 (bornite), $CuFeS_2$ (chalcopyrite) and $CuFe_2S_3$ (cubanite),[31, 37] and there are many literature reports of its synthesis, though only a few involving the decomposition of dithiocarbamate complexes. Methods to synthesise nanoparticulate copper-iron sulfides include; solvothermal and microwave-assisted decomposition of metal salts with sulfur sources, colloidal synthesis and laser ablation of bulk $CuFeS_2$.[70–74, 21] In a similar synthesis to that of (Zn,Fe)S wurtzite, Garje *et al.* solvothermally decomposed bimetallic SSPs [Cu(AftsczH)Cl_2] and [Cu(Aftscz)$_2$] (Figure 5-1) in ethylene glycol under reflux to produce $CuFeS_2$ nanoparticles.[69] There are two reports of dithiocarbamate complexes being used in the synthesis of copper-iron sulfide nanoparticles. In 2010, Gupta *et al.* used the 'hot-injection' method to synthesise $CuFeS_2$ nanoparticles of approximately 12 nm diameter by injecting a solution of [Cu(S_2CNEt_2)$_2$] and [Fe(S_2CNEt_2)$_3$] in OLA/dichlorobenzene into a solution of sulfur in OLA/TOP at 180 °C.[75] In 2012, Feng and co-workers synthesised $CuFeS_2$ nanoparticles of even smaller diameter, approximately 6 nm, also using the 'hot-injection' technique.[76] A solution of NaS_2CNEt_2 in DDT was injected into a hot (140 °C) solution of $FeCl_3$ and $CuCl_2$ - OLA/DDT.[76]

5.1.9 Nickel-Cobalt Sulfides

Although the focus of the work with ternary chalcogenides in this chapter is on mixed iron sulfides, many other combinations of mixed-metal sulfide materials are possible.[31, 37] The mixed nickel and cobalt sulfide material has several possible phases including $NiCo_8S_8$

(pentlandite structure), $NiCo_2S_4$ and $CoNi_2Co_4$ (both thiospinel structure).[2, 77, 37] Nanoparticles of $NiCo_8S_8$ were synthesised by Bezverkhyy *et al.* in a two-step process similar to that for $(FeNi)_9S_8$. Firstly, $Co(NO_3)_2$ and $Ni(NO_3)_2$ were reacted with Na_2S in water, then the dried precipitate was reacted with H_2S/H_2 for 3 hrs at 300 °C.[2] Urchin-like nanostructures of $NiCo_2S_4$ were synthesised by Jiang and co-workers in a two-step process involving the hydrothermal decomposition of $NiCl_2$ and $CoCl_2$ with urea in an autoclave at 140 °C, followed by a further reaction with Na_2S at 160 °C.[30] Nanoparticles of $CoNi_2S_4$ were formed by Pang *et al.*, *via* the decomposition of $[Co(O_2CMe)_2]$ and $[Ni(O_2CMe)_2]$ with sulfur powder dissolved in OA/anisole in an autoclave for 24 hrs.[77]

5.2 Results and Discussion

5.2.1 Metal Dithiocarbamate Precursors

5.2.1.1 Synthesis

The metal dithiocarbamate complexes were synthesised following literature methods according to Equation 5-1.[78] All syntheses were carried out in water, except in the case of copper, for which it was found that synthesis in methanol gave a higher yield. $[Co(S_2CN^iBu_2)_3]$ (**24**) was obtained as an emerald green crystalline powder, $[Cu(S_2CN^iBu_2)_2]$ (**25**) as a black powder, and $[Zn(S_2CN^iBu_2)_2]$ (**26**) and $[In(S_2CN^iBu_2)_3]$ (**27**) as white powders. All complexes were analysed by IR, MS, EA and, where possible, NMR spectroscopy (copper complex being paramagnetic).

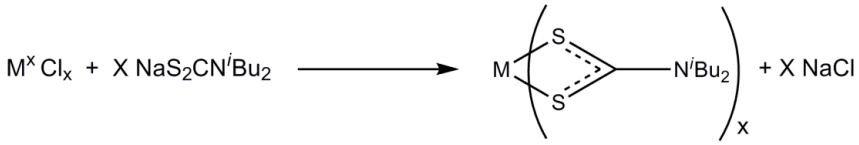

M = Co, X = 3 (**24**)
M = Cu, X = 2 (**25**)
M = Zn, X = 2 (**26**)
M = In, X = 3 (**27**)

Equation 5-1

5.2.1.2 Stability

As with the iron and nickel dithiocarbamate precursors, complexes **24** – **27** were analysed by TGA in order to probe their relative stabilities (Figure 5-2). The TGA graphs show that all lose mass sharply in one step between approximately 250 and 300 °C. The zinc complex

(**26**) vaporises at the lowest temperature (245 °C), followed by the copper complex (**25**) at 255 °C, then the cobalt complex (**24**) at 280 °C, with the indium complex (**27**) having the highest thermal stability, only vaporising at 305 °C. For comparison [Fe($S_2CN^iBu_2$)$_3$] (**3**) decomposes at 233 °C, while [Ni($S_2CN^iBu_2$)$_2$] (**21**) decomposes at 270 °C.

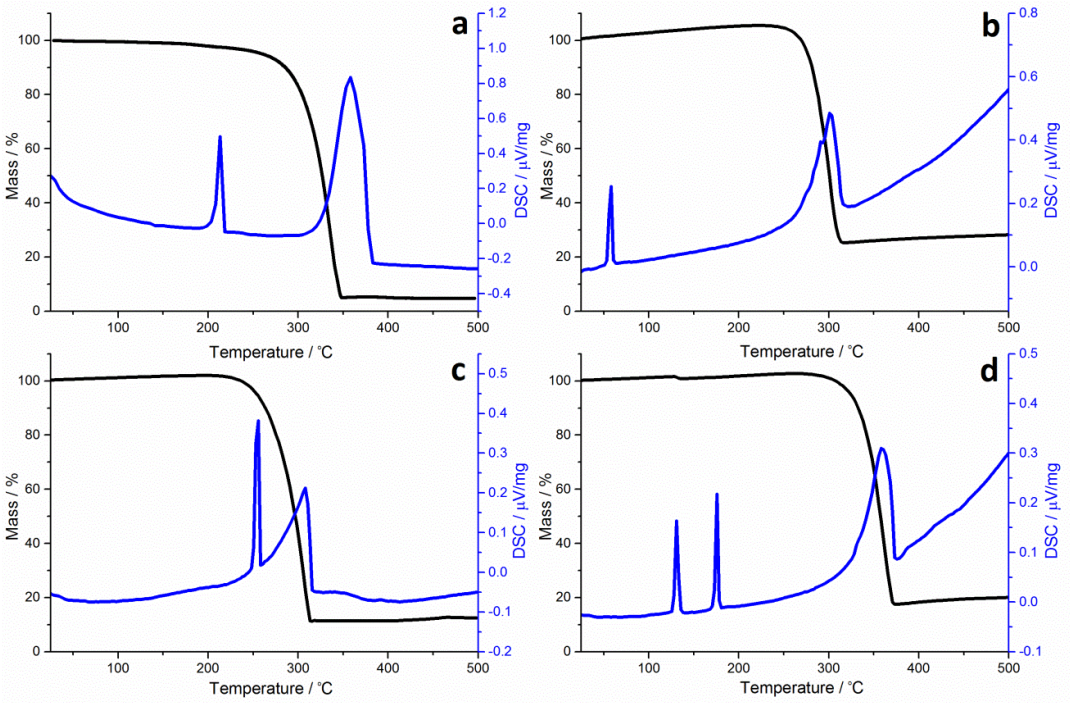

Figure 5-2 - TGA (black) and DSC (blue) graphs for complexes a) 24, b) 25, c) 26 and d) 27.

The residual masses left at the end of the experiments indicates both the cobalt (**24**) and the zinc (**26**) complexes melt then evaporate with little decomposition, with a mass equal to less than elemental metal left in both cases. The copper complex (**25**) leaves behind a mass approximately equal to CuS_2 and the residual mass of the indium complex (**27**) is equal to InS, indicating decomposition for these complexes. Several of the DSC graphs show sharp peaks prior to decomposition which can be accounted for by the presence of residual methanol in sample **25** and water in sample **27**. Melting points are observed for **24** (215 °C) and **27** (175 °C). This information, combined with the DSC data, suggests that **24** melts then evaporates, while **27** melts then decomposes. Complex **25** appears to decompose in one step, while **26** sublimes.

5.2.2 Binary Metal Sulfide Synthesis

Metal dithiocarbamate complexes **24** – **27** were decomposed according to the setup described in Section 3.2 using the solvothermal 'heat-up' method, at 230 °C with a SSP

concentration of 5 mM in OA. Upon cooling the particles were worked up by washing with methanol and centrifuging to give dry black powders. The addition of tetraisobutylthiuram disulfide (**6**) to decompositions with iron and nickel dithiocarbamate complexes enabled metastable phases to be accessed. The decompositions of **24** - **27** were repeated with **6**, to see if this additive had any effect on the phase or morphology of the resulting nanoparticles of the cobalt, copper, zinc and indium sulfides.

5.2.2.1 Cobalt Sulfide

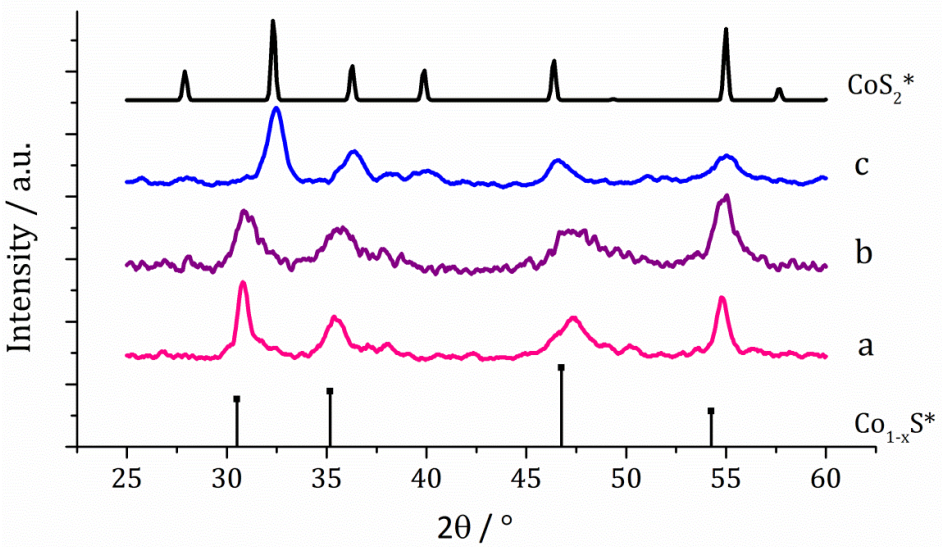

Figure 5-3 - XRD patterns for samples prepared from (a) 24, (b) 24 with 2 eq. 6 and (c) 24 with 10 eq. 6, with reference patterns for bulk $Co_{1-x}S$ (ICDD card No. 42-0826) and CoS_2 (ICDD card No. 41-1471).

Black powders were obtained from the decomposition of $[Co(S_2CN^iBu_2)_3]$ (**24**) both with and without 2 eq. $(S_2CN^iBu_2)_2$ (**6**). In both cases XRD analysis reveals that $Co_{1-x}S$ (ICDD card No. 42-0826) is formed, though the patterns are quite broad suggesting small particulate size, and there are some additional peaks that could not be assigned indicating the samples are not phase pure (Figure 5-3). This is similar to the work of O'Brien *et al.*, who deposited $Co_{1-x}S$ thin films using cobalt thiobiuret single-source precursors.[19] The sample produced in the presence of **6** shows a slight shifting of peaks to the right, possibly indicating the presence of some CoS_2. To investigate this further, **24** was decomposed with 10 eq. of **6** and XRD analysis shows the crystalline phase corresponds to CoS_2 (ICDD card No. 41-1471, see Figure 5-3).

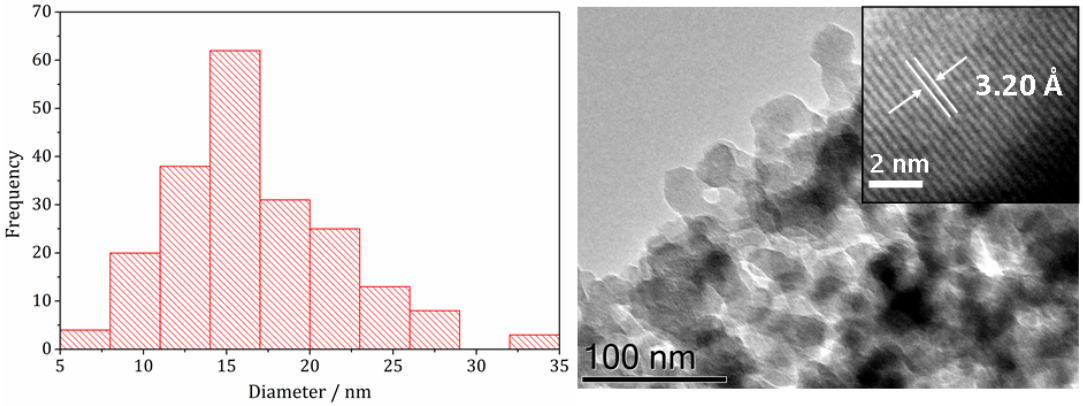

Figure 5-4 - Particle size histogram (left) and TEM image with HRTEM insert (right) of the sample prepared from 24 with 10 eq. 6.

TEM analysis of the nanoparticles produced in all three experiments shows their size and morphology is little affected by the change in phase, appearing to be roughly spherical in all cases (Figure 5-4). The average particle sizes are 15 nm (SD 6 nm), for the sample prepared in the absence of thiuram disulfide, 17 nm (SD 5 nm) for the sample prepared with 2 eq. of **6,** and 17 nm (SD 6 nm) for the sample prepared with 10 eq. of **6**. An HRTEM image of the latter is shown in Figure 5-4, where *d*-spacings of 3.20 Å, consistent with the [111] lattice plane of CoS_2 (3.20 Å, ICDD card No. 41-1471), can be seen.

5.2.2.2 Copper sulfide

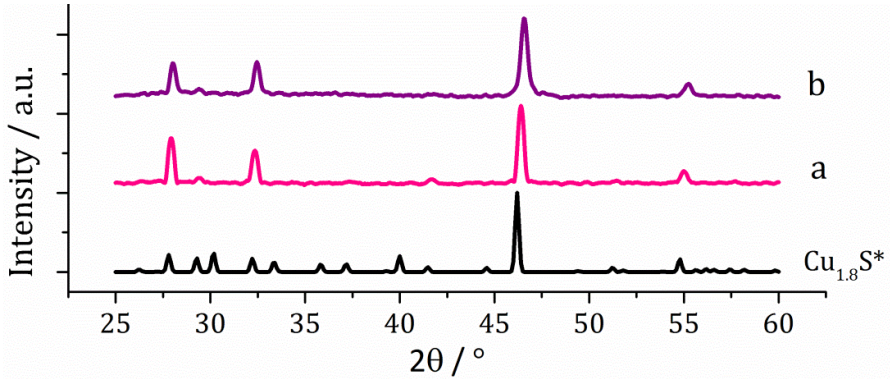

Figure 5-5 - XRD patterns for samples prepared from (a) 25 and (b) 25 with 6, with reference pattern for bulk $Cu_{1.8}S$ (ICDD card No. 47-1748).

The powder samples prepared from the decomposition of $[Cu(S_2CN^iBu_2)_2]$ (**25**) both with and without the thiuram disulfide additive **6** were brown in appearance, and XRD analysis revealed that the crystalline phase produced corresponded to $Cu_{1.8}S$ (digenite) in both cases. When O'Brien and co-workers decomposed $[Cu(S_2CNMe^nHex)_2]$, nanoparticles of Cu_2S were produced.[41] O'Brien used the 'hot-injection' method in TOP/TOPO at 200 °C in

his work, which, along with the differing precursor, may explain the difference in the material formed. Burda *et al.* formed $Cu_{1.8}S$ by decomposing $[Cu(S_2CNEt_2)_2]$ using the 'hot-injection' method with TOP/TOPO at 250 °C, but TOPS was added in order to obtain $Cu_{1.8}S$ without copper metal impurities.[42] Unfortunately, the authors do not report any images of their particles, so comparison is not possible.

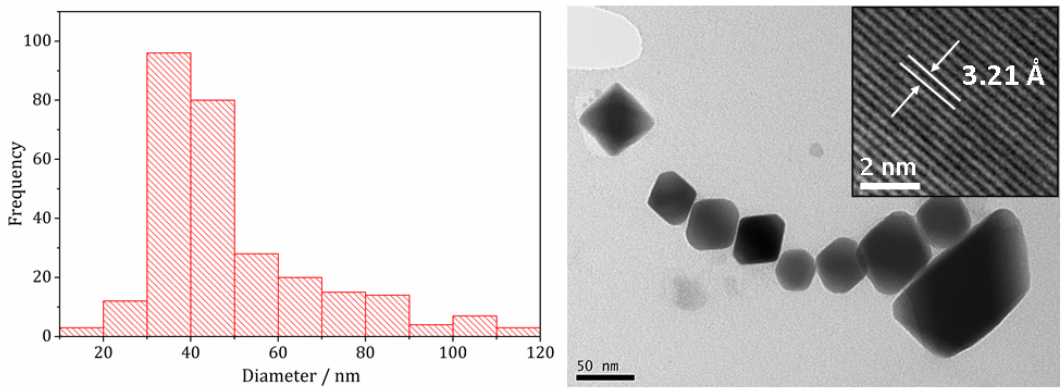

Figure 5-6 - Particle size histogram (left) and TEM image with HRTEM insert (right) of the sample prepared from 25.

The addition of 2 eq. of thiuram disulfide (**6**) does not appear to have had any significant effect on the phase, size or morphology of the copper sulfide nanoparticulate material produced. TEM analysis of the samples revealed the particles to be well-faceted being approximately hexagonal (Figure 5-6). The sample prepared in the absence of thiuram disulfide has an average particle size of 50 nm (SD 21 nm), while the sample prepared with 2 eq. of **6** has an average size of 48 nm, but much higher polydispersity of size (SD 56 nm). A HRTEM image of the former sample is shown in Figure 5-6, which shows *d*-spacings of 3.21 Å, consistent with the [0 0 15] lattice plane of $Cu_{1.8}S$ (3.21 Å, ICDD card No. 47-1748).

5.2.2.3 Zinc Sulfide

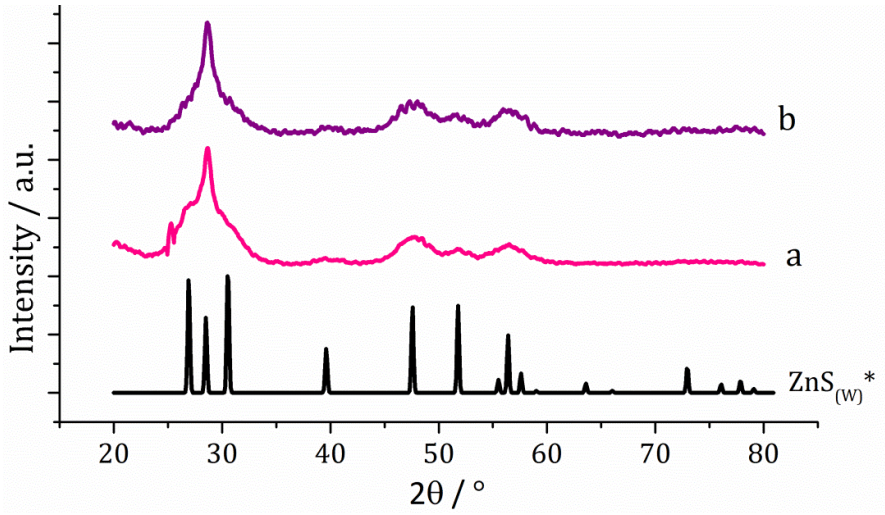

Figure 5-7 - XRD patterns for samples prepared from (a) 26 and (b) 26 with 6, with reference pattern for bulk $ZnS_{(W)}$(2H) (ICDD card No. 36-1450).

The powder samples prepared from the decomposition of $[Zn(S_2CN^tBu_2)_2]$ (**26**) with and without **6** were both off-white in appearance. XRD analysis revealed that the crystalline phase produced corresponded to $ZnS_{(W)}$ (wurtzite) in both cases (Figure 5-7). Interestingly the peak at 28.5 ° 2θ for the [002] lattice plane is more intense than in the reference pattern for bulk $ZnS_{(W)}$ (ICDD card No. 36-1450). This suggests preferential growth along the *c* axis. This feature of the XRD patterns obtained from **26** decomposed with and without **6** is mirrored in the XRD patterns reported by other groups, who synthesised $ZnS_{(W)}$ nanowires by decomposing zinc dithiocarbamate single-source precursors using the heat-up method.

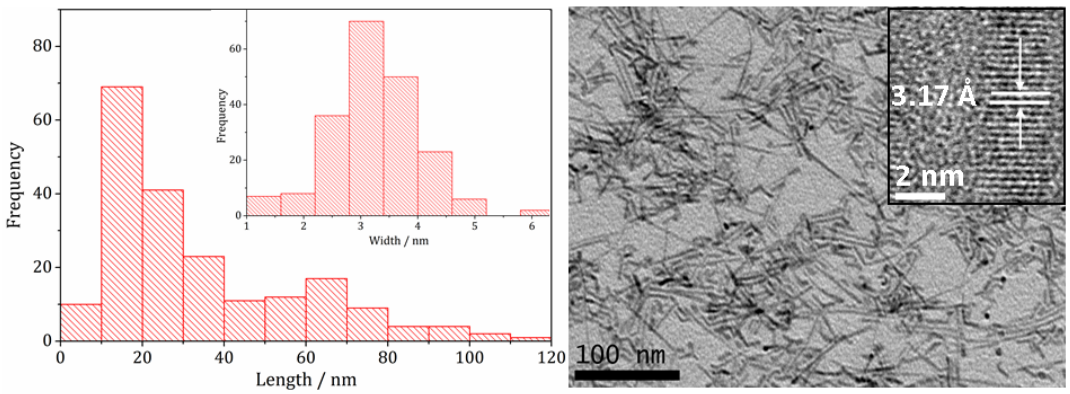

Figure 5-8 - Particle length histogram with width histogram insert (left) and TEM image with HRTEM insert (right), of the sample prepared from 26.

TEM showed high aspect ratio nanowires (Figure 5-8). HRTEM of the particles shows d-spacings of 3.17 Å, corresponding to the [002] lattice plane in $ZnS_{(W)}$ (ICDD card No. 36-1450), consistent with the XRD data. The sample prepared in the absence of thiuram disulfide had an average particle length of 34 nm (SD 26 nm) and width of 3.3 nm (SD 0.8 nm). The sample prepared with 2 eq. of **6** was very similar, having an average length of 45 nm (SD 25 nm) and width of 3.2 nm (SD 0.8 nm).

5.2.2.4 Indium Sulfide

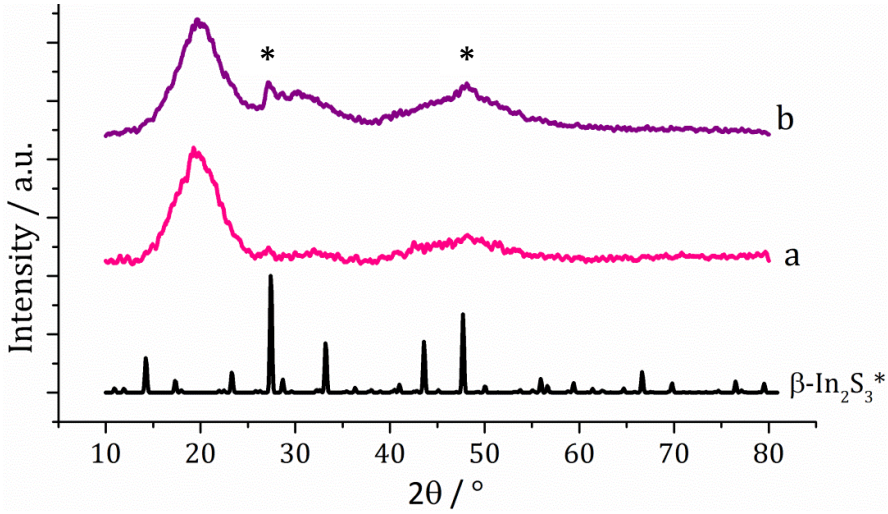

Figure 5-9 - XRD patterns for samples prepared from (a) 27 and (b) 27 with 6, with reference pattern for bulk β-In_2S_3 (ICDD card No. 25-0390). * Indicates with peaks for β-In_2S_3.

Bright yellow powders were obtained from the decomposition of $[In(S_2CN^iBu_2)_3]$ (**27**), both with and without 2 eq. of **6**. XRD analysis shows very broad peaks, not easily assignable to any reference spectrum, but very similar to the XRD pattern reported by O'Brien *et al.* of the indium sulfide material obtained from the decomposition of $[In(S_2CNEt_2)_3]$ in TOP/TOPO *via* the 'hot-injection' method.[53] The authors ascribed the large, low angle peak between 10 and 20 ° 2θ as evidence for amorphous material along with the coprecipitation of TOPO.[53] During the work-up of samples obtained from **27** it was noted that there was a strong sulphurous smell present. The large low angle peak seen in the XRD patterns may also be due to this sulfur impurity. The sample prepared from the decomposition of **27** and **6** shows some better defined peaks emerging from the broad humps around 30 and 50 ° 2θ for In_2S_3 (indicated with * symbol). This suggests that the presence of **6** promotes the formation of crystalline material, possibly by acting as an additional sulfur source.

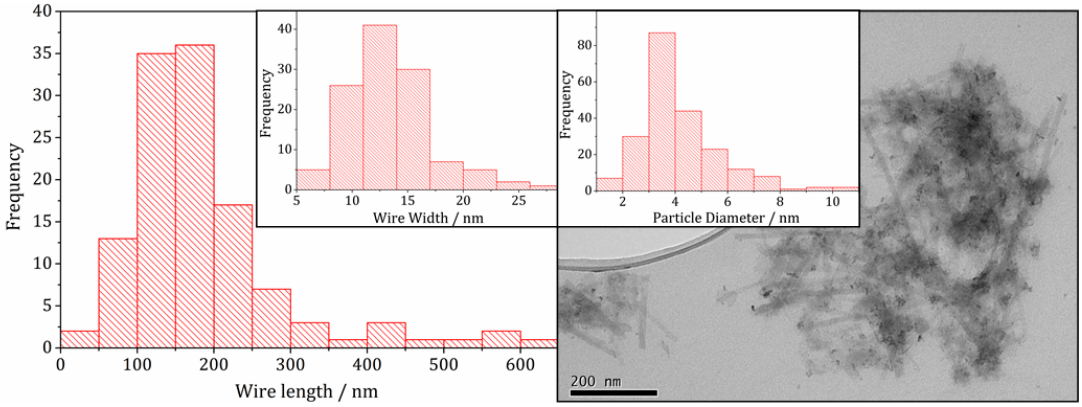

Figure 5-10 - Wire length histogram with wire width histogram insert (left) and TEM image with particle diameter histogram insert (right), of the sample prepared from 27.

The samples were analysed by TEM and found to be very similar in appearance (see Figure 5-10 for an image of **27** decomposed without **6** as an example). Both samples possessed two kinds of morphology: long wires and very small particles. In the case of the sample prepared from the decomposition of **27** in the absence of **6**, the long wires were found to have an average length of 186 nm (SD 106 nm) and width of 13.8 nm (SD 4.7 nm), while the particles were extremely small with an average diameter of 4.26 nm (SD 1.7 nm). The small particle size may account (in part) for the extreme broadening of the XRD peaks. Unfortunately, HRTEM analysis was not possible as the samples degraded in the electron beam, similarly to the material produced by O'Brien.[53]

To summarise, in this Section we have shown that using the metal diisobutyl-dithiocarbamate complex as a single source precursor we are able to synthesise pure, crystalline nanoparticulate metal sulfide material in the case of cobalt ($Co_{1-x}S$), copper ($Cu_{1.8}S$) and zinc ($ZnS_{(W)}$). The addition of the thiuram disulfide additive **6** has enabled access to a further cobalt sulfide phase (CoS_2).

5.2.3 Ternary Metal Sulfide Synthesis

Following the success in synthesising binary metal sulfide nanomaterials from metal dithiocarbamates other than iron and nickel, the precursors were then investigated for their ability towards the synthesis of ternary metal sulfide nanoparticles. In particular the FeMS (M = metal) system was investigated, beginning with the mixed iron-nickel sulfide system. Doping with nickel has been reported to stabilise the Fe_3S_4 structure, which could improve the material's catalytic activity towards CO_2 reduction.[15] This system has therefore been studied in detail, in a similar way to the work in the previous Chapters on iron and nickel sulfides. The other ternary metal sulfide systems have not been studied in

as much detail, the aim was to simply prove that the precursors were suitable for ternary sulfide synthesis. In addition, the effect of using the thiuram disulfide additive (**6**) on the systems was also investigated.

5.2.3.1 Iron-Nickel Sulfide

Decompositions Varying Temperature

Complex [$Fe(S_2CN^iBu_2)_3$] (**3**, 2.5 mM) was decomposed with [$Ni(S_2CN^iBu_2)_2$] (**21**, 2.5 mM) in OA according to the method described in Section 3.2 of Chapter 3. The reaction was performed at different decomposition temperatures: 150, 180, 230, 260 and 280 °C. Temperature dependent colour changes were observed, similar to those reported for the decomposition of **3** alone (as described in Section 3.4.1). Precursors **3** and **21** formed a dark brown solution in OA, which suddenly become clear and pale yellow in colour at 85 °C, then at 90 °C quickly turned black. These temperatures are 10 °C higher than those observed for the iron-only decomposition. After 1 hr the nanoparticles were isolated as black powders. XRD analysis reveals a relationship between decomposition temperature and the crystalline metal sulfide phase (Figure 5-11). At low temperature (150 °C) mostly amorphous material is formed, at 180 °C peaks for $FeNi_2S_4$ begin to emerge, then at 230 °C a mixture of $FeNi_2S_4$, Fe_7S_8 and α-NiS exists. Increasing the temperature further to 260 °C sees the emergence of peaks for $(Fe,Ni)_9S_8$ in this mixture, and at 280 ° the crystalline phase of the sample appears to be comprised of pure $(Fe,Ni)_9S_8$. This indicates $FeNi_2S_4$ (violarite) is a metastable phase in this system, while $(Fe,Ni)_9S_8$ (pentlandite) is a more thermodynamically favourable phase.

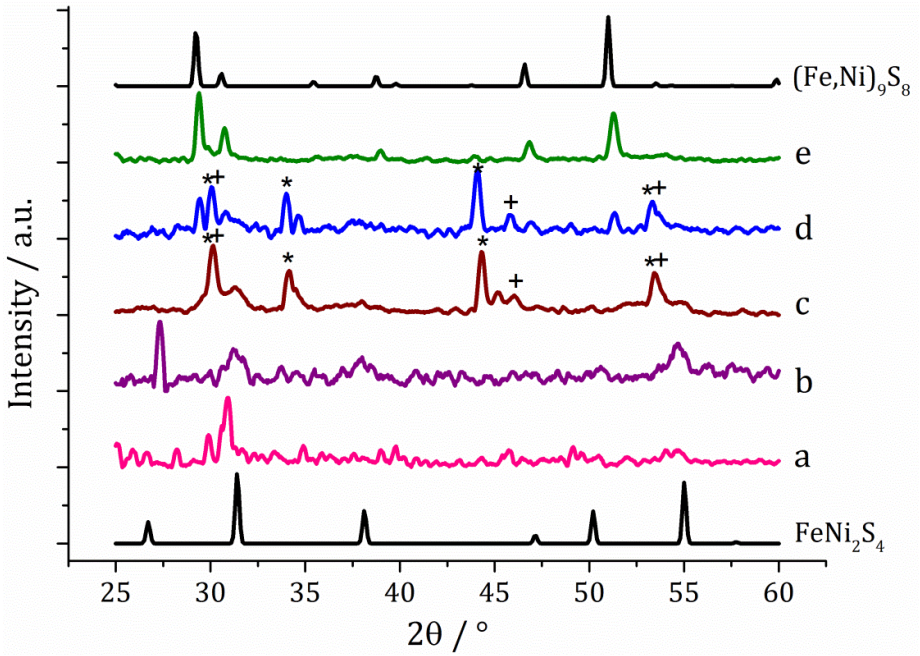

Figure 5-11 - XRD patterns for samples prepared from 3 with 21 at (a) 150 °C, (b) 180 °C, (c) 230 °C, (d) 260 °C and (e) 280 °C, with reference patterns for $FeNi_2S_4$ (ICDD card No. 47-1740) and $(Fe,Ni)_9S_8$ (ICDD card No. 75-2024). '*' Indicates Fe_7S_8 peaks and '+' indicates α-NiS peaks.

Pure $(Fe,Ni)_9S_8$ produced at 280 °C was analysed by TEM and HRTEM and found to be comprised of roughly hexagonal nanoparticles, of 53.1 nm (SD 18 nm) average diameter. This is much smaller than the nanoparticulate pentlandite reported previously by Bezverkhyy *et al.* (average diameter = 240 nm), though the authors used a very different synthesis method.[2] HRTEM analysis of the particles reveals d-spacings of 3.55 Å, corresponding to the [220] lattice plane in $(Fe,Ni)_9S_8$ (3.57 Å, ICDD card No. 75-2024).

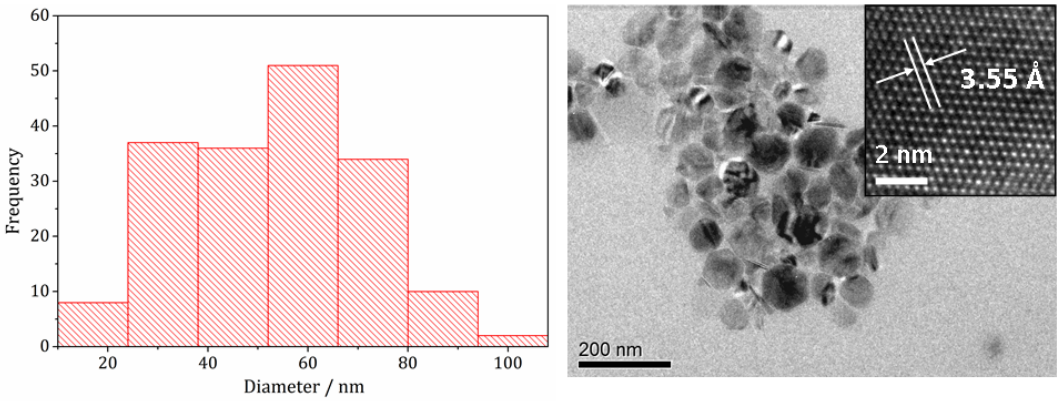

Figure 5-12 - Particle size histogram (left) and TEM image with HRTEM insert (right) of the $(Fe,Ni)_9S_8$ sample prepared from 3 with 21 at 280 °C.

In Chapters 3 and 4, the additive tetraisobutylthiuram disulfide (**6**) was found to increase the stability of metastable phases, allowing access to the thiospinel phases Fe_3S_4 and Ni_3S_4. The temperature study on the ternary iron-nickel sulfide system was therefore repeated (at 150, 180, 230, 260 and 280 °C) with the addition of 4 equivalents of **6** (2 eq. to each precursor) to see if the metastable thiospinel phase of this system ($FeNi_2S_4$) could be accessed pure. XRD analysis reveals a similar trend to the samples prepared without **6**; at low temperature mostly amorphous material is produced, with some violarite peaks emerging at 180 °C (Figure 5-13). In contrast to the previous results, however, at 230 °C pure $FeNi_2S_4$ is formed, without Fe_7S_8 and α-NiS impurities. This indicates that the additive **6** is able to stabilise the thiospinel $FeNi_2S_4$ phase and prevent the formation of binary metal sulfide phases.

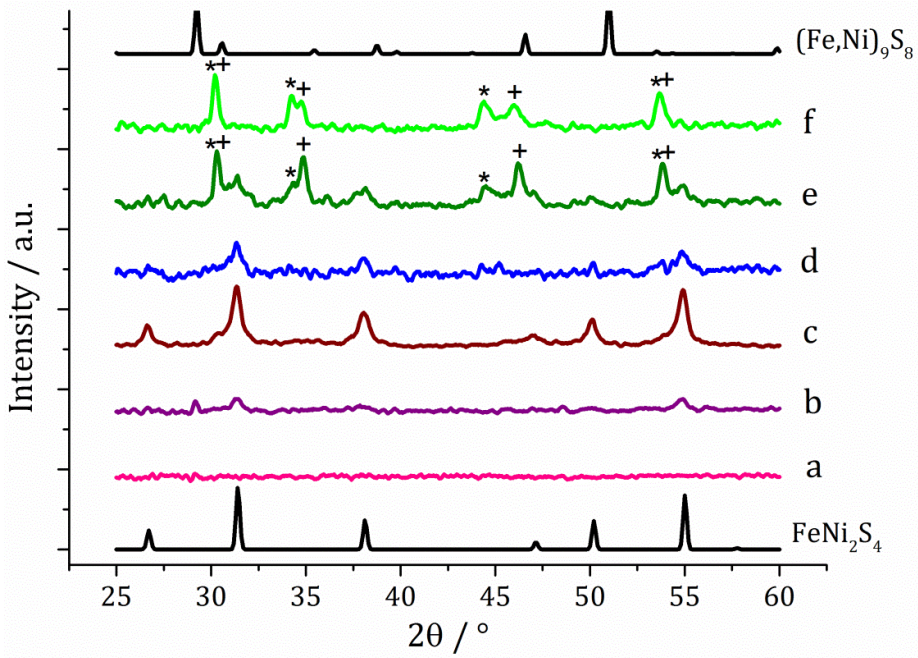

Figure 5-13 - XRD patterns for samples prepared from 3 with 21 and 6 at (a) 150 °C, (b) 180 °C, (c) 230 °C, (d) 260 °C, (e) 280 °C, and (f) 300 C, with reference patterns for $FeNi_2S_4$ (ICDD card No. 47-1740) and $(Fe,Ni)_9S_8$ (ICDD card No. 75-2024). '*' Indicates Fe_7S_8 peaks and '+' indicates α-NiS peaks.

At 260 °C the peaks for $FeNi_2S_4$ broaden and peaks for Fe_7S_8 and α-NiS begin to appear, and at 280 °C the sample is mainly Fe_7S_8 and α-NiS, with some $FeNi_2S_4$ remaining. At this temperature without thiuram disulfide additive **6**, the crystalline phase appeared to be pure $(Fe,Ni)_9S_8$ (pentlandite). In order to see if $(Fe,Ni)_9S_8$ could be accessed in the presence of **6** but at higher temperature (previous results suggested it was a high temperature, themodynamically more stable phase in this system), a decomposition was performed at 300 °C with 2 eq of **6**. The XRD analysis of the resulting material showed the crystalline

phase to be a roughly 1:1 mixture of Fe_7S_8 and α-NiS, with neither $FeNi_2S_4$ nor $(Fe,Ni)_9S_8$ present. This suggests the presence of **6** prevents the formation of $(Fe,Ni)_9S_8$, and makes the binary metal sulfide phases more thermodynamically favourable. In Chapters 3 – 4 it was shown that if precursors **3** and **21** are decomposed separately with **6** at 300 °C, Fe_7S_8 and α-NiS (respectively) are formed.

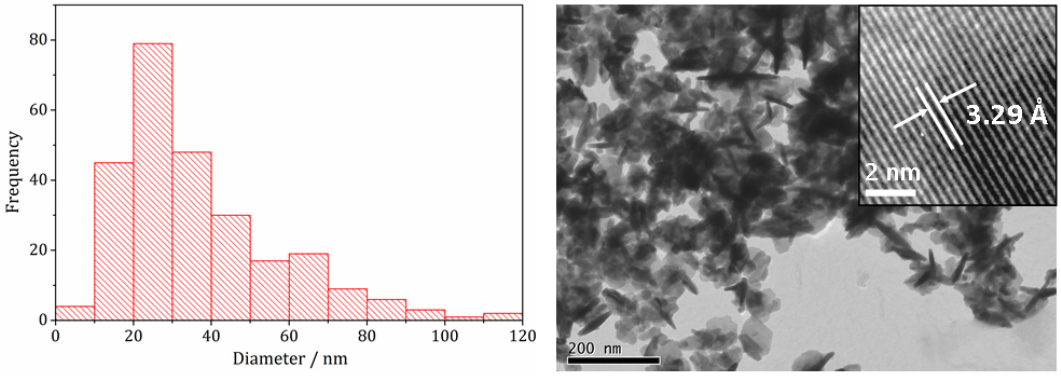

Figure 5-14 - Particle size histogram (left) and TEM image with HRTEM insert (right) of the $FeNi_2S_4$ sample prepared from 3 with 21 and 6 at 230 °C.

Analysing the $FeNi_2S_4$ particles produced at 230 °C by TEM (Figure 5-14) showed them to be roughly hexagonal, interlocking sheets, with an average diameter of 36.5 nm (SD 21 nm). This is slightly smaller than the $(Fe,Ni)_9S_4$ nanoparticles formed in the absence of **6** (average diameter 53.1 nm). HRTEM analysis of the nanoparticles reveals d-spacings of 3.29 Å, corresponding to the [220] lattice plane in $FeNi_2S_4$ (3.35 Å, ICDD card No. 47-1740). In studies with and without **6**, the lowest temperature at which an appreciable amount of crystalline material could be obtained was 230 °C, so this temperature was taken forward for concentration studies to see if other, metastable phases could be accessed.

Decompositions Varying Precursor Concentration

Complexes $[Fe(S_2CN^iBu_2)_3]$ (**3**) and $[Ni(S_2CN^iBu_2)_2]$ (**21**) were decomposed in OA according to the method described in Section 3.2 of Chapter 3, at 230 °C in a 1:1 ratio and varying concentrations of 5, 10, 20 and 25 mM. XRD analysis of the products (combined with the previous result for 2.5 mM) reveals a trend in the phase of metal sulfide produced with increasing concentration of precursors (Figure 5-15). At low concentration (2.5 mM) the majority of the crystalline sample corresponds to Fe_7S_8, with some $FeNi_2S_4$ and α-NiS. At higher concentrations (5, 10, 20 and 25 mM) the crystalline phase of the material produced is predominantly the thiospinel $FeNi_2S_4$, with some α-NiS impurity. This is

consistent with the concentration study performed on **3** alone, where at low precursor concentrations (5 mM) Fe_7S_8 was formed, and as the concentration was increased (up to 50 mM) the phase changed to the thiospinel Fe_3S_4. It should be noted that no greigite was detected in the mixed-metal study. When a similar study was performed on **21** alone, there was no observed effect on nickel sulfide phase; α-NiS being formed at all concentrations, supporting the ternary sulfide findings.

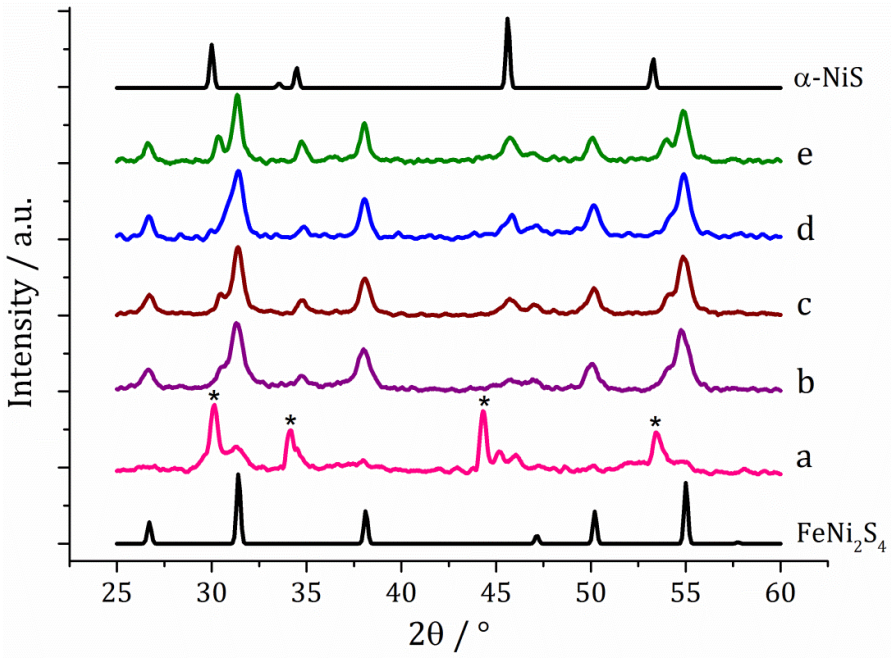

Figure 5-15 - XRD patterns for samples prepared from 3 with 21 at concentrations of (a) 2.5 mM, (b) 5 mM, (c) 10 mM, (d) 20 mM and (e) 25 mM, with reference patterns for $FeNi_2S_4$ (ICDD card No. 47-1740) and α-NiS (ICDD card No. 02-1273). '*' Indicates peaks for Fe_7S_8.

The concentration study was repeated with the addition of 4 equivalents of the thiuram disulfide **6** to see if any additional metastable iron-nickel sulfide phases are accessible. Similarly to the study without **6**, powder XRD analysis shows a concentration-dependent phase change (Figure 5-16). At lower concentrations pure violarite is formed (**3**:**21**:**6** = 2.5:2.5:10 mM and 5:5:20 mM), but when the concentration is increased to **3**:**21**:**6** = 10:10:40 mM, the majority of the crystalline material matches the pattern for $(Fe,Ni)S_2$ (bravoite, a nickelian pyrite) and at **3**:**21**:**6** = 20:20:80 mM the pattern matches pure $(Fe,Ni)S_2$. Peaks are broad suggesting small particles, which is consistent with the concentration study of the nickel precursor **21** in the presence of **6**. There, at high concentration (**21**:**6** = 20:40 mM) the nickel pyrite NiS_2 was produced. In the ternary system, when the concentration is increased further to **3**:**21**:**6** = 25:25:100 mM, additional peaks to at slightly higher 2θ angles appear, indicative of the presence of FeS_2 (pyrite).

This is particularly interesting because in the binary iron sulfide system reported in Chapter 3, pyrite is not accessible at high concentrations, even with the addition of **6**. It should be noted that at higher concentration, low angle (10 – 20 °) broad peaks are observed, identical to those seen, in the binary iron sulfide study with **6** and when also **6** was decomposed alone at high concentration. These are presumed to be the result of excess sulfur.

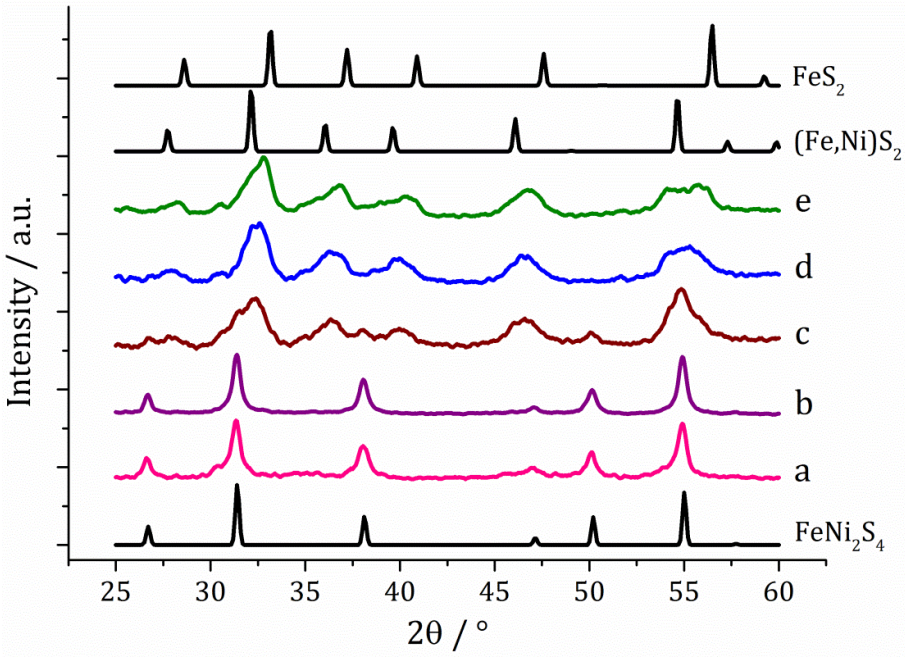

Figure 5-16 - XRD patterns for samples prepared from 3 with 21 and 6 (1:1:2) at concentrations of 3 and 21 of (a) 2.5 mM, (b) 5 mM, (c) 10 mM, (d) 20 mM and (e) 25 mM, with reference patterns for $FeNi_2S_4$ (ICDD card No. 47-1740), $(Fe,Ni)S_2$ (ICDD card No. 88-1710) and FeS_2 (ICDD card No. 42-1340).

The particles produced at concentration **3**:**21**:**6 =** 20:20:80 mM were analysed by TEM, being roughly spherical and with small crystallite size (average diameter 6.7 nm, SD = 1.9 nm), as indicated by the broad peaks in the XRD pattern. The particles closely resemble the NiS_2 nanoparticles formed at high concentration of **21** decomposed with **6** (**21**:**6** = 20:40 mM, shown in Figure 4-12 (c)), which had an average diameter of 4.2 nm (SD = 1.3 nm). HRTEM analysis (Figure 5-17) of the $(Fe,Ni)S_2$ nanoparticles reveals *d*-spacings of 3.10 and 2.45 Å, which match the [111] and [200] planes of $(Fe,Ni)S_2$ (3.21 and 2.49 Å respectively, ICDD card No. 89-3058).

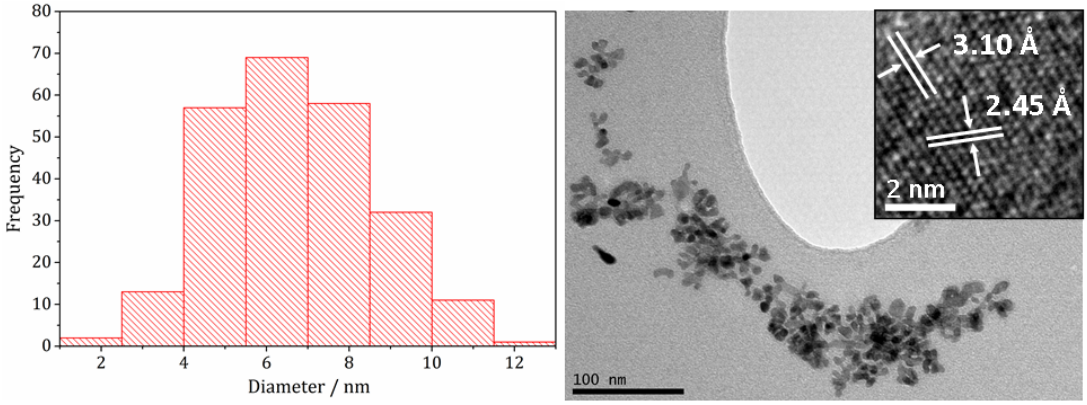

Figure 5-17 - Particle size histogram (left) and TEM image with HRTEM insert (right) of the (Fe,Ni)S_2 sample prepared from 3 with 21 and 6 at concentration 20:20:80 mM.

In summary, products of the mixed iron and nickel ternary sulfide system were found to be highly dependant upon decomposition temperature and precursor concentration, with similarities to both the iron sulfide and nickel sulfide binary systems. The pentlandite phase $(Fe,Ni)_9S_8$, thiospinel phase $FeNi_2S_4$ and pyrite phase $(Fe,Ni)S_2$ could be selectively produced by varying reaction temperature, precursor concentration and employing the tetra-isobutylthiuram disulfide additive **6**. We believe that this is the first reported synthesis of the latter two phases in nanoparticulate form.

5.2.3.2 Iron-Copper Sulfide

Brown $[Cu(S_2CN^iBu_2)_2]$ (**25**, 2.5 mM) was decomposed in 1:1 ratio with $[Fe(S_2CN^iBu_2)_3]$ (**3**, 2.5 mM), using standard conditions. This reaction was then repeated with the addition 4 eq. of thiuram disulfide **6**, and the resulting brown powders were analysed. No discernable colour changes occurred during these reactions and, in both cases, purple coloured clear dispersions resulted in chlorinated solvents. XRD analysis revealed that the crystalline phase produced corresponded to $CuFeS_2$ (chalcopyrite) in both cases. This is in accordance to previous literature reports on the synthesis of iron-copper sulfide nanoparticles *via* the solvothermal method, involving dithiocarbamates. [75, 76] HRTEM analysis (Figure 5-19) of the $CuFeS_2$ nanoparticles reveals a *d*-spacing of 2.99 Å, which matches the [112] plane (3.21 Å, $CuFeS_2$ ICDD card No. 37-0471).

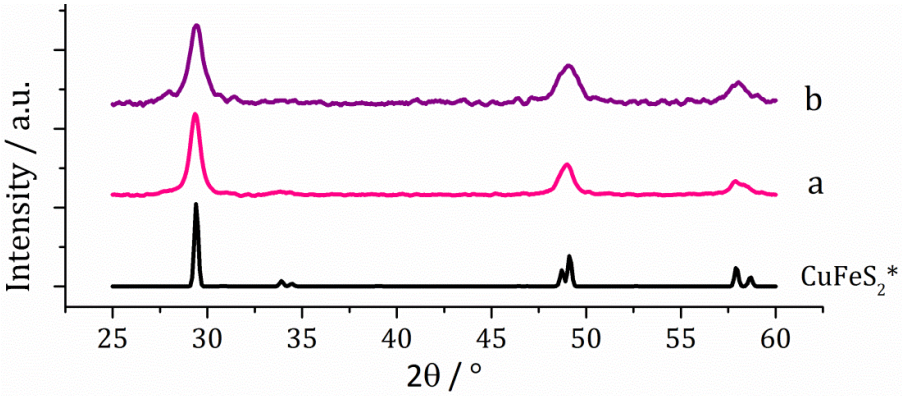

Figure 5-18 - XRD patterns for samples prepared from (a) 25 with 3 and (b) 25 with 3 and 6, with reference pattern for bulk $CuFeS_2$ (ICDD card No. 37-0471).

TEM analysis revealed the addition of the thiuram disulfide additive **6** had little effect on the size or morphology of the nanoparticles, which were roughly spherical in both cases (see Figure 5-19 for a TEM image of the sample prepared in the absence of **6** as an example). Average particle diameters were 11 nm (SD = 4 nm) without **6**, and 10 nm (SD = 4 nm) with **6**. Of the two previous reports using dithiocarbamate complexes, the closest to this work involves the hot-injection of $[Cu(S_2CNEt_2)_2]$ and $[Fe(S_2CNEt_2)_3]$ in OLA/dichlorobenzene into a solution of sulfur in OLA/TOP at 180 °C.[75] Though an additional sulfur source and a lower temperature is used, the same phase of iron-copper sulfide is formed, $CuFeS_2$, with very similar sized nanoparticles (12 ± 4 nm diameter).[75] This indicates that dithiocarbamate precursor decomposition occurs below 180 °C, and during nanoparticle formation the duration of burst nucleation and number of nucleation sites is not affected by increasing the temperature.

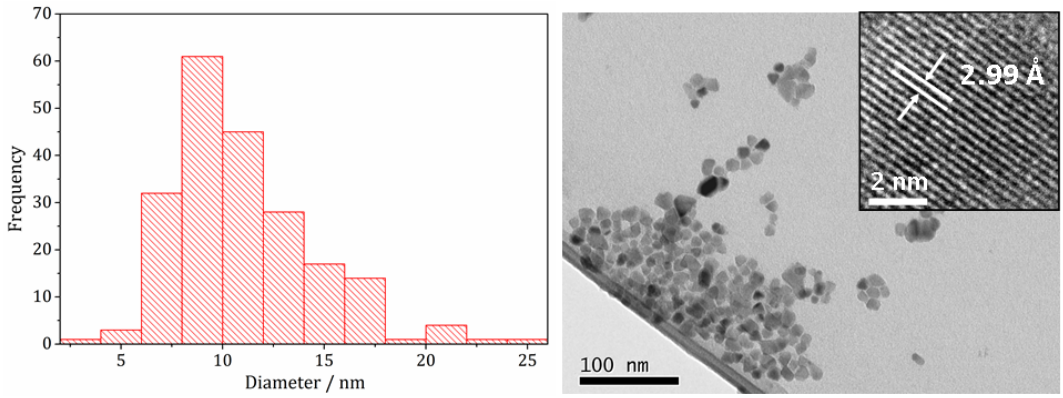

Figure 5-19 - Particle size histogram (left) and TEM image with HRTEM insert (right) of the sample prepared from 25 with 3.

5.2.3.3 Iron-Zinc Sulfide

White $[Zn(S_2CN^iBu_2)_2]$ (**26**, 2.5 mM) was decomposed in 1:1 ratio with dark brown $[Fe(S_2CN^iBu_2)_3]$ (**3**, 2.5 mM), under standard conditions. This reaction was then repeated with 4 eq. of thiuram disulfide **6**, and the resulting brown powders were analysed. As with the previous decompositions of $[Fe(S_2CN^iBu_2)_3]$ alone and in the presence of $[Ni(S_2CN^iBu_2)_2]$, as the dark brown OA precursor solutions were being heated to decomposition temperature, they became suddenly clear and pale yellow at 85 °C, then at 100 °C quickly turned completely black. The zinc precursor **26** produces a clear colourless solution in OA so this effect may just be associated with the iron precursor **3**.

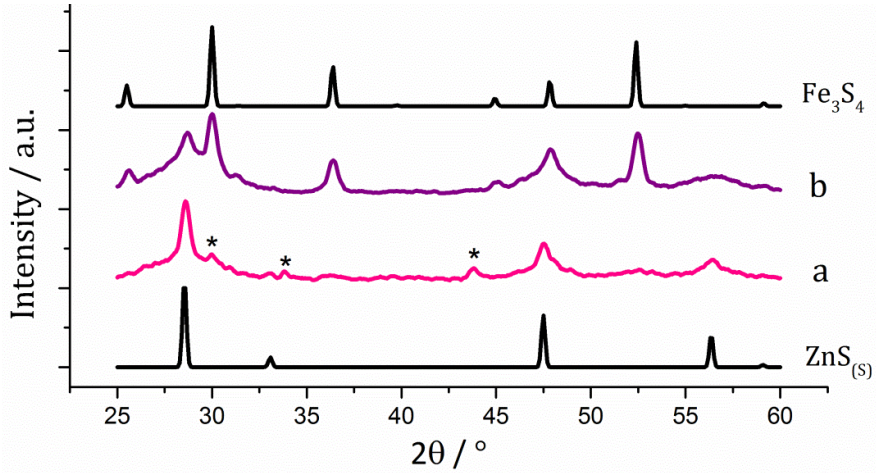

Figure 5-20 - XRD patterns for samples prepared from (a) 26 with 3 and (b) 26 with 3 and 6, with reference patterns for bulk $ZnS_{(S)}$ (ICDD card No. 77-2100) and Fe_3S_4 (ICDD card No. 16-0713). '*' Indicates peaks for Fe_7S_8.

XRD analysis revealed that the crystalline phase produced corresponded to a mixture of iron sulfide and zinc sulfide phases in both cases (Figure 5-20). Interestingly, the zinc sulfide phase observed in both samples matches well to the pattern for $ZnS_{(S)}$, the sphalerite structure of ZnS, rather than the wurtzite phase ($ZnS_{(W)}$) as observed above in the zinc sulfide binary system described in Section 5.2.2.3. Notably the characteristic peak for $ZnS_{(W)}$ at 39.8 ° 2θ is absent. The peaks match well for $ZnS_{(S)}$, and are not shifted to lower angles, as previously observed for mixed iron and zinc sulfide systems,[66] suggesting no ternary mixed-metal sulfide has been formed. The reason for this is unclear, but the results suggest that precursors decompose separately at different temperatures, giving rise to separate nucleation events and forming binary metal sulfide nanoparticles. The sample prepared in the absence of **6** appears to also have peaks for the iron sulfide Fe_7S_8 and the sample prepared with **6** contains peaks which match well to Fe_3S_4, the thiospinel

phase of iron sulfide. This is consistent with previous results reported on the iron sulfide binary phase system in Chapter 3.

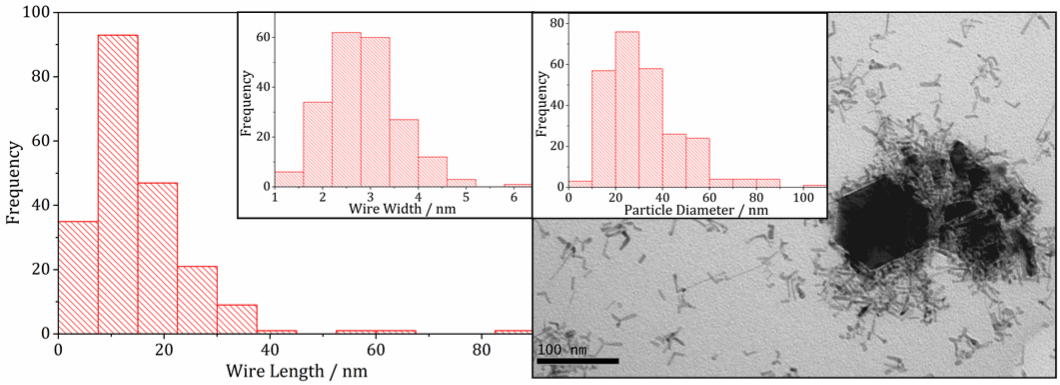

Figure 5-21 - Wire length histogram with wire width histogram insert (left) and TEM image with particle diameter histogram insert (right), of the sample prepared from 26 with 3.

TEM images of the resulting samples support the XRD analysis, clearing showing a two phase system (see Figure 5-21), and very similar observations were made for the sample prepared in the presence of **6**. Samples are comprised of large hexagonal particles (average diameter 32nm, SD 16 nm) which resemble the iron sulfide phases observed in the binary system reported in Chapter 3, and very thin nanowires (length = 16 nm, SD 15 nm, width = 2.9 nm, SD 0.8 nm) which resemble the zinc sulfide material produced in the binary system reported in Section 5.2.2.3. Garje *et al*. were able to synthesise an iron-rich wurtzite, $(Zn,Fe)S_{(W)}$, by solvothermally decomposing a bimetallic precursor (Figure 5-1), thereby ensuring both iron and zinc monomers (as well as sulfur) were present simultaneously during decomposition.[67] To emulate this, decomposition *via* the 'hot-injection' method could be investigated.

5.2.3.4 Iron-Indium Sulfide

Pale yellow $[In(S_2CN^iBu_2)_3]$ (**27**, 2.5 mM) was decomposed in 1:1 ratio with dark brown $[Fe(S_2CN^iBu_2)_3]$ (**3**, 2.5 mM), under standards conditions. This reaction was then repeated with the addition 4 eq of thiuram disulfide **6**, and the resulting brown powders were analysed. Similar to the iron-zinc decompositions, as the dark brown iron-indium precursor solutions were being heated to decomposition temperature, they suddenly become clear and bright yellow in colour at 100 °C, then at 120 °C quickly turned completely black. The indium precursor **26** produces a bright yellow solution in OA so this effect may just be to do with the iron precursor **3**, as was noted for the iron-zinc case.

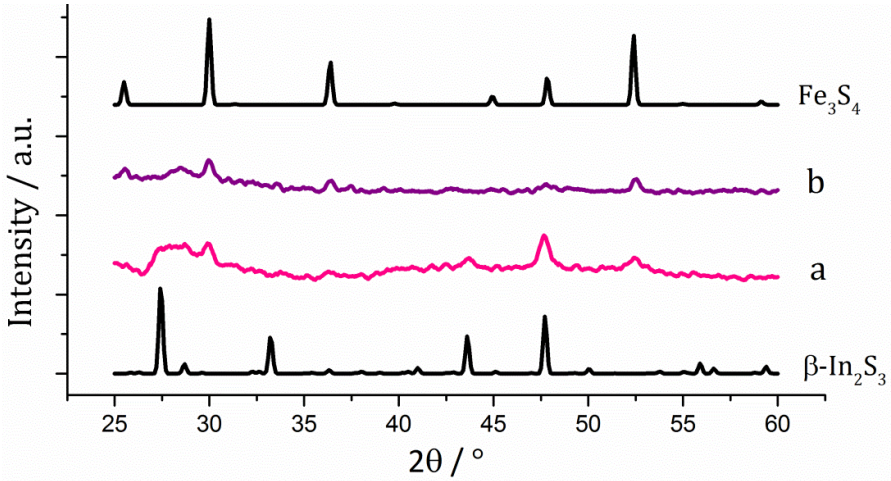

Figure 5-22 - XRD patterns for samples prepared from (a) 27 with 3, (b) 27 with 3 and 6, with reference patterns for β-In_2S_3 (ICDD card No. 25-0390) and Fe_3S_4 (ICDD card No. 16-0713).

The samples were analysed by powder XRD and neither of the patterns matched that of the mixed iron-indium sulfide $FeIn_2S_4$ (Figure 5-22). The XRD patterns for both samples were quite poor indicating low crystallinity, but peaks for Fe_3S_4 are detectable in both, as well as β-In_2S_3 in the sample prepared with **6**. No ternary mixed-metal sulfide appears to have been formed. As with the iron-zinc sulfide case the reason for this is unclear, but may be due to the precursors decomposing separately at different temperatures. Interestingly, unlike the iron-zinc sulfide samples, peaks for pyrrhotite are not observed in the sample prepared without **6**, but peaks matching Fe_3S_4 are seen in both samples. This could suggest that the presence of the indium precursor **27** or indium sulfide product β-In_2S_3 helps to stabilise the iron sulfide thiospinel.

5.2.3.5 Nickel-Cobalt Sulfide

Green [$Ni(S_2CN^iBu_2)_2$] (**21**, 2.5 mM) was decomposed in 1:1 ratio with the green [$Co(S_2CN^iBu_2)_3$] (**24**, 2.5 mM), under standard conditions. This reaction was then repeated with the addition 4 eq. of thiuram disulfide **6**, and the resulting brown powders were analysed. There was no obvious colour change as seen with the iron containing systems as the reaction was brought to decomposition temperature. XRD analysis revealed no shift in peaks between the two samples, indicating **6** has no observable effect on the phase of ternary sulfide produced in this system. In addition, to elucidate whether the nickel or cobalt rich thiospinel structures had been formed ($CoNi_2S_4$ or $NiCo_2S_4$ respectively), both samples were analysed by energy-dispersive X-ray spectroscopy (EDX) and found to have atomic compositions of cobalt, nickel and sulfur of 1.76:1.60:4 and 1.52:1.32:4,

respectively. Though the ratios of metal to sulfur vary slightly, they remain approximately 1.1:1 Co:Ni, indicating in both cases an intermediate $(Ni,Co)_3S_4$ phase. The difference between the XRD patterns for $CoNi_2S_4$ and $NiCo_2S_4$ is very small, nickel and cobalt having very similar ionic radii and electronegativity, and the patterns obtained for the samples synthesised here closely match them both.

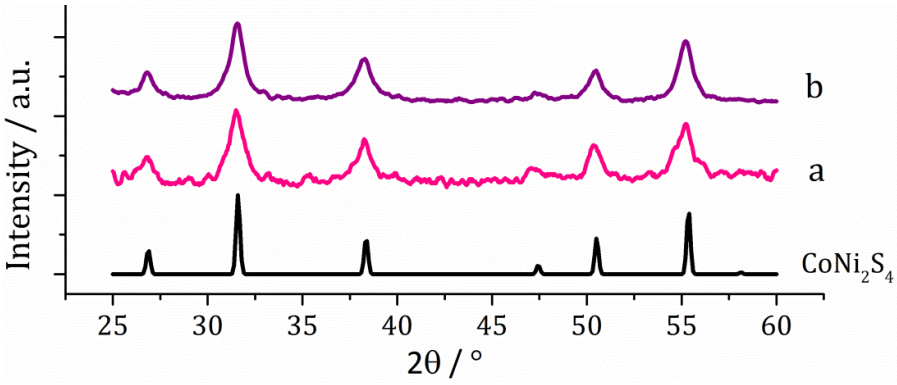

Figure 5-23 - XRD patterns for samples prepared from (a) 24 with 3 and (b) 24 with 3 and 6, with reference pattern for bulk $CoNi_2S_4$ (ICDD card No. 22-0334).

TEM analysis revealed the addition **6** had little effect on the size or morphology of the nanoparticles formed, which were roughly spherical in both cases (see Figure 5-24 for a TEM image of the sample prepared with **6** as an example). The average particle diameters were 10 nm (SD = 5 nm) for the sample prepared without **6**, and 10 nm (SD = 4 nm) with **6**. Nanoparticles of $CoNi_2S_4$ were previously reported by Pang *et al.*, *via* the decomposition of $Co(O_2CCH_3)_2$ and $Ni(O_2CCH_3)_2$ with sulfur powder dissolved in OA/anisole in an autoclave.[77] The nanoparticles were reported to have 'quasi-spherical' morphology with an average diameter of approximately 8 – 15 nm, similar to those produced in the current study. HRTEM analysis (Figure 5-24) of the current $(Ni,Co)_3S_4$ nanoparticles reveals a *d*-spacing of 2.67 Å, which matches the [222] plane (2.72 Å, $CoNi_2S_4$ ICDD card No. 24-0334).

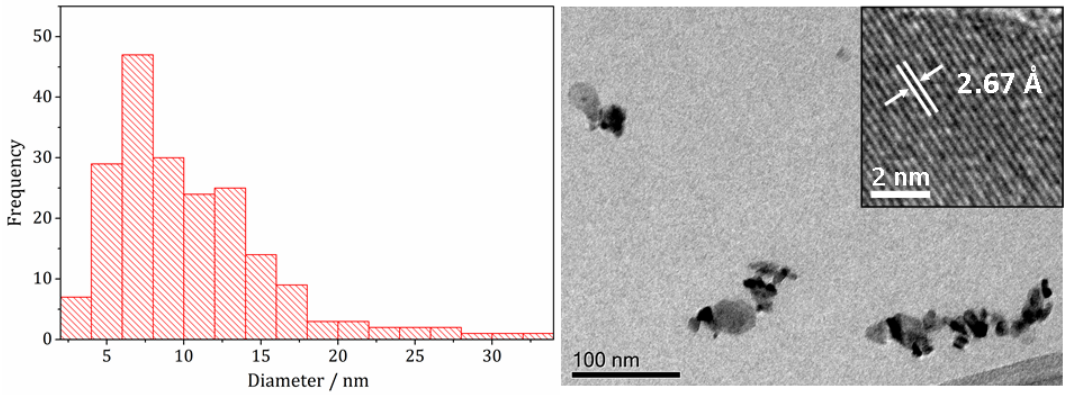

Figure 5-24 - Particle size histogram (left) and TEM image with HRTEM insert (right) of the $(Ni,Co)_3S_4$ sample prepared from 25 with 3 and 6.

In summary, of the attempts to synthesise ternary metal sulfide systems iron-nickel sulfide, iron-copper sulfide and nickel-cobalt sulfide materials were successfully prepared, and in the iron-nickel case, with various phases. Attempts to synthesise iron-zinc sulfide and iron-indium sulfide were unsuccessful, producing only binary metal sulfides, which may be due to the precursor complexes decomposing at different temperatures. If this is the case, ternary sulfides may be accessible in these systems *via* the 'hot-injection' decomposition method which would force the precursors to decompose simultaneously. There was insufficient time for this to be investigated in the current study, but could be attempted in future work.

5.3 Conclusions

Complexes $[M^x(S_2CN^iBu_2)_x]$ (M = Co, x = 3; Cu, x = 2; Zn, x = 2; and In, x = 3) were investigated as precursors for binary metal sulfide nanoparticles, and, in conjunction with $[Fe(S_2CN^iBu_2)_3]$ and $[Ni(S_2CN^iBu_2)_2]$, for ternary metal sulfides. In the case of cobalt, $Co_{1-x}S$ and $CoNi_2S_4$ were successfully synthesised and for copper $Cu_{1.8}S$ and $CuFeS_2$ were produced. In the case of zinc, the binary sulfide $ZnS_{(W)}$ could be synthesised, but the ternary iron-zinc sulfide could not, with only the binary metal sulfides being observed. The indium precursor produced In_2S_3 of low crystallinity and, as with the zinc, the ternary sulfide with iron was not produced. In addition the ternary iron-nickel sulfide system was investigated and several phases were successfully synthesised, in particular the thiospinel $FeNi_2S_4$ was produced in nanoparticulate form, which has to date not been reported in the literature.

The effect of adding tetraisobutylthiuram disulfide (**6**) to the decomposition solutions was also studied, and found to have a great effect on the ternary iron-nickel sulfide system. At high precursor concentration in the presence of **6** the nickel pyrite $(Fe,Ni)S_2$ was synthesised with small nanoparticles (average diameter 6.7 nm) and low polydispersity (SD 1.9 nm), which has also not be reported in the literature to date. The additive **6** also allowed access to the cobalt sulfide CoS_2 at high concentration, as seen previously with the nickel binary sulfide NiS_2, which was formed at high concentration (see Chapter 4). Though **6** appeared to have little effect in the studies on other metals, high concentration decompositions were not attempted due to time constraints and this should be further investigated to see if other pyrite structures are accessible. The additive **6** also aided in the synthesis of the mixed iron and nickel thiospinel $FeNi_2S_4$, allowing synthesis of pure material at higher temperatures, stabilising the phase in some way. This is very similar to the effect of **6** on the binary iron sulfide system, where the thiospinel Fe_3S_4 was produced in the presence of **6**. Clearly **6** effects the conditions under which metastable phases of iron and iron-nickel sulfide materials can form, stabilising them in some way.

5.4 Experimental

Chemicals

All reagents were procured commercially from Aldrich and used without further purification.

Physical Measurements

All ^{1}H and $^{13}C\{^{1}H\}$ NMR spectra were obtained on either a Bruker Avance III 400 or Avance 600 spectrometer, the latter being equipped with a cryoprobe. All spectra were recorded using $CDCl_3$ which was dried and degassed over molecular sieves prior to use; ^{1}H and $^{13}C\{^{1}H\}$ chemical shifts are reported relative to $SiMe_4$. The mass spectra were obtained using either Micromass 70-SE spectrometer using Electron Ionisation (EI) or a Thermo Finnigan MAT900xp spectrometer using Fast Atom Bombardment (FAB). Elemental analysis was carried using Elemental Analyser (CE-440) (Exeter Analytical Inc). Thermogravimetric analysis (TGA) was performed using a Netzsch STA 449C TGA system. Data was recorded from 25 to 600 °C with a constant heating rate of 10 °C $minute^{-1}$.

XRD patterns were measured on a Bruker AXS D4 diffractometer using $CuK\alpha_1$ radiation. The diffraction patterns obtained were compared to database standards. For TEM

characterisation a 4 µl droplet of nanoparticle suspension (chloroform) was placed on a holey carbon-coated copper TEM grid and allowed to evaporate in air under ambient laboratory conditions for several minutes. TEM images were obtained using a JEOL-1010 microscope at 100 kV equipped with a Gatan digital camera. HRTEM measurements were collected using a Jeol 2100 TEM with a LaB_6 source operating at an acceleration voltage of 200 kv. Micrographs were taken on a Gatan Orius Charge-coupled device (CCD).

5.4.1 Metal Dithiocarbamate Precursor Synthesis

$[Co(S_2CN^iBu_2)_3]$ (24)

$^iBu_2NH$ (2.20 mL, 12.61 mmol) was added to NaOH (0.50 g, 12.61 mmol) dissolved in 50 mL distilled H_2O. To this mixture CS_2 (0.76 mL, 12.61 mmol) was added dropwise over 10 minutes and the mixture stirred overnight. A red solution of $CoCl_2 \cdot 6H_2O$ (1.00 g, 4.20 mmol) dissolved in 100 mL of water was added dropwise over 5 minutes, whereupon a dark green precipitate formed. This mixture was vigorously stirred for 2 hrs, filtered, washed with water (3 x 30 mL) and evaporated to dryness. The resulting green powder was dissolved in 100 mL of dichloromethane (DCM) and stirred with magnesium sulphate for 30 mins, after which the mixture was filtered and the filtrate dried *in vacuo*. Yield 1.8347 g, 65 %. **Anal. Calc. for $C_{27}H_{54}N_3S_6Co$:** C, 48.25; H, 8.10; N, 6.25. Found: C, 48.17; H, 8.16; N, 6.46. **MS:** *m/z* 671 [M^+], 467 [$M^+ - S_2CN^iBu_2$].

$[Cu(S_2CN^iBu_2)_2]$ (25)

$^iBu_2NH$ (2.62 mL, 15 mmol) was added to NaOH (0.60 g, 15 mmol) dissolved in 100 mL methanol. To this mixture CS_2 (0.90 mL, 15 mmol) was added dropwise over 10 minutes and the mixture stirred overnight. A solution of $CuCl_2$ (0.67 g, 5 mmol) dissolved in 50 mL of methanol was added dropwise over 5 minutes, whereupon a black precipitate formed. This mixture was vigorously stirred for 4 hrs, filtered, and then washed and dried following the procedure for **24**, yielding a black powder, 2.3615 g, 75 %. **Anal. Calc. for $C_{18}H_{36}N_2S_4Cu$:** C, 45.78; H, 7.68; N, 5.93. Found: C, 45.59; H, 7.71; N, 6.20. **MS:** *m/z* 471 [M^+], 172 [SCN^iBu_2].

$[Zn(S_2CN^iBu_2)_2]$ (26)

The synthesis follows that of **25** with the exception that H_2O was used as the solvent and $ZnSO_4 \cdot 7H_2O$ (1.44 g, 5 mmol) was used as the metal salt yielding an off-white powder,

2.0863 g, 88 %. **Anal. Calc. for $C_{18}H_{36}N_2S_4Zn$:** C, 45.60; H, 7.65; N, 5.91. Found: C, 46.61; H, 7.97; N, 5.59. **^{1}H NMR δ/ppm ($CDCl_3$):** 0.97 (d, *J* = 6.6 Hz, 24H, CH_3), 2.39 (m, *J* = 6.8 Hz, 4H, C*H*), 3.70 (d, *J* = 7.5 Hz, 8H, CH_2). **^{13}C{^{1}H} NMR δ/ppm ($CDCl_3$):** 20.3 (*C*H_3), 27.1 (*C*H), 62.2 (*C*H_2), 204.5 (*C*S_2). **MS:** *m/z* 472 [M^+], 268 [M^+ - $S_2CN^iBu_2$], 383 [$ZnS(SCN^iBu_2)_2$ - ^{i}Bu].

[$In(S_2CN^iBu_2)_3$] (27)

The synthesis follows that of **26** with the exception that $InCl_3$ (1.11 g, 5 mmol) was used as the metal salt yielding a white powder. Large colourless crystals were obtained by slow evaporation from DCM. Yield 3.2758 g, 90 %. **Anal. Calc. for $C_{27}H_{54}N_3S_6In$:** C, 44.55; H, 7.48; N, 5.77. Found: C, 44.59; H, 7.53; N, 5.54. **^{1}H NMR δ/ppm ($CDCl_3$):** 0.95 (d, *J* = 6.6 Hz, 24H, CH_3), 2.41 (m, *J* = 6.8 Hz, 4H, C*H*), 3.63 (d, *J* = 7.5 Hz, 8H, CH_2). **^{13}C{^{1}H} NMR δ/ppm ($CDCl_3$):** 20.5 (*C*H_3), 27.1 (*C*H), 64.0 (*C*H_2), 203.6 (*C*S_2). **MS:** *m/z* 670 [M^+ - ^{i}Bu], 523 [M^+ - $S_2CN^iBu_2$], 467 [$In(S_2CN^iBu_2)_2$ - ^{i}Bu].

5.4.2 Binary Metal Sulfide Synthesis

The decomposition setup as described in Section 3.2 of Chapter 3 was utilised. In a typical synthesis [$M^x(S_2CN^iBu_2)_x$] (M = Co, x = 3; Cu, x = 2; Zn, x = 2; and In, x = 3) (5 mM) was added to OA (20 mL) in a three-neck RBF attached to a condenser and evacuated and refilled with nitrogen repeatedly for 15 minutes. The solution was heated to 230 °C and held there for one hour. The mixture was allowed to cool to RT slowly, whereupon methanol (80 mL) was added with stirring. The mixture was centrifuged and then the solution decanted leaving behind the resultant nanoparticles. This procedure was repeated 3 times and finally the material was allowed to dry in air.

5.4.2.1 Cobalt Sulfide

Decompositions as in Section 5.4.2 but using: 1) **24**; 2) **24** and **6** (10 mM); 3) **24** and **6** (50 mM).

5.4.2.2 Copper Sulfide

Decompositions as in Section 5.4.2 but using: 1) **25**; 2) **25** and **6** (10 mM).

5.4.2.3 Zinc Sulfide

Decompositions as in Section 5.4.2 but using: 1) **26**; 2) **26** and **6** (10 mM).

5.4.2.4 Indium Sulfide

Decompositions as in Section 5.4.2 but using: 1) **27**; 2) **27** and **6** (10 mM).

5.4.3 Ternary Metal Sulfide Synthesis

5.4.3.1 Iron-Nickel Sulfide

Temperature Studies: Decompositions as in Section 5.4.2 but using **3** (2.5 mM) and **21** (2.5 mM) at temperatures: 1) 150 °C; 2) 180 °C; 3) 230 °C; 4) 260 °C; 5) 280 °C, then repeated at these temperatures with the addition of **6** (10 mM), with an additional decomposition at 300 °C.

Concentration Studies: Decompositions as in Section 5.4.2 but using varying concentrations of **3**:**21** of: 1) 5:5 mM; 2) 10:10 mM; 3) 20:20 mM; 4) 25:25 mM. The decompositions were then repeated with the addition of 4 equivalents of **6**, such that the concentrations of **3**:**21**:**6** were: 1) 5:5:20 mM; 2) 10:10:40 mM; 3) 20:20:80 mM; 4) 25:25:100 mM.

5.4.3.2 Iron-Copper Sulfide

Decompositions as in Section 5.4.2 but using: 1) **25** (2.5 mM) and **3** (2.5 mM); 2) **25** (2.5 mM), 3 (2.5 mM) and **6** (10 mM).

5.4.3.3 Iron-Zinc Sulfide

Decompositions as in Section 5.4.2 but using: 1) **26** (2.5 mM) and **3** (2.5 mM); 2) **26** (2.5 mM), 3 (2.5 mM) and **6** (10 mM).

5.4.3.4 Iron-Indium Sulfide

Decompositions as in Section 5.4.2 but using: 1) **27** (2.5 mM) and **3** (2.5 mM); 2) **27** (2.5 mM), 3 (2.5 mM) and **6** (10 mM).

5.4.3.5 Nickel-Cobalt Sulfide

Decompositions as in Section 5.4.2 but using: 1) **24** (2.5 mM) and **21** (2.5 mM); 2) **24** (2.5 mM), 3 (2.5 mM) and **21** (10 mM).

5.5 References

1 R. C. Hoodless, R. B. Moyes, and P. B. Wells, *Catal. Today*, 2006, 114, 377.
2 I. Bezverkhyy, P. Afanasiev, and M. Danot, *J. Phys. Chem. B*, 2004, 108, 7709.
3 M.-R. Gao, Y.-F. Xu, J. Jiang, and S.-H. Yu, *Chem. Soc. Rev.*, 2013, 42, 2986.
4 C.-H. Lai, M.-Y. Lu, and L.-J. Chen, *J. Mater. Chem.*, 2012, 22, 19.
5 M. A. Ehsan, T. a N. Peiris, K. G. U. Wijayantha, M. M. Olmstead, Z. Arifin, M. Mazhar, K. M. Lo, and V. McKee, *Dalton. Trans.*, 2013, 42, 10919.
6 M. Feng, Y. Lu, Y. Yang, M. Zhang, Y.-J. Xu, H.-L. Gao, L. Dong, W.-P. Xu, and S.-H. Yu, *Sci. Rep.*, 2013, 3, 2994.
7 K. Ramasamy, M. A. Malik, N. Revaprasadu, and P. O'Brien, *Chem. Mater.*, 2013, 25, 3551.
8 M. Afzaal, M. A. Malik, and P. O'Brien, *J. Mater. Chem.*, 2010, 20, 4031.
9 B. D. Yuhas, C. Prasittichai, J. T. Hupp, and M. G. Kanatzidis, *J. Am. Chem. Soc.*, 2011, 133, 15854.
10 J. B. Varley, H. A. Hansen, N. L. Ammitzboll, L. C. Grabow, A. A. Peterson, J. Rossmeisl, and J. K. Norskov, *ACS Catal.*, 2013, 3, 2640.
11 R. E. Mielke, K. J. Robinson, L. M. White, S. E. McGlynn, K. McEachern, R. Bhartia, I. Kanik, and M. J. Russell, *Astrobiology*, 2011, 11, 933.
12 M. J. Russell and W. Martin, *Trends Biochem. Sci.*, 2004, 29, 358.
13 C. Huber and G. Wachtershauser, *Science*, 1997, 276, 245.
14 M. J. Russell and A. J. Hall, *J. Geol. Soc. London.*, 1997, 154, 377.
15 S. Haider, R. Grau-Crespo, A. J. Devey, and N. H. de Leeuw, *Geochim. Cosmochim. Acta*, 2012, 88, 275.
16 P. O'Brien and R. Nomura, *J. Mater. Chem.*, 1995, 5, 1761.
17 M. Kemmler, M. Lazell, P. O. Brien, D. J. Otway, and J. Park, *J. Mater. Sci. Mater. Electron.*, 2002, 13, 531.
18 P. O'Brien, D. J. Otway, and J. R. Walsh, *Thin Solid Films*, 1998, 315, 57.
19 K. Ramasamy, M. A. Malik, J. Raftery, F. Tuna, and P. O'Brien, *Chem. Mater.*, 2010, 22, 4919.
20 F. Srouji, M. Afzaal, J. Waters, and P. O'Brien, *Chem. Vap. Depos.*, 2005, 11, 91.
21 K. Aup-Ngoen, T. Thongtem, S. Thongtem, and A. Phuruangrat, *Mater. Lett.*, 2013, 101, 9.
22 J.-Q. Sun, X.-P. Shen, K.-M. Chen, Q. Liu, and W. Liu, *Solid State Commun.*, 2008, 147, 501.
23 J. Joo, H. Bin Na, T. Yu, J. H. Yu, Y. W. Kim, F. Wu, J. Z. Zhang, and T. Hyeon, *J. Am. Chem. Soc.*, 2003, 125, 11100.
24 Q. Lu, F. Gao, and D. Zhao, *Nano Lett.*, 2002, 2, 725.
25 N. Pradhan, B. Katz, and S. Efrima, *J. Phys. Chem. B*, 2003, 107, 13843.
26 H. Zhang, B.-R. Hyun, F. W. Wise, and R. D. Robinson, *Nano Lett.*, 2012, 12, 5856.
27 Y. C. Zhang, G. Y. Wang, X. Y. Hu, and W. W. Chen, *Mater. Res. Bull.*, 2006, 41, 1817–1824.
28 K. V. Anand, M. K. Chinnu, R. M. Kumar, R. Mohan, and R. Jayavel, *J. Alloys Compd.*, 2010, 496, 665.
29 M. X. Wang, L. S. Wang, G. H. Yue, X. Wang, P. X. Yan, and D. L. Peng, *Mater. Chem. Phys.*, 2009, 115, 147.
30 H. Chen, J. Jiang, L. Zhang, H. Wan, T. Qi, and D. Xia, *Nanoscale*, 2013, 5, 8879.
31 A. Wold and K. Dwight, *Solid State Chemistry: Synthesis, Structure, and Properties of Selected Oxides and Sulfides*, Chapman and Hall, 1993.
32 C. N. R. Rao and K. P. R. Pisharody, *Prog. Solid State Chem.*, 1976, 10, 207.

33 W. Maneeprakorn, M. A. Malik, and P. O'Brien, *J. Mater. Chem.*, 2010, 20, 2329.

34 K. Ramasamy, W. Maneerprakorn, M. A. Malik, and P. O'Brien, *Philos. Trans. R. Soc. London. Ser. A*, 2010, 368, 4249.

35 K. Ramasamy, M. A. Malik, P. O'Brien, and J. Raftery, *Dalton. Trans.*, 2010, 39, 1460.

36 A. L. Abdelhady, K. Ramasamy, M. A. Malik, P. O'Brien, S. J. Haigh, and J. Raftery, *J. Mater. Chem.*, 2011, 21, 17888.

37 M. E. Fleet, *Rev. Mineral. Geochemistry*, 2006, 61, 365.

38 P. Zhang and L. Gao, *J. Mater. Chem.*, 2003, 13, 5638.

39 P. W. Dunne, C. L. Starkey, M. Gimeno-Fabra, and E. H. Lester, *Nanoscale*, 2014, 6, 2406.

40 T. H. Larsen, M. Sigman, A. Ghezelbash, R. C. Doty, and B. a Korgel, *J. Am. Chem. Soc.*, 2003, 125, 5638.

41 N. Revaprasadu, M. A. Malik, and P. O'Brien, *South African J. Chem.*, 2004, 57, 40.

42 Y. Lou, A. C. S. Samia, J. Cowen, K. Banger, X. Chen, H. Lee, and C. Burda, *Phys. Chem. Chem. Phys.*, 2003, 5, 1091.

43 Z. Liu, D. Xu, J. Liang, J. Shen, S. Zhang, and Y. Qian, *J. Phys. Chem. B*, 2005, 109, 10699.

44 S. . Scott and H. . Barnes, *Geochim. Cosmochim. Acta*, 1972, 36, 1275.

45 M. Chunggaze, M. A. Malik, and P. O'Brien, *Dalton. Trans.*, 2006, 4499.

46 Y. Zhang, H. Xu, and Q. Wang, *Chem. Commun.*, 2010, 46, 8941.

47 L. D. Nyamen, A. a. Nejo, V. S. R. Pullabhotla, P. T. Ndifon, M. A. Malik, J. Akhtar, P. O'Brien, and N. Revaprasadu, *Polyhedron*, 2014, 67, 129.

48 G. Zhu, S. Zhang, Z. Xu, J. Ma, and X. Shen, *J. Am. Chem. Soc.*, 2011, 133, 15605.

49 H. G. Ansell and R. S. Boorman, *J. Electrochem. Soc.*, 1971, 118, 133.

50 A. Lutfi Abdelhady, K. Ramasamy, M. A. Malik, and P. O'Brien, *Mater. Lett.*, 2013, 99, 138.

51 S. W. Haggata, M. Motevalli, P. O'Brien, Q. Mary, W. College, M. E. Road, L. El, J. C. Knowles, and B. Materials, *Chem. Mater.*, 1995, 7, 716.

52 M. Afzaal, M. A. Malik, and P. O'Brien, *Chem. Commun.*, 2004, 334.

53 N. Revaprasadu, M. A. Malik, J. Carstens, and P. O. Brien, *J. Mater. Chem.*, 1999, 9, 2885.

54 D. P. Dutta, G. Sharma, A. K. Tyagi, and S. K. Kulshreshtha, *Mater. Sci. Eng. B*, 2007, 138, 60.

55 D. J. Vaughan and J. R. Craig, *Am. Mineral.*, 1947, 70, 1036.

56 G. Kullerud, *Can. Mineral.*, 1963, 7, 353.

57 V. Raghavan, *J. Phase Equilibria Diffus.*, 2004, 25, 373.

58 M. R. Thornber, *J. Appl. Electrochem.*, 1983, 13, 253.

59 P. Bayliss, *Am. Mineral.*, 1989, 74, 1168.

60 R. Pastorek, P. Štarha, T. Peterek, and Z. Trávníček, *Polyhedron*, 2011, 30, 2795.

61 Q. Lu, J. Hu, K. Tang, Y. Qian, G. Zhou, and X. Liu, *Chem. Lett.*, 1999, 28, 481.

62 X. Chen, Z. Zhang, X. Zhang, J. Liu, and Y. Qian, *J. Cryst. Growth*, 2005, 277, 524.

63 Y. Shi, Y. Wang, and L. Wu, *J. Phys. Chem. C*, 2013, 117, 20054.

64 V. Blagojević, G. A. Gledhill, A. Hamilton, S. B. Upadhyay, P. M. Nikolić, M. B. Pavlović, and D. I. Raković, *Infrared Phys.*, 1991, 31, 387.

65 A. A. Vaipolin, Y. A. Nikolaev, I. K. Polushina, V. Y. Rud', Y. V. Rud', E. I. Terukov, and N. Fernelius, *Semiconductors*, 2003, 37, 681.

66 Q. J. Feng, D. Z. Shen, J. Y. Zhang, Y. M. Lu, Y. C. Liu, and X. W. Fan, *Mater. Chem. Phys.*, 2006, 96, 158.

67 S. D. Disale and S. S. Garje, *J. Organomet. Chem.*, 2011, 696, 3328.

68 Y. Li, C. Cao, and Z. Chen, *Mater. Lett.*, 2011, 65, 2432.

69 S. D. Disale and S. S. Garje, *Appl. Organomet. Chem.*, 2009, 23, 492.

70 A. M. Wiltrout, N. J. Freymeyer, T. Machani, D. P. Rossi, and K. E. Plass, *J. Mater. Chem.*, 2011, 21, 19286.
71 V. S. Gurin, *Colloids Surfaces A Physicochem. Eng. Asp.*, 1998, 142, 35.
72 A. M. Malyarevich, K. V Yumashev, N. N. Posnov, V. P. Mikhailov, and V. S. Gurin, *Appl. Phys. B*, 2000, 70, 111.
73 A. M. Malvarevich, K. V Yumashev, N. N. Posnov, V. P. Mikhailov, and V. S. Gurin, *J. Appl. Spectrosc.*, 2000, 67, 359.
74 E. A. Nevar, N. A. Savastenko, V. Bruser, D. A. Lopatik, F. May, A. V Butsen, N. V Tarasenko, and V. S. Burakov, *J. Appl. Spectrosc.*, 2010, 77, 136.
75 Y.-H. A. Wang, N. Bao, and A. Gupta, *Solid State Sci.*, 2010, 12, 387.
76 D. Liang, R. Ma, S. Jiao, G. Pang, and S. Feng, *Nanoscale*, 2012, 4, 6265.
77 W. Du, Z. Zhu, Y. Wang, J. Liu, W. Yang, X. Qian, and H. Pang, *RSC Adv.*, 2014, 4, 6998.
78 G. Hogarth, *Prog. Inorg. Chem.*, 2005, 53, 71.

6 Decomposition Pathway Studies

6.1 Introduction

Various studies have been reported into the mechanism of metal chalcogenide formation by single-source precursor decomposition, due initially to the relevance of such processes in the vulcanisation of rubber, and later for the synthesis of semiconducting nanoparticles (quantum dots). Rubber vulcanisation is a way of introducing covalent crosslinks (often organo-sulfur bridges) between polymer chains in order to increase elasticity and durability, and is a high temperature process (approximately 140 °C).[1–4] Zinc dithiocarbamates in conjunction with primary amines have been used as accelerators for cyclic disulfide crosslinking agents, but the role that these species play in the vulcanisation mechanism is still not fully understood.[5, 4, 2]

In order to better understand the results presented in Chapters 3 – 5, the decomposition pathway of a representative dithiocarbamate precursor, namely $[Ni(S_2CN^iBu_2)_2]$ was studied. This was chosen as it was one of the more extensively investigated in this thesis, and is potentially far simpler than the decomposition of iron dithiocarbamates, for which precursors can have high- or low-spin electronic configurations and also undergo metal-based redox transformations. We also aimed to address the role of thiuram disulfide additive **6**.

Before reviewing the relevant literature on mechanisms of metal dithiocarbamate decomposition, a brief overview of some related metal chalcogenide single-source precursors is presented. In particular, metal xanthate complexes have been studied as single source precursors for metal sulfide nanoparticles by several groups,[6–9] and decomposition pathway(s) proposed.[6, 8, 10] The accepted mechanism is based on the Chugaev reaction for the pyrolysis of xanthates (Figure 6-1).[11, 12] This involves a pericyclic reaction, resulting in an intramolecular sulfur protonation and release of an alkene, followed by further decomposition of the intermediate resulting in a metal sulfide, xanthic acid and carbonyl sulfide (OCS).[8] Addition of a Lewis base is suggested to promote the reaction by either facilitating sulfur protonation by nucleophilic attack on the CS_2 carbon or forming a protonated intermediate, or by weakening a metal – sulfur bond by coordination to the metal centre, thus activating the ligand as a leaving group.[8]

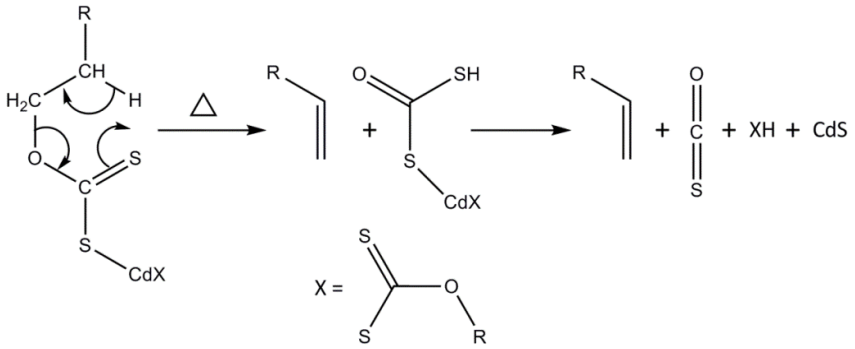

Figure 6-1 - Proposed Chugaev-like mechanism for cadmium xanthate complex decomposition

O'Brien and co-workers have published several papers on the decomposition pathway of metal chalcogenide single-source precursors for CVD, particularly utilising mass spectrometry.[13–15] For example, the pyrolysis of diselenocarbamate metal complexes was studied by GC-MS and EI-MS and found to give in selenium clusters.[13] The first step in the thermal decomposition was shown to be the loss of an alkyl group, followed by elimination of an $EtSe_2Et$ group. It is suggested that this group is the source of the selenium clusters observed for some precursors.[13] O'Brien has also studied the room temperature decomposition of $[Pb\{(C_6H_5)_2PSSe\}_2]$ in an oleylamine/dodecanethiol solution, experimentally and using density function theory (DFT) calculations.[15] Attack of a thioalkoxide ion (RS^-) from the solvent at phosphorus was suggested to initiate decomposition, indicating that the solvent is non-innocent, and not just acting as a heat-sink/capping agent.[15]

There are several other reports in the literature proposing the non-innocent nature of the solvent employed in single-source precursor decomposition reactions, particularly primary amines such as oleylamine, which are suggested to promote the solvothermal decomposition of metal dithiocarbamate complexes.[4, 5, 8, 16–18] Previous studies which attempt to elucidate the mechanism of metal dithiocarbamate decomposition have primarily focussed on the zinc and cadmium bis(dithiocarbamate) complexes, having the most relevance to rubber vulcanisation and quantum dots, respectively.[4, 5, 14, 19, 20] Some studies have looked at the solid state pyrolysis of these precursors in order to evaluate their suitability for use as precursors for CVD, and although this work is not directly relevant to solvothermal decomposition it could shed some light on some aspects of that pathway.[6, 20, 21] In particular Wold *et al.* investigated the pyrolysis products from the solid-state decomposition of $[Zn(S_2CNEt_2)_2]$ by GC-MS, and detected ethyl isothiocyanate (Figure 6-2), CS_2 and Et_2NH.[19]

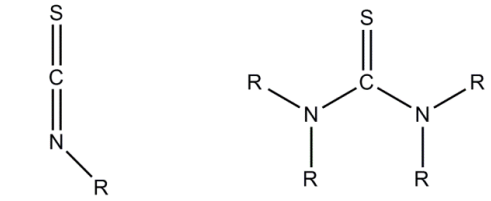

Isothiocyanate Thiourea (R = H or alkyl group)

Figure 6-2 - Structures of common decomposition by-products isothiocyanate and thiourea.

The role of the primary amine solvent has been investigated by several groups, with particular focus on $[Zn(S_2CNMe_2)_2]$.[5, 4, 17] All the reports begin with the assumption that the precursor complex forms an amine adduct. It should be noted like $[Zn(S_2CNR_2)_2]$, nickel(II) bis(dithiocarbamates) have been found to act as Lewis acids, although their ability to do so depends upon the electron-withdrawing ability of the dithiocarbamate substituents.[22] Complexes with chelating ligands have also been reported, such as the 1,10-phenanthroline adduct, $[Ni(S_2CNEt_2)_2(1,10\text{-phen})]$, which crystallise upon slow cooling of an acetone solution of $[Ni(S_2CNEt_2)_2]$ and a slight excess of 1,10-phenanthroline.[23]

The first investigation into the solvothermal decomposition of $[Zn(S_2CNMe_2)_2]$ was performed by Gelling in 1974 on the pre-synthesised $[Zn(S_2CNMe_2)_2(^nBuNH_2)]$ adduct.[5] The authors claim to synthesise this penta-coordinated adduct according to the method described by Higgins and Saville, though there is little analytical data presented in either paper.[24] The $[Zn(S_2CNMe_2)_2(^nBuNH_2)]$ adduct was then heated to 100 °C in toluene in a sealed tube for 4 hrs which Gelling suggests produces ZnS, *N*-butyl-*N*',*N*'-dimethylthiourea, ($\{NMe_2\}\{NH^nBu\}CS$), the ammonium dithiocarbamate salt $[Me_2NH_2][S_2CNMe_2]$ and a small amount of *N*,*N*'-dibutylthiourea ($\{NH^nBu\}_2CS$, see Figure 6-3).[5] Though this assignment of the by-product may be correct, the only evidence is IR data.[5] Monitoring the levels of $[Zn(S_2CNMe_2)_2]$ and $(NMe_2)(NH^nBu)CS$ during the decomposition by IR spectroscopy led to the proposal of a mixed-ligand intermediate, $[Zn(S_2CNMe_2)(S_2CNH^nBu)]$.[5] The authors propose a decomposition mechanism where the first step is nucleophilic attack of the coordinated primary amine group on the CS_2 carbon, leading to amine exchange generating the mixed ligand intermediate (Figure 6-3).[5]

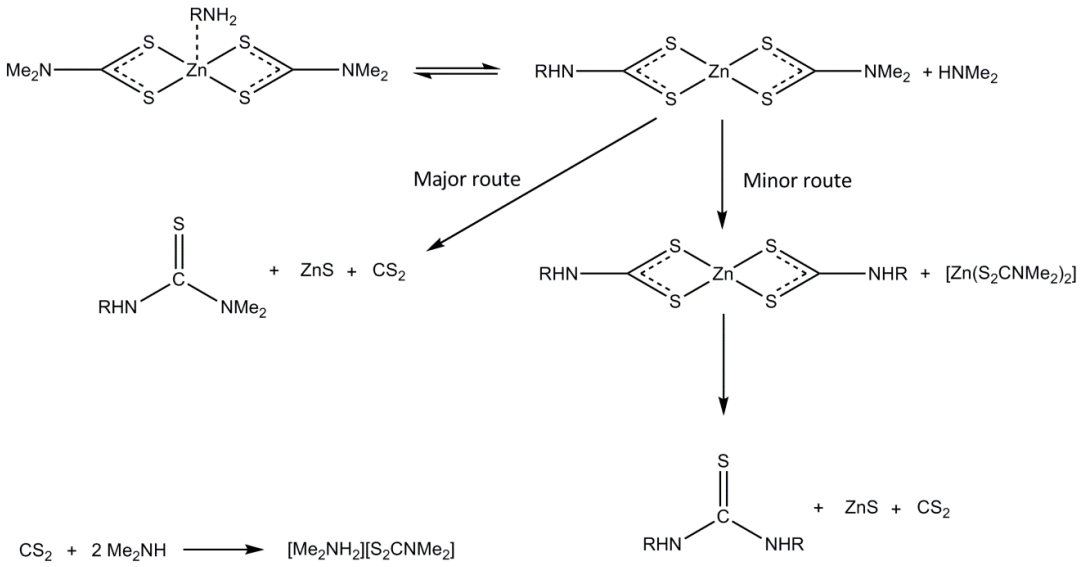

Figure 6-3 - [Zn(S$_2$CNMe$_2$)$_2$(RNH$_2$)] solvothermal decomposition pathway proposed by Gelling.

The second step is divided between two pathways, one is decomposition of this intermediate leading to (NMe$_2$)(NH^{n}Bu)CS, CS$_2$ and zinc sulfide. Due to new peaks observed in the *in situ* IR spectra, suggestive of an additional intermediate species, the authors propose an additional minor route to the decomposition pathway, which involves a further amine exchange producing the [Zn(S$_2$CNH^{n}Bu)$_2$] intermediate, which then decomposes to form ZnS, (NH^{n}Bu)$_2$CS and CS$_2$ (the latter two species being observed by IR, post-reaction). The formation of [Me$_2$NH$_2$][S$_2$CNMe$_2$] is proposed to result from the reaction of two decomposition by-products, CS$_2$ with two equivalents of Me$_2$NH (Figure 6-3).[5] To support the necessity of a primary amine intermediate the authors attempt the decomposition of the secondary amine adduct [Zn(S$_2$CNMe$_2$)$_2$(^{n}Bu$_2$NH)], resulting in only the initial amine exchange and no decomposition, while heating the tertiary amine adduct had no effect at all.[5]

There is literature evidence supporting the first step of Gelling's proposed mechanism, with several papers describing the nucleophilic attack of a primary amine on the electron-deficient backbone carbon of a thiolate precursor.[16, 8] In a paper by Chin *et al.*, the thiobenzoate precursor [Pb(SCOC$_6$H$_5$)$_2$], decomposed without heating upon addition of a primary or secondary amine.[16] Nucleophilic attack of the amine on the electron deficient carbonyl carbon is proposed and supported by DFT calculations.[16] Further evidence of nucleophilic attack on an *sp*^{2} hybridised carbon of a thiolate precursor is given by Fackler and co-workers.[25, 26] NMR evidence of the transformation of metal xanthates to dithiocarbamates upon reaction with primary and secondary amines was presented, in

particular a detailed study of the reaction of $[Pt(S_2COEt)_2]$ with piperidine resulted in formation of $[Pt(S_2CNC_5H_{10})_2]$.[25] Similar work has been reported for nickel xanthate complexes with secondary amines, where thiourethanes, $R_2NC(S)OR'$, together with nickel bis(dithiocarbamate) complexes were formed.[27] Metal dithiocarbamate complexes have also been generated from the reaction of alkyl trithiocarbonate complexes with secondary amines, with concomitant elimination of thiol.[26, 28–30]

Gelling's premise that decomposition proceeds *via* primary amine substitution at the backbone CS_2 carbon is supported by several studies on the decomposition of primary amine dithiocarbamate complexes, most notably by Caudle *et al.*[20, 14] who probed the solid-state thermal decomposition of $[Cd(S_2CNHR)_2]$ (R = C_3S_7, C_5S_{11}, $C_{12}H_{25}$) and observed CdS and isothiocyanate were produced, together with the primary amine and CS_2 as co-products.[20] They deduced that a net transfer of protons must be occurring during decomposition for these species to be formed, and propose a decomposition pathway, the first step being a proton transfer from the NHR group of one ligand to a CS_2 sulfur atom leading to the release of an isothiocyanate group (Figure 6-4).[20] Furthermore, addition of a tertiary amine to a solution of $[Cd(S_2CNHR)_2]$ also led to decomposition, supporting the notion that decomposition is linked to deprotonation of the ligand NRH group, and possibly explaining why Gelling did not observe decomposition of the secondary and tertiary amine $[Zn(S_2CNMe_2)_2]$ adducts.[20]

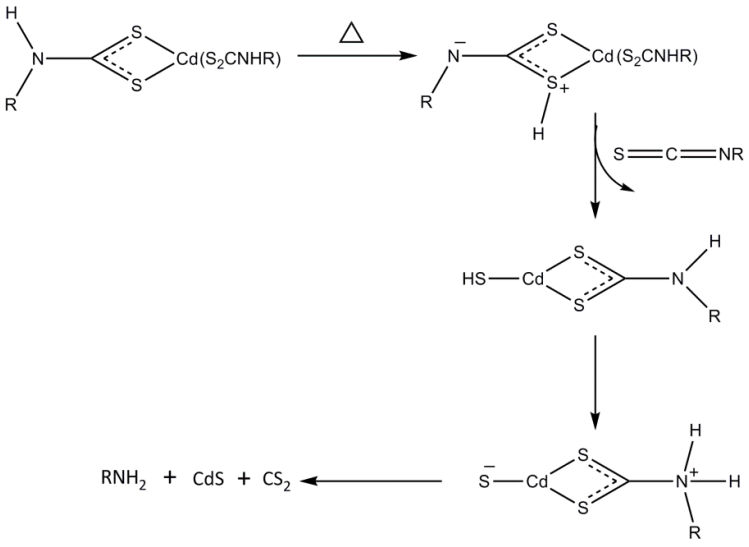

Figure 6-4 - Thermal decomposition mechanism for $[Cd(S_2CNHR)_2]$ proposed by Caudle.

Gelling's mechanism for the solvothermal decomposition of $[Zn(S_2CNMe_2)_2]$ was further developed by Reedijk and co-workers, using a combination of analysis techniques including NMR spectroscopy, high-performance liquid chromatography (HPLC) and thin

layer chromatography (TLC).[4] When [$Zn(S_2CNMe_2)_2$] was heated at 140 °C for 1 hr in *n*-hexylamine ($^nHexNH_2$) zinc sulfide, *N*-hexyl-*N*',*N*'-dimethylthiourea ({NMe_2}{NH^nHex}CS), [Me_2NH_2][S_2CNMe_2] and *N*,*N*'-dihexylthiourea ({NH^nHex}$_2$CS) were detected.[4] Kinetic studies on the rate of formation of the thioureas (NMe_2)(NH^nHex)CS and (NH^nHex)$_2$CS showed the latter formed more slowly and was more abundant at the end of the decomposition.[4] This indicates that [$Zn(S_2CNMe_2)_2$] decomposes to form (NMe_2)(NH^nHex)CS which reacts further to form (NH^nHex)$_2$CS. In support of this theory, (NMe_2)(NH^nHex)CS was shown to react with *n*-hexylamine to form (NH^nHex)$_2$CS.[4]

To explain the observed results a decomposition mechanism was proposed (Figure 6-5), which, like Gelling's mechanism, is initiated by the reversible nucleophilic attack of primary amine on the thiocarboxy carbon.[4] However, unlike Gelling's mechanism, based on the organic by-products observed by HPLC and NMR Reedijk proposes an amine dithiocarbamaic transition state (Figure 6-5) which can decompose *via* two routes: **A**) proton transfer to a sulfur atom or **B**) proton transfer to the other amine leaving group.[4] Route **A** produces [$Zn(SH)(S_2CNMe_2)$] and the mixed thiourea (NMe_2)(NH^nHex)CS, while route **B** goes through a [$Zn(S_2CNMe_2)(S_2CNH^nHex)$] intermediate, much like the one proposed by Gelling.[4, 5] Reedijk notes that the thiourea, (NH^nHex)$_2$CS, can be made a number of ways including primary amine attack on the [$Zn(S_2CNMe_2)(S_2CNH^nHex)$] intermediate at the NH^nHex thiocarboxy carbonyl, or attack on (NMe_2)(NH^nHex)CS by primary amine, as mentioned above.[4] The authors do not present any evidence for the amide exchange they propose, but suggest that it must occur for the by-products observed to be formed.[4]

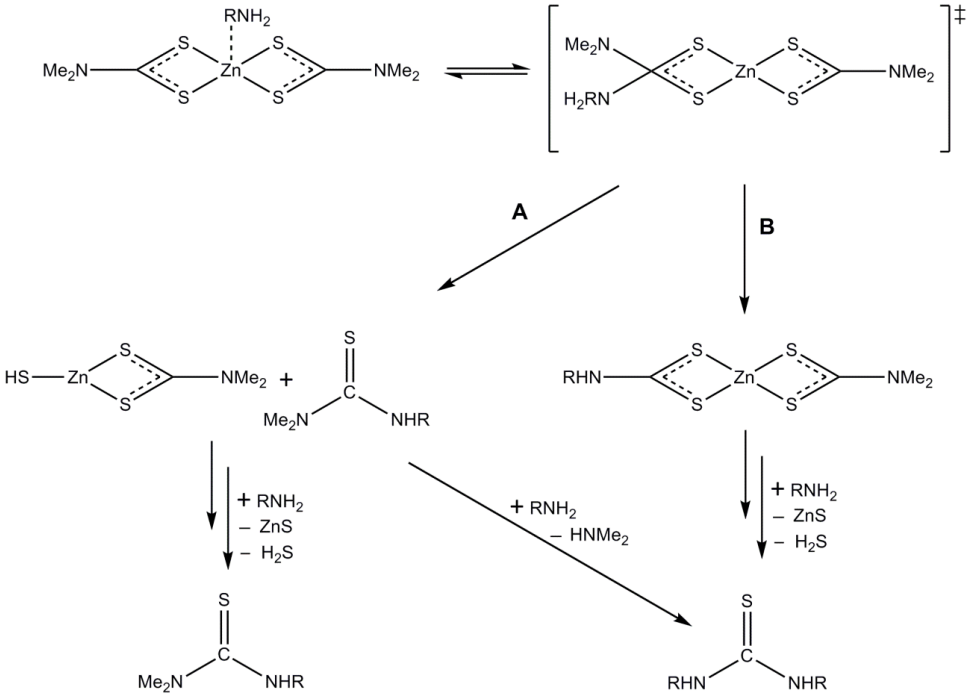

Figure 6-5 - Solvothermal decomposition mechanism for $[Zn(S_2CNMe_2)_2]$ proposed by Reedijk.

As with the Gelling study, decomposition in secondary and tertiary amines was also attempted, and, like the previous results, amine exchange is observed in the former reaction, while no observable reaction takes place in the latter.[4] The authors suggest that as the secondary amine only has one available proton, when the amine dithiocarbamatic transition state is formed, the amine proton must interact with either the transition state's other secondary amine nitrogen atom, or a sulfur atom to proceed with decomposition.[4] The authors claim this proton is less available and so less likely to be in the specific orientation for sulfur protonation, therefore amine exchange proceeds preferentially and decomposition is not observed.[4] This, however, is a somewhat tenuous explanation.

Most recently, Lee and co-workers have investigated the decomposition pathway of $[Zn(S_2CNMe_2)_2]$ using NMR.[17] As with Gelling's work, the authors claim to pre-synthesise an amine adduct, $[Zn(S_2CNMe_2)_2(^nOctNH_2)_2]$, by stirring $[Zn(S_2CNMe_2)_2]$ with two equivalents of amine and noting a shift in the NH-$CH_2C_7H_{15}$ $^{13}C\{^1H\}$ NMR spectrum, though no further evidence for the adduct is presented.[17] This species is then heated in toluene for 1 hr at 50, 80 and 100 °C, so it can be supposed that if an adduct was not formed previously, two equivalents of amine is still present in solution during the decomposition and available for subsequent adduct formation.[17] The products were analysed by ^1H – and $^{13}C\{^1H\}$-NMR spectroscopy and peaks in the latter spectra suggest two quaternary carbon

environments are present at different times during the decomposition. The reaction at 80 °C yielded products with two quaternary peaks, while only one of these peaks is seen at 50 °C and the other at 100 °C.[17] This is attributed to nucleophilic attack of the coordinated primary amine on the electron deficient thiocarboxy carbonyl of the dithiocarbamate ligand backbone (as suggested by Reedijk), forming an intermediate (Intermediate 1, Figure 6-6) which is assigned to the new quaternary carbon peak that appears at 80 °C and remains at 100 °C.[4, 17] The authors claim that at 50 °C this intermediate does not exist, so the only quaternary carbon peak seen is due to the ligand CS_2.[17] At 80 °C attack of the primary amine on one of the $[Zn(S_2CNMe_2)_2]$ dithiocarbamate ligands occurs, so a mixed species is seen resulting in two distinct quaternary carbon peaks.[17] At 100 °C the authors claim further nucleophilic attack on the other dithiocarbamate ligand results in a second, fully saturated intermediate (Intermediate 2, Figure 6-6), which accounts for the lack of the precursor CS_2 quaternary peak.[17]

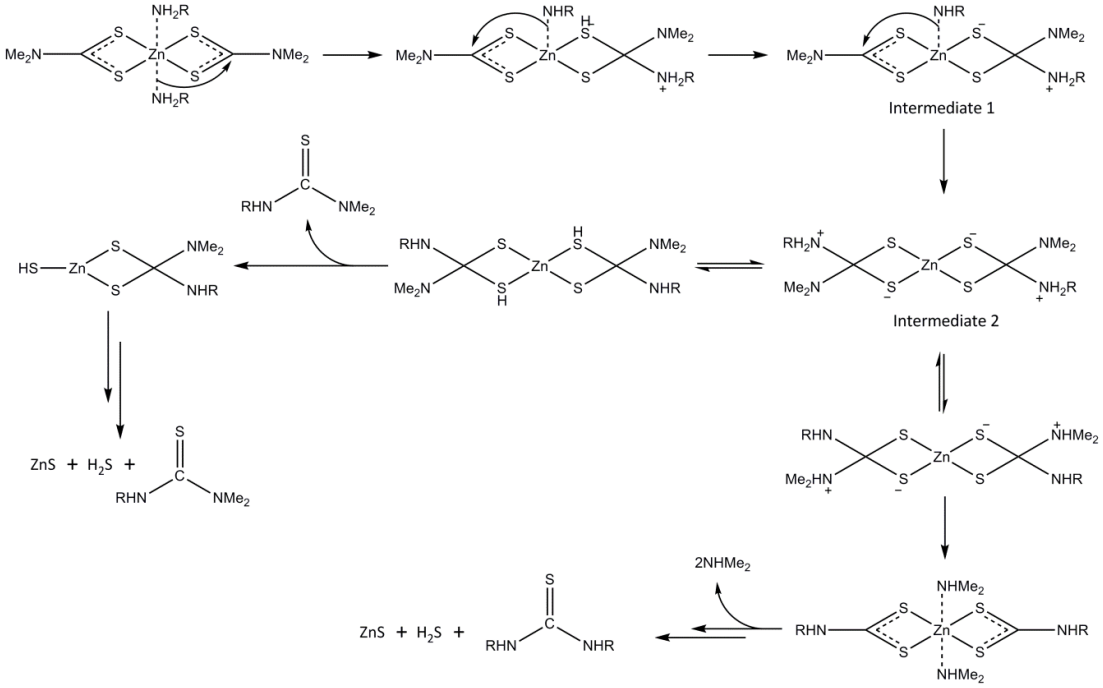

Figure 6-6 - $[Zn(S_2CNMe_2)_2]$ solvothermal decomposition pathway proposed by Lee.

This explanation of the NMR results is unlikely, however, for a number of reasons. Firstly, the fact that these intermediates are stable enough to survive until the end of the reaction, and be measured by NMR, is implausible. It is much more likely that they would be highly unstable transition states if they are indeed formed at all. Secondly, there is no reason to suggest that at 80 °C single nucleophilic attack occurs and at 100 °C a second attack occurs, the fact that two peaks are seen in the ^{13}C-NMR spectrum could easily be due to a mixture of unreacted precursor and an intermediate or by-product, which accumulates towards

the end of the decomposition (for after 1 hr at 100 °C the authors claim to synthesise zinc sulfide elsewhere in the paper).[17] In order to support their hypothesis, the authors perform 2D NMR spectroscopy – gradient heteronuclear multiple-bond correlation (gHMBC) – and observe cross-peaks between the new quaternary carbon and protons associated with Me_2NH and octylamine.[17] This, however, would also be observed for the known by-product thiourea, *N*-octyl-*N*',*N*'-dimethylthiourea in this case, observed by both Reedijk and Gelling.[4, 5]

Lee *et al*. account for the detection of the symmetric thiourea *N*,*N*'-dioctylthiourea by a side reaction to the main decomposition mechanism, where the fully substituted second intermediate loses two equivalents of the secondary amine $HNMe_2$, leading to the formation of the fully amide exchanged complex $[Zn(S_2CNH^nOct)_2]$ (Figure 6-6).[17] This then decomposes through primary amine attack on the thiocarboxy-carbons, yielding the symmetric thiourea *N*,*N*'-dioctylthiourea.[17] Like Gelling and Reedijk, the authors perform an analogous reaction in a secondary amine, and only observe amine-exchange to form $[Zn(S_2CNH^nOct)_2]$.[17] They explain this result by suggesting that the steric bulk of the secondary amine about the thiocarboxy-carbon prevents protonation of sulfur by the incoming amine, which is a crucial step in the decomposition.[17]

Though Lee *et al*. present a plausible decomposition mechanism for a metal dithiocarbamate complex in the presence of a primary amine, here we will show their mechanism is based on incorrectly assigned ^{13}C-NMR spectra. Further, the work of Gelling and Lee are both performed in toluene using a pre-formed, but poorly characterised, $[Zn(S_2CNMe_2)_2]$ amine adduct, conditions which vary significantly from those generally used to create metal sulfide nanoparticles. In order to follow the decomposition of $[Ni(S_2CN^iBu_2)_2]$ a combination of NMR, MS, powder XRD and *in situ* UV-vis was employed. Attaining a thorough understanding of decomposition mechanism will provide an insight in how to tailor the decomposition to target particular metal sulfide phase. The benefits of which will transcend primarily nickel sulfide synthesis and be applicable the wider role of metal dithiocarbamates for nanoparticle formation.

This work forms part of a wider project on metal sulfide synthesis and catalysis involving several researchers from the fields of electrochemistry, X-ray absorption spectroscopy (XAS) and computational modelling. This expertise was utilised to support this experimental work by employing DFT calculations (performed by Maxime Mercy and Alberto Roldan Martinez), and *in situ* XAS (performed and interpreted by Husn-Ubayda

Islam). The combined experimental-theoretical approach has led to a full picture of thermal decomposition of nickel bis(dithiocarbamate) complexes into nickel sulfides which is applicable to general metal sulfide nanoparticle synthesis from metal dithiocarbamate decompositions.

6.2 Results and Discussion

6.2.1 Nickel bis(dithiocarbamate) Precursor and Stability

$[Ni(S_2CN^iBu_2)_2]$ (**21**) was previously synthesised and characterised by single crystal X-ray diffraction (Chapter 4) and its stability in the solid state was investigated. TGA/DSC data showed it melts at 177°C and evaporates at 252°C, with no evidence of thermal decomposition up to 344°C when it is completely lost by evaporation (Chapter 4, Figure 4-2c). Its solvothermal stability was tested by heating **21** in the non-coordinating solvent dodecane ($C_{12}H_{26}$) at 200 °C for 1 hr resulting in no visible change to the clear green solution and upon cooling spectroscopic data confirmed the presence of only **21**. This finding was corroborated by in situ EXAFS measurements which showed no significant change to the coordination environment of nickel during and after heating in this solvent. In the same way, heating **21** in trihexylamine or 1,4-diazabicyclo[2.2.2]octane (DABCO) at 150 °C for 1 hr produced no evidence of decomposition or amide-exchange products. Further, heating **21** in dihexylamine gave no evidence of decomposition to nickel sulfides up to 190 °C. Literature reports suggest that under these conditions amide-exchange and sequential conversion of **21** into $[Ni(S_2CN^iBu_2)(S_2CN^nHex_2)]$ and $[Ni(S_2CN^nHex_2)_2]$ should occur.[4, 5, 17] Spectroscopic data including $^{13}C\{^1H\}$ NMR and MS of the resulting solution showed evidence of this exchange. MS of the reaction liquor shows evidence for $[Ni(S_2CN^iBu_2)(S_2CNHex_2)]$ $[MH_3]^+$ 525.3560 (found), 525.1976 (calculated) and also un-reacted **21** $[\mathbf{21}.H_3]^+$ 469.4402 (found) 469.1350 (calc). There was no evidence in the MS for the fully substituted complex $[Ni(S_2CNHex_2)_2]$ although it may have been fragmented in the ionisation process. Green crystals from the reaction liquor produced $^{13}C\{^1H\}$ NMR spectra revealing two quaternary carbon peaks, one at 208.4 ppm due to **21**, and a second at 206.5 due to $[Ni(S_2CNHex_2)_2]$ (independently synthesised and found to have a quaternary carbon peak at 206.4 ppm).

6.2.2 Solvothermal Decomposition of $[Ni(S_2CN^iBu_2)_2]$ (21)

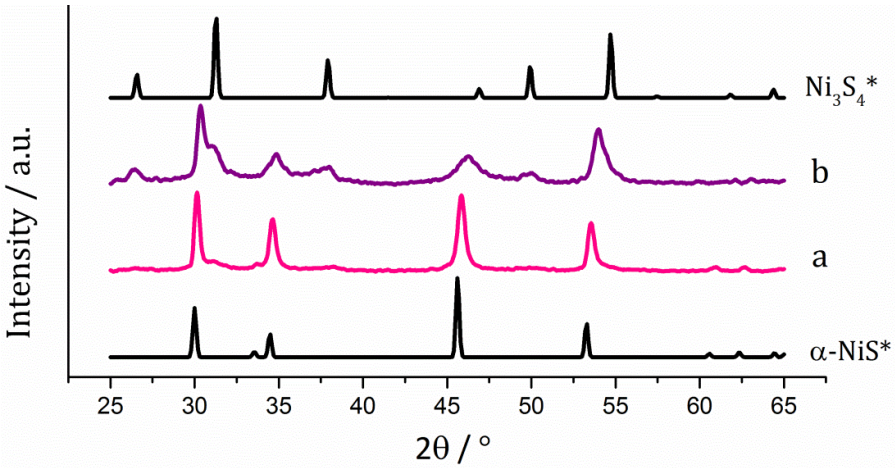

Figure 6-7 - XRD patterns for NPs obtained from 21 decomposed in (a) oleylamine (b) *n*-hexylamine, with reference patterns for bulk α-NiS (ICDD card No. 02-1273) and Ni_3S_4 (ICDD card No. 43-1469).

As shown in Chapter 4, heating **21** in the oleylamine for 1 hr at 230 °C gave nanoparticles of hexagonal α-NiS. Colour changes were observed during heating, such that at 118 °C the clear green solution turned brown and then black by 145 °C. After heating **21** for 1 hr at 150 °C hexagonal α-NiS was formed (Figure 6-7), consistent with the previous result at 230 °C. TEM analysis shows the particles are hexagonal with an average diameter of *ca*. 40 nm, while HRTEM shows lattice fringes with a spacing of 2.67 Å consistent with [002] lattice plane of α-NiS (Figure 6-8a).

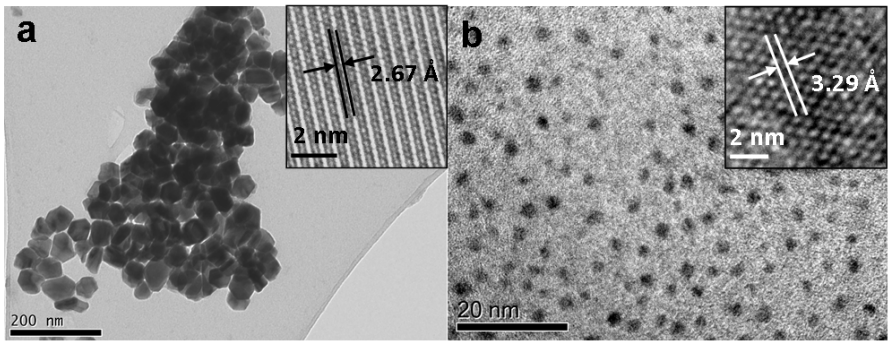

Figure 6-8 TEM data with inset HRTEM and marked lattice planes of particles resulting from the decomposition of 21 in (a) oleylamine (b) *n*-hexylamine.

While oleylamine is commonly used in nanoparticle synthesis, its low purity (ca. 70% from commercial sources) provides challenges when probing mechanistic information spectroscopically. In order to follow the decomposition in a primary amine, *n*-hexylamine was used as this can be purchased in a purer form than oleylamine and its sulfur-

containing organic decomposition products are commercially available to use as spectroscopic standards. As such, the decomposition mechanism of **21** in *n*-hexylamine was first studied in order to attain a clearer understanding.

Heating **21** in *n*-hexylamine led to the initially clear green solution turning brown (at 70 °C) and then black (at 90 °C). Heating was continued to 120 °C for 1 hr. Upon cooling, powder XRD confirmed the crystalline phase of the isolated nanoparticles to be a mixture of polydymite (Ni_3S_4) and α-NiS (Figure 6-7). TEM showed the particles to be spherical with an average diameter of *ca.* 1.9 nm, while HRTEM shows spacings of 2.83 and 3.29 Å consistent with the [311] and [220] lattice plane of Ni_3S_4 (Figure 6-8b). The discrepancy in nanoparticle phase formed when decomposing **21** in either oleylamine or *n*-hexylamine is likely a result of the different decomposition temperatures and the nickel sulfide phase diagram since α-NiS in the solid state is reported to be stable to higher temperatures than Ni_3S_4.[31] As such, the higher temperature decomposition in oleylamine (150°C for 1 hr) as compared to *n*-hexylamine (120°C for 1 hr) provides a plausible explanation for this discrepancy.

6.2.3 Nature of $[Ni(S_2CN^iBu_2)_2]$ (21) in *n*-hexylamine

To elucidate a decomposition mechanism, *in situ* UV-vis and EXAFS were employed to monitor changes to the metal centre. Complex **21** has a d^8 square planar geometry and, as such, is expected to be diamagnetic and easily observable in ^1H and $^{13}C\{^1H\}$ NMR spectra. However addition of *n*-hexylamine results in significant peak broadening of the ^1H and $^{13}C\{^1H\}$ NMR spectra. Such peak broadening could be due to the formation of a paramagnetic complex, which may result from the formation of an octahedral geometry at nickel.

The UV-vis spectrum of **21** at room temperature in *n*-hexylamine is quite different to its spectrum in hexane (Figure 6-9). This suggests a change in the nickel co-ordination environment on addition of amine, possibly to an octahedral complex.

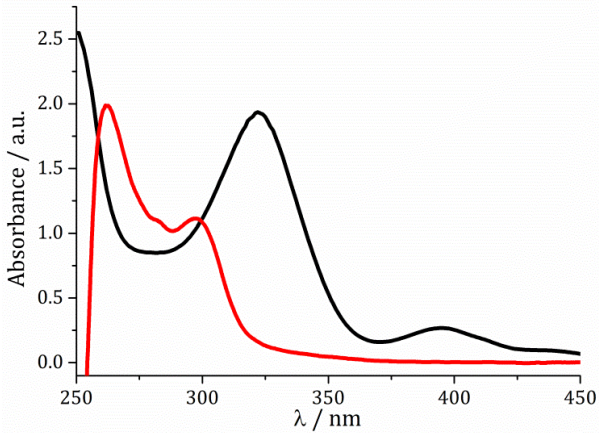

Figure 6-9 - UV-vis spectra of 21 in hexane (red line) and *n*-hexylamine (black line).

In order to further substantiate the nature of **21** in *n*-hexylamine, XAS was performed and confirms a change in geometry to an octahedral species. Thus, XANES and XAFS modelling fit for two nickel-nitrogen distances corresponding to nickel-amine interactions at 2.03 Å, in addition to two slightly different nickel-sulfur interactions at 2.32 and 2.47 Å, which are lengthened from 2.20 Å found in **21** in both the solid state and when dissolved in dodecane.

DFT simulations were carried out and compared with the XAS information. To reduce computational cost $[Ni(S_2CNEt_2)_2]$ was modelled in $EtNH_2$. The optimized square planar Ni-S distances in $[Ni(S_2CNEt_2)_2]$ compare well with the EXAFS data in the solid state for **21** (2.20 Å and 2.21 Å for EXAFS and simulated distances respectively). Two amine groups were then added in an octahedral geometry and differences were tested. Four minima were localised on the potential energy surface: two isomers, *cis* and *trans*, and for each complex, singlet and triplet states, the structures and energies are shown in Figure 6-10. The paramagnetic triplet complexes (**a**^{3}) are the lowest in energy this is in agreement with the XAS showing an octahedral species in solution. The conformer **a**^{3}***trans*** is the most stable and it can be attributed to the most likely geometry about **21** when dissolved in a primary amine.

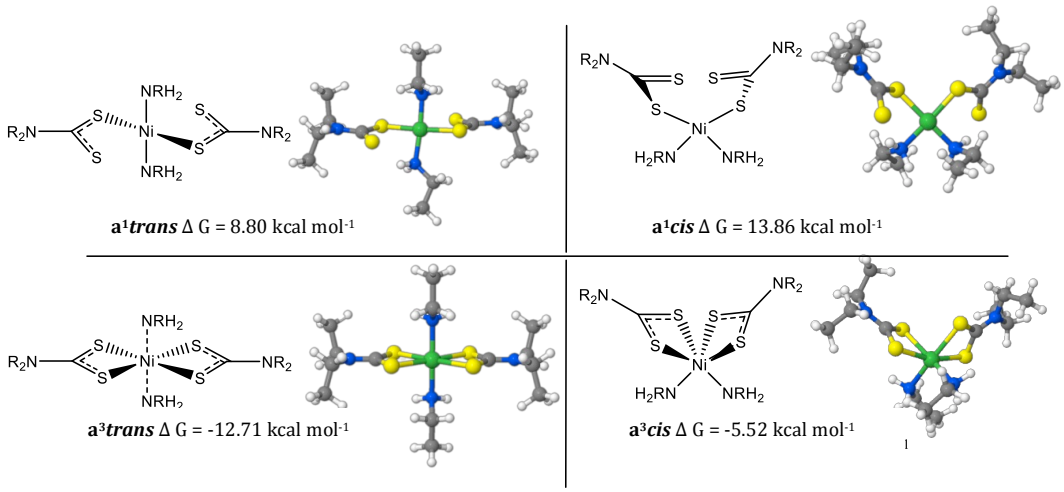

Figure 6-10 - $[Ni(S_2CNR_2)_2(amine)_2]$ complexes and their relative stabilities (Gibbs free energies in kcal.mol^{-1}) with reference to $[Ni(S_2CNR_2)_2]$ at B3PW91 level with continuous solvent model (pentylamine).

6.2.4 Heating $[Ni(S_2CN^iBu_2)_2]$ (21) in *n*-hexylamine

Studies were next carried out in order to probe the mechanism of decomposition of **21** in *n*-hexylamine. The *in situ* UV-vis spectroscopy revealed that, up to 75 °C, peaks at 285, 298 nm associated with **21** in *n*-hexylamine, decreased with concomitant growth of a peak at 325 nm (Figure 6-11). The latter is similar to that of **21** in hexane and is associated with formation of a square planer complex, presumably by loss of coordinating amine(s). These findings are supported by *in situ* XAS for which linear combination analysis indicates 56% square planar and 44% octahedral conformation at 70 °C, increasing to 65% square planar and 35% octahedral coordination at 80°C, thus showing that upon heating between 70-80 °C, octahedral **21**, reverting to back to a square planar complex.

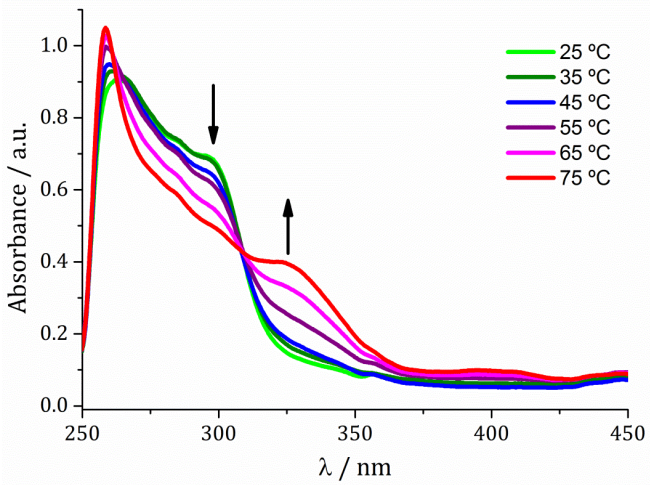

Figure 6-11 - *In situ* UV-vis monitoring of heating 21 in *n*-hexylamine (0.16 mM) from 25 - 75°C

The prior observation that **21** does not decompose in dodecane up to 200 °C, suggests that when **21** dissolves in *n*-hexylamine it forms an octahedral adduct, which when heated forms another square planar complexes, different to **21**. Given amide-exchange about metal dithiocarbamates has been shown to occur for secondary amines here and by others,[4, 5, 17] then a plausible intermediate would be the amide exchange product of **21** with *n*-hexylamine.

6.2.5 Modelled Amide-Exchange

To show the feasibility of amide-exchange, a plausible mechanism was modelled at 298 K using computational methods based on DFT at B3PW91/6-31G(d,p) level. The process was shown to proceed *via* two processes; firstly, an initial exchange forming [Ni($S_2CN^iBu_2$)(S_2CN{H}Hex)] (**28**) followed by a second exchange to give [Ni(S_2CN{H}Hex)$_2$] (**29**). The exchange is shown to proceed *via* the transfer of a proton from the primary amine group to the amino substituent *via* a metathesis-like 4-membered transition state (TS1 and TS2 Figure 6-12) with a concerted dissociation and formation of two bonds (C-N and N-H) leading to an quasi iso-energetic compound. An activation energy of ΔG‡(TS1) = +53.2 kcal.mol^{-1} is required to perform one exchange, a second exchange can proceed with approximately the same activation energy ΔG‡(TS2) = +52.66 kcal.mol^{-1}.

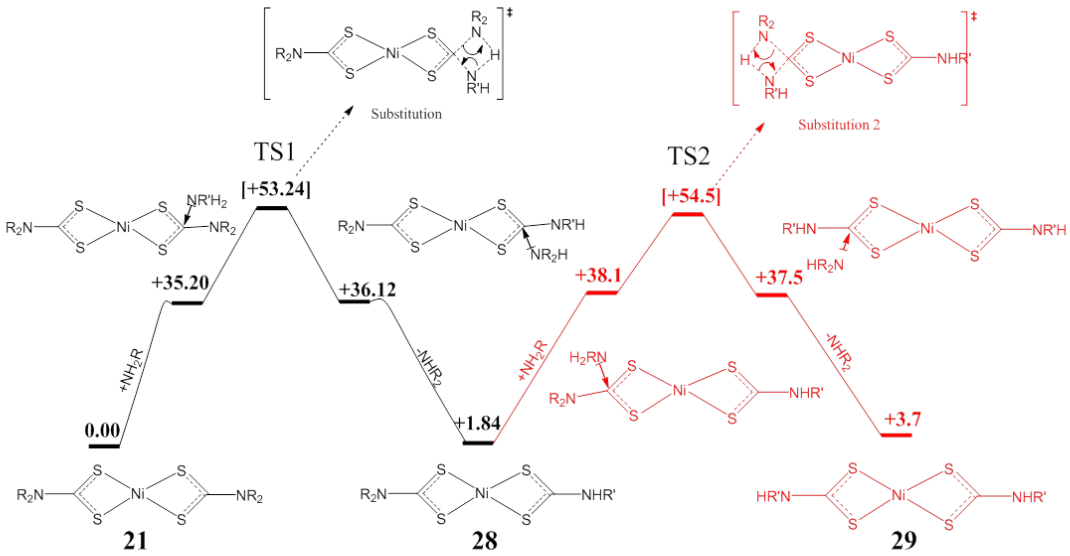

Figure 6-12 - Modelled amide exchange energy profile, energies in kcal.mol^{-1}.

6.2.6 Solvothermal Decomposition of [Ni(S_2CN{H}Hex)$_2$] (29)

In order to substantiate that **21** decomposes in *n*-hexylamine *via* initial formation of the amide-exchange complex, [Ni(S_2CN{H}Hex)$_2$], **29**, we independently prepared **29** and studied its coordination properties and thermal decomposition. Heating **29** in dodecane for 1 hr at 120 °C gave a green-brown solution up until 90 °C, above which it turned black, consistent with decomposition to nickel sulfides. Decomposition of **29** in a non-coordinating solvent at 90 °C, the same temperature observed for the onset of decomposition of **21** in *n*-hexylamine, together with observation that **21** is stable in non-co-ordinating solvents up to 200 °C, suggests the square planar complex formed during decomposition is not likely to be **21**. Complex **29** is a more plausible intermediate during the decomposition of **21** in *n*-hexylamine. This is further substantiated by analysing **29** by UV-vis spectroscopy in *n*-hexylamine and hexane, the latter spectrum closely resembling that of the intermediate square-planar complex observed during the decomposition of **21** in *n*-hexylamine (Figure 6-13). Moreover, XANES analysis indicated the square-planar structure formed during the decomposition of **21** in *n*-hexylamine is similar to **29**.

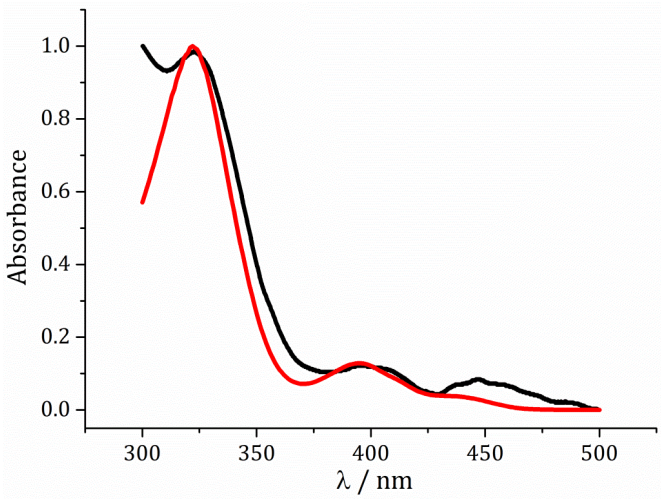

Figure 6-13 - UV-vis spectral comparison of 29 in a non-coordinating solvent (red) and the square planar complex formed during the decomposition of 21 in *n*-hexylamine (black).

XRD analysis of isolated nanoparticles from the decomposition of **29** in dodecane revealed the crystalline phase to be a mixture of polydymite (Ni_3S_4) and α-NiS (Figure 6-14(a)). TEM analysis showed spherical particles with an average diameter of *ca*. 20 nm, while HRTEM showed lattice planes spacings of 2.36 Å consistent with [004] plane of Ni_3S_4 (Figure 6-14(b)). The increase in particle size as compared to the decomposition of **21** in *n*-hexylamine can be attributed to the lack of a capping agent to prevent Oswald ripening during decomposition.

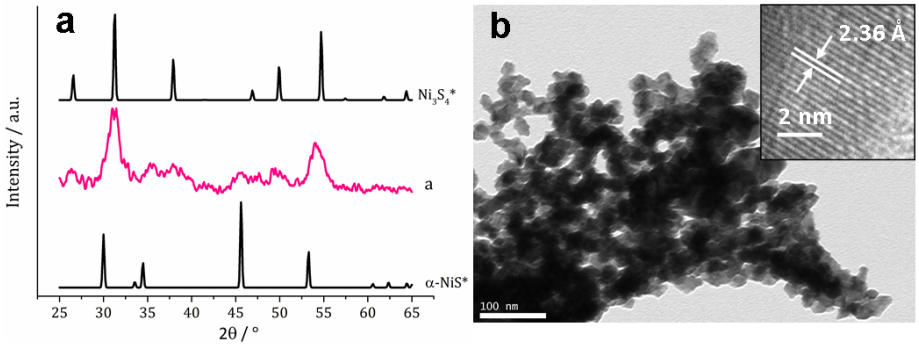

Figure 6-14 - Analysis of nanoparticles obtained from 29 decomposed in dodecane (a) powder XRD pattern, with reference patterns for bulk α-NiS (ICDD card No. 02-1273) and Ni_3S_4 (ICDD card No. 43-1469). (b) TEM data with inset HRTEM and marked lattice planes.

In addition to solvothermal decomposition, the solid state decomposition of **29** can be followed by TGA/DSC (Figure 6-15), showing a two-stage decomposition process. Firstly, an endothermic mass loss equivalent to isothiocyanate occurs at 145 °C followed by an endothermic mass loss equivalent to a whole dithiocarbamate moiety at 175 °C leaving a residual mass of NiS. This is quite different from the TGA/DSC analysis of **21** whereby stability to >350°C was observed followed by evaporation.

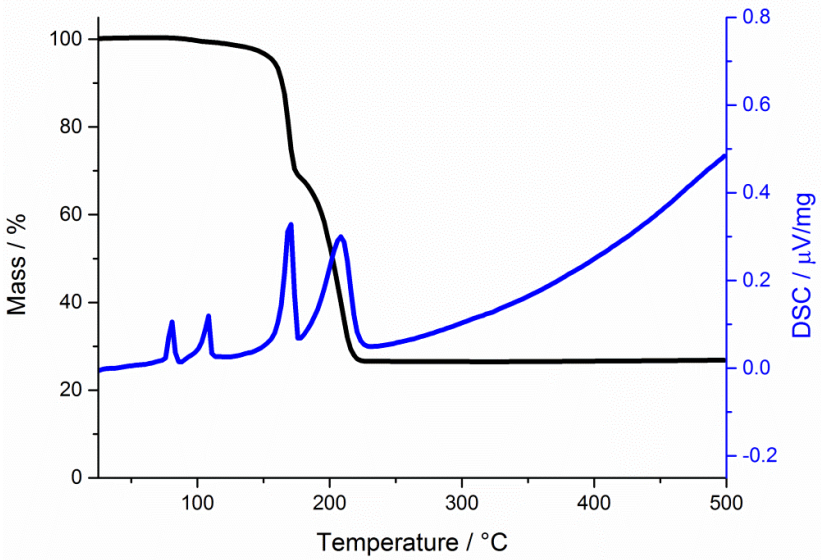

Figure 6-15 - TGA (black) & DSC (blue) graphs for 29.

The solid state decomposition of **29** and subsequent detection of isothiocyanate is in accord with the findings of Caudle *et al.*,[20] whereby cadmium bis(dithiocarbamate) complexes were postulated to decompose through a *n*-alkyldithiocarbamato species (herein **29**) *via* a carbon-sulfur bond scission coupled with deprotonation of the N-H

group. The lack of an N-H group in **21** explains why dialkylated derivatives are inert to this mode of carbon-sulfur bond cleavage.

Given the detection of organic products from the solid state decomposition of **29** the organic decomposition products from the decomposition of **29** in dodecane have been analysed by $^{13}C\{^{1}H\}$ NMR spectroscopy and mass spectrometry. A resonance at 129 ppm is observed in the $^{13}C\{^{1}H\}$ NMR spectrum, associated with the quaternary carbon in *n*-hexylisothiocyanate, which is confirmed by mass spectrometry (M^+, 144.06 *m/z*). The identical decomposition products suggest that whilst **29** is in solution it may decompose by a similar mechanism to the solid-state.

6.2.7 Continued Monitoring of Solvothermal Decomposition of 21 in *n*-hexylamine

In situ UV-vis and XAS measurements have previously suggested that dissolving **21** in *n*-hexylamine gives an octahedral complex. Upon heating to 75-80°C the octahedral complex undergoes amide-exchange to form a square planar complex proposed to be **29**. On heating to 95 °C *in situ* UV-vis shows absorptions associated with **29** begin to decrease with no subsequent growth of additional peaks in this region (Figure 6-16(a)). Linking this with the visual observation of the solution turning black at 90-95°C, suggests this to be the onset of nanoparticle formation. Indeed XAS confirms that heating to 90-95 °C the spectral quality decreases rapidly, this is associated with the inhomogeneity of the sample resulting from nanoparticle generation. Peaks associated with **29** in the UV-vis spectra continue to diminish upon heating to 120 °C, whereby they are no longer present after 30 mins of heating. At the same time a peak at 260 nm grows and sharpens (Figure 6-16(b)). Subsequent UV-vis analysis has shown that this peak is in an identical position to that of *n*-hexylthiourea.

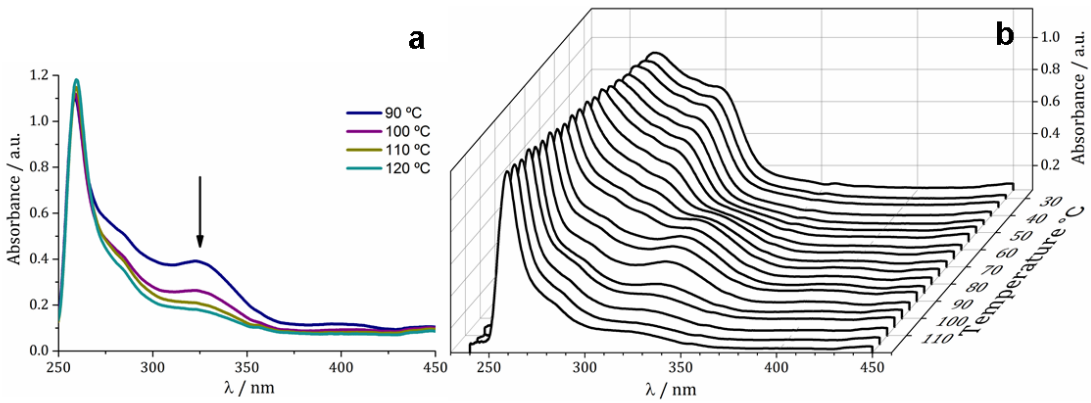

Figure 6-16 - *In situ* UV-vis spectra of 21 heated *n*-hexylamine. (a) Displaying decrease in presence of peaks associated with 29. (b) Displaying a waterfall plot of all *in situ* UV-vis data.

After decomposition was complete, the organic products were analysed by $^{13}C\{^{1}H\}$ NMR spectroscopy. A quarternary carbon peak was observed at 181 ppm an identical position to that of commercially purchased *n*-hexylthiourea, an organic decomposition product observed in the *in situ* UV-vis spectroscopy. Mass spectra of the reaction liquor showed the major organic component to be *n*-hexylthiourea (M^+ 245.18 *m/z*) with an additional peak at M^+ 144.06 *m/z* consistent with *n*-hexylisothiocyanate. Alkylisothiocyanates have been observed by others in the decomposition of related cadmium(II) bis(dithiocarbamate) complexes.[20]

The formation of organic co-products was also monitored by taking aliquots of the reaction mixture at 120 °C at timed intervals up 1 hr. Analysis of $^{13}C\{^{1}H\}$ NMR spectra showed the disappearance of peaks assigned to **21** with concomitant growth of a resonance at 181 ppm, consistent with the quaternary carbon of *n*-hexylthiourea (Figure 6-17). Formation of *n*-hexylthiourea has also been observed in the decomposition of zinc bis(dithiocarbamate) complexes in *n*-hexylamine.[4] The detection of *n*-hexylthiourea as an organic decomposition product is obviously different to solely *n*-hexylisothiocyanate seen when decomposing **29** in dodecane. To explain this, *n*-hexylisothiocyanate was heated to 120 °C in *n*-hexylamine and $^{13}C\{^{1}H\}$ NMR spectroscopy confirmed the transformation into *n*-hexylthiourea suggesting that the isothiocyanate acts as a precursor to the thiourea within a primary amine.

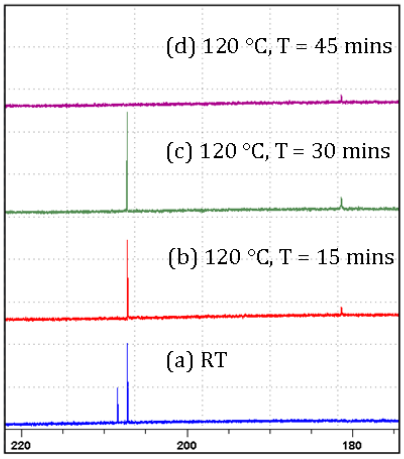

Figure 6-17 –Periodic sampling of 21 decomposed in *n*-hexylamine $^{13}C\{^{1}H\}$ NMR spectra showing quarternary carbon region.

6.2.8 Monitoring the Solvothermal Decomposition of 21 in Oleylamine

With the mechanistic insight gained from the decomposition in *n*-hexylamine the mechanism for decomposition in oleylamine was then probed. In general the

decomposition followed a similar trend. UV-vis spectra showed dissolving **21** significantly changes the Ni environment. Peak broadening in the ^{1}H NMR spectra also suggests a paragmagnetic species is formed upon addition of oleylamine to **21**. XAS then confirms addition of oleylamine to **21** results in an octahedral complex, whereby two Ni-N bond distances from nickel-oleylamine interactions exist at 2.05 Å and four Ni-S bond distances are lengthened to 2.37 Å and 2.51 Å. XAS shows this species is in the **a**^{3}***trans*** arrangement consistent with calculations in Section 6.2.3.

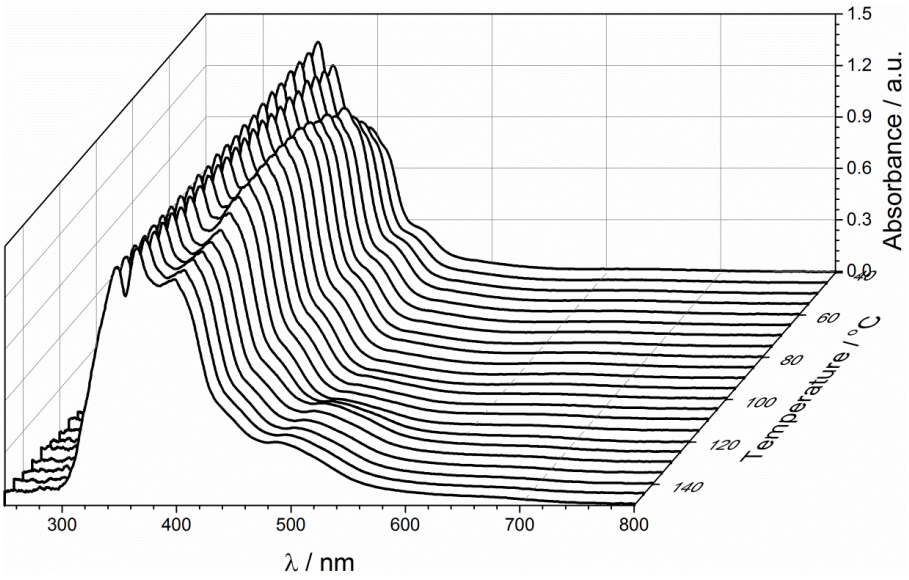

Figure 6-18 - Waterfall plot of *in situ* UV-vis spectra of 21 heated oleylamine.

Heating the mixture shows first the formation of a square planar complex, followed by its decomposition. The square planar complex is observed by *in situ* EXAFS at 118 °C with four Ni-S bond distances at 2.20 Å and two Ni-C interatomic distances at 2.68 Å. *In situ* UV-vis confirms peaks associated with the octahedral complex decrease with concomitant growth of peaks associated with a square planar complex at 115 °C with complete conversion by 125 °C. The peaks associated with the square planar complex start to decrease at 145 °C consistent with nanoparticle formation (Figure 6-18). XAS suggests *ca.* 135 °C to be the onset of decomposition, due to the rapid decrease in spectral quality associated with inhomogeneity of the sample.

Performing ^{13}C{^{1}H} NMR spectroscopy on the reaction liquor after decomposition showed the presence a quaternary carbon peak at 181.9 ppm, typical of a thiourea. The presence of oleylamine thiourea (M^{+}, 557 *m/z*) in the decomposition liquor was confirmed by mass spectroscopy. In addition mass spectroscopy showed the presence of di-

isobutyloleylamine-R,R'-thiuram monosulfide (M^+, 516 *m/z*), suggesting a different decomposition pathway may exist for decomposition in longer chain primary amines.

The slower rate/higher temperature of formation of a square planar complex in oleylamine when compared to *n*-hexylamine suggests the kinetics of amide exchange could be affected by the size of the amine **21** is decomposed within. As such, when **21** is heated in oleylamine the amide exchange may only proceed as far as a single substitution to give [Ni($S_2CN^iBu_2$)(S_2CN{H}Oleyl)] (**30**). It would follow that post decomposition organic products and their subsequent reactions may be affected, *e.g.* the transformation from isothiocyanate to thiourea could be slower. This would keep the isothiocyanate present in solution for a longer period allowing additional reactions to take place. The observation of thiuram-monosulfide with both NR_2 and NHR' groups by mass spectrometry supports the idea that amide-exchange has occurred on only one of the dithiocarbamates of **21**, prior to decomposition, resulting in the square planar complex formed with oleylamine being the mono-substituted complex **30**.

The thiuram-monosulfide could then plausibly form, from a reaction of the dialkyl dithiocarbamate portion of **30** after the first decomposition step. In addition, the lack of thiuram-monosulfide in the decomposition of **21** in *n*-hexylamine suggests the decomposition of **21** in *n*-hexylamine proceeds *via* the bis-substituted complex **29**. The two proposed decomposition routes (*via* **29** or **30**) have been summarised in Figure 6-19.

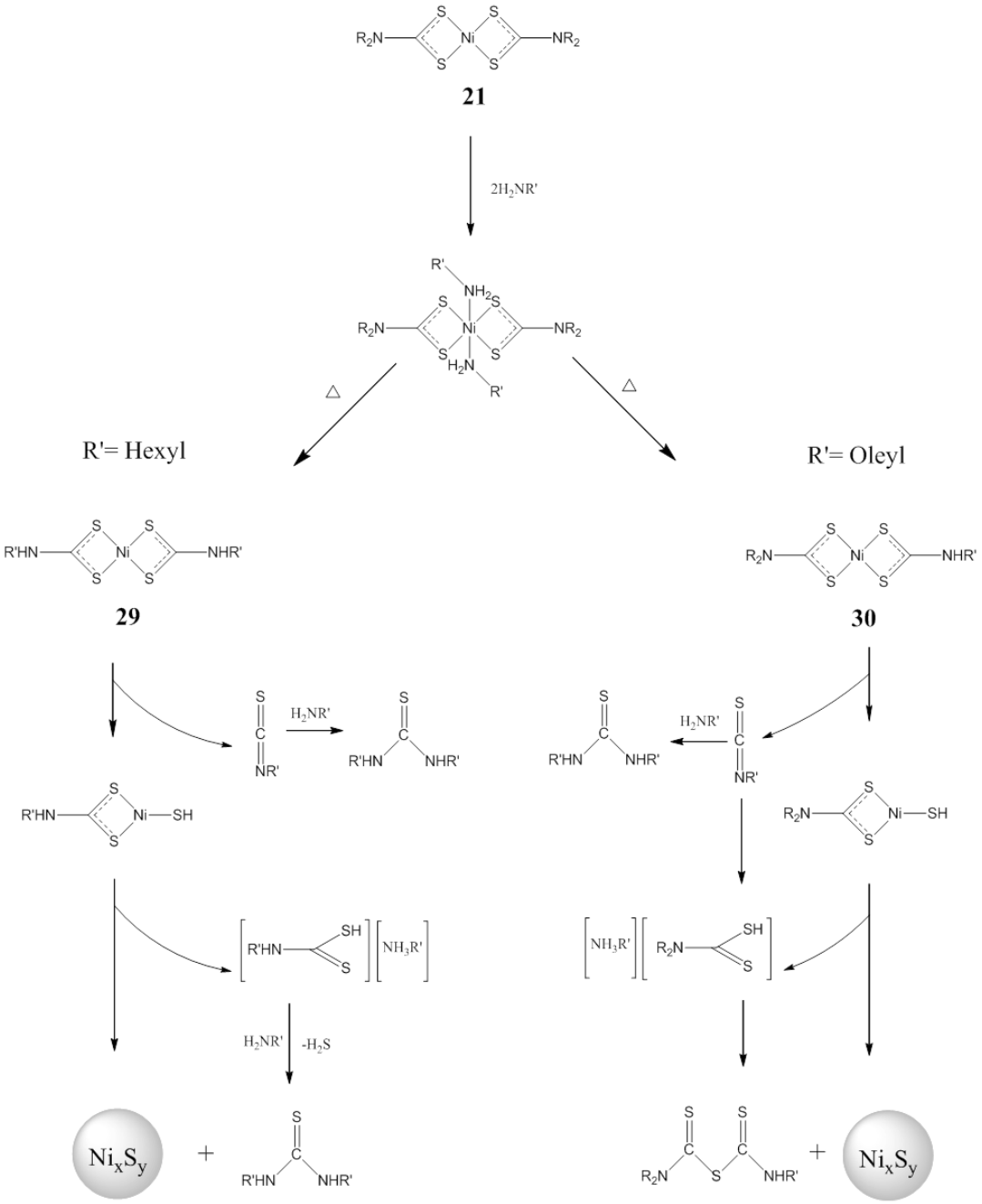

Figure 6-19 - Primary amine dependant decomposition scheme.

6.2.9 Preliminary Iron and Zinc Dithiocarbamate Studies

Preliminary work has been performed on the decomposition of iron(III) tris(dithiocarbamate) complexes and zinc(II) bis(dithiocarbamate) complexes, namely *in situ* XAS reactions. Initial findings indicate the zinc dithiocarbamate complex decomposes *via* a very similar mechanism to the nickel case, with initial formation of an octahedral complex in solution with amine, followed by loss of two ligands to result in a four-

coordinate species which then goes on to decompose. The iron dithiocarbamate decomposition is complicated somewhat by spin-crossover conversion and oxidation state changes. Further work on this is being performed by Husn-Ubayda Islam and is not developed here.

6.3 Conclusions

The solvothermal decomposition mechanism for nickel dithiocarbamate complex [Ni($S_2CN^iBu_2$)$_2$] (**21**) in primary amines, has been investigated using powder XRD, NMR, MS and UV-vis spectroscopy, in conjunction with XAS and computational modelling performed by colleagues at UCL. Oleylamine is a common primary amine solvent employed in the decomposition of metal dithiocarbamate complexes, but because this compound is difficult to model and to synthesise model compounds of, therefore *n*-hexylamine was chosen as the solvent for these studies. The decomposition of **21** in *n*-hexylamine was found to proceed *via* amide exchange on the dithiocarbamate backbone with amine from the solvent forming a new complex [Ni(S_2CNH^nHex)$_2$] (**29**). This new complex then goes on to decompose *via* deprotonation of the *N*-alkyldithiocarbamate ligand and formation of an isothiocyanate by-product (which goes on to react with more solvent amine to form a thiourea).

In order to test the applicability of this mechanism to decomposition of **21** in oleylamine, studies were performed in oleylamine resulting in similar results with a few exceptions. The decomposition in oleylamine was found to produce some different by-products, namely thiuram monosulfide. It is suggested that due to oleylamine's bulk, amide exchange is slower and exchange of one amide is seen (rather than full exchange of both) forming [Ni($S_2CN^iBu_2$)(S_2CN{H}Oleyl)] (**30**). Steric hindrance also slows down the side reaction between the isothiocyanate by-product (formed from decomposition of the *N*-alkyldithiocarbamate half of **30**) and solvent oleylamine, such that sufficient isothiocyanate levels exist in solution to react with dithiocarbamic acid released from a subsequent decomposition step. These by-products may react to form the mixed *iso*-butyl, oleylamine thiuram monosulfide, which is observed in the MS of the decomposition liquor.

These results indicate the solvent plays a crucial role in decomposition of dithiocarbamate complexes. They suggest that the nature of the solvent directly influences the decomposition pathway, such that the complex that decomposes to form the metal sulfide is not the original precursor, but in fact an intermediate complex formed from amide

exchange with the solvent. This could mean that, in the case of *N*,*N*-dialkyldithiocarbamate complexes of the type $[Ni(S_2CNR_2)_2]$ (R = alkyl not H), the alky groups of the dithiocarbamate ligands are less important to the decomposition of the precursor, only influencing how effectively amide exchange with the solvent occurs. In addition the nature of an amine solvent may greatly affect the decomposition pathway, such that if it is bulky and has a low rate of amide exchange with the dithiocarbamate ligand backbone, the decomposition pathway is affected, as well as secondary reactions occurring in solution to produce by-products.

6.4 Experimental

Chemicals

Dodecane (99 %), sodium hydroxide (technical grade) and N,N'-dihexylthiourea (97 %) and were purchased from Fisher Scientific UK and used and stored as supplied with no further purification. Oleylamine (technical grade, 70 %), carbon disulfide, 1,4-diazabicyclo(2.2.2)octane (DABCO, ≥ 99 %), N-ethylmethylamine, N-hexyl *iso*thiocyanate (95 %), potassium ferricyanide(III) (99 %) were purchased from Sigma Aldrich Ltd and used and stored as supplied with no further purification. Di*iso*butylamine (99 %) was purchased from Alfa Aesar and used without any further purification. Hexylamine (99 %) was purchased from Sigma Aldrich Ltd and distilled before use.

Physical Measurements

All ^{1}H and $^{13}C\{^{1}H\}$ NMR spectra were obtained on either a Bruker Avance III 400 or Avance 600 spectrometer, the latter being equipped with a cryoprobe. All spectra were recorded using $CDCl_3$ which was dried and degassed over molecular sieves prior to use; ^{1}H and $^{13}C\{^{1}H\}$ chemical shifts are reported relative to $SiMe_4$. The mass spectra were obtained using either Micromass 70-SE spectrometer using Electron Ionisation (EI) or a Thermo Finnigan MAT900xp spectrometer using Chemical Ionisation (CI). Elemental analysis was carried using Elemental Analyser (CE-440) (Exeter Analytical Inc). Thermogravimetric analysis (TGA) was performed using a Netzsch STA 449C TGA system. Data was recorded from 25 to 600 °C with a constant heating rate of 10 °C $minute^{-1}$.

XRD patterns were measured on a Bruker AXS D4 diffractometer using $CuK\alpha_1$ radiation. The diffraction patterns obtained were compared to database standards. For TEM

characterisation a 4 µl droplet of nanoparticle suspension (chloroform) was placed on a holey carbon-coated copper TEM grid and allowed to evaporate in air under ambient laboratory conditions for several minutes. TEM images were obtained using a JEOL-1010 microscope at 100 kV equipped with a Gatan digital camera. HRTEM measurements were collected using a Jeol 2100 TEM with a LaB_6 source operating at an acceleration voltage of 200 kv. Micrographs were taken on a Gatan Orius Charge-coupled device (CCD).

6.4.1 Synthesis of $Ni[S_2CN(H)C_6H_{13}]_2$ (29)

Carbon disulfide (1.80 mL, 30 mmol) was added dropwise to a solution of *n*-hexylamine (4 mL, 30 mmol) in MeOH (30 mL) cooled in an ice bath to 3 °C. NaOH (1.20 g, 30 mmol) dissolved into the minimum amount of water (5 mL) was added slowly dropwise to the solution and the whole reaction stirred for 3 hours. A solution of $NiCl_2.6H_2O$ (3.5657 g, 15 mmol) in water (20 mL) was then added dropwise over two minutes producing a green precipitate. The mixture was stirred for 30 minutes, filtered, washed with water (3 x 30 mL) and evaporated to dryness. The green powder product was then dissolved in 100 mL of DCM and stirred with $MgSO_4$ for 30 mins, after which the mixture was filtered and the filtrate dried *in vacuo*. Yield 4.1957 g, 68 % **Anal. Calc. for $C_{14}H_{28}N_2S_4Ni$:** C, 40.88; H, 6.86; N, 6.81. Found: C, 39.89; H, 6.70; N, 6.59. **^{1}H NMR δ/ppm ($CDCl_3$):** 0.92 (t, *J* 6.78, 6H, CH_3), 1.33 (m, 12H, CH_2CH_2CH_2), 1.62 (m, 4H, CH_2), 3.44 (q, *J* 6.78, 4H, CH_2), 6.87 (s, 2H, N*H*). **^{13}C{^{1}H} NMR δ/ppm ($CDCl_3$):** 14.11 (*C*H_3), 22.59 (*C*H_2), 26.44 (*C*H_2), 28.64 (*C*H_2), 31.38 (*C*H_2), 43.84 (*C*H_2), 210.30 (*C*S_2). **MS:** *m/z* 410 [M^+], 346 [M^+ - S_2], 259 [M^+ - S(H){S(H)C_6H_{13}}], 245 [M^+ - S(H){SN(H)C_6H_{13}}], 201 [M^+ - S{S_2CN(H)C_6H_{13}}].

6.4.2 Decompositions

All decomposition experiments were carried out under an inert atmosphere of nitrogen using Schlenk techniques. The decomposition setup as described in Chapter 3, Section 3.2 was utilised. In a typical synthesis **21** (5 mM) was added to a solvent (20 mL) in a three-neck RBF attached to a condenser and evacuated and refilled with nitrogen repeatedly for 15 minutes. The solution was heated to a certain temperature and held there for 1 hr. The mixture was allowed to cool to RT slowly, whereupon methanol (80 mL) was added with stirring. The mixture was centrifuged and then the solution decanted leaving behind the resultant nanoparticles. This procedure was repeated 3 times and finally the material was allowed to dry in air.

Decomposition of 21 in dodecane

$[Ni(S_2CN\{C_4H_9\}_2)_2]$ (0.1 mmol, 0.0467 g) refluxed in dodecane (20 mL) for 1 hour at 200 °C with stirring. After 1 hr at this temperature the green precursor solution had not changed in appearance at all. The mixture was allowed to cool and crystals of $Ni[S_2CN(C_4H_9)_2]_2$ precursor formed in solution. The decomposition liquor was then analysed. **MS:** *m/z* 467 $[Ni(S_2CN\{C_4H_9\}_2)_2^+]$, 435 $[Ni\{S_2CN(C_4H_9)_2\}_2^+ - S]$, 403 $[Ni\{S_2CN(C_4H_9)_2\}_2^+ - S_2]$, 174 $[Ni\{S_2CN(C_4H_9)_2\}_2^+ - S(C_4H_9)\{S_2CN(C_4H_9)_2\}]$. **$^{13}C\{^1H\}$ NMR δ/ppm ($CDCl_3$):** 208.92 $[Ni(S_2CN\{C_4H_9\}_2)_2]$.

Decomposition of 21 in DABCO

$[Ni(S_2CN\{C_4H_9\}_2)_2]$ (0.1 mmol, 0.0467 g) was added to 1,4-diazabicyclo(2.2.2)octane (DABCO, 17.8 mmol, 2 g) in dodecane (20 mL) and heated for 10 minutes at 70 °C until all the DABCO was dissolved. The green solution was then refluxed for 1 hr at 165 °C with stirring. After 1 hr at this temperature the solution had not changed in appearance at all. The mixture was allowed to cool and crystals of $[Ni(S_2CN\{C_4H_9\}_2)_2]$ precursor formed in solution. The decomposition liquor was then analysed. **MS:** *m/z* 467 $[Ni(S_2CN\{C_4H_9\}_2)_2^+]$, 435 $[Ni\{S_2CN(C_4H_9)_2\}_2^+ - S]$, 403 $[Ni\{S_2CN(C_4H_9)_2\}_2^+ - S_2]$, 174 $[Ni\{S_2CN(C_4H_9)_2\}_2^+ - S(C_4H_9)\{S_2CN(C_4H_9)_2\}]$. **$^{13}C\{^1H\}$ NMR δ/ppm ($CDCl_3$):** 208.50 $[Ni(S_2CN\{C_4H_9\}_2)_2]$.

Decomposition of 21 in Oleylamine

$[Ni(S_2CN\{C_4H_9\}_2)_2]$ (0.1 mmol, 0.0467 g) refluxed in oleylamine (20 mL) for 1 hr at 150 °C with stirring, producing a black precipitate dispersed into the solvent. The mixture was allowed to cool over 1 hr, then washed and centrifuged with 3 x 60 mL methanol. The resulting black powder was dispersed into 100 mL chloroform, then filtered and dried *en vacuo*. The decomposition liquor was sampled before washing and analysed. **MS:** *m/z* 514 $[\{SCN(H)C_{18}H_{35}\}S\{SCN(C_4H_9)_2\}^+]$, 577 $[SC\{N(H)C_{18}H_{35}\}_2^+]$. **$^{13}C\{^1H\}$ NMR δ/ppm ($CDCl_3$):** 181.86 $[SC\{N(H)C_{18}H_{35}\}_2]$.

Decomposition of 21 in *n*-hexylamine

$Ni[S_2CN(C_4H_9)_2]_2$ (0.1 mmol, 0.0467 g) refluxed in *n*-hexylamine (20 mL) for 1 hr at 120 °C with stirring, producing a black precipitate dispersed into the solvent. The mixture was allowed to cool over 1 hr, then washed and centrifuged with 3 x 60 mL methanol. The resulting black powder was dispersed into 100 mL chloroform, then filtered and dried *en vacuo*. Mass produced 0.0255 g. The decomposition liquor was sampled before washing

and analysed. **MS:** *m/z* 245 [SC{N(H)C_6H_{13}}$_2^+$ + H^+]. **$^{13}C\{^1H\}$ NMR δ/ppm ($CDCl_3$):** 128.84 [SCNC_6H_{13}].

Decomposition of 29 in Dodecane

[Ni($S_2CNHC_6H_{13}$)$_2$] (0.1 mmol, 0.0411 g) refluxed in dodecane (20 mL) for 1 hr at 150 °C with stirring, producing a black precipitate. The mixture was allowed to cool to room temperature over 1 hr, then washed and centrifuged with 3 x 60 mL methanol. The resulting black powder was dispersed into 100 mL chloroform, then filtered and dried *en vacuo*. Mass produced 0.0173 g. The decomposition liquor was sampled before washing and analysed. **MS:** *m/z* 272 [SC{N(CH_2)C_6H_{13}}$_2^+$; 2 CH_2 groups from the fragmentation of dodecane]. **$^{13}C\{^1H\}$ NMR δ/ppm ($CDCl_3$):** 128.81 [SCNC_6H_{13}].

Decomposition of 29 in Oleylamine

[Ni($S_2CNHC_6H_{13}$)$_2$] (0.1 mmol, 0.0411 g) refluxed in oleylamine (20 mL) for 1 hr at 150 °C with stirring, producing a black precipitate. The mixture was allowed to cool to room temperature over 1 hr, then washed and centrifuged with 3 x 60 mL methanol. The resulting black powder was dispersed into 100 mL chloroform, then filtered and dried *en vacuo*. Mass produced 0.0114 g. The decomposition liquor was sampled before washing and analysed. **MS:** *m/z* 488 [{SCN(H)$C_{18}H_{35}$}S{SCN(H)C_6H_{13}}$^+$ + H^+]. **$^{13}C\{^1H\}$ NMR δ/ppm ($CDCl_3$):** 128.29 [SCNC_6H_{13}].

Decomposition of 29 in *n*-hexylamine

[Ni($S_2CNHC_6H_{13}$)$_2$] (0.1 mmol, 0.0411 g) refluxed in *n*-hexylamine (20 mL) for 1 hr at 120 °C with stirring, producing a black precipitate. The mixture was allowed to cool to room temperature over 1 hr, then washed and centrifuged with 3 x 60 mL methanol. The resulting black powder was dispersed into 100 mL chloroform, then filtered and dried *en vacuo*. Mass produced 0.0105 g. **MS:** *m/z* 245 [SC{N(H)C_6H_{13}}$_2^+$ + H^+]. **$^{13}C\{^1H\}$ NMR δ/ppm ($CDCl_3$):** 181.83 [SC{N(H)C_6H_{13}}$_2$], 128.82 [SCNC_6H_{13}].

6.4.3 Model Reactions

$[(C_4H_9)_2NH_2][S_2CN(C_4H_9)_2]$ Reaction with *N*-hexyl Isothiocyanate

$[(C_4H_9)2NH_2][S_2CN(C_4H_9)_2]$ (0.2 mmol, 0.0669 g) was added to a solution of $SCNC_6H_{13}$ (0.2 mmol, 0.0286 g) in dodecane (20 mL) and refluxed for 1 hr at 120 °C with stirring. The clear colourless solution was then allowed to cool to room temperature over 1 hr and the decomposition liquor analysed. **MS:** *m/z* 144 $[SCNC_6H_{13}^+]$, 173 $[SC(H)N(C_4H_9)_2^+]$, 130 $[(C_4H_9)_2NH_2^+]$, 273 $[SC\{N(H)C_6H_{13}\}\{NC_4H_9\}^+ + H^+]$. **$^{13}C\{^1H\}$ NMR δ/ppm ($CDCl_3$):** 182.02 $[SC\{N(H)C_6H_{13}\}\{NC_4H_9\}]$, 193.03 $[S_2CN(C_4H_9)_2]$, 194.50 $[SC\{N(C_4H_9)_2\}]$.

$[(C_4H_9)_2NH_2][S_2CN(C_4H_9)_2]$ Reaction with *N*-hexyl Thiourea

$[(C_4H_9)_2NH_2][S_2CN(C_4H_9)_2]$ (0.2 mmol, 0.0669 g) was added to a solution of $SC\{N(H)C_6H_{13}\}_2$ (0.2 mmol, 0.0488 g) in dodecane (20 mL) and refluxed for 1 hr at 120 °C with stirring. The clear colourless solution was then allowed to cool to room temperature over 1 hr and the decomposition liquor analysed. **MS:** *m/z* 173 $[SC(H)N(C_4H_9)_2^+]$, 130 $[(C_4H_9)_2NH_2^+]$, 245 $[SC\{N(H)C_6H_{13}\}_2^+ + H]$, 273 $[SC\{N(H)C_6H_{13}\}\{NC_4H_9\}^+ + H^+]$. **$^{13}C\{^1H\}$ NMR δ/ppm ($CDCl_3$):** 182.02 $[SC\{N(H)C_6H_{13}\}\{NC_4H_9\}^+]$.

***N*-Hexyl Isothiocyanate Reaction with *n*-hexylamine**

A solution of $SCNC_6H_{13}$ (0.1 mmol, 0.0143 g) in *n*-hexylamine (20 mL) was refluxed for 1 hr at 120 °C with stirring. The clear colourless solution was then allowed to cool to room temperature over 1 hr and the decomposition liquor analysed. **MS:** *m/z* 245 $[SC\{N(H)C_6H_{13}\}_2^+ + H^+]$. **$^{13}C\{^1H\}$ NMR δ/ppm ($CDCl_3$):** 182.02 $[SC\{N(H)C_6H_{13}\}_2^+]$.

6.4.4 UV-Vis

The optical properties were analysed via an Ocean Optics USB4000 UV-vis spectrometer with a Micropack DH-2000-BAL deuterium halogen lightsource, and a Perkin Elmer Lambda-25 UV-vis spectrometer.

6.5 References

1 F. W. H. Kruger and W. J. McGill, *J. Appl. Polym. Sci.*, 2003, 42, 2669.

2 J. van Rooyen, PhD Thesis, University of Port Elizabeth South Africa, 2007.

3 J. D. J. Van Dyke, M. Gnatowski, A. Koutsandreas, and A. Burczyk, *J. Appl. Polym. Sci.*, 2002, 90, 871.

4 A. Dirksen, P. J. Nieuwenhuizen, M. Hoogenraad, J. G. Haasnoot, and J. Reedijk, *J. Appl. Polym. Sci.*, 2001, 79, 1074.

5 I. R. Gelling, *Rubber Chem. Technol.*, 1974, 46, 524.

6 M. Afzaal, C. L. Rosenberg, M. a. Malik, A. J. P. White, and P. O'Brien, *New J. Chem.*, 2011, 35, 2773.

7 D. P. Dutta, G. Sharma, S. Ghoshal, N. P. Kushwah, and V. K. Jain, *J. Nanosci. Nanotechnol.*, 2006, 6, 235.

8 N. Pradhan, B. Katz, and S. Efrima, *J. Phys. Chem. B*, 2003, 107, 13843.

9 S. Ghoshal, N. P. Kushwah, D. P. Dutta, and V. K. Jain, *Appl. Organomet. Chem.*, 2005, 19, 1257.

10 Y. Zhou, J. He, C. Li, L. Hong, and Y. Yang, *Macromolecules*, 2011, 44, 8446.

11 C. H. DePuy and R. W. King, *Chem. Rev.*, 1960, 60, 431.

12 M. Afzaal, M. A. Malik, and P. O'Brien, *J. Mater. Chem.*, 2010, 20, 4031.

13 M. Chunggaze, M. A. Malik, and P. O'Brien, *J. Mater. Chem.*, 1999, 9, 2433.

14 M. Chunggaze, M. A. Malik, and P. O'Brien, *Dalton. Trans.*, 2006, 4499.

15 J. Akhtar, M. Afzaal, M. a. Vincent, N. a. Burton, J. Raftery, I. H. Hillier, and P. O'Brien, *J. Phys. Chem. C*, 2011, 115, 16904.

16 Z. Zhang, S. H. Lee, J. J. Vittal, and W. S. Chin, *J. Phys. Chem. B*, 2006, 110, 6649.

17 Y. K. Jung, J. Il Kim, and J.-K. Lee, *J. Am. Chem. Soc.*, 2010, 132, 178.

18 S. Mourdikoudis and L. M. Liz-Marzan, *Chem. Mater.*, 2013, 25, 1465.

19 R. D. Pike, H. Cui, R. Kershaw, K. Dwight, A. Wold, T. N. Blanton, A. A. Wernberg, and H. J. Gysling, *Thin Solid Films*, 1993, 224, 221.

20 L. H. van Poppel, T. L. Groy, and M. T. Caudle, *Inorg. Chem.*, 2004, 43, 3180.

21 G. Barone, T. Chaplin, T. G. Hibbert, A. T. Kana, M. F. Mahon, K. C. Molloy, I. D. Worsley, I. P. Parkin, and L. S. Price, *J. Chem. Soc., Dalton. Trans.*, 2002, 1085.

22 H. Krebs, E. F. Weber, and H. Fassbender, *Zeitschrift für Anorg. und Allg. Chemie*, 1954, 276, 128.

23 F. P. Emmenegger, *Inorg. Chem.*, 1989, 28, 2210.

24 G. M. C. Higgins and B. Saville, *J. Chem. Soc.*, 1963, 2812.

25 J. P. J. Fackler, D. Coucouvanis, W. C. Seidel, R. C. Masek, and W. Holloway, *J. Chem. Soc. Chem. Commun.*, 1967, 924.

26 W. C. Seidel and J. P. J. Fackler, *Inorg. Chem.*, 1969, 8, 1631.

27 A. Vizi-Orosz and L. Markó, *Transit. Met. Chem.*, 1986, 11, 408.

28 D. C. Bradley, I. F. Rendall, and K. D. Sales, *J. Chem. Soc., Dalton. Trans.*, 1973, 2228.

29 S. C. Sendlinger, J. R. Nicolson, E. B. Lobkovsky, J. C. Huffman, D. Rehder, and G. Christou, *Inorg. Chem.*, 1993, 32, 204.

30 C. Bianchini, A. M. C. Mealli, and G. Scapacci, *J. Chem. Soc., Dalton. Trans.*, 1982, 799.

31 G. Kullerud and R. A. Yund, *J. Petrol.*, 1962, 3, 126.

7 Conclusions and Future Work

7.1 Conclusions

The aim of the work contained in this thesis was to investigate the use of dithiocarbamate complexes as single-source precursors to metal sulfide nanoparticles, with a focus on iron and nickel sulfides due to their applications in catalysis. Chapter 2 focused on the synthesis of iron dithiocarbamate molecular precursors and assessed their suitability for subsequent decomposition to form iron sulfide nanoparticles. Particularly of interest was the iron thiospinel greigite (Fe_3S_4), and consequently both iron(II) and iron(III) precursors were studied.

The carbonyl protected forms of iron(II) bis(dithiocarbamate) complexes were synthesised as the iron(II) source since the unprotected complexes were known to be extremely air sensitive and thus difficult to handle. The iron(II) bis(dithiocarbamate) dicarbonyl complexes were found to be suitable replacements, being stable in the solid state at room temperature, but also decomposing to form the unprotected complex well before its subsequent decomposition, thereby potentially avoiding any possible unwanted impurities in the resulting nanoparticles. Interestingly, the trend in Fe-CO bond strength (indicated by TGA thermolysis temperature) differed to previous reports, indicating a more complex bonding system than previously thought.

Decomposition studies on iron(II) and (III) dithiocarbamate complexes found that greigite is not accessible with a combination of these precursors under the tested reaction conditions, pyrrhotite (Fe_7S_8) being the only product formed. Pyrrhotite contains iron(II) and not iron(III), indicating all the iron(III) dithiocarbamate precursor was reduced during decomposition. In order to investigate this further, a series of studies were performed on the iron(III) precursors systematically changing different reaction variables in order to probe the changes to materials formed. Decomposition temperature and precursor concentration were found to have a particularly important effect on the phase of the iron sulfide nanoparticles formed. Greigite was found to be a metastable phase in this system, forming at lower temperature and higher precursor concentration.

The addition of a redox active additive to the decomposition system had a significant effect on the phase of iron sulfide produced. When sufficient levels were used, addition of thiuram disulfide ($[S_2CN^iBu_2]_2$) changed the decomposition system conditions such that

greigite survived at higher temperatures and lower concentrations of iron(III) tris(dithiocarbamate) complex. This could be the result of thiuram disulfide forming a capping layer around the greigite nanoparticles, thereby stabilising the iron sulfide phase, or it could be due to a change in the overall decomposition mechanism.

The nickel dithiocarbamate decomposition system was also studied in detail, with differing results to the iron sulfide system. Temperature studies (without the thiuram disulfide additive) revealed the formation of α-NiS, a known high temperature nickel sulfide (in solid state synthesis), being formed at lower temperatures than β-NiS, a known low temperature phase of nickel sulfide (though there is a precedent for this trend). Precursor concentration had no effect on the phase of nickel sulfide formed in the absence of thiuram disulfide, α-NiS being formed at all concentrations investigated. These results indicate α-NiS is kinetically more favoured, metastable phase in this system.

However, the effect of thiuram disulfide on the system was found to be closely related to its action on the iron(III) dithiocarbamate system. At low temperature, the metastable nickel thiospinel polydymite (Ni_3S_4) is formed while at high temperature the relatively more thermodynamically stable α-NiS is produced. The effect of precursor concentration in the presence of thiuram disulfide is more complex than in the iron case. At low concentrations α-NiS and polydymite are produced, but increasing the concentration leads to the formation of a different nickel sulfide phase, bravoite (NiS_2), which has pyrite structure. The iron analogue was not observed in the iron dithiocarbamate system. This may be due to differing relative stabilities of the nickel and iron sulfide phases.

Other metal dithiocarbamate complexes of cobalt, copper, zinc and indium were investigated as precursors for binary metal sulfide nanoparticles, and, in conjunction with $[Fe(S_2CN^iBu_2)_3]$ and $[Ni(S_2CN^iBu_2)_2]$, for ternary metal sulfides. Metal sulfides were successfully synthesised in the cobalt, copper and zinc cases, but the indium precursor produced material of low crystallinity. Ternary iron nickel, iron copper and nickel cobalt sulfides were successfully synthesised from mixtures of dithiocarbamate precursors. In particular the thiospinel $FeNi_2S_4$ was produced in nanoparticulate form, which has to date not been reported in the literature. However, in the iron zinc and iron indium systems investigated only the binary metal sulfides were observed.

The effect of adding thiuram disulfide to the decomposition solutions was also studied, and found to have a great effect on the ternary iron nickel sulfide system. At high

precursor concentration in the presence of thiuram disulfide the nickel pyrite (Fe,Ni)S_2 was synthesised, which has also not be reported in the literature to date. The additive thiuram disulfide also allowed access to the cobalt sulfide CoS_2 at high concentration, as seen previously with the nickel binary sulfide NiS_2, which was formed at high concentration. Though thiuram disulfide appeared to have little effect in the studies on other metals, high concentration decompositions were not attempted due to time constraints. Thiuram disulfide also aided in the synthesis of the mixed iron and nickel thiospinel $FeNi_2S_4$, allowing synthesis of pure material at higher temperatures, stabilising the phase in some way. This is very similar to the effect of thiuram disulfide on the binary iron and nickel sulfide systems.

In order to better understand the mechanism of solvothermal decomposition of metal dithiocarbamate complexes, the decomposition was investigated using NMR, XRD, MS and UV-vis analysis techniques, in conjunction with XAS and computational modelling. The nickel dithiocarbamate system was used as a model because it has been well studied in this thesis and shown to be related to the iron dithiocarbamate system, but did not have the added complication spin crossover effects, as in the iron case.

The results revealed a possible decomposition mechanism where the primary amine solvent plays a significant role. Decomposition is suggested to proceed *via* an amide substituted intermediate, [Ni($S_2CN^iBu_2$)(S_2CN{H}Oleyl)], and so the role of the dithiocarbamate alkyl groups may be less important than the nature of the primary amine solvent present. The addition of thiuram disulfide to the decomposition solution may affect this amide exchange by slowing down the rate of [Ni($S_2CN^iBu_2$)(S_2CN{H}Oleyl)] formation. This would in turn lead to a decrease in the overall rate of metal sulfide formation, thereby allowing kinetically favoured, metastable phases survive because there is insufficient time for them to convert to thermodynamically more favoured phases.

7.2 Future Work

In order to further elucidate the role of the thiuram disulfide additive in the decomposition of metal dithiocarbamate complexes, the decomposition of nickel dithiocarbamate in the presence of thiuram disulfide could be investigated *via* NMR, MS, XRD and UV-vis, in the same way as the nickel dithiocarbamate system was studied. The relative rates of by-product formation could be indicative of thiuram disulfide supressing the solvent-dithiocarbamate amide exchange, when compared to the decomposition

without the additive. In addition, to support the hypothesis that the nickel dithiocarbamate decomposition is a good model for all metal dithiocarbamate systems, other metals should be investigated, particularly the iron system, which may be easier to interpret with the knowledge gained about the nickel decomposition.

More studies into the effect of thiuram disulfide on metal sulfide formation at high precursor concentrations should be performed, the current work only briefly touching on iron, nickel and cobalt sulfides. It may be possible to access rare metastable phases of other metal sulfides using this method, which could have interesting catalytic properties. In addition, the synthesis of $[Fe(S_2CNH^nHex)_3]$ should be performed and this precursor decomposed at low temperature to attempt to form metastable phases of iron sulfide, which are not accessible at the higher temperatures required to form crystalline material for the dialkyl derivatives.

Additionally, the greigite nanoparticles formed in this study should be tested for catalytic reduction of CO_2, having previously been postulated to have potential as such. The ability to synthesise pure greigite nanoparticles using high precursor concentration allows the possibility to dope other metals into the greigite structure, which may affect its catalytic ability. Nickel, in particular, has been suggested to potentially improve greigite's catalytic activity towards CO_2 activation. The suitability of metal dithiocarbamates for metal doping should be investigated in light of the successes reported in this thesis with ternary metal sulfides formation using these precursors.

8 Appendix – Crystallographic Data

Table 8.1. Crystal data and structure refinement for $[Fe(S_2CNEt_2)_3]$ (**2**).

Chemical formula	$C_{15}H_{30}FeN_3S_6$	
Formula weight	500.63	
Temperature	123(2) K	
Radiation, wavelength	MoKα, 0.71073 Å	
Crystal system, space group	monoclinic, $P2_1/n$	
Unit cell parameters	a = 14.001(2) Å	α = 90°
	b = 10.1767(15) Å	β = 111.189(2)°
	c = 16.886(2) Å	γ = 90°
Cell volume	2243.3(6) Å^3	
Z	4	
Calculated density	1.482 g/cm^3	
Absorption coefficient μ	1.236 mm^{-1}	
F(000)	1052	
Crystal colour and size	red, 0.45 × 0.25 × 0.20 mm^3	
Data collection method	Bruker SMART 1K CCD diffractometer	
	ω rotation with narrow frames	
θ range for data collection	2.59 to 28.32°	
Index ranges	h –17 to 18, k –13 to 13, l –22 to 22	
Completeness to θ = 28.32°	94.6 %	
Reflections collected	18316	
Independent reflections	5277 (R_{int} = 0.0302)	
Reflections with $F^2>2\sigma$	4616	
Absorption correction	semi-empirical from equivalents	
Min. and max. transmission	0.6062 and 0.7901	
Refinement method	Full-matrix least-squares on F^2	
Weighting parameters a, b	0.0420, 0.5629	
Data / restraints / parameters	5277 / 0 / 344	
Final R indices [$F^2>2\sigma$]	R_1 = 0.0284, wR_2 = 0.0774	
R indices (all data)	R_1 = 0.0336, wR_2 = 0.0796	
Goodness-of-fit on F^2	1.064	
Largest and mean shift/su	0.002 and 0.000	
Largest diff. peak and hole	0.388 and –0.520 e Å^{-3}	

Table 8.2. Crystal data and structure refinement for $[Fe(S_2CNMe_2)_2(CO)_2]$ (**13**).

Chemical formula	$C_7H_{12}FeN_2OS_4$	
Formula weight	324.28	
Temperature	150(2) K	
Radiation, wavelength	MoKα, 0.71073 Å	
Crystal system, space group	monoclinic, $P2_1/c$	
Unit cell parameters	a = 6.280(2) Å	α = 90°
	b = 17.371(6) Å	β = 97.973(6)°
	c = 13.051(5) Å	γ = 90°
Cell volume	1410.0(8) Å^3	
Z	4	
Calculated density	1.528 g/cm^3	
Absorption coefficient μ	1.639 mm^{-1}	
F(000)	664	
Crystal colour and size	red, 0.10 × 0.08 × 0.06 mm^3	
Data collection method	Bruker SMART 1K CCD diffractometer	
	ω rotation with narrow frames	
θ range for data collection	3.15 to 28.24°	
Index ranges	h –8 to 8, k –23 to 22, l –16 to 16	
Completeness to θ = 26.00°	88.2 %	
Reflections collected	9651	
Independent reflections	2955 (R_{int} = 0.1161)	
Reflections with $F^2>2\sigma$	1136	
Absorption correction	semi-empirical from equivalents	
Min. and max. transmission	0.8532 and 0.9081	
Refinement method	Full-matrix least-squares on F^2	
Weighting parameters a, b	0.0000, 0.0000	
Data / restraints / parameters	2955 / 0 / 154	
Final R indices [$F^2>2\sigma$]	R_1 = 0.0450, wR_2 = 0.0788	
R indices (all data)	R_1 = 0.1017, wR_2 = 0.0913	
Goodness-of-fit on F^2	0.501	
Largest and mean shift/su	0.000 and 0.000	
Largest diff. peak and hole	0.516 and –0.487 e Å^{-3}	

Table 8.3. Crystal data and structure refinement for $[Fe(S_2CN^iBu_2)_2(CO)_2]\cdot C_5H_{12}$ (**15**).

Chemical formula	$C_{25}H_{48}FeN_2O_2S_4$	
Formula weight	592.74	
Temperature	150(2) K	
Radiation, wavelength	MoKα, 0.71073 Å	
Crystal system, space group	monoclinic, $P2_1/c$	
Unit cell parameters	a = 10.050(2) Å	α = 90°
	b = 17.757(4) Å	β = 105.611(4)°
	c = 18.502(4) Å	γ = 90°
Cell volume	3180.0(11) Å^3	
Z	4	
Calculated density	1.238 g/cm^3	
Absorption coefficient μ	0.760 mm^{-1}	
F(000)	1272	
Crystal colour and size	red, 0.18 × 0.16 × 0.16 mm^3	
	ω rotation with narrow frames	
θ range for data collection	2.29 to 28.26°	
Index ranges	h –13 to 13, k –23 to 22, l –23 to 23	
Completeness to θ = 26.00°	99.4 %	
Reflections collected	26073	
Independent reflections	7370 (R_{int} = 0.0875)	
Reflections with $F^2>2\sigma$	3726	
Absorption correction	semi-empirical from equivalents	
Min. and max. transmission	0.8754 and 0.8881	
Refinement method	Full-matrix least-squares on F^2	
Weighting parameters a, b	0.0539, 0.0000	
Data / restraints / parameters	7370 / 0 / 306	
Final R indices [$F^2>2\sigma$]	R1 = 0.0490, wR2 = 0.1035	
R indices (all data)	R1 = 0.1092, wR2 = 0.1164	
Goodness-of-fit on F^2	0.861	
Largest and mean shift/su	0.001 and 0.000	
Largest diff. peak and hole	0.525 and –0.656 e Å^{-3}	

Table 9.4. Crystal data and structure refinement for $[Ni(S_2CN^iBu_2)_2]$ (**21**).

Chemical formula	$C_{18}H_{36}N_2NiS_4$	
Formula weight	467.44	
Temperature	150(2) K	
Radiation, wavelength	MoKα, 0.71073 Å	
Crystal system, space group	monoclinic, $P2_1/c$	
Unit cell parameters	a = 11.851(3) Å	α = 90°
	b = 12.693(3) Å	β = 96.779(5)°
	c = 16.623(5) Å	γ = 90°
Cell volume	2483.1(11) Å^3	
Z	4	
Calculated density	1.250 g/cm^3	
Absorption coefficient μ	1.122 mm^{-1}	
F(000)	1000	
Crystal colour and size	green, 0.50 × 0.32 × 0.23 mm^3	
	ω rotation with narrow frames	
θ range for data collection	1.73 to 28.33°	
Index ranges	h –15 to 15, k –16 to 16, l –21 to 21	
Completeness to θ = 26.00°	99.5 %	
Reflections collected	18784	
Independent reflections	5749 (R_{int} = 0.0374)	
Reflections with $F^2>2\sigma$	4892	
Absorption correction	semi-empirical from equivalents	
Min. and max. transmission	0.6038 and 0.7824	
Refinement method	Full-matrix least-squares on F^2	
Weighting parameters a, b	0.0431, 0.0000	
Data / restraints / parameters	5749 / 0 / 370	
Final R indices [$F^2>2\sigma$]	R_1 = 0.0298, wR_2 = 0.0741	
R indices (all data)	R_1 = 0.0362, wR_2 = 0.0765	
Goodness-of-fit on F^2	1.038	
Largest and mean shift/su	0.001 and 0.000	
Largest diff. peak and hole	0.799 and –0.284 e Å^{-3}	